NORTHWESTERN UNIVERSITY

Superluminal and Subluminal Lasers for Precision Metrology

A DISSERTATION

SUBMITTED TO THE GRADUATE SCHOOL

IN PARTIAL FULFILLMENT OF THE REQUIREMENTS

for the degree

DOCTOR OF PHILOSOPHY

Field of Electrical Engineering and Computer Science

BY

Joshua Marcus Yablon

EVANSTON, IL

December 2017

ABSTRACT

Superluminal and Subluminal Lasers for Precision Metrology

Joshua Marcus Yablon

Optical interferometry is a powerful technique which has been widely utilized for well over a century in making the world's most precise measurements. By measuring how the interference between two waves is affected by a physical process, one can deduce the magnitude of this process. Because the wavelength of a typical laser beam is very short, the phase shift between two beams of light can be enormously affected by very small perturbations.

There will always be a need for even more sensitive interferometers. Our approach to increasing sensitivity is to use so-called fast-light (or superluminal) lasers and slow-light (or subluminal) lasers in which the group velocity of the intra-cavity lasing beam is faster and slower, respectively, than the vacuum speed of light. We have successfully demonstrated lasers with both superluminal and subluminal effects, which promise to be of significant utility in high precision optical metrological applications.

In this thesis, we first present the demonstration of a superluminal Diode-Pumped Alkali Laser (DPAL) with a Raman resonance induced dip in the center of the gain profile, with a factor of sensitivity *enhancement* as high as 190 relative to a conventional laser. This laser has potential applications in many precision measurement applications such as rotation, vibration, and

gravitational wave detection. We also present the demonstration of a subluminal Raman laser with a factor of sensitivity *suppression* as high as 663 relative to a conventional laser. Such a laser is highly self-stabilized, and is expected to have a far smaller Schawlow-Townes linewidth. As a result, this laser may also offer significant utility in the fields of high-precision optical metrology, as well as passive frequency stabilization.

ACKNOWLEDGEMENTS

I would like to first thank my primary adviser, Professor Selim Shahriar, for giving me the chance to study under his guidance. Selim welcomed me into his group when I first arrived at Northwestern, and he has taken an active role in my development as a student, scientist, engineer, and researcher, as well as my development as a person. Selim is extremely smart and knowledgeable, and is very generous with his time despite the fact that he is always busy. Although he and I have had occasional disagreements on how to solve a theoretical issue, how to design an experiment, or even how to word a particular sentence in a paper, I know that he cares about the best interests of the project as well as the students and postdocs working on them. I will always be indebted to Selim for the opportunity he gave me to work with him, and for the countless hours he dedicated to help me edit papers, discuss experimental issues, and dispense advice on science and life in general. I would also like to thank Professor Matthew Grayson and Professor Horace Yuen for participating on my thesis committee, and for providing me with valuable guidance and feedback during my PhD qualifying exam and prospectus exam. During my first two years in graduate school I took several fantastic courses with Professor Grayson, and am a much more edified and knowledgeable person (particularly in the fields of solid state physics and engineering) for having taken them.

All my past and present lab mates have been great to work with, and have been always willing to help in any way possible. In particular, I would like to thank Zifan Zhou and Shih Tseng for their help. Zifan helped me tremendously with computer simulations -- he was always eager to help, and we had many useful discussions, particularly about the many subtleties of laser dynamics. Without him, the “computer simulations” parts of this thesis (as well as my first-authored journal

articles) would not be nearly as thorough. Meanwhile, Shih built many of the circuits I used in my experiments. He is truly a circuit wizard -- he has been an indispensable resource for me (as well as for all the other grad students in our group) throughout graduate school, and many of the experiments I conducted simply would not have been possible without him. I would also like to thank Jeffrey Sundwall, the head of the Northwestern machine shop. Any time I needed a custom-built part from the machine shop, I would speak to Jeff about how to design these parts. He was highly knowledgeable and extremely competent, and almost always had advice on how to improve the design. Simply put, my research (and subsequently this thesis) would not have been possible without the help of such highly skilled and competent individuals. I will always be thankful for the opportunity to have collaborated with them.

I would like to thank my parents, Jay and Deborah Yablon, for being such dedicated parents. You have always taught me right from wrong and encouraged me to be the best person I can be. Thank you for always supporting me (financially and emotionally) and sticking by my side, even during the dreaded pre-teen and teenage years. Also, thank you to my sister Paula -- I know I wasn't always the easiest person to have as a big brother, but you somehow tolerated me all these years! Just two weeks ago Paula gave birth to a little bundle of joy named Ezra, and I'm excited to get to know him and watch him grow up.

I am one of the lucky few who has been fortunate to have known all four of my grandparents, two of whom are still alive today. They are both Holocaust survivors who managed to escape from their homeland of Germany during Hitler's reign of terror. As children, they watched family and friends get brutalized and murdered, and made enormous sacrifices and endured tremendous hardship so that my generation wouldn't have to. They have taught me to always be thankful for what I have, and that success can be achieved through hard work. My

grandfather came to the United States speaking not a word of English, yet worked his way through college, got his PhD in Electrical Engineering, and had a long and distinguished career. Refugees like my grandparents are what make America great.

Finally, I would like to thank my wife, Lindsey Shapiro Yablon, for always being there and supporting me throughout my graduate school experience. We met in in Chicago in June of 2011, and she has stuck with me since then, patiently waiting for me to get my PhD. Lindsey is a kind, thoughtful, intelligent, beautiful woman and I am incredibly lucky to have her as my wife. She is also the mother of my wonderful son Benjamin, who brightens my life every day with his toothless smile and his adorable baby noises. He may be only five months old, but I already cannot imagine a world without him.

TABLE OF CONTENTS

CHAPTER 1

INTRODUCTION TO OPTICAL INTERFEROMETRY

Optical interferometry has been utilized for well over a century in making the world's most precise measurements. The basic idea behind interferometry is quite simple: in order to detect and measure a physical process, one can measure how the interference between two waves is affected by this process. The principle of superposition (and therefore constructive and destructive interference) is characteristic of all waves so that interferometry can, in principle, be performed with any type of wave (water waves, waves on a string, electromagnetic waves, atomic waves, etc.) The reason electromagnetic waves are generally used for precision applications is because the wavelength of light is less than one micron (one millionth of a meter), so that the phase shift between two beams of light can be enormously affected by very small perturbations. It should also be mentioned that atomic waves, which have wavelengths several orders of magnitude smaller than electromagnetic waves, may one day replace electromagnetic waves as the paradigm of precision interferometry -- indeed, atomic wave interferometry is an active field of research, however the technology is likely several decades away from being feasible for most metrological applications.

The idea of using optical interferometry for precision measurements has been around since the 1860's when James Clerk Maxwell first discovered that light is an electromagnetic wave. One of the earliest and most significant successes of optical interferometry was the Michelson-Morley experiment [1], which was performed in the year 1887. At the time, physicists postulated that since light could propagate through vacuum, there must exist a medium called the "luminiferous aether" through which the propagation of electromagnetic radiation in vacuum is mediated. Albert

Michelson and Edward Morley supposed that unless the sun is universally at rest, the aether should have some non-zero velocity relative to the sun, so that the speed of the "aether wind" measured from the Earth should vary as the Earth revolves around the sun. This would imply that the speed of light should be slightly different in the Spring than it is in the Fall, due to different amounts of "aether drag". They built an interferometer to measure the interference fringes of light to see if the locations of these fringes varied over the course of a year. After failing to distinguish a first-order change in the locations of these fringes, they concluded that if the aether *does* exist, the Earth drags the aether along with it as it revolves around the sun. In subsequent experiments performed in the early 1900's [2,3,4,5,6,7], second-order changes in the interference fringes also went undetected, leading physicists to abandon the theory of the luminiferous aether altogether. This ultimately led to the discovery of the Lorentz transformation, eventually resulting in Einstein's theory of Special Relativity which not only *explained* the null result of the Michelson-Morley experiment, but in fact *required* it.

In the 21st century, optical interferometry continues to be an important technique for making precision measurements. In February of 2016, the Laser Interferometer Gravitational-Wave Observatory (LIGO), a worldwide collaboration with over 1,000 scientists across the globe, announced that after more than two decades of trying in earnest, they had finally detected their first gravitational wave [8]. This detection was the first of countless events that will be detected going forward -- the sensitivity of LIGO will only continue to improve, enabling it to detect events originating from weaker sources and from greater distances. As a result, LIGO should eventually be able to detect gravitational waves every second of every minute of every hour of every day. This has profound implications, because the ability to detect the signatures of gravitational radiation enables astrophysicists to measure and characterize the nature of astronomical events

such as black hole and neutron star mergers, supernova explosions, and may even provide direct evidence regarding the creation of the universe.

No matter how sensitive an interferometer is, there will always be a need to make it even more sensitive. For many years, our laboratory has investigated theoretically and experimentally how *slow light* (light with group velocity less than the vacuum speed of light) and *fast light* (light with group velocity greater than the vacuum speed of light) can be used to enhance optical interferometry. As will be described in this thesis, we have concluded that the best way to achieve such a goal is to use so-called fast-light (or *superluminal*) lasers and slow-light (or *subluminal*) lasers in which the group velocity of the *intra-cavity lasing beam* is faster and slower, respectively, than the vacuum speed of light. We have conducted several experiments where we successfully demonstrated the existence of superluminal and subluminal effects in lasers with corresponding enhancements and reductions in sensitivity. This thesis describes these experiments, the results of these experiments, and their significance.

1.1 Interference

A wide variety of physical effects can be detected by combining two (or more) beams of light and measuring the interference between them. Before the invention of lasers, white light was often used in interferometry, so that the location of an interference fringe depended on the particular wavelength component. When measuring the physical effect of interest, these fringes would shift; the magnitude of this shift would be used to determine the magnitude of the effect being measured.

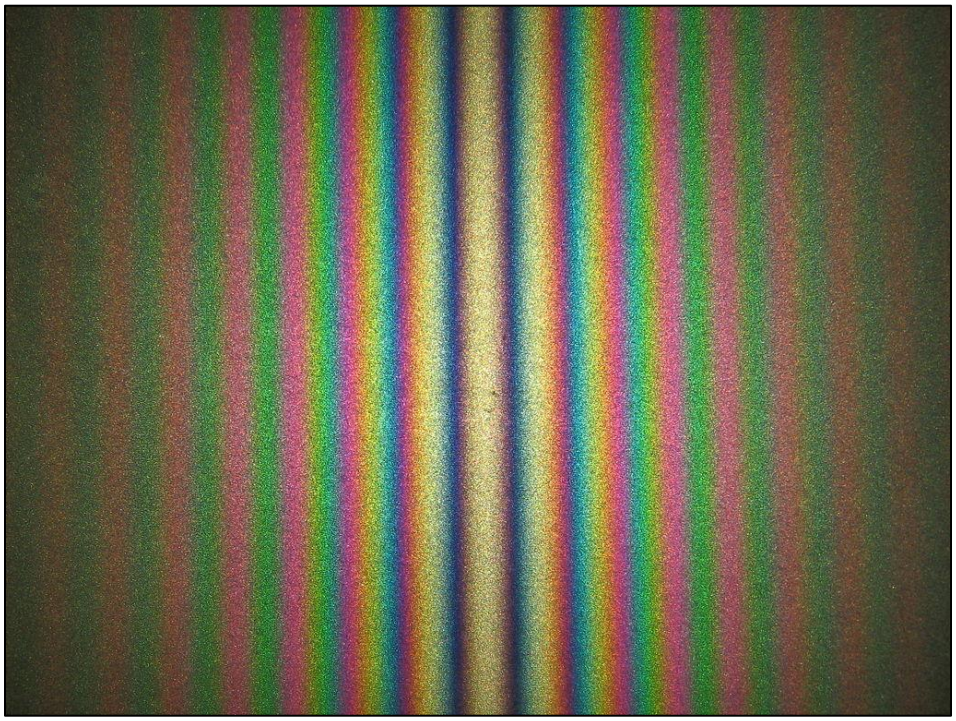

Fig. 1.1: Interference fringes resulting from white light propagating through a double slit. The m^{th} fringe for a particular wavelength λ is located at an angle θ_m such that $dsin(\theta_m) = m\lambda$, where d is the distance between slits.

In modern optical interferometry, lasers are almost always used as the light source because laser light is monochromatic, coherent, and collimated. The basic idea behind laser interferometry is to split a laser beam into two, let the beams propagate through their own paths, and finally

recombine them. Since laser light is coherent, it has a definite phase; the phase shift between the two beams is indicative of the optical path length difference between the two paths. Due to the short wavelength of light (on the order of half a micron), a very small perturbation can result in a very large phase shift. The magnitude of this phase shift is related to the amplitude of the resulting interference signal, as shown in Figure 1.2. This amplitude is proportional to the square root of intensity, which is measured with a photodetector.

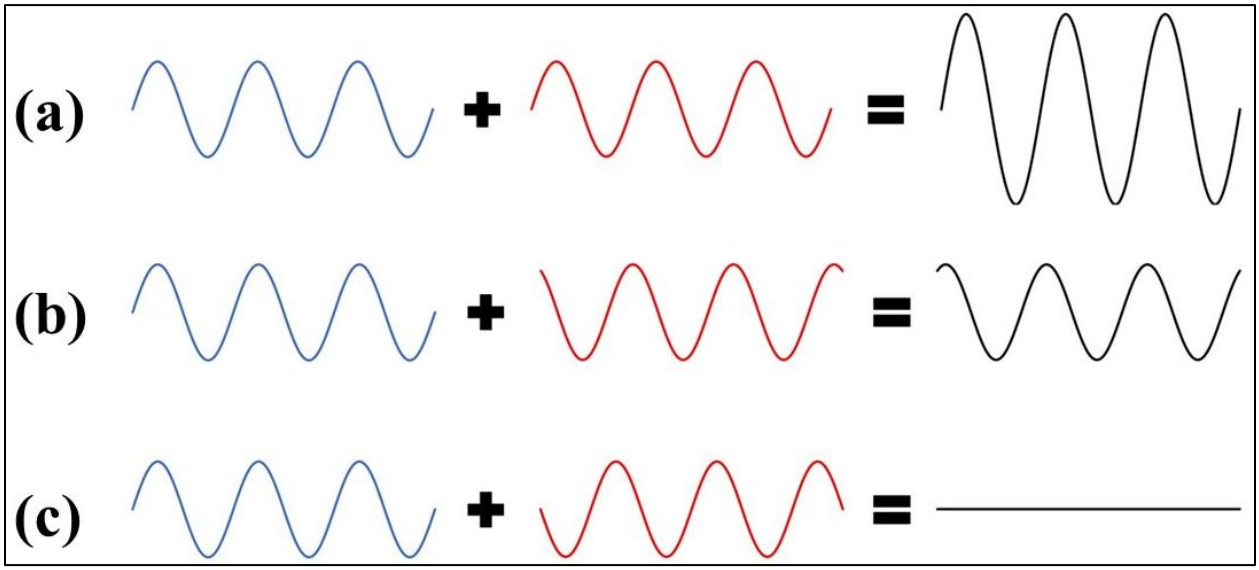

Fig. 1.2: Varying degrees of constructive/destructive interference. (a) Beams are in phase, so that the sum has twice the amplitude of the constituent parts. This interference is fully constructive; (b) Beams are 2 radians out of phase; in this case, the sum is approximately equal in amplitude to the constituent parts; (c) beams are 180° out of phase so that the sum is null. This interference is fully destructive.

There are many types of optical interferometers such as Michelson, Sagnac, Fizeau, Fabry-Pérot, Mach-Zehnder, and many more. The following section will describe a few examples of these interferometers, how they work, and situations in which different types of interferometers would be used to make different types of measurements.

1.2 Examples of Interferometers

1.2.1 Michelson Interferometer

The Michelson interferometer may be one of the simpler types of interferometers, but it is also one of the most historically important, as it was used in the Michelson-Morley experiment [1] and is used currently in LIGO. In such a setup, a laser beam is split into two by a 50/50 beam splitter (labeled BS in Figure 1.3). The beam propagating in the y-direction travels a distance of L_1, hits a mirror, and propagates back, thus traveling a total distance of $2L_1$ before arriving back at the BS. Similarly, the beam propagating in the x-direction travels a distance of $2L_2$ before arriving back at the BS. The BS then combines these beams and diverts it into a photodetector.

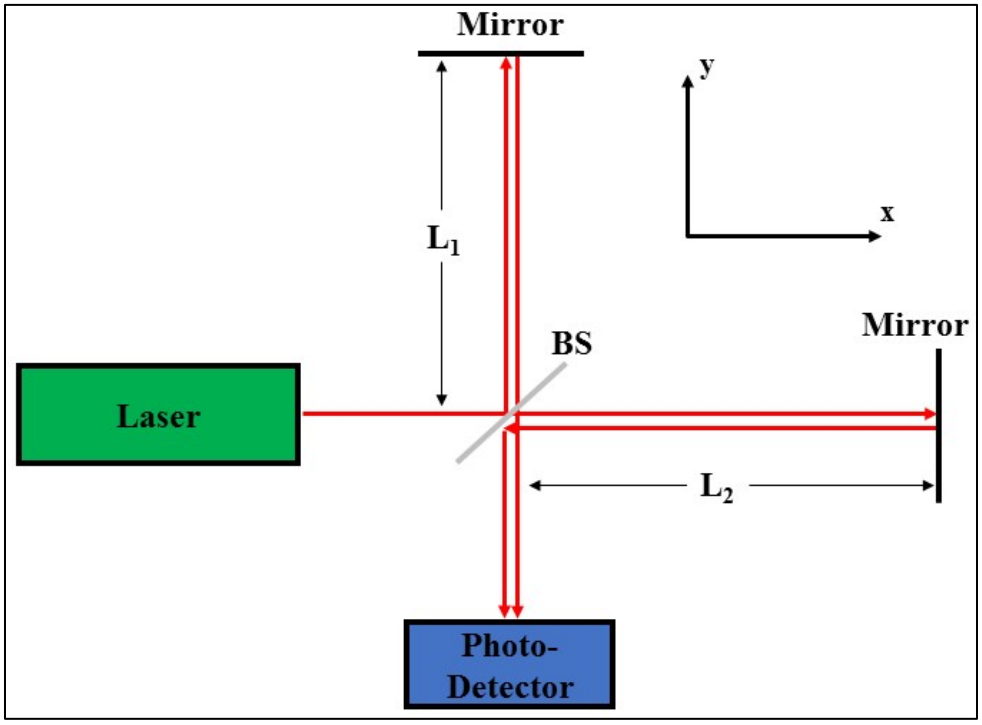

Fig. 1.3: Schematic of Michelson interferometer

When the laser beam first hits the BS, the electric field can be written as $\vec{E} = \overrightarrow{E_o} e^{-i\omega t}$, so that upon re-arrival at the BS, the electric fields of beam 1 and beam 2, $\overrightarrow{E_1}$ and $\overrightarrow{E_2}$, respectively, are:

$$\overrightarrow{E_1} = \frac{\overrightarrow{E_o}}{2} e^{i(2kL_1 - \omega t)} \tag{1.1}$$

$$\overrightarrow{E_2} = \frac{\overrightarrow{E_o}}{2} e^{i(2kL_2 - \omega t)} \tag{1.2}$$

where $k = \left|\vec{k}\right| = \frac{2\pi}{\lambda}$ is the wavevector and $\omega = 2\pi f$ is the (angular) frequency of the beam. The BS combines these two beams (while throwing away half the power from each of them), so that the electric field entering the photodetector is:

$$\overrightarrow{E_{PD}} = \frac{\overrightarrow{E_1} + \overrightarrow{E_2}}{2} = \frac{1}{2}\left(\frac{\overrightarrow{E_o}}{2} e^{i(2kL_1 - \omega t)} + \frac{\overrightarrow{E_o}}{2} e^{i(2kL_2 - \omega t)}\right) = \frac{\overrightarrow{E_o}}{4} e^{-i\omega t}\left(e^{i2kL_1} + e^{i2kL_2}\right) \tag{1.3}$$

The intensity received by the photodetector is proportional to the square of the electric field:

$$\begin{aligned} I = \frac{cn\varepsilon_o}{2}\left|\overrightarrow{E_{PD}}\right|^2 &= \frac{cn\varepsilon_o {E_o}^2}{8}\left|e^{-i\omega t}\right|^2 [1 + \cos(2k(L_2 - L_1))] \\ &= \frac{cn\varepsilon_o {E_o}^2}{4}\left|e^{-i\omega t}\right|^2 cos^2(k(L_2 - L_1)) \end{aligned} \tag{1.4}$$

where *n* is the refractive index, which is approximately unity in air. Even the fastest available photodetectors have sampling rates several orders of magnitude lower than optical frequencies, so that the *time-averaged* intensity is the physically-relevant quantity.

$$\langle I \rangle = \frac{cn\varepsilon_o {E_o}^2}{4}\langle\left|e^{-i\omega t}\right|^2\rangle cos^2(k(L_2 - L_1)) = \frac{cn\varepsilon_o {E_o}^2}{8} cos^2(k(L_2 - L_1)) \tag{1.5}$$

Therefore, intensity maxima are seen when $\Delta L \equiv L_2 - L_1 = 0, \pm\frac{\lambda}{2}, \pm\lambda, \pm\frac{3\lambda}{2}$, etc. while intensity minima are seen when $\Delta L = \pm\frac{\lambda}{4}, \pm\frac{3\lambda}{4}, \pm\frac{5\lambda}{4}$, etc. In a scenario where one of the mirrors

is fixed while the other mirror is moveable, the photodetector signal goes from a maximum to a minimum when the mirror is displaced by a distance of $\lambda/4$. Since optical wavelengths are a few hundred nanometers in length, the Michelson interferometer measures displacements quite sensitively. One of the most famous and modern uses of Michelson interferometry is in the detection of gravitational waves, which will be described in the next section.

1.2.2 Gravitational Wave Detector

Gravitational radiation is produced by the acceleration of mass, analogous to how electromagnetic radiation is produced by the acceleration of charge. The Einstein field equations [9] are a set of ten differential equations governing the behavior of gravitational waves, analogous to how Maxwell's equations govern the behavior of electric and magnetic fields. However, gravitational waves are far more difficult to detect than their electromagnetic counterparts because gravitational forces are generally much weaker than electromagnetic forces. The strongest (and therefore easiest-to-detect) gravitational waves come from large astronomical events such as black hole mergers, but because these events most often occur millions (or billions) of light years away, the gravitational radiation is very weak by the time it reaches Earth. In the far field, the phase fronts of a gravitational wave are planar and the Einstein field equations are simplified. If the propagation direction of a far-field gravitational wave is denoted as z, then the x and y components of the spacetime metric can be written as:

$$dx^2 = c^2[1 + hcos(\omega_{GRAV}t)]dt^2 \tag{1.6}$$

$$dy^2 = c^2[1 - hcos(\omega_{GRAV}t)]dt^2 \tag{1.7}$$

where x and y are the "polarization axes" while h and ω_{GRAV} are the stress/strain coefficient and angular frequency, respectively, of the gravitational wave. Equations 1.6 and 1.7 indicate that a gravitational wave stretches and compresses space in the x and y directions in a manner such that when one polarization direction is fully stretched, the other direction is fully compressed. This process of stretching and compressing occurs at a frequency of ω_{GRAV} and with a strain (fractional change in length) of h. The reason gravitational waves are incredibly difficult to detect is because h is very small (usually no more than 10^{-20}). Because $h \ll 1$, Equations 1.6 and 1.7 can be approximated as:

$$dx \cong c\left[1 + \frac{h}{2}(\omega_{GRAV}t)\right]dt \tag{1.8}$$

$$dy \cong c\left[1 - \frac{h}{2}(\omega_{GRAV}t)\right]dt \tag{1.9}$$

To detect a gravitational wave, a Michelson interferometer can be set up as shown in Figure 1.4. Without loss of generality, the following calculation assumes that the gravitational wave propagates in the z-direction, that the legs of the interferometer (the x- and y- axes) are aligned with the polarization of the gravitational wave, and that each leg has a length of L.

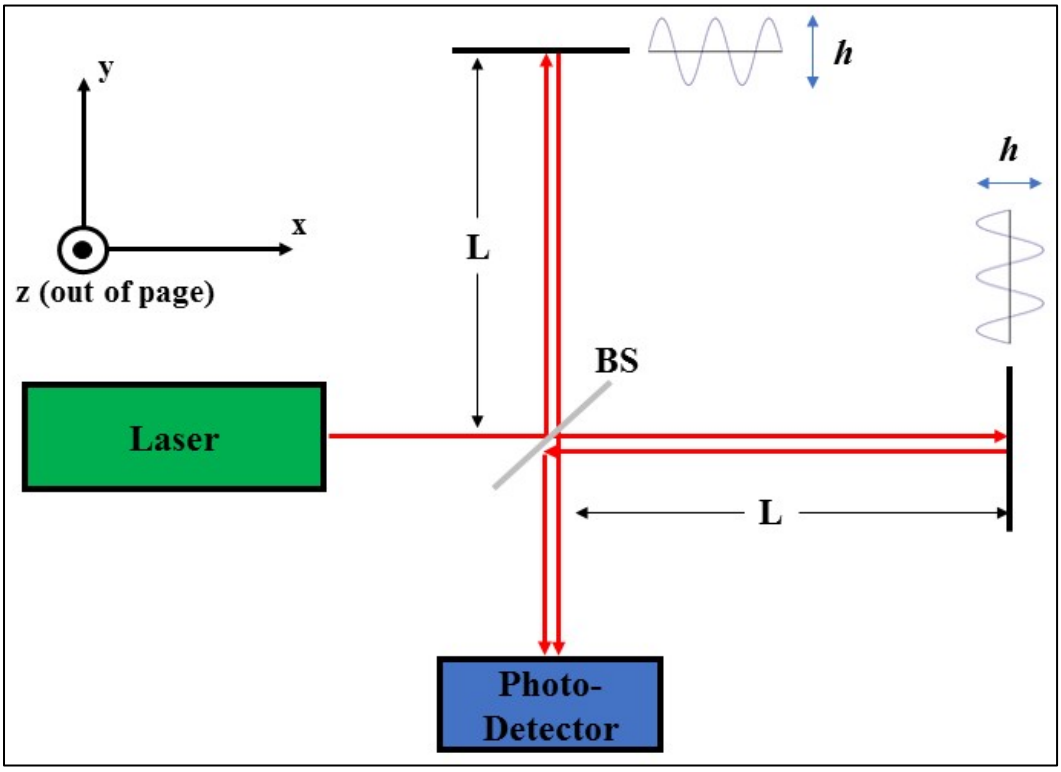

Fig. 1.4: Michelson Interferometer with a far-field gravitational wave propagating through it

If the optical frequency emitted from the laser is ω, then the instantaneous differential phases in the x- and y-directions are:

$$\delta\varphi_X = \frac{\omega h}{2} cos(\omega_{GRAV} t) \tag{1.10}$$

$$\delta\varphi_Y = -\frac{\omega h}{2} cos(\omega_{GRAV} t) \tag{1.11}$$

Because the legs of gravitational wave detectors are long (for example, in LIGO, L=4 km), the phase of the gravitational wave and therefore the values of $\delta\varphi_X$ and $\delta\varphi_Y$ can change as the light is propagating through the interferometer. Therefore, upon arrival at the photodetector, the accumulated phase delays are:

$$\Delta\varphi_X = \int_{t'=t}^{t'=t+\tau} (\delta\varphi_X)dt' = \frac{\omega h}{2}\int_{t'=t}^{t'=t+\tau} cos(\omega_{GRAV}t')dt'$$

$$= \frac{\omega h}{2\omega_{GRAV}}\left[sin\big(\omega_{GRAV}(t+\tau)\big) - sin(\omega_{GRAV}(t)\right] \quad (1.12)$$

$$= \frac{\omega h}{2\omega_{GRAV}}\left[sin\left(\omega_{GRAV}\left(t+\frac{2L}{c}\right)\right) - sin(\omega_{GRAV}(t)\right]$$

$$\Delta\varphi_Y = -\Delta\varphi_X = \frac{\omega h}{2\omega_{GRAV}}\left[sin(\omega_{GRAV}(t) - sin\left(\omega_{GRAV}\left(t+\frac{2L}{c}\right)\right)\right] \quad (1.13)$$

where $\tau \equiv \frac{2L}{c}$ is the light propagation time inside the interferometer. Therefore, the phase difference between the two beams upon re-arrival at the beam splitter is:

$$\Delta\varphi = \Delta\varphi_X - \Delta\varphi_Y = \frac{\omega h}{\omega_{GRAV}}\left[sin\big(\omega_{GRAV}(t+\tau)\big) - sin(\omega_{GRAV}t)\right] \quad (1.14)$$

Therefore, the sum of the electric fields entering the photodetector is:

$$\vec{E} = \vec{E}_1 + \vec{E}_2 = \frac{\vec{E}_o}{2}cos\left(\omega t - \frac{\Delta\varphi}{2}\right) + \frac{\vec{E}_o}{2}cos\left(\omega t + \frac{\Delta\varphi}{2}\right) \quad (1.15)$$

For $|\Delta\varphi| \ll 1$, $cos\left(\omega t \pm \frac{\Delta\varphi}{2}\right) \cong cos(\omega t) \mp \frac{\Delta\varphi}{2}sin(\omega t)$. Therefore:

$$\vec{E} \cong \vec{E}_o\left[cos(\omega t) + \frac{\Delta\varphi}{2}sin(\omega t)\right]$$

$$= \vec{E}_o\Big\{cos(\omega t) \quad (1.16)$$

$$+ \frac{\omega h}{\omega_{GRAV}}\left[sin\big(\omega_{GRAV}(t+\tau)\big) - sin(\omega_{GRAV}t)\right]sin(\omega t)\Big\}$$

Therefore, there are sidebands with frequencies of $\omega_N \equiv \omega \pm N\omega_{GRAV}$, where N is an integer. This is because the gravitational wave provides *phase modulation* on the two interfering beams. The

first-order sidebands ($N = \pm 1$) are the least difficult to detect. The intensities of the first-order sidebands, $\left|\overrightarrow{E_{SB}}\right|^2$ are:

$$\frac{\left|\overrightarrow{E_{SB}}\right|^2}{\left|\overrightarrow{E_o}\right|^2} = \left(\frac{\omega h}{\omega_{GRAV}}\right)^2 sin^2(\omega_{GRAV}\tau) \tag{1.17}$$

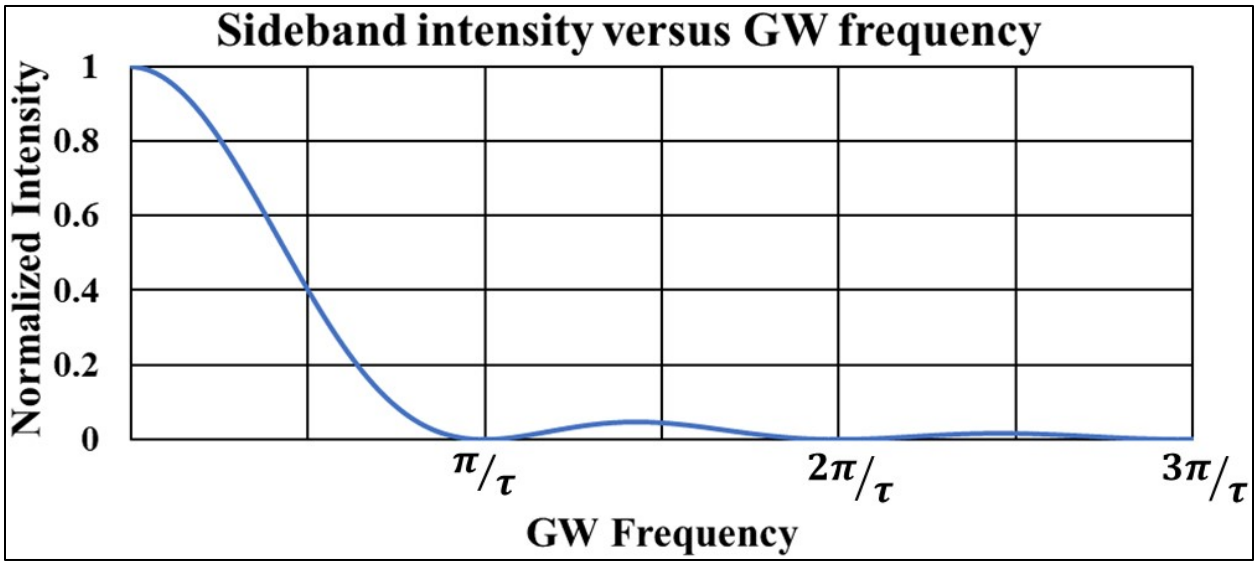

Fig. 1.5: Normalized intensity of the first-order sidebands in the Michelson gravitational wave detector

Evidently the detector sensitivity is highest for low-frequency gravitational waves ($\omega_{GRAV} \ll \frac{\pi}{\tau}$), and has "dead bands" located at integer multiples of π/τ. The LIGO detectors have arms that are 4 km long so that $\tau = \frac{2L}{c} = 26.7\ \mu s$; thus, gravitational wave frequencies at integer multiples of 117.8 kHz cannot be detected. Most gravitational waves of interest have frequencies as low as 1 Hz and as high as a few kHz, so these dead bands are not much of an issue in most cases.

In February 2016, LIGO announced the first direct detection of a gravitational wave emitted from a binary black hole merger [8]. This international collaboration with over 1,000

scientists across the world had finally made the first successful detection of a gravitational wave after working on this project for over 20 years. With a strain of approximately 10^{-20}, the 4 km legs expanded and contracted by a length less than the diameter of a proton. The detection of these miniscule perturbations was arguably the most impressive feat of engineering ever achieved by humankind, and, more importantly, opened a new realm of experimental astrophysics which had been previously inaccessible. Since then, LIGO has detected several more gravitational waves, and continues to improve detector sensitivity and data analysis methods.

1.2.3 Sagnac Interferometer

The Sagnac interferometer is a type of optical interferometer which finds most of its applications in the field of gyroscopy, which is the measurement of rotation. In a Sagnac interferometer, a laser beam is split into two; the transmitted beam travels counter-clockwise around a loop while the reflected beam travels clockwise, as shown in Figure 1.6. These two beams overlap spatially so that if there is no rotation ($\Omega = 0$), the two beams propagate the same distance and over the same period of time, and therefore arrive back at the BS in phase, thus undergoing constructive interference. However, in the presence of rotation, one beam travels slightly farther (and takes a slightly longer time) than the other beam, so that they arrive back at the BS with a non-zero phase difference. This phase difference results in some degree of destructive interference, which is seen by the photodetector as a reduction in intensity.

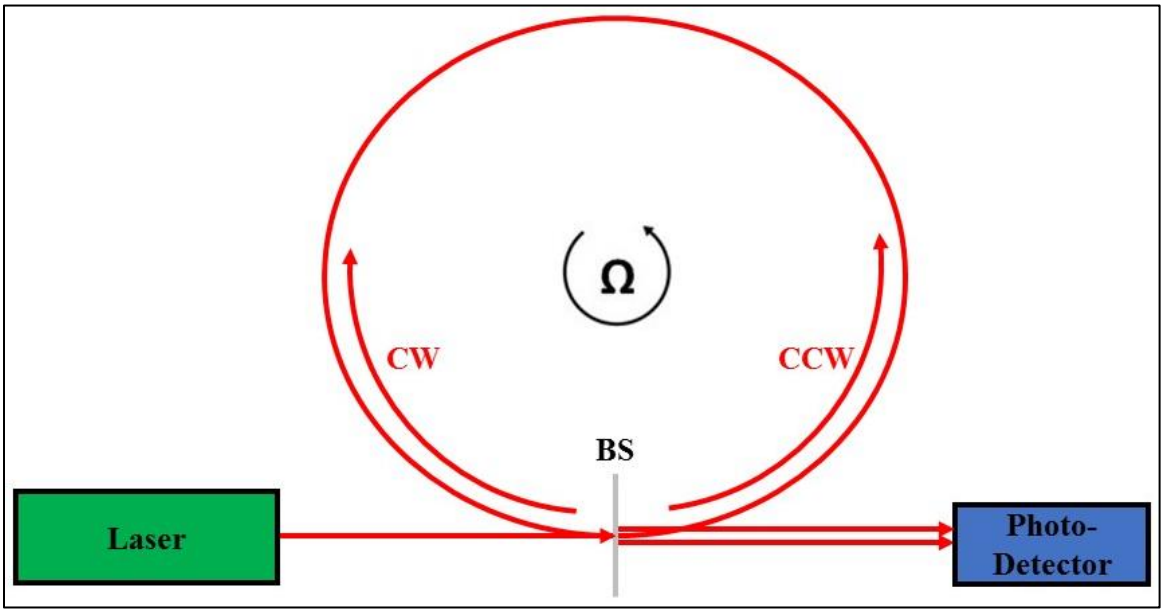

Fig. 1.6: A Sagnac interferometer. For simplicity of our calculation, we have drawn a circular loop. However, a Sagnac interferometer can be triangular, rectangular, etc.

If the radius of the loop is R and the rate of rotation is Ω, relativistic addition of velocities gives the velocity of the counter-clockwise-propagating phase front as:

$$V_{CCW} = \frac{V_{PH} + R\Omega}{1 + \left(\frac{V_{PH} R\Omega}{c^2}\right)} \tag{1.18}$$

while the velocity of the clockwise-propagating phase front is:

$$V_{CW} = \frac{V_{PH} - R\Omega}{1 - \left(\frac{V_{PH} R\Omega}{c^2}\right)} \tag{1.19}$$

where $V_{PH} \equiv \frac{c}{n}$ is the phase velocity of light, where n is the refractive index of the medium filling the interferometer. The distance traveled by the counter-clockwise beam exceeds that traveled by the clockwise beam, with roundtrip paths given by:

$$L_{CCW} = 2\pi R + R\Omega t_{CCW} \tag{1.20}$$

$$L_{CW} = 2\pi R - R\Omega t_{CCW} \tag{1.21}$$

where t_{CCW} and t_{CW} are the roundtrip propagation times of the counter-clockwise and clockwise phase fronts, respectively. The definition of velocity yields:

$$t_{CCW} = \frac{L_{CCW}}{V_{CCW}} \tag{1.22}$$

$$t_{CW} = \frac{L_{CW}}{V_{CW}} \tag{1.23}$$

Putting together equations 1.20 and 1.22 and equations 1.21 and 1.23 results in:

$$t_{CCW} = \frac{2\pi R}{V_{CCW} - R\Omega} = \frac{2\pi R(c^2 + R\Omega V_{PH})}{V_{PH}(c^2 - (R\Omega)^2)} \tag{1.24}$$

$$t_{CW} = \frac{2\pi R}{V_{CW} + R\Omega} = \frac{2\pi R(c^2 - R\Omega V_{PH})}{V_{PH}(c^2 - (R\Omega)^2)} \tag{1.25}$$

The time delay between the two beams is therefore:

$$\Delta t_o = t_{CCW} - t_{CW} = \frac{4\pi R^2 \Omega}{c^2 - (R\Omega)^2} = \frac{4A\Omega}{c^2 - (R\Omega)^2} = \frac{4A\Omega}{c^2(1 - \beta^2)} \tag{1.26}$$

where $A = \pi R^2$ is the area enclosed and $\beta \equiv \frac{R\Omega}{c}$. In the non-relativistic limit, $\beta \ll 1$, so that:

$$\Delta t_o \approx \frac{4A\Omega}{c^2} \tag{1.27}$$

Therefore, the phase difference between the two beams is:

$$\Delta\varphi_o = \omega \Delta t_o = \frac{4A\Omega\omega}{c^2} = \frac{8\pi A\Omega}{c\lambda_o} \tag{1.28}$$

where ω and λ_o are the angular frequency and vacuum wavelength of the laser, respectively. More generally, if the axis of rotation is not perpendicular to the gyroscope, then:

$$\Delta\varphi_o = \frac{8\pi \vec{A} \cdot \vec{\Omega}}{c\lambda_o} \tag{1.29}$$

where $\vec{A}$ is the "area vector" which has a magnitude of A and is perpendicular to the gyroscopic plane, and $\vec{\Omega}$ is the angular velocity vector. According to Equation 1.29, the phase shift is proportional to enclosed area. It can be shown using Stokes' theorem that the phase shift (in the non-relativistic limit where $R\Omega \ll c$) is always proportional to enclosed area, regardless of shape [10]. In addition, the phase shift is independent of refractive index. This result may be counter-intuitive, but it arises from the fact that the medium is *co-rotating* with the rest of the apparatus. As will be shown in Chapter 2, the lack of dependence on the refractive index ceases to exist when the medium is not co-rotating with the rest of the interferometer.

CHAPTER 2

DISPERSION IN OPTICAL METROLOGY

2.1 Introduction to Dispersion

The index of refraction governs the angle at which light refracts when passing through a boundary from medium 1 (the incident medium) to medium 2 (the transmitted medium) via Snell's law: $n_1 sin(\theta_1) = n_2 sin(\theta_2)$, where θ_1 and θ_2 the respective angles of incidence, measured relative to the normal. If the index of a medium is dependent on the frequency of the light propagating through it, then different frequencies refract at different angles. One of the most famous examples of this is the prism, shown in Figure 2.1.

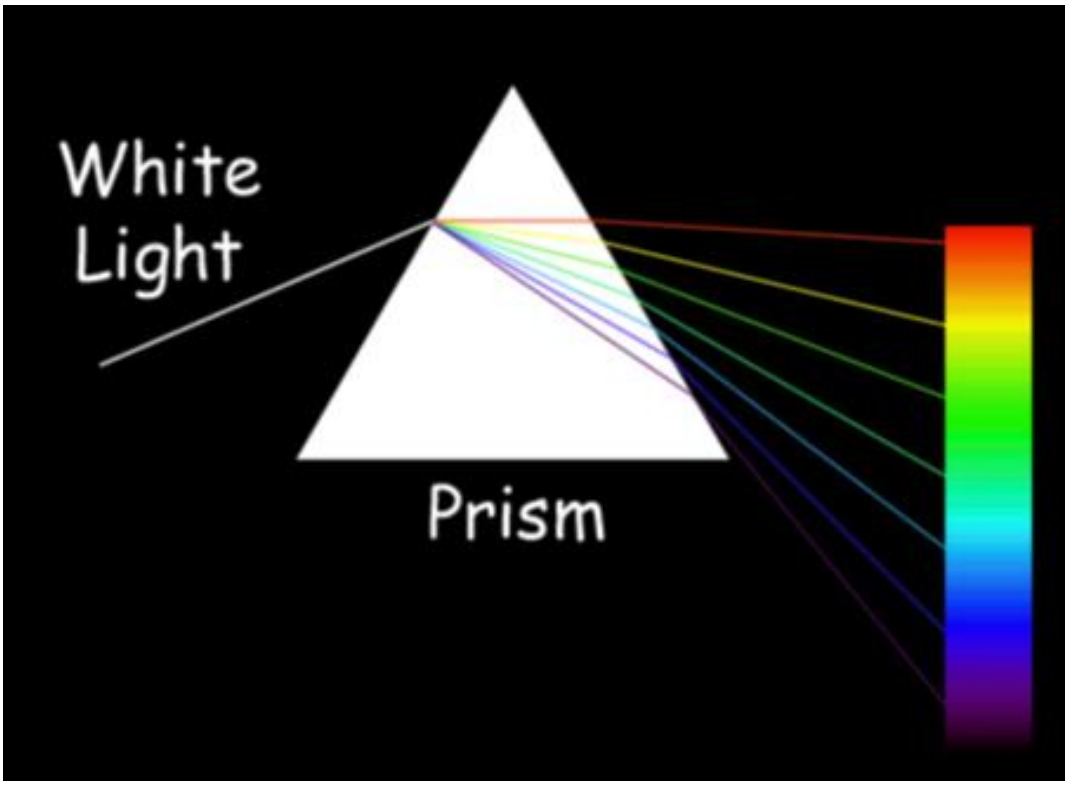

Fig. 2.1: The angle of refraction is governed by Snell's law. Because the index in glass is wavelength-dependent, a prism separates white light into a rainbow, where red has the longest visible wavelength and violet has the shortest visible wavelength.

A prism spatially separates different frequencies because the index of refraction of glass is not constant in the optical frequency regime. The index as a function of (vacuum) wavelength in glass is shown in Figure 2.2, which shows that within the visible range of the electromagnetic spectrum, the plot of index versus wavelength has a non-zero slope.

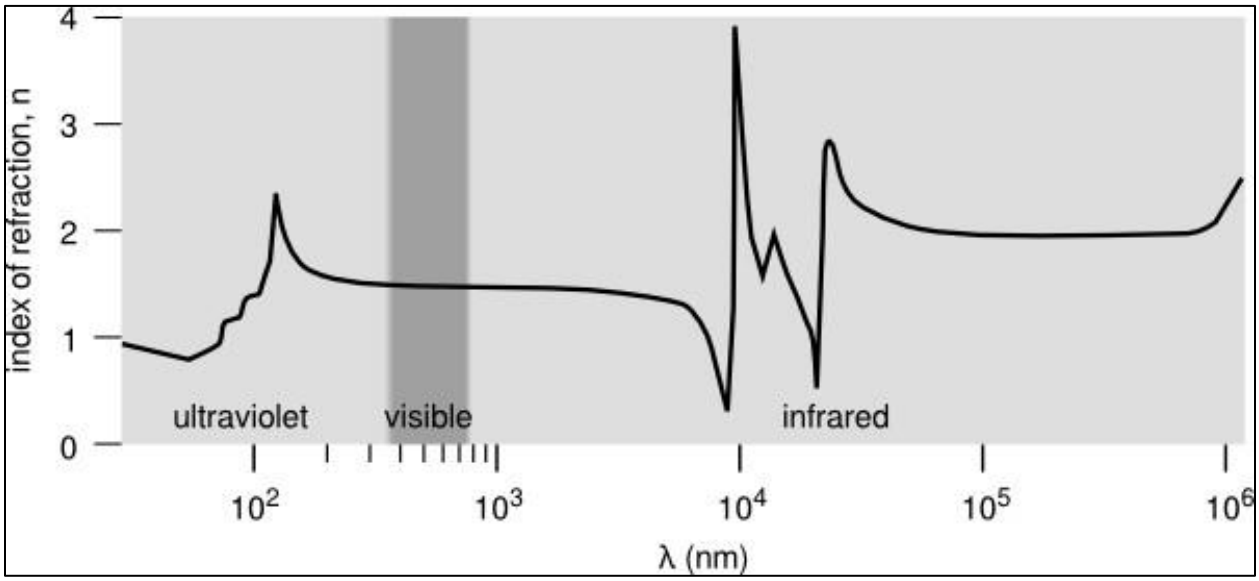

Fig. 2.2: Index of glass versus optical wavelength. Outside the visible spectrum, the curve has many sharp peaks and valleys. However, in the visible range, the index has a roughly-constant slope. This non-zero slope causes the prism to spatially separate optical wavelengths into a rainbow.

The index of refraction also governs the velocity at which light propagates through a medium, with the relationship $v = \frac{c}{n}$, where c is the speed of light in vacuum. If an electromagnetic pulse propagates through a medium with a frequency-dependent index, then different spectral components of this pulse have different velocities, which causes the pulse to spread out or *disperse* as it propagates through the medium. As such, a medium with a frequency-dependent refractive index is said to exhibit *dispersion*. In reality, all media (aside from vacuum) exhibit dispersion, because the phenomenon of dispersion fundamentally arises from the interaction between atoms and light, as will be shown in Chapter 3.

In the absence of dispersion, all electromagnetic frequencies propagate with the same velocity v, so that $v = f\lambda$ for all values of f and λ, or equivalently, $\omega = kv$ for all values of ω and k, meaning that ω increases linearly with k. On the other hand if ω is *not* linear in k (i.e. $\frac{d\omega}{dk} \neq constant$), then the medium is dispersive. Consider a dispersive medium in which the first two terms of the Taylor expansion of $\omega(k)$ around a central frequency ω_o (with corresponding central wave vector k_o) are considered:

$$\omega(k) \cong \omega_o + \left.\frac{d\omega}{dk}\right|_{k=k_o} \cdot (k - k_o) \equiv \omega_o + \omega_o{}' \cdot (k - k_o) \tag{2.1}$$

Consider now a "wave packet" which is spectrally-narrow enough so that all frequency components are within the spectral region where this approximation of linear dispersion is valid. If this wave packet propagates in the x-direction through the medium, then the electric field of the wave packet at time $t = 0$, denoted as $E(x, t = 0)$, can be spectrally decomposed as follows:

$$E(x, t = 0) = \int_{-\infty}^{\infty} \mathcal{E}(k) e^{ikx} dk \tag{2.2}$$

where $\mathcal{E}(k) = \mathcal{F}\{E(x, t = 0)\}$ is the one-dimensional spatial Fourier transform of the electric field at $t = 0$. After $t = 0$, the electric field can be expressed as:

$$\begin{aligned} E(x,t) &= \int_{-\infty}^{\infty} \mathcal{E}(k) e^{i(kx - \omega t)} dk = \int_{-\infty}^{\infty} \mathcal{E}(k - k_o) e^{i\{(k-k_o)x - \omega t\}} d(k - k_o) \\ &= e^{i(k_o x - \omega_o t)} \int_{-\infty}^{\infty} \mathcal{E}(k) e^{i(k-k_o)(x - \omega_o' t}\, dk \end{aligned} \tag{2.3}$$

The term before the integral is a monochromatic wave with velocity $v = \frac{\omega_o}{k_o}$, which is called the "phase velocity". The second term gives the "envelope" of the wave packet, which evidently

propagates at a velocity of $\omega_o' = \left.\frac{d\omega}{dk}\right|_{k=k_o}$. This is called the "group velocity". Group velocity can also be expressed in terms of the refractive index and its first derivative with respect to frequency:

$$v_g = \frac{d\omega}{dk} = \frac{c}{n_o + \omega_o \frac{dn}{d\omega}} \tag{2.4}$$

where n_o is the index of refraction corresponding to the phase velocity $\frac{\omega_o}{k_o}$. The "group velocity refractive index" or *group index*, n_g, is defined in a manner analogous to that of the normal (phase velocity) refractive index:

$$n_g \equiv \frac{c}{v_g} = n_o + \omega_o \frac{dn}{d\omega} \tag{2.5}$$

When $n_g > 1$, the group velocity is less than c, which is called "subluminal" or "slow light". When $n_g < 1$, the group velocity is greater than c, which is called "superluminal" or "fast light".

The *susceptibility* of a material, $\tilde{\chi}$, is a complex number which will be discussed more in Chapter 3; for the purposes of the current discussion, the real part of $\tilde{\chi}$, $Re[\tilde{\chi}] \equiv \chi_R$, is defined as follows:

$$n = \sqrt{1 + \chi_R} \tag{2.6}$$

If $\chi_R \ll 1$, which is the case for dilute atomic media, then $n = \sqrt{1 + \chi_R} \cong 1 + \frac{\chi_R}{2}$, so that:

$$n_g = n_o + \omega_o \frac{dn}{d\omega} \cong 1 + \frac{\chi_R}{2} + \frac{\omega_o}{2} \frac{d\chi_R}{d\omega} \tag{2.7}$$

2.2 Using Dispersion to Enhance Interferometry

Equipped with an understanding of dispersion, we now can try to implement dispersion into optical interferometry for the purpose of enhancing sensitivity. We will first solve the case of the *Sagnac interferometer* with a *non-co-rotating*, *linearly-dispersive* medium. This is followed by analysis of a Sagnac *resonator* with a *co-rotating*, linearly-dispersive medium, as well as the Sagnac resonator with a co-rotating, *non-linearly-dispersive* medium. After analyzing the benefits and drawbacks of each of these systems, we finally solve the case of the *Sagnac laser* with a *co-rotating*, *non-linearly-dispersive* medium, which we believe is the most promising system in which to enhance metrological sensitivity via material dispersion, for reasons which will be shown in this chapter. Although this chapter is dedicated to the analysis of enhancement in Sagnac interferometers, it is important to note that this analysis can be extended to all types of optical interferometers.

2.2.1 Slow-Light Enhancement in a Sagnac Interferometer

At the end of Chapter 1, we derived the somewhat counter-intuitive result that the sensitivity of a Sagnac interferometer is independent of *n*, the refractive index of the medium filling it. As will be shown in this section, the sensitivity *does* depend on index when the medium is *not* co-rotating with the rest of the apparatus. To solve the case of a *non-co-rotating* medium, it is instructive to consider the scenario illustrated in Figure 2.3, where an intra-cavity medium with constant index n_o fills the cavity and flows with velocity V_M relative to the rest frame of the gyroscope.

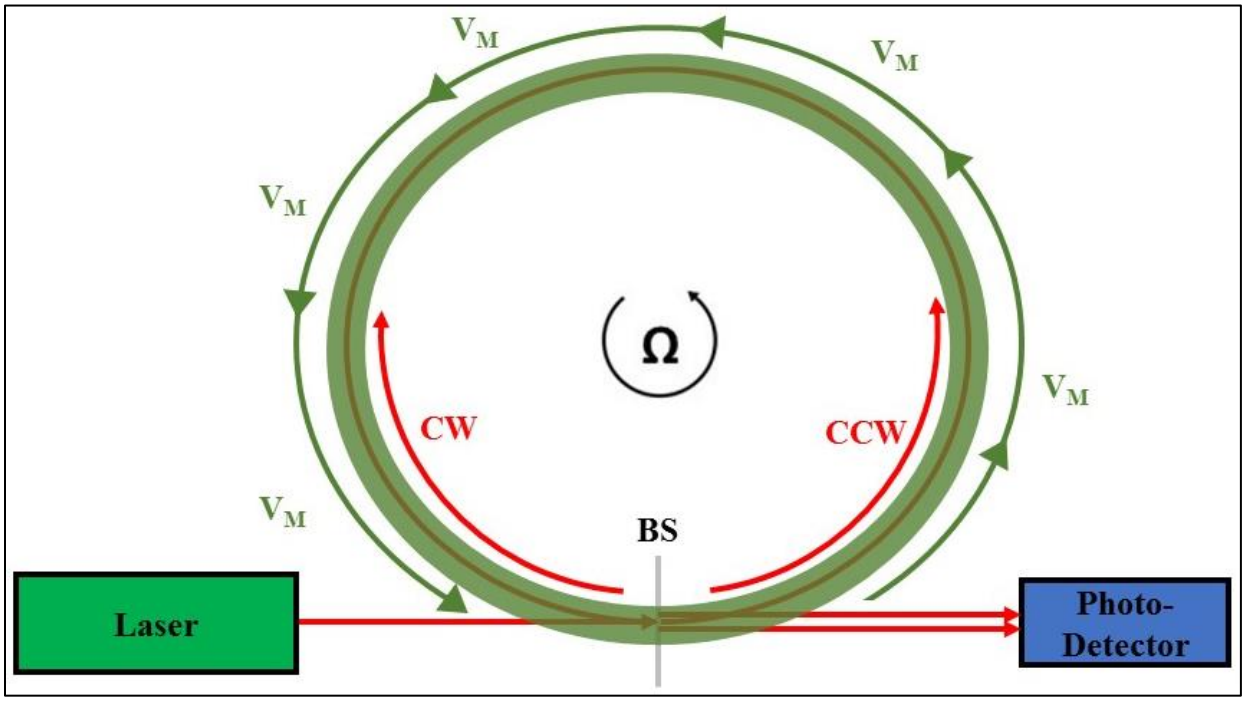

Fig. 2.3: Sagnac interferometer with non-co-moving medium

The scenario in which the reference frame and laser source are non-rotating while the medium is rotating is equivalent to a scenario in which the reference frame and laser source are rotating while the medium is non-rotating. In this case, Fresnel drag results in the two beams being Doppler shifted relative to one another, which causes the beam in one direction to be upshifted in frequency with a corresponding downshift of frequency in the opposite direction. This Doppler-induced splitting of frequencies opens the possibility of investigating the effects of dispersion, in which case the two directions would experience different refractive indices.

From the reference frame of the medium, the Doppler shifts in the counter-clockwise and clockwise beams are:

$$\Delta\omega_{CCW} = \frac{\omega V_M}{c} \tag{2.8}$$

$$\Delta\omega_{CW} = -\frac{\omega V_M}{c} \tag{2.9}$$

where V_M is the velocity of the medium relative to the rest of the apparatus, as denoted in Figure 2.3. In the case of a constant-index (non-dispersive) medium, the velocity of the counter-clockwise and clockwise phase fronts relative to a stationary non-rotating frame are:

$$v_{CCW} = \frac{c}{n_o} + v\left(1 - \frac{1}{{n_o}^2}\right) \tag{2.10}$$

$$v_{CW} = \frac{c}{n_o} - v\left(1 - \frac{1}{{n_o}^2}\right) \tag{2.11}$$

where n_o is the refractive index of the medium filling the gyroscope, and $v = R\Omega$. The factor of $1 - \frac{1}{{n_o}^2}$ is called the Fresnel drag coefficient [11] which arises from the fact that light is slowed down or sped up inside the medium when the medium is moving relative to the light source. If the dispersion relation is Taylor-expanded around a frequency of ω_o, then to first-order, the refractive index takes on the following form:

$$n(\omega) \simeq n(\omega_o) + (\omega - \omega_o)\cdot\frac{\partial n}{\partial\omega}\Big|_{\omega=\omega_o} \equiv n_o + \Delta\omega\cdot\frac{\partial n}{\partial\omega} \tag{2.12}$$

In such a medium, the velocity of the counter-clockwise and clockwise phase fronts relative to a stationary non-rotating frame are:

$$v_{CCW} = \frac{c}{n_o}\left(1 - \frac{1}{n_o}\left(\Delta\omega_{CCW}\cdot\frac{\partial n}{\partial\omega}\right)\right) + v\left(1 - \frac{1}{{n_o}^2}\right) \tag{2.13}$$

$$v_{CW} = \frac{c}{n_o}\left(1 - \frac{1}{n_o}\left(\Delta\omega_{CW}\cdot\frac{\partial n}{\partial\omega}\right)\right) - v\left(1 - \frac{1}{{n_o}^2}\right) \tag{2.14}$$

As should be expected, Equations 2.13 and 2.14 simplify to Equations 2.10 and 2.11 in the absence of dispersion. Putting together Equations 2.8, 2.9, 2.12, 2.13, and 2.14 results in:

$$v_{CCW} = \frac{c}{n_o} + \left(\frac{V_M}{{n_o}^2} \cdot \omega \frac{\partial n}{\partial \omega}\right) + v\left(1 - \frac{1}{{n_o}^2}\right) = \frac{c}{n_o} + \left(\frac{V_M}{{n_o}^2}(n_g - n_o)\right) + v\left(1 - \frac{1}{{n_o}^2}\right) \quad (2.15)$$

$$v_{CW} = \frac{c}{n_o} - \left(\frac{V_M}{{n_o}^2} \cdot \omega \frac{\partial n}{\partial \omega}\right) - v\left(1 - \frac{1}{{n_o}^2}\right) = \frac{c}{n_o} - \left(\frac{V_M}{{n_o}^2}(n_g - n_o)\right) - v\left(1 - \frac{1}{{n_o}^2}\right) \quad (2.16)$$

where we recognize that $n_g = n_o + \omega \frac{\partial n}{\partial \omega}$ is the group index. If the medium remains stationary while the rest of the gyroscope rotates, then $V_M = -v$. In this scenario, Equations 2.15 and 2.16 reduce to:

$$v_{CCW} = \frac{c}{n_o} - v\left(1 - \frac{1}{{n_o}^2} + \frac{(n_g - n_o)}{{n_o}^2}\right) \equiv \frac{c}{n_o} - v\alpha_L \quad (2.17)$$

$$v_{CW} = \frac{c}{n_o} + v\left(1 - \frac{1}{{n_o}^2} + \frac{(n_g - n_o)}{{n_o}^2}\right) \equiv \frac{c}{n_o} + v\alpha_L \quad (2.18)$$

where $\alpha_L \equiv 1 - \frac{1}{{n_o}^2} + \frac{(n_g - n_o)}{{n_o}^2}$ is the so-called *Laub drag coefficient* [12]. The distances over which the counter-clockwise and clockwise modes propagate, respectively, are:

$$L_{CCW} = 2\pi R + R\Omega t_{CCW} = t_{CCW} V_{CCW} \quad (2.19)$$

$$L_{CW} = 2\pi R - R\Omega t_{CW} = t_{CW} V_{CW} \quad (2.20)$$

Therefore, the propagation times are:

$$t_{CCW} = \frac{2\pi R}{V_{CCW} - R\Omega} = \frac{2\pi R}{\left(\frac{c}{n_o} - v\alpha_L\right) - R\Omega} \quad (2.21)$$

$$t_{CW} = \frac{2\pi R}{V_{CW} + R\Omega} = \frac{2\pi R}{\left(\frac{c}{n_o} + v\alpha_L\right) + R\Omega} \quad (2.22)$$

so that the time delay is:

$$\Delta t = t_{CCW} - t_{CW} \approx \frac{4\pi R^2 \Omega {n_o}^2 (1 - \alpha_L)}{c^2} = \frac{4A\Omega}{c^2} \cdot {n_o}^2 (1 - \alpha_L) = {n_o}^2 (1 - \alpha_L) \cdot \Delta t_o \quad (2.23)$$

with a corresponding phase delay of:

$$\Delta\varphi = {n_o}^2(1-\alpha_L)\cdot\Delta\varphi_o = -\left(n_g-(n_o+1)\right)\cdot\Delta\varphi_o \tag{2.24}$$

where Δt_o and $\Delta\varphi_o$ are the time delay and phase delay, respectively, of the *co-moving medium* case analyzed in Chapter 1. When $n_g \gg 1$, the absolute value of the phase shift, $|\Delta\varphi|$, approaches $n_g\Delta\varphi_o$. Thus, the phase sensitivity of an optical gyroscope can be enhanced by circulating a medium with a high value of n_g around the perimeter. Since $n_g > 1$ corresponds to a group velocity less than the speed of light, this increase in sensitivity can be referred to as "slow light enhancement" or "subluminal enhancement".

In the example of the gyroscope with a non-co-moving medium, there were two relevant frames of reference: the rest frame of the medium and the rest frame of the optical components. This gyroscope therefore measures the *relative* rotation between these two frames, but cannot be used to measure *absolute* rotation, which is important for many applications in astrophysics, geology, and inertial guidance [13]. In order to measure absolute rotation, there must be only one frame of reference. This can be achieved by using a *resonator*.

2.2.2 Fast-Light Enhancement in a Sagnac Resonator with Linear Dispersion

The main drawback of the slow-light-enhanced interferometer from Section 2.2.1 is that it cannot measure *absolute* rotation. However, this constraint can be overcome by considering the Sagnac effect in a *resonator*, where the longitudinal eigenmode frequencies are modified as a result of rotation. We can then create a gyroscope by monitoring the resonant frequencies of two counter-propagating modes in a resonator as is it rotated, the schematic of which is illustrated in Figure 2.4. In this system, the clockwise and counter-clockwise resonance frequencies are monitored by

detecting and locking to their respective cavity transmission peaks. Two Acousto-Optic Modulators (AOMs) – one clockwise and one counter-clockwise – are controlled by Voltage-Controlled Oscillators (VCOs) so that the AOM output frequencies are always equal to their respective cavity resonance frequencies. The beat frequency between the outputs of the two AOMs is then measured, from which the rate of rotation is deduced.

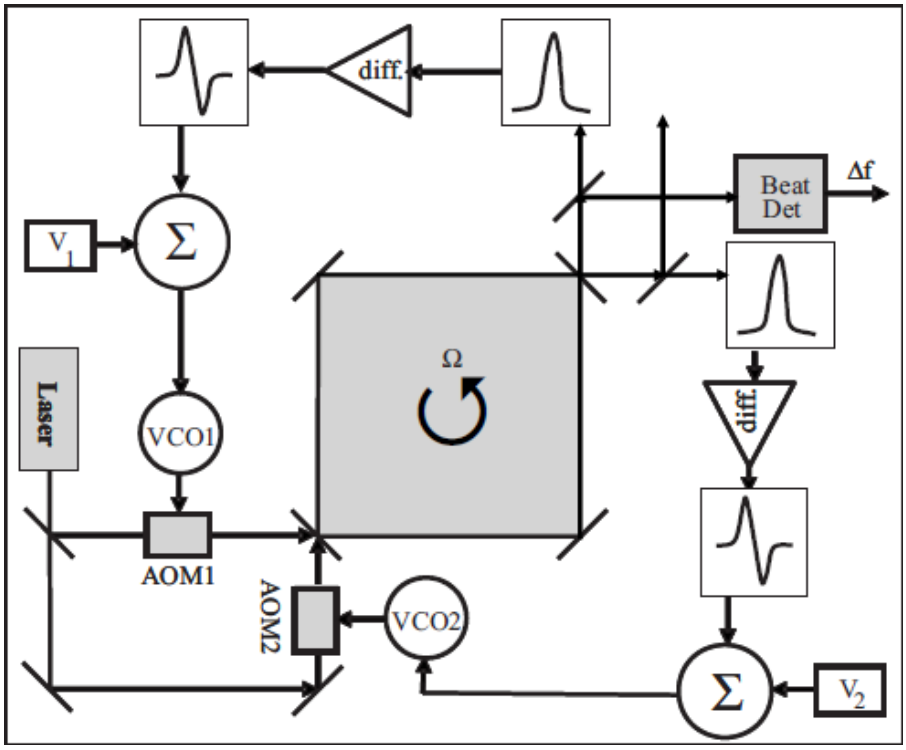

Fig. 2.4: Schematic of a gyroscope where the counter-propagating resonance frequencies are produced with acousto-optic modulators, and are interfered to produce a beat note

In the absence of rotation, the counter-clockwise and clockwise modes both have an angular frequency of $\omega_o = v_{PH}\left(\frac{2\pi m}{P}\right)$ where $v_{PH} = \frac{c}{n_o}$ is the phase velocity, P is the cavity perimeter, and m is the mode number which is equal to $\frac{P}{\lambda}$ where λ is wavelength. However, if the

cavity is rotating at a rate of Ω, the phase velocities of the counter-clockwise and clockwise modes, v_{CCW} and v_{CW}, respectively, are modified so that:

$$v_{CCW} = \frac{v_{PH} + R\Omega}{1 + \left(\frac{V_{PH} R\Omega}{c^2}\right)} \tag{2.25}$$

$$v_{CW} = \frac{v_{PH} - R\Omega}{1 - \left(\frac{v_{PH} R\Omega}{c^2}\right)} \tag{2.26}$$

Therefore, the (angular) frequency splitting between the two modes is:

$$\delta\omega_o \equiv \omega_{CCW} - \omega_{CW} = \left(\frac{2\pi m}{P}\right)(v_{CCW} - v_{CW}) \tag{2.27}$$

Plugging Equations 2.25 and 2.26 into Equation 2.27 yields:

$$\delta\omega_o = \frac{v_{PH}}{cn_o}\left(\frac{2\pi m}{P}\right)(2\Omega R) = \frac{\omega_o}{cn_o}(2\Omega R) = \frac{\omega_o}{cn_o}\left(\frac{4\Omega A}{P}\right) \tag{2.28}$$

where $A = \pi R^2$ is the enclosed area. Once again, the frequency splitting between the counter-propagating modes is proportional to the rotation rate Ω. More generally, if the axis of rotation is not perpendicular to the plane of the gyroscope, then:

$$\delta\omega_o = \frac{\omega_o}{cn_o}\left(\frac{4\vec{\Omega} \cdot \vec{A}}{P}\right) \tag{2.29}$$

where $\vec{A}$ is the area normal vector and $\vec{\Omega}$ is the rotation vector. The rotation rate about a particular axis can therefore be deduced by measuring the beat frequency between the counter-propagating laser modes.

In the case of counter-clockwise rotation, as shown in Figure 2.4, the counter-clockwise mode is downshifted by $\frac{\delta\omega_o}{2}$ while the clockwise mode is upshifted by $\frac{\delta\omega_o}{2}$. Thus, in principle, the rotation rate Ω can be measured by beating either of these modes with a stable reference laser.

However, from an experimental standpoint, it is best to look at the beat frequency between the two modes in order to eliminate common-mode effects such as mirror vibrations and thermal fluctuations.

The above derivation of the frequency splitting in the Sagnac resonator assumed a constant index of refraction. The results of this calculation differ drastically when dispersion is considered, and provide the theoretical basis for fast-light enhancement in optical interferometry. Once again, we consider a medium in which the dispersion relation is Taylor-expanded to first order about a central frequency of ω_o:

$$n(\omega) \simeq n(\omega = \omega_o) + \Delta\omega \cdot \frac{\partial n}{\partial \omega} \equiv n_o + \Delta\omega \cdot \frac{\partial n}{\partial \omega} \tag{2.30}$$

Without loss of generality, the counter-clockwise and clockwise frequencies in this *dispersive* gyroscope are split by a frequency $\delta\omega_D$, whose value is to be determined in this calculation. The counter-clockwise and clockwise resonance frequencies can therefore be written as:

$$\omega_{CCW} = \omega_o - \frac{\delta\omega_D}{2} = v_{CCW}\left(\frac{2\pi m}{P}\right) \tag{2.31}$$

$$\omega_{CW} = \omega_o + \frac{\delta\omega_D}{2} = v_{CW}\left(\frac{2\pi m}{P}\right) \tag{2.32}$$

where the phase velocities of the counter-clockwise and clockwise beams are:

$$v_{CCW} = \frac{c}{n(\omega = \omega_{CCW})} + R\Omega = \frac{c}{n_o - \left(\frac{\delta\omega_D}{2}\frac{\partial n}{\partial \omega}\right)} + R\Omega \tag{2.33}$$

$$v_{CW} = \frac{c}{n(\omega = \omega_{CW})} - R\Omega = \frac{c}{n_o + \left(\frac{\delta\omega_D}{2}\frac{\partial n}{\partial \omega}\right)} - R\Omega \tag{2.34}$$

Putting together Equations 2.31 and 2.33 and Equations 2.32 and 2.34 yields:

$$\delta\omega_D = \frac{2\Omega R\omega_o}{cn_o}\left(\frac{1}{n_o + \omega_o\frac{\partial n}{\partial\omega}}\right) = \frac{\omega_o}{cn_o}\left(\frac{4\Omega A}{P}\right)\cdot\frac{1}{n_g} = \delta\omega_o\cdot\frac{1}{n_g} \tag{2.35}$$

Therefore, the frequency splitting in the Sagnac resonator is enhanced by a factor of ${n_g}^{-1}$. In the subluminal case ($|n_g| > 1$), rotation-induced frequency sensitivity is reduced; in the superluminal case ($|n_g| < 1$), rotation-induced frequency sensitivity is increased. Theoretically, a lower bound for the value of n_g does not exist (in fact, n_g can even be negative, in which case the direction of the group velocity is opposite that of the phase velocity). Thus, the sensitivity of a fast-light interferometer can, in principle, diverge. However, there does not (and cannot) exist a material in which $n_g = 0$ over the entire electromagnetic spectrum; higher-order nonlinearities in the refractive index will impose an upper limit on the factor of sensitivity enhancement. As will be shown in the next section, this upper limit can still be several orders of magnitude greater than unity, particularly for "small" values of $\delta\omega_o$.

2.2.3 Fast-Light Enhancement in a Sagnac Resonator with Nonlinear Dispersion

With linear dispersion, $n(\omega_o + \Delta\omega) = n(\omega_o) + \frac{\partial n}{\partial\omega}\Delta\omega \equiv n_o + n_1\Delta\omega$, so that:

$$\delta\omega_D = \frac{\delta\omega_o}{n_g} = \frac{\delta\omega_o}{n_o + n_1\omega_o} \tag{2.36}$$

However, linear dispersion is realistic only for small deviations about the central frequency ω_o. A more realistic model of dispersion can be developed by considering the dispersion profile created by a two-level absorptive resonance. This two-level model will be validated in Chapter 3, but for now we take it for granted:

$$n(\omega) = 1 - \frac{A\Gamma(\omega - \omega_0)}{\Gamma^2 + (\omega - \omega_0)^2} \tag{2.37}$$

where 2Γ is the full-width half maximum (FWHM) width of the resonance, and A is the imaginary part of $\tilde{\chi}$ at the center of that resonance ($A = \chi_I|_{\omega=\omega_0}$). This expression can be Taylor-expanded about ω_0:

$$n(\omega) = n(\omega_o) + \frac{\partial n}{\partial \omega}(\omega - \omega_o) + \frac{1}{2}\frac{\partial^2 n}{\partial \omega^2}(\omega - \omega_o)^2 + + \frac{1}{6}\frac{\partial^3 n}{\partial \omega^3}(\omega - \omega_o)^3 + \cdots \tag{2.38}$$

The second term in Equation 2.37 is odd with respect to ω_0, so that $\frac{\partial^2 n}{\partial \omega^2} = 0$. Taking the next-highest order of the Taylor expansion into account yields:

$$n(\omega) \cong 1 + n_1 \Delta\omega + n_3(\Delta\omega)^3 \tag{2.39}$$

where $n_1 \equiv \frac{\partial n}{\partial \omega}$ and $n_3 \equiv \frac{1}{6}\frac{\partial^3 n}{\partial \omega^3}$. Evaluating the derivatives of Equation 2.37 yields the result that $n_1 = -\frac{A}{\Gamma}$ and $n_3 = -\frac{n_1}{\Gamma^2}$. Substituting Equation 2.39 into Equation 2.35 therefore yields a frequency splitting of:

$$\delta\omega_D = \left[\left(\frac{4\Gamma}{\delta\omega_o}\right)^{2/3}\right]\delta\omega_o \equiv \eta \cdot \delta\omega_o \tag{2.40}$$

The enhancement factor, η, is evidently nonlinear, and decreases as $\delta\omega_o$ increases. For large values of $\delta\omega_o$, η approaches unity, meaning that fast-light enhancement vanishes when the detuning is far outside the absorptive resonance (for $|\omega - \omega_0| \gg \Gamma$). This should make sense because the index of refraction far off resonance is roughly constant.

2.2.4 Cavity Broadening and Minimum Measurable Rotation Rate in a Fast-Light Sagnac Resonator

We have shown that the presence of a fast-light medium inside a Sagnac resonator can significantly enhance the resonance frequency shift, even when higher-order nonlinearities in the dispersion profile are considered. However, as will be shown in this section, this enhancement in frequency shift does not necessarily lead to an enhancement in gyroscope sensitivity, due to concomitant cavity linewidth broadening.

In the linear dispersion regime, if the roundtrip cavity length L_o is changed by ΔL, then:

$$L_o + \Delta L = m\lambda = \frac{2\pi mc}{[\omega_o + \Delta\omega] \cdot n(\omega_o + \Delta\omega)} \tag{2.41}$$

where $\omega_o + \Delta\omega$ is the new cavity resonance frequency, and $n(\omega_o + \Delta\omega)$ is the index at this new frequency. However, the linewidth of a cavity resonance is enhanced by the same factor, so that:

$$\gamma_D = \frac{\gamma_o}{n_g} = \frac{\gamma_o}{n_o + n_1\omega_o} \tag{2.42}$$

where γ_o and γ_D are the empty cavity and dispersive cavity linewidths, respectively. Similarly, in the non-linear dispersion regime, the cavity linewidths have the following relationship:

$$\gamma_D = \frac{\gamma_o}{n_o + n_1\omega_o + n_3\omega_o(\gamma_D)^2} = \frac{\gamma_o}{n_g + n_3\omega_o(\gamma_D)^2} \tag{2.43}$$

where $n_o \equiv n(\omega = \omega_o)$, $n_1 \equiv \frac{\partial n}{\partial \omega}$, and $n_3 \equiv \frac{1}{6}\frac{\partial^3 n}{\partial \omega^3}$. If $n_g = 0$, then:

$$\gamma_D = \frac{\gamma_o}{n_3\omega_o(\gamma_D)^2} = (\Gamma^2\gamma_o)^{1/3} \tag{2.44}$$

However, for $\Delta L \neq 0$, n_g changes as ΔL changes, so that [11]:

$$\gamma_D = \frac{\gamma_o}{n_g\big|_{\omega=\omega_o+\Delta\omega_o}} \cong \frac{\eta}{3}\gamma_o \equiv \zeta \cdot \gamma_o \tag{2.45}$$

Therefore, the cavity linewidth is broadened by a factor of ζ, which is approximately *one-third* that of the frequency shift enhancement.

The sensitivity of a Sagnac gyroscope is limited by its ability to resolve frequency-shifted peaks. Even though the insertion of a fast-light medium into a Sagnac resonator enhances the frequency split between counter-propagating modes, it also broadens these modes. In Figure 2.5(a), a small rotation rate produces a small shift in frequency. By inserting a fast-light medium into the cavity, the splitting between peaks is enhanced, but the peaks themselves are broadened by the same factor, as shown in Figure 2.5(b). The ideal scenario is illustrated in Figure 2.5(c), where the peaks are split by the same amount as in (b), but where the widths of the peaks remain the same as in (a).

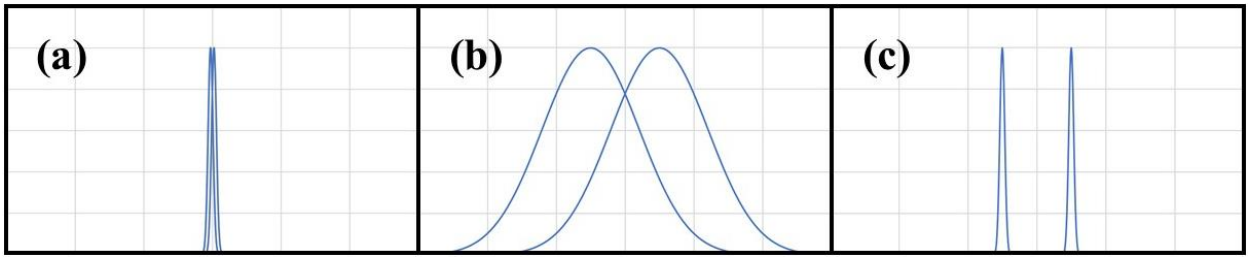

Fig. 2.5: (a) Two peaks with small widths are very close to one another; (b) The distance between the centers of the peaks is enhanced by a factor of η, but so is γ, the linewidth; (c) The ideal scenario in which the splitting is enhanced by η but the linewidth is not.

According to Equation 2.28, the empty-cavity splitting of counter-propagating resonance frequencies is:

$$\delta\omega_o = \frac{\omega_o}{cn_o}\left(\frac{4\Omega A}{P}\right) \equiv S \cdot \Omega \tag{2.46}$$

where we define S as the "scale factor". Meanwhile, the minimum measurable frequency shift is:

$$\delta\omega_{o(MIN)} = \frac{\gamma_o}{SNR} \tag{2.47}$$

where Γ_o is the empty cavity linewidth and SNR is the signal-to-noise ratio. Therefore, the minimum measurable rotation rate, $\Omega_{o(MIN)}$, is:

$$\Omega_{o(MIN)} = \frac{\delta\omega_{o(MIN)}}{S} = \frac{\gamma_o}{S \cdot SNR} \tag{2.48}$$

On the other hand, according to Equation 2.40, the *dispersive*-cavity splitting of counter-propagating resonance frequencies is:

$$\delta\omega_D = \eta \cdot \delta\omega_o = \eta \cdot S \cdot \Omega \tag{2.49}$$

The dispersive cavity linewidth is broadened by a factor of ζ relative to the empty cavity. Therefore, the minimum measurable rotation rate in the dispersive cavity, $\Omega_{D(MIN)}$, is:

$$\Omega_{D(MIN)} = \frac{\delta\omega_{D(MIN)}}{S} = \frac{\gamma_o \cdot \zeta}{S \cdot SNR \cdot \eta} = \Omega_{o(MIN)} \cdot \left(\frac{\zeta}{\eta}\right) \tag{2.50}$$

$\zeta \cong \frac{\eta}{3}$ according to Equation 2.45, so that the sensitivity of the white-light gyroscope is enhanced relative to the empty cavity gyroscope by a factor of approximately three. This slight improvement may not be worth the extra complications and sources of drift associated with adding a dispersive element. As will be discussed in the next section, a fast-light (or "superluminal") laser offers a promising solution.

2.3 Fast Light Sagnac Laser

The ideal scenario illustrated in Figure 2.5(c) can be realized by inserting into the cavity a *gain medium* in addition to the dispersive element: in other words, by using a fast-light Sagnac *laser* instead of a fast-light Sagnac resonator.

The minimum-measurable linewidth of a conventional *non-dispersive* laser is given by:

$$\delta\omega_{MIN(CONVENTIONAL-LASER)} = \frac{1}{\tau_C}\sqrt{\frac{P_{OUT}\tau_M}{\hbar\omega_o}} \tag{2.51}$$

where τ_C is the cavity photon lifetime (which is the inverse of the cavity linewidth γ_C), τ_M is the measurement time and P_{OUT} is the laser output power. For a laser in the coherent state, the number of photons, N, follows a Poisson distribution where the expectation value and standard deviation of the number of photons are $\langle N\rangle$ and $\sqrt{\langle N\rangle}$, respectively. The quantity $\sqrt{P_{OUT}\tau_M/\hbar\omega_o}$ is the square root of the number of photons observed during the measurement time τ_M, and is therefore is equal to the uncertainty in the number of photons in the coherent state. Given this expression for the minimum-measurable laser linewidth, the expression for the minimum-measurable cavity length change is:

$$\delta L_{MIN(CONVENTIONAL-LASER)} = \frac{\delta\omega_{MIN(CONVENTIONAL-LASER)}}{\omega_o}L_o = \frac{L_o}{\omega_o\tau_C}\sqrt{\frac{P_{OUT}\tau_M}{\hbar\omega_o}} \tag{2.52}$$

This (non-dispersive) Sagnac laser is already an improvement on the (non-dispersive) Sagnac resonator, because laser linewidths are generally several orders of magnitude smaller than resonator linewidths, so that $\delta L_{MIN(CONVENSTIONAL-LASER)}$ is smaller by the same factor. However, the contrast between the *fast-light* Sagnac laser the *fast-light* Sagnac resonator is even more significant, because dispersion of the intra-cavity lasing beam does not affect any of the parameters

in Equation 2.51, so that the laser linewidth should remain unchanged in the presence of fast light. Therefore, a superluminal laser gyroscope gives the best of all three worlds: enhancement of the frequency shift between counter-propagating modes, ultra-narrow laser linewidths, and no dispersion-induced linewidth broadening. In Chapter 4, we will explicitly solve the single-mode laser equations to verify that the frequency shift of a fast-light Sagnac laser (in the linear dispersion limit) is indeed enhanced by a factor of $n_g{}^{-1}$, just as it is with a fast-light Sagnac resonator; for now, we will take this result for granted. Therefore, the minimum-measurable cavity length change in a fast-light Sagnac laser would be:

$$\begin{aligned} \delta L_{MIN(DISPERSIVE-LASER)} &= \delta L_{MIN(CONVENTIONAL-LASER)} \cdot \left(\frac{\zeta}{\eta}\right) \\ &= \frac{\delta L_{MIN(CONVENTIONAL-LASER)}}{\eta} \end{aligned} \tag{2.53}$$

where $\zeta = 1$ due to the fact that the frequency splitting between counter-propagating modes in a fast-light Sagnac laser occurs without concomitant linewidth broadening. This factor of η increase in sensitivity makes this type of system very promising for future generations of highly-sensitive optical interferometers.

CHAPTER 3

ATOM-LIGHT INTERACTION

3.1 Classical Description of Atom-Light Interaction

Because atoms and photons are quantized, the interaction between them is inherently quantum mechanical. Therefore, the true description governing the interaction between light and matter requires quantization of both the electromagnetic field and the atom. However, the tools of classical mechanics and classical electrodynamics provide a much more intuitive and surprisingly accurate description of this process. The goal of this section is to introduce the classical model of atom-light interaction, with the goal of strengthening intuition for the subsequent sections, which will make use of quantum mechanics.

In the classical model, an atom has an equilibrium position located a distance of $x = x_o$ away from the nucleus, as shown in Figure 3.1. The Taylor expansion of the potential energy around this equilibrium position is:

$$U(x) = U(x_o) + (x - x_o) \cdot \left.\frac{\partial U}{\partial x}\right|_{x=x_o} + \frac{(x - x_o)^2}{2!} \cdot \left.\frac{\partial^2 U}{\partial x^2}\right|_{x=x_o} + \frac{(x - x_o)^3}{3!} \cdot \left.\frac{\partial^3 U}{\partial x^3}\right|_{x=x_o} + \frac{(x - x_o)^3}{4!} \cdot \left.\frac{\partial^3 U}{\partial x^3}\right|_{x=x_o} + \cdots \tag{3.1}$$

The first term in this Taylor expansion is an arbitrary constant, because potential is a *relative* quantity. Therefore, we can *choose* to set $U(x_o)$ equal to zero. The second term in the expansion is also equal to zero because by definition, the sum of external forces is equal to zero in equilibrium: $\left.\frac{\partial U}{\partial x}\right|_{x=x_o} = -F(x = x_0) = 0$. The first nonzero term in the Taylor expansion is the

quadratic term. Limiting the expansion to only this quadratic term is equivalent to treating the system as an ideal *mass-on-a-spring* in which the restoring force is:

$$F_{SPRING} = -\left.\frac{\partial U}{\partial x}\right|_{x=x_o} \cong -\frac{\partial}{\partial x}\left(\frac{(x-x_o)^2}{2}\cdot\left.\frac{\partial^2 U}{\partial x^2}\right|_{x=x_o}\right)$$

$$= -\left.\frac{\partial^2 U}{\partial x^2}\right|_{x=x_o}\cdot\frac{\partial}{\partial x}\left(\frac{(x-x_o)^2}{2}\right) = -2\left.\frac{\partial^2 U}{\partial x^2}\right|_{x=x_o}\cdot(x-x_o) \qquad (3.2)$$

$$\equiv -k(x-x_o)$$

where the "spring constant" k is equal to $2\left.\frac{\partial^2 U}{\partial x^2}\right|_{x=x_o}$. There is also presumably some damping force, which, for the purposes of providing a simple mathematical formulation, is assumed to be proportional to the instantaneous velocity: $F_{DAMPING} \equiv -\sigma\frac{dx}{dt}$.

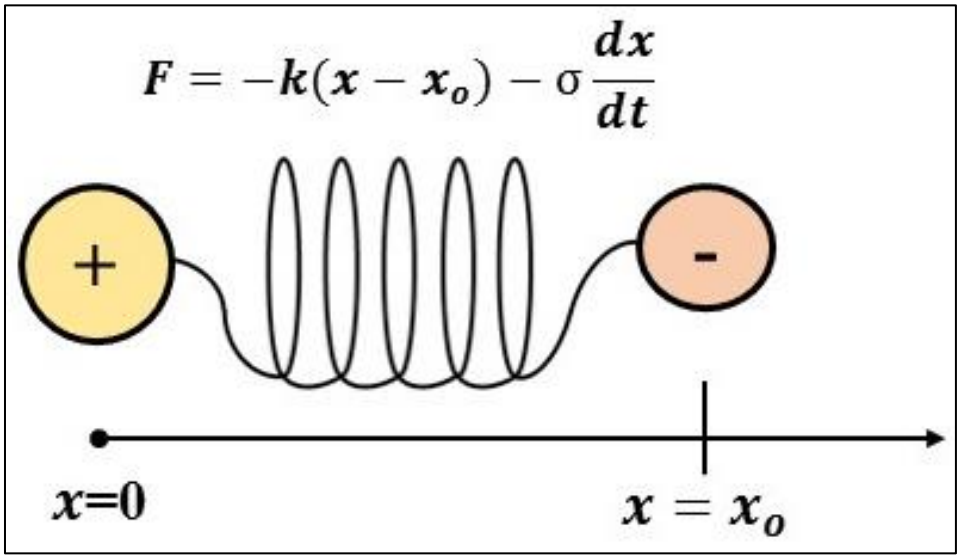

Fig. 3.1: Damped mass-on-a-spring system in which the electron (-) has an equilibrium position of $x = x_o$ away from the nucleus (+)

Now suppose that a classical electromagnetic wave with electric field $E = -E_0\cos(\omega t)$ propagates through this system. The mass of the nucleus is far greater than the mass of the electron,

so that the nucleus position is roughly constant (this is called the Born-Oppenheimer approximation) while the electron is subjected to a driving force of:

$$F_{DRIVING} = -qE = qE_0\cos(\omega t) \tag{3.3}$$

where q is the magnitude of the electron charge. The sum of forces exerted on the electron is:

$$\sum F = F_{SPRING} + F_{DAMPING} + F_{DRIVING} = -k(x - x_o) - \sigma\frac{dx}{dt} + qE_0\cos(\omega t) \tag{3.4}$$

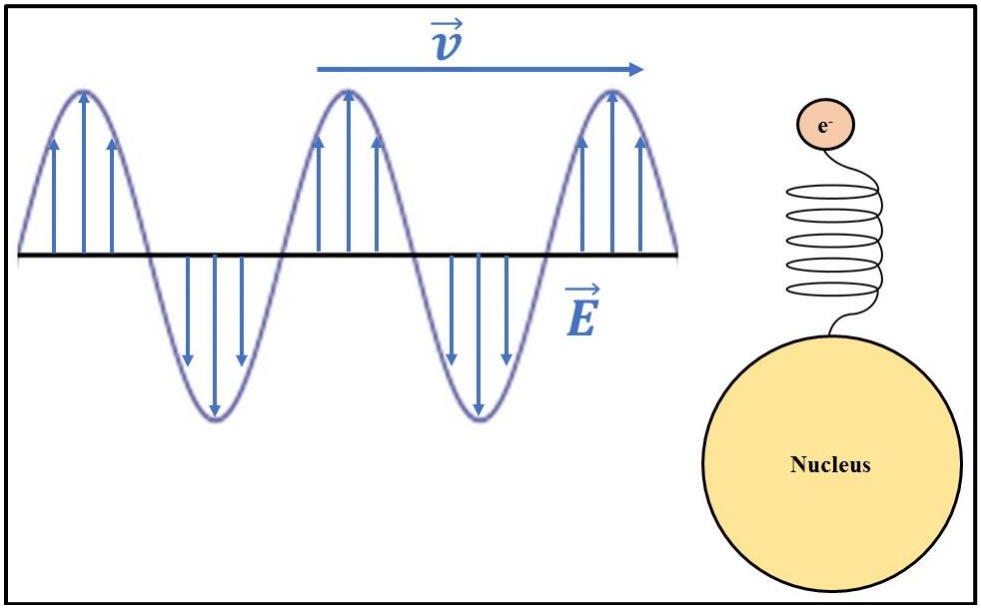

Fig. 3.2: An oscillating electric field provides the driving force for this mass-on-a-spring system, where the nucleus is assumed to be stationary

Re-defining $x = 0$ as the equilibrium position of the spring and letting $\sigma \equiv m\gamma$, the differential equation governing this system simplifies to:

$$m\left(\frac{d^2x}{dt^2} + \gamma\frac{dx}{dt} + {\omega_o}^2 x\right) = qE_0\cos(\omega t) \tag{3.5}$$

where m is the electron mass and $\omega_o \equiv \sqrt{k/m}$ is the resonant frequency of the simple harmonic oscillator. This differential equation is identical to that of the canonical *damped harmonic*

oscillator with a sinusoidal driving force. The solutions to this class of differential equations take on the following form:

$$x(t) = \tilde{x}(t) = x_o e^{-i\omega t} \tag{3.6}$$

where the tilde above the x indicates that it is a complex function. Inserting Equation 3.6 into Equation 3.5 yields:

$$m\left(-\omega^2 x_o e^{-i\omega t} - i\gamma\omega x_o e^{-i\omega t} + {\omega_o}^2 x_o e^{-i\omega t}\right) = qE_0 e^{-i\omega t} \tag{3.7}$$

Therefore:

$$x_o = \frac{{}^{q}\!/_{m}}{{\omega_o}^2 - \omega^2 - i\gamma\omega} E_o \tag{3.8}$$

Because $\tilde{x}(t)$ is complex, it has an amplitude and a phase. The phase represents the lag of the electron response relative to the applied field, and is equal to:

$$\theta_{LAG} = tan^{-1}\left(\frac{Im[\tilde{x}(t)]}{Re[\tilde{x}(t)]}\right) = tan^{-1}\left(\frac{\gamma\omega}{{\omega_o}^2 - \omega^2}\right) \tag{3.9}$$

The dipole moment of a single atom is equal to the electron charge multiplied by the separation between the electron and nucleus:

$$\tilde{p}(t) = q\tilde{x}(t) = \frac{{}^{q^2}\!/_{m}}{{\omega_o}^2 - \omega^2 - i\gamma\omega} E_o e^{-i\omega t} \tag{3.10}$$

If there are *N* atoms per unit volume, then the bulk polarization of the medium is:

$$\tilde{P}(t) = N\tilde{p}(t) = \frac{{}^{Nq^2}\!/_{m}}{{\omega_o}^2 - \omega^2 - i\gamma\omega} \tilde{E}(t) \tag{3.11}$$

In general, the complex *material susceptibility*, $\tilde{\chi}$, can be defined through the following relation [14]:

$$\tilde{P} \equiv (\varepsilon_o \tilde{\chi})\tilde{E} \tag{3.12}$$

so that:

$$\tilde{\chi} = \frac{{Nq^2}/{\varepsilon_o m}}{{\omega_o}^2 - \omega^2 - i\gamma\omega} \tag{3.13}$$

The amplitude and phase of $\tilde{\chi}$ represent the magnitude and lag, respectively, between the applied field and the polarization of the medium. Additionally, the *permittivity*, $\tilde{\varepsilon}$, can be defined as:

$$\tilde{\varepsilon} = \varepsilon_o(1 + \tilde{\chi}) = \varepsilon_o\left(1 + \frac{{Nq^2}/{\varepsilon_o m}}{{\omega_o}^2 - \omega^2 - i\gamma\omega}\right) \tag{3.14}$$

This permittivity can then be substituted into the wave equation:

$$\nabla^2 E = \tilde{\varepsilon}\mu_o \frac{\partial^2 E}{\partial t^2} \tag{3.15}$$

Equation 3.15 admits plane wave solutions of the form:

$$E(z,t) = E_o e^{i(\tilde{k}z - \omega t)} \tag{3.16}$$

where $\tilde{k}$ is the complex wave number: $\tilde{k} = \sqrt{\tilde{\varepsilon}\mu_o}\omega = Re[\tilde{k}] + i \cdot Im[\tilde{k}] \equiv k_R + ik_I$. Equation 3.16 therefore becomes:

$$\tilde{E}(z,t) = E_o e^{-k_I z} e^{i(k_R z - \omega t)} \tag{3.17}$$

The imaginary part of $\tilde{k}$ evidently represents attenuation of the electric field, which is dampened to a factor of $1/e$ its initial value after propagating a distance of $1/k_I$. The energy absorption coefficient, α, is equal to $2k_I$, so that the energy density (which is proportional to the square of the electric field) is damped to a factor of $1/e$ after propagating a distance of $1/\alpha$.

The real part of $\tilde{k}$ is inversely proportional to the wavelength and therefore is related to the *refractive index*, which is equal to $\frac{ck_R}{\omega}$. If $(Re[\tilde{\varepsilon}] - \varepsilon_o) \ll 1$, then:

$$\tilde{k} = \sqrt{\tilde{\varepsilon}\mu_o}\omega \cong \frac{\omega}{c}\left[1 + \left(\frac{Nq^2}{2m\varepsilon_o}\right)\left(\frac{1}{{\omega_o}^2 - \omega^2 - i\gamma\omega}\right)\right] \tag{3.18}$$

Therefore, the index and the absorption coefficient, respectively, are:

$$n = \frac{ck_R}{\omega} = 1 + \left(\frac{Nq^2}{2m\varepsilon_o}\right)\frac{({\omega_o}^2 - \omega^2)}{({\omega_o}^2 - \omega^2)^2 + (\gamma\omega)^2} \tag{3.19}$$

$$\alpha = 2k_I = \left(\frac{Nq^2}{mc\varepsilon_o}\right)\frac{(\gamma\omega)}{({\omega_o}^2 - \omega^2)^2 + (\gamma\omega)^2} \tag{3.20}$$

Figure 3.3 plots these two quantities together.

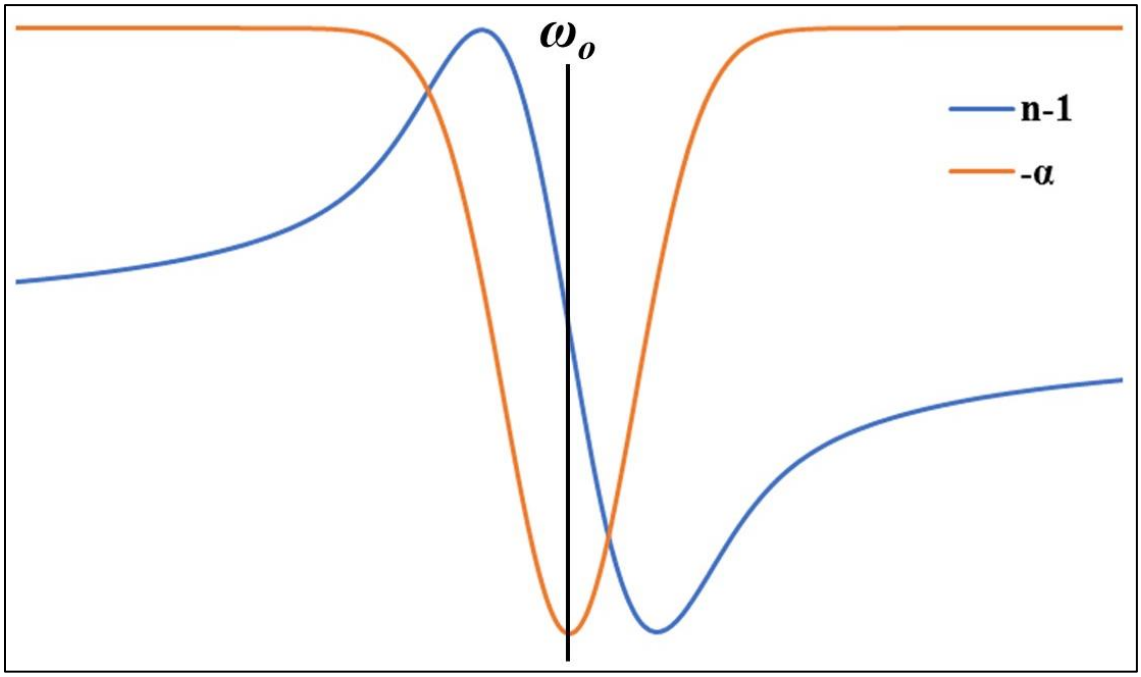

Fig. 3.3: The refractive index (minus one) and the (negative) coefficient of absorption plotted together. Near resonance, absorption increases while the slope of the refractive index is at its maximum value.

The dispersion profile appears to be roughly proportional to the derivative of the absorption profile. This is not precisely true – at the most fundamental level, they (along with the real and imaginary parts of *any* complex function) are related by the so-called Kramers-Kronig relations, which will be derived in the next section.

3.2 The Kramers-Kronig Relations

Figure 3.3 shows that on resonance, atomic absorption of the electromagnetic wave is maximized while the slope of the refractive index is also maximized. It may appear that the index is proportional to the derivative of the coefficient of absorption, but in fact they are related by the so-called *Kramers-Kronig relations*, which arise from the causal relationship between the applied field and the atomic response [15,16,17]. In their most general form, the Kramers-Kronig relations describe the relationship between the real and imaginary parts of *any* complex function obeying causality. This relationship is particularly useful in the field of optics, because atomic response to an applied field is most conveniently described as a complex function with an amplitude spectrum and a phase spectrum. The derivation of the Kramers-Kronig relations begins with the definition of a time-dependent material polarization:

$$\tilde{P}(t) = \varepsilon_o \int_{-\infty}^{\infty} \tilde{E}(t')\tilde{\chi}(t-t')dt' \tag{3.21}$$

Causality requires that if the electric field is turned on at $t = 0$, the polarization must be zero at all times before $t = 0$. Therefore $\tilde{\chi}(t) = 0$ for $t < 0$, or equivalently, $\tilde{\chi}(t - t') = 0$ for $t < t'$. Therefore, $\tilde{\chi}(t)$ can be expressed as:

$$\tilde{\chi}(t) \longrightarrow \Theta(t)\tilde{\chi}(t) \tag{3.22}$$

where $\Theta(t)$ is the "step function" in which $\Theta(t < 0) = 0$ and $\Theta(t \geq 0) = 1$. Therefore, $\tilde{\chi}(\omega)$, the Fourier transform of $\tilde{\chi}(t)$, can be expressed as:

$$\tilde{\chi}(\omega) = \mathcal{F}\{\Theta(t)\tilde{\chi}(t)\}$$

$$= \int_{-\infty}^{\infty} \Theta(t)\tilde{\chi}(t)e^{i\omega t}dt = \int_{-\infty}^{\infty} \Theta(t)\left[\int_{-\infty}^{\infty} \tilde{\chi}(\omega')e^{-i\omega' t}d\omega'\right]e^{i\omega t}dt \tag{3.23}$$

$$= \int_{-\infty}^{\infty} \tilde{\chi}(\omega')d\omega' \int_{-\infty}^{\infty} \Theta(t)e^{i(\omega-\omega')t}dt$$

The second integral in this term is the Fourier transform of the step function:

$$\int_{-\infty}^{\infty} \Theta(t)e^{i(\omega-\omega')t}dt = \mathcal{F}\{\Theta(t)\} = \frac{1}{2}\delta(\omega) + \frac{i}{2\pi\omega} \tag{3.24}$$

where $\delta(\omega)$ is the *Dirac delta function* which is equal to zero everywhere except at $\omega = 0$, and has a total area of $\int_{-\infty}^{\infty} \delta(\omega)d\omega = 1$. Equations 3.23 and 3.24 therefore yield:

$$\tilde{\chi}(\omega) = \frac{1}{2}\int_{-\infty}^{\infty} \tilde{\chi}(\omega')\delta(\omega-\omega')d\omega' + \frac{i}{2\pi}\int_{-\infty}^{\infty} \frac{\tilde{\chi}(\omega')}{\omega-\omega'}d\omega' = \frac{i}{\pi}\int_{-\infty}^{\infty} \frac{\tilde{\chi}(\omega')}{\omega-\omega'}d\omega' \tag{3.25}$$

This gives the relationship between $\chi_R(\omega)$ and $\chi_I(\omega)$, the real and imaginary parts of $\tilde{\chi}(\omega)$.

$$\chi_R(\omega) = \frac{2}{\pi}\int_0^{\infty} \frac{\omega'\chi_I(\omega')}{\omega'^2-\omega^2}d\omega' \tag{3.26}$$

$$\chi_I(\omega) = -\frac{2\omega}{\pi}\int_0^{\infty} \frac{\chi_R(\omega')}{\omega'^2-\omega^2}d\omega' \tag{3.27}$$

Equations 3.26 and 3.27 are the Kramers-Kronig relations, which elucidates the relationship between $\chi_R(\omega)$ and $\chi_I(\omega)$. This is a powerful result because if we know $\chi_R(\omega)$, we can then calculate $\chi_I(\omega)$, and vice versa. It should be evident at this point that the relationship between these two quantities is of tremendous importance in quantifying, understanding, predicting, and designing various dispersion phenomena which are central to this thesis.

3.3 Semiclassical Description of Atom-Light Interaction

In Section 3.1, we introduced the classical model of atom-light interaction, which led to the calculation of the dispersion and absorption profiles of an atomic medium. This section introduces the semiclassical model of this interaction in which the electromagnetic field is still modeled classically, but the atom is now modeled quantum mechanically.

3.3.1 Hamiltonian of a Two-Level Atom

The hydrogen atom is an ideal system to model mathematically because it is a two-body system and therefore its solutions can be expressed in closed form. Furthermore, for reasons that will soon be discussed in greater detail, the hydrogen atom is a good approximation for all alkali atoms which are utilized exclusively in our laboratory and in all the experiments covered in this thesis. A hydrogen atom has one electron for which the Hamiltonian can be written as [18]:

$$\hat{H} = \frac{\hat{p}^2}{2m} + \hat{V}(r) = \frac{\hat{p}^2}{2m} + \frac{q}{4\pi\varepsilon_o \hat{r}^2} \tag{3.28}$$

where $\hat{p} = -i\hbar\hat{\nabla}$ is the momentum operator, m is the electron mass, q is the elementary charge, and r is the distance from the electron to the nuclear proton. The eigenfunctions of this Hamiltonian are the hydrogen wavefunctions [19]:

$$\psi_{nlm} = \sqrt{\left(\frac{2}{na}\right)^3 \frac{(n-l-1)!}{2n[(n+l)!]^3}}\, Y_l^m(\theta,\varphi) \cdot e^{-r/na} \left(\frac{2r}{na}\right)^l \left[L_{n-l-1}^{2l+1}\left(2r/na\right)\right] \tag{3.29}$$

where the quantity under the square root is the normalization constant, $Y_l^m(\theta,\varphi)$ are the spherical harmonics, and $L_{n-l-1}^{2l+1}\left(2r/na\right)$ are the associated Laguerre polynomials. For even values of l, the hydrogen wavefunctions are even with respect to parity; for odd values of l, the hydrogen

wavefunctions are odd with respect to parity. The probability distribution of the electron position is equal to $|\psi_{nlm}|^2$. Images of the hydrogen wavefunctions are shown in Figure 3.4.

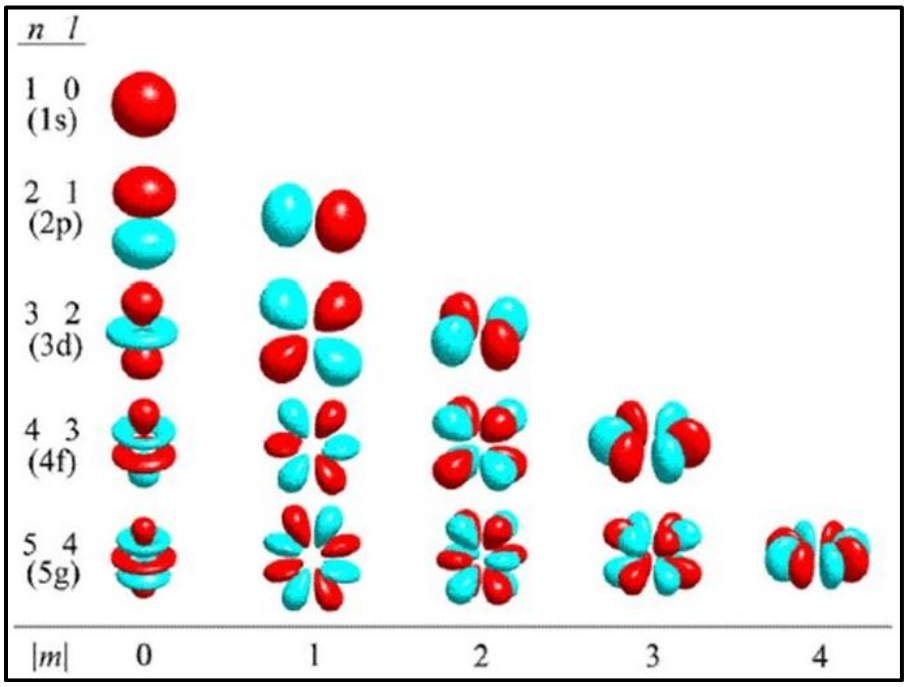

Fig. 3.4: The hydrogen wavefunctions, ψ_{nlm}, for values of $n \leq 5$. l can have values from 0 to $(n-1)$, and m can have values from $-l$ to l. Red and blue represent positive and negative values, respectively.

The "hydrogenic potential", $V(r) \propto \frac{q}{4\pi\varepsilon_o r^2}$, is a good approximation for the potential of the valence electron in any alkali atom, because an alkali atom can be treated roughly as a two-body problem where one "body" is the valence electron while the other "body" is the nucleus which is screened to some extent by the cloud of all other tightly-bound electrons. Accordingly, the hydrogen wavefunctions serve as a good approximation for all alkali wavefunctions.

If we now define $\overrightarrow{p_o}$ as the vector pointing from the nucleus to the valence electron, then the atomic dipole moment can be written as $\overrightarrow{d_o} = -q\overrightarrow{p_o}$. In the presence of an electric $\vec{E}$, the dipole-field interaction energy is $E_I = \overrightarrow{d_o} \cdot \vec{E}$.

In its most general form, the electric field of an electromagnetic wave can be written as $\vec{E}(\vec{r},t) = \hat{\varepsilon}E_o cos\left(\vec{k}\cdot\vec{r} - \omega t - \varphi\right)$ where $\hat{\varepsilon}$ is the unit vector in the direction of the electric field, $\vec{k}$ is the wavevector (where $\left|\vec{k}\right| = \frac{2\pi}{\lambda}$), and ω is the angular frequency. Therefore, the interaction energy of this electric dipole in the presence of an oscillating electric field, E_I, can be written as:

$$E_I = \overrightarrow{d_o}\cdot\vec{E} = (-q\overrightarrow{p_o})\cdot\left(\hat{\varepsilon}E_o cos\left(\vec{k}\cdot\vec{r} - \omega t - \varphi\right)\right) \tag{3.30}$$

Since optical wavelengths are on the order of 10^{-6} m while atomic radii are on the order of 10^{-10} m, an atom in the presence of optical-wavelength electromagnetic radiation sees a spatially-uniform field which oscillates sinusoidally in time. Without loss of generality, if $\vec{r} = 0$, $\varphi = 0$, $\hat{\varepsilon} = \hat{x}$ and $\vec{k} = k\hat{z}$, then the electric field seen by the atom is $\vec{E}(t) = \hat{x}E_o cos(\omega t)$. The interaction energy is then simplified to:

$$E_I = \overrightarrow{d_o}\cdot\vec{E} = (-q\overrightarrow{p_o})\cdot\left(\hat{x}E_o cos(\omega t)\right) = -(\overrightarrow{p_o}\cdot\hat{x})qE_o cos(\omega t) \tag{3.31}$$

If p_o is the projection of the dipole moment onto the x-axis, Equation 3.31 becomes:

$$E_I = -(\overrightarrow{p_o}\cdot\hat{x})qE_o cos(\omega t) = -|p_o|qE_o cos(\omega t) \tag{3.32}$$

Therefore, the Hamiltonian is equal to:

$$\widehat{H} = \left[\frac{\hat{p}^2}{2m} + \frac{q}{4\pi\varepsilon_o\hat{r}^2}\right] + [-q\widehat{p_o}E_o cos(\omega t)] \equiv \widehat{H}_o + \widehat{H}_I \tag{3.33}$$

where $\widehat{p_o}$ is the *dipole operator*, and $\widehat{H}_o$ and $\widehat{H}_I$ are referred to as the "unperturbed" and "interaction" terms of the Hamiltonian, respectively.

3.3.2 Dirac Notation of the Two-Level Atom

In certain scenarios, an atom can be simply modeled as a two-level system with a complex wavefunction $|\psi(t)\rangle$:

$$|\psi(t)\rangle = c_1(t)|\psi_1\rangle + c_2(t)|\psi_2\rangle \tag{3.34}$$

where $|\psi_1\rangle$ and $|\psi_2\rangle$ are energy eigenstates with energies of $E_1 = \hbar\omega_1$ and $E_2 = \hbar\omega_2$, respectively, while $c_1(t)$ and $c_2(t)$ are time-varying *complex* numbers, constrained under the normalization condition:

$$\langle\psi|\psi\rangle = |c_1(t)|^2 + |c_2(t)|^2 = 1 \tag{3.35}$$

The basis of a two-level system consists of two eigenfunctions, $|\psi_1\rangle$ and $|\psi_2\rangle$. In matrix notation, the electron wavefunction can therefore be represented in the "$|\psi_1\rangle$, $|\psi_2\rangle$" basis as:

$$|\psi(t)\rangle = \begin{bmatrix} c_1(t) \\ c_2(t) \end{bmatrix} \tag{3.36}$$

The Schrödinger equation [18] governs the dynamics of the electron wavefunction:

$$i\hbar\frac{\partial|\psi\rangle}{\partial t} = \hat{H}|\psi\rangle = \left(\hat{H}_o + \hat{H}_I\right)|\psi\rangle \tag{3.37}$$

In matrix notation, Equation 3.37 would be written as:

$$i\hbar\frac{\partial}{\partial t}\begin{bmatrix} c_1(t) \\ c_2(t) \end{bmatrix} = \begin{bmatrix} \langle\psi_1|\left(\hat{H}_o + \hat{H}_I\right)|\psi_1\rangle & \langle\psi_2|\left(\hat{H}_o + \hat{H}_I\right)|\psi_1\rangle \\ \langle\psi_1|\left(\hat{H}_o + \hat{H}_I\right)|\psi_2\rangle & \langle\psi_2|\left(\hat{H}_o + \hat{H}_I\right)|\psi_2\rangle \end{bmatrix}\begin{bmatrix} c_1(t) \\ c_2(t) \end{bmatrix} \tag{3.38}$$

where $|\psi_1\rangle$ and $|\psi_2\rangle$ are the energy eigenstates of the *unperturbed* Hamiltonian, so that $\langle\psi_m|\left(\hat{H}_o\right)|\psi_n\rangle = \hbar\omega_m\delta_{mn}$. As mentioned earlier, these energy eigenstates are either strictly even (for even values of the quantum number l) or strictly odd (for odd values of the quantum number l) with respect to $\vec{r} = 0$, the position of the nucleus. Because the $\hat{x}$ operator is odd with respect to $\vec{r} = 0$, the inner products $\langle\psi_1|(\hat{x})|\psi_1\rangle$ and $\langle\psi_2|(\hat{x})|\psi_2\rangle$ are both equal to zero. On the other hand, if $l(|\psi_1\rangle)$ is even and $l(|\psi_2\rangle)$ is odd (or vice versa), then the inner products $\langle\psi_1|(\hat{x})|\psi_2\rangle$ and $\langle\psi_2|(\hat{x})|\psi_1\rangle$ are non-zero. In this case, the Hamiltonian in matrix form would be:

$$\widehat{H} = \widehat{H}_o + \widehat{H}_I = \begin{bmatrix} \hbar\omega_1 & 0 \\ 0 & \hbar\omega_2 \end{bmatrix} + \begin{bmatrix} 0 & qp_oE_o cos(\omega t) \\ qp_oE_o cos(\omega t) & 0 \end{bmatrix} = \begin{bmatrix} \hbar\omega_1 & qp_oE_o cos(\omega t) \\ qp_oE_o cos(\omega t) & \hbar\omega_2 \end{bmatrix} \tag{3.39}$$

Letting $\Omega_o \equiv \frac{qp_oE_o}{\hbar}$, the Hamiltonian simplifies to:

$$\widehat{H} = \hbar \begin{bmatrix} \omega_1 & \Omega_o cos(\omega t) \\ \Omega_o cos(\omega t) & \omega_2 \end{bmatrix} = \hbar \begin{bmatrix} \omega_1 & \frac{\Omega_o}{2}\left(e^{i\omega t} + e^{-i\omega t}\right) \\ \frac{\Omega_o}{2}\left(e^{i\omega t} + e^{-i\omega t}\right) & \omega_2 \end{bmatrix} \tag{3.40}$$

3.3.3 The Rotating Wave Approximation

The Rotating Wave Approximation (RWA) is now made [20], which eliminates highly-detuned terms from the Hamiltonian. This can be done because the highly-detuned terms have very weak coupling to the atomic energy levels and therefore contribute a negligible amount to the solution. The RWA simplifies the Hamiltonian to:

$$\widehat{H} \cong \hbar \begin{bmatrix} \omega_1 & \frac{\Omega_o}{2} e^{i\omega t} \\ \frac{\Omega_o}{2} e^{-i\omega t} & \omega_2 \end{bmatrix} \tag{3.41}$$

The RWA is a powerful tool because it enables the Hamiltonian to be made time-independent through the Rotating Wave Transformation (RWT). The first step of the RWT is to define a rotation operator (or Q-matrix) as follows:

$$\hat{Q} \equiv \begin{bmatrix} e^{i\theta_1 t} & 0 \\ 0 & e^{i\theta_2 t} \end{bmatrix} \tag{3.42}$$

Now, we let the "rotated state" $|\tilde{\psi}\rangle$ be defined as:

$$|\tilde{\psi}\rangle \equiv \hat{Q}|\psi\rangle = \begin{bmatrix} e^{i\theta_1 t} & 0 \\ 0 & e^{i\theta_2 t} \end{bmatrix} \begin{bmatrix} c_1 \\ c_2 \end{bmatrix} = \begin{bmatrix} c_1 e^{i\theta_1 t} \\ c_2 e^{i\theta_2 t} \end{bmatrix} \equiv \begin{bmatrix} \tilde{c_1} \\ \tilde{c_2} \end{bmatrix} \tag{3.43}$$

Therefore:

$$\frac{\partial|\tilde{\psi}\rangle}{\partial t} = \begin{bmatrix} i\theta_1 c_1 e^{i\theta_1 t} \\ i\theta_2 c_2 e^{i\theta_2 t} \end{bmatrix} = \begin{bmatrix} i\theta_1 & 0 \\ 0 & i\theta_2 \end{bmatrix} \begin{bmatrix} c_1 e^{i\theta_1 t} \\ c_2 e^{i\theta_2 t} \end{bmatrix} \equiv \widehat{M}|\tilde{\psi}\rangle \tag{3.44}$$

where $\widehat{M} \equiv \begin{bmatrix} i\theta_1 & 0 \\ 0 & i\theta_2 \end{bmatrix}$. Applying the product rule for derivatives yields:

$$\frac{\partial|\tilde{\psi}\rangle}{\partial t} = \frac{\partial}{\partial t}\left[\hat{Q}|\psi\rangle\right] = \frac{\partial \hat{Q}}{\partial t}|\psi\rangle + \hat{Q}\frac{\partial|\psi\rangle}{\partial t} = \widehat{M}\hat{Q}|\psi\rangle + \hat{Q}\frac{\partial|\psi\rangle}{\partial t} \tag{3.45}$$

Putting together Equations 3.37 and 3.45 gives:

$$\frac{\partial|\tilde{\psi}\rangle}{\partial t} = \widehat{M}\hat{Q}|\psi\rangle + \hat{Q}\frac{\partial|\psi\rangle}{\partial t} = \widehat{M}\hat{Q}|\psi\rangle - \frac{i}{\hbar}\hat{Q}\widehat{H}|\psi\rangle \tag{3.46}$$

Since $\hat{Q}^{-1}\hat{Q} = \hat{I}$, where $\hat{I}$ is the identity matrix, Equation 3.46 can be rewritten as:

$$\frac{\partial|\tilde{\psi}\rangle}{\partial t} = \widehat{M}\hat{Q}|\psi\rangle - \frac{i}{\hbar}\hat{Q}\widehat{H}\hat{Q}^{-1}\hat{Q}|\psi\rangle = \widehat{M}|\tilde{\psi}\rangle - \frac{i}{\hbar}\hat{Q}\widehat{H}\hat{Q}^{-1}|\tilde{\psi}\rangle = \left[\widehat{M} - \frac{i}{\hbar}\hat{Q}\widehat{H}\hat{Q}^{-1}\right]|\tilde{\psi}\rangle \tag{3.47}$$

Therefore, the Schrödinger equation in the "rotating frame" is:

$$i\hbar\frac{\partial|\tilde{\psi}\rangle}{\partial t} = \left[i\hbar\widehat{M} + \hat{Q}\widehat{H}\hat{Q}^{-1}\right]|\tilde{\psi}\rangle \equiv \widehat{\tilde{H}}|\tilde{\psi}\rangle \tag{3.48}$$

where $\widehat{\tilde{H}}$ is the "Rotating Wave Hamiltonian", which can be written in matrix form as:

$$\widehat{\tilde{H}} = \hbar\begin{bmatrix} (\omega_1 - \theta_1) & \frac{\Omega_o}{2}e^{i(\theta_1 - \theta_2 + \omega)t} \\ \frac{\Omega_o}{2}e^{-i(\theta_1 - \theta_2 + \omega)t} & (\omega_2 - \theta_2) \end{bmatrix} \tag{3.49}$$

Letting $\omega = \theta_2 - \theta_1$ gets rid of the time-dependence, so that:

$$\widehat{\tilde{H}} = \hbar\begin{bmatrix} (\omega_1 - \theta_1) & \frac{\Omega_o}{2} \\ \frac{\Omega_o}{2} & (\omega_2 - \theta_2) \end{bmatrix} \tag{3.50}$$

Setting $\theta_1 = \omega_1$, $\theta_2 = \omega_1 + \omega$, and defining $\delta \equiv \omega - (\omega_2 - \omega_1)$, the Rotating Wave Hamiltonian is simplified to:

$$\widehat{\widetilde{H}} = \hbar \begin{bmatrix} 0 & \frac{\Omega_o}{2} \\ \frac{\Omega_o}{2} & -\delta \end{bmatrix} \tag{3.51}$$

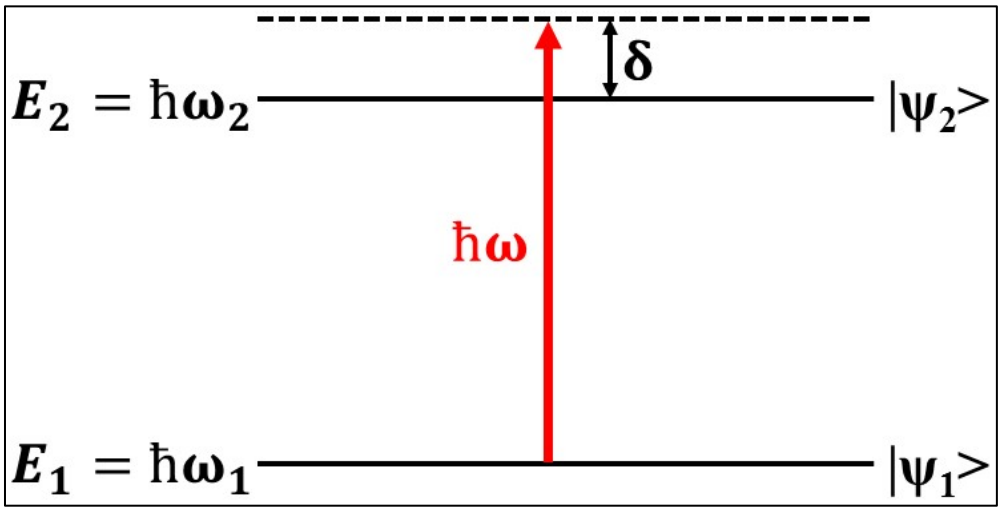

Fig. 3.5: δ is defined as $\omega - (\omega_2 - \omega_1)$, which is the detuning between the electromagnetic frequency and the transition frequency

Combining Equations 3.43, 3.48 and 3.51 yields:

$$i\hbar \frac{d}{dt} \begin{bmatrix} \widetilde{c_1} \\ \widetilde{c_2} \end{bmatrix} = \hbar \begin{bmatrix} 0 & \frac{\Omega_o}{2} \\ \frac{\Omega_o}{2} & -\delta \end{bmatrix} \begin{bmatrix} \widetilde{c_1} \\ \widetilde{c_2} \end{bmatrix} \tag{3.52}$$

This results in two equations:

$$\frac{d\widetilde{c_1}}{dt} = -i \frac{\Omega_o}{2} \widetilde{c_2} \tag{3.53}$$

$$\frac{d\widetilde{c_2}}{dt} = i \left[\delta \widetilde{c_2} - \frac{\Omega_o}{2} \widetilde{c_1} \right] \tag{3.54}$$

The time derivative of Equation 3.54 is:

$$\frac{d^2\widetilde{c_2}}{dt^2} = i \left[\delta \frac{d\widetilde{c_2}}{dt} - \frac{\Omega_o}{2} \frac{d\widetilde{c_1}}{dt} \right] = i \left[\delta \frac{d\widetilde{c_2}}{dt} - \frac{\Omega_o}{2} \left(-i \frac{\Omega_o}{2} \widetilde{c_2} \right) \right] = i\delta \frac{d\widetilde{c_2}}{dt} - \frac{{\Omega_o}^2}{4} \widetilde{c_2} \tag{3.55}$$

This second-order differential equation in $\widetilde{c_2}$ takes the same form as a harmonic oscillator and therefore admits solutions of the following form:

$$\widetilde{c_2}(t) = Ae^{i\Omega_1 t} + Be^{-i\Omega_2 t} \tag{3.56}$$

Plugging Equation 3.56 into Equation 3.55 results in:

$$-\left[{\Omega_1}^2 Ae^{i\Omega_1 t} + {\Omega_2}^2 Be^{i\Omega_2 t}\right] = i\delta\left[i\Omega_1 Ae^{i\Omega_1 t} - i\Omega_2 Be^{i\Omega_2 t}\right] - \frac{{\Omega_o}^2}{4}\left[Ae^{i\Omega_1 t} + Be^{i\Omega_2 t}\right] \tag{3.57}$$

This results in two quadratic equations:

$${\Omega_1}^2 - \delta\Omega_1 - \frac{{\Omega_o}^2}{4} = 0 \tag{3.58}$$

$${\Omega_2}^2 + \delta\Omega_2 - \frac{{\Omega_o}^2}{4} = 0 \tag{3.59}$$

Therefore:

$$\Omega_1 = \frac{1}{2}\left[\delta \pm \sqrt{\delta^2 + {\Omega_o}^2}\right] \tag{3.60}$$

$$\Omega_2 = \frac{1}{2}\left[-\delta \pm \sqrt{\delta^2 + {\Omega_o}^2}\right] \tag{3.61}$$

If the system starts out in thermal equilibrium and $\hbar(\omega_2 - \omega_1) \gg k_B T$, then $\widetilde{c_1}(t = 0) = 1$ and $\widetilde{c_2}(t = 0) = 0$, so that $A = -B$. Therefore:

$$\widetilde{c_2}(t) = A\left(e^{\frac{i}{2}\left[\delta \pm \sqrt{\delta^2 + {\Omega_o}^2}\right]t} - e^{-\frac{i}{2}\left[-\delta \pm \sqrt{\delta^2 + {\Omega_o}^2}\right]t}\right) = iAe^{i\delta t}\sin\left(\frac{\sqrt{\delta^2 + {\Omega_o}^2}}{2}t\right) \tag{3.62}$$

Substituting Equation 3.62 into Equation 3.53 yields:

$$\widetilde{c_1}(t) = Ae^{i\delta t}\cos\left(\frac{\sqrt{\delta^2 + {\Omega_o}^2}}{2}t\right) \tag{3.63}$$

Normalization requires that $\left|\tilde{c_1}^2\right| + \left|\tilde{c_2}^2\right| = 1$, so that $A = \frac{1}{\sqrt{2}}$. Therefore:

$$c_1(t) = \tilde{c_1} e^{-i\theta_1 t} = \tilde{c_1} e^{-i\omega_1 t} = \frac{e^{-i(\omega_1 - \delta)t}}{\sqrt{2}} \cos\left(\frac{\sqrt{\delta^2 + {\Omega_o}^2}}{2} t\right) \tag{3.64}$$

$$c_2(t) = \tilde{c_2} e^{-i\theta_2 t} = \tilde{c_2} e^{-i(\omega_1 + \omega)t} = i\frac{e^{i\omega_2 t}}{\sqrt{2}} \sin\left(\frac{\sqrt{\delta^2 + {\Omega_o}^2}}{2} t\right) \tag{3.65}$$

The time evolution of $|\psi(t)\rangle$ has finally been solved. The phases of coefficients c_1 and c_2 oscillate rapidly (at optical frequencies) but their amplitudes oscillate much more slowly, with a frequency of $\Omega \equiv \frac{\sqrt{{\Omega_o}^2 + \delta^2}}{2}$. This is the so-called *Rabi frequency*. The percentage of atoms in eigenstates $|\psi_1\rangle$ and $|\psi_2\rangle$, respectively, are:

$$|c_1|^2 = \cos^2(\Omega t) \tag{3.66}$$

$$|c_2|^2 = \sin^2(\Omega t) \tag{3.67}$$

Although the semiclassical two-level approach has been instructive, it is important to remember that the electric field has been treated as a *classical* entity. The most rigorous treatment governing the interaction between an electromagnetic wave and a two-level atomic system requires the quantization of *both* the atom and the field. The fully-quantized approach to solving this system takes into account the interaction between the atom and the vacuum and thermal photons, which results in "spontaneous" decay. This fully-quantized approach leads to the Wigner-Weisskopf theory [21] from which rates of spontaneous emission can be calculated.

The second deficiency in the semiclassical two-level model arises in a system where there is a *statistical ensemble* of atoms, rather than a single atom. This approach does not mathematically

distinguish between a *pure state* (where every atom is in the same state or the same superposition of states) and a *mixed state* (where not every atom is in the same superposition of states). The distinction between these two scenarios is illustrated in Figure 3.6.

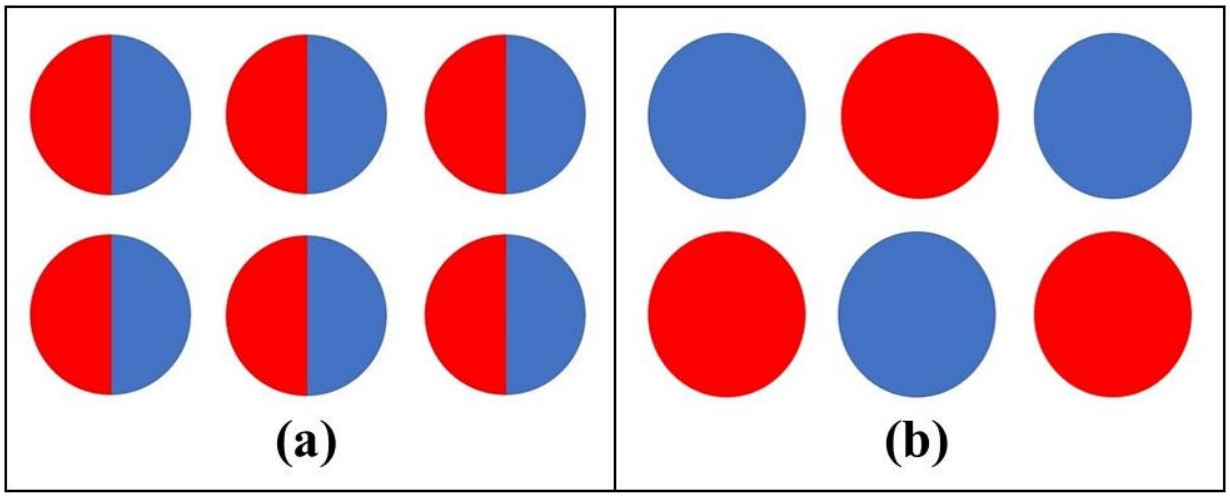

Fig. 3.6: (a): Pure state. All six atoms are in a 50/50 superposition of "red" and "blue" (or $|\psi_1\rangle$ and $|\psi_2\rangle$ in the case of the two-level atom); (b) Mixed state. Three atoms are in state $|\psi_1\rangle$ while the other three atoms are in state $|\psi_2\rangle$

3.3.4 The Density Matrix Approach

The density matrix approach solves both deficiencies of the semiclassical approach by providing a mathematical framework in which the coherent decay of atomic states can be treated as a phenomenological effect (without needing to explicitly calculate these rates from first principles), and in which pure and mixed states can be distinguished. The density matrix is defined as the following *outer product*:

$$\hat{\rho} \equiv \begin{bmatrix} |c_1|^2 & c_1 c_2{}^* \\ c_2 c_1{}^* & |c_2|^2 \end{bmatrix} \equiv \begin{bmatrix} \rho_{11} & \rho_{12} \\ \rho_{21} & \rho_{22} \end{bmatrix} \equiv \frac{1}{N} \sum_{m=1}^{N} |\psi_m\rangle\langle\psi_m| \tag{3.68}$$

where c_1 and c_2 are the coefficients of $|\psi_1\rangle$ and $|\psi_2\rangle$, respectively. The summation is taken over each atom, where N is the number of atoms. In a two-level system, the density matrix is a 2×2

matrix, where the diagonal terms represent the *average* populations of the energy levels and the off-diagonal terms represent the *average* phase coherence between the two states. The time derivative of the density matrix is:

$$\frac{\partial \hat{\rho}}{\partial t} = \frac{1}{N}\sum_{m=1}^{N}\left(\frac{\partial|\psi_m\rangle}{\partial t}\right)\langle\psi_m| + |\psi_m\rangle\left(\frac{\partial\langle\psi_m|}{\partial t}\right)$$

$$= -\frac{i}{\hbar}\sum_{m=1}^{N}\{\hat{H}|\psi_m\rangle\langle\psi_m| - |\psi_m\rangle\langle\psi_m|\hat{H}^*\} = -\frac{i}{\hbar}\{\hat{H}\hat{\rho} - \hat{\rho}\hat{H}\} \tag{3.69}$$

$$= -\frac{i}{\hbar}[\hat{H}, \hat{\rho}]$$

where $[\hat{H}, \hat{\rho}]$ is the commutator of the Hamiltonian and the density matrix. Equation 3.69 is called the *Liouville equation* [22], which governs the time evolution of a mixed state. The Liouville equation is equivalent to the Schrödinger equation in the density matrix formalism.

Decay terms are treated phenomenologically by introducing a decay matrix, $\hat{\rho}_{DECAY}$, which keeps track of the decay rate from state $|j\rangle$ to state $|k\rangle$, for all $|j\rangle$ and $|k\rangle$. The Liouville equation with phenomenological decay terms considered is therefore:

$$\frac{\partial \hat{\rho}}{\partial t} = \dot{\hat{\rho}} = -\frac{i}{\hbar}[\hat{H}, \hat{\rho}] + \hat{\rho}_{DECAY} \tag{3.70}$$

It is once again favorable to solve this system in the rotating-wave reference frame, which makes the Hamiltonian time-independent. Since $|\widetilde{\psi_m}\rangle \equiv \hat{Q}|\psi_m\rangle$, then:

$$|\widetilde{\psi_m}\rangle\langle\widetilde{\psi_m}| = \hat{Q}|\psi_m\rangle\langle\psi_m|\hat{Q}^* = \hat{Q}\rho_{mm}\hat{Q}^* \equiv \widetilde{\rho_{mm}} \tag{3.71}$$

The terms in the density matrix are averaged over all N atoms, so that:

$$\tilde{\hat{\rho}} \equiv \begin{bmatrix}\widetilde{\rho_{11}} & \widetilde{\rho_{12}}\\ \widetilde{\rho_{21}} & \widetilde{\rho_{22}}\end{bmatrix} = \begin{bmatrix}\rho_{11} & \rho_{12}e^{-i\omega t}\\ \rho_{21}e^{i\omega t} & \rho_{22}\end{bmatrix} \tag{3.72}$$

It can be shown [23,24] that the equation of motion for this rotated density matrix (the optical Bloch equation) takes on the same form as the non-rotated density matrix, so that:

$$\dot{\tilde{\hat{\rho}}} = -\frac{i}{\hbar}\left[\tilde{\hat{H}}, \tilde{\hat{\rho}}\right] + \dot{\tilde{\hat{\rho}}}_{DECAY} \tag{3.73}$$

where the phenomenological decay matrix is:

$$\dot{\tilde{\hat{\rho}}}_{DECAY} = \begin{bmatrix} \Gamma\widetilde{\rho_{22}} & -\frac{\Gamma}{2}\widetilde{\rho_{12}} \\ -\frac{\Gamma}{2}\widetilde{\rho_{21}} & -\Gamma\widetilde{\rho_{22}} \end{bmatrix} \tag{3.74}$$

In matrix form, the equation of evolution is therefore:

$$\begin{bmatrix} \dot{\widetilde{\rho_{11}}} & \dot{\widetilde{\rho_{12}}} \\ \dot{\widetilde{\rho_{21}}} & \dot{\widetilde{\rho_{22}}} \end{bmatrix} = \frac{i}{\hbar}\left\{ \begin{bmatrix} \widetilde{\rho_{11}} & \widetilde{\rho_{12}} \\ \widetilde{\rho_{21}} & \widetilde{\rho_{22}} \end{bmatrix} \begin{bmatrix} 0 & \frac{\Omega_o}{2} \\ \frac{\Omega_o}{2} & -\delta \end{bmatrix} - \begin{bmatrix} 0 & \frac{\Omega_o}{2} \\ \frac{\Omega_o}{2} & -\delta \end{bmatrix} \begin{bmatrix} \widetilde{\rho_{11}} & \widetilde{\rho_{12}} \\ \widetilde{\rho_{21}} & \widetilde{\rho_{22}} \end{bmatrix} \right\} + \begin{bmatrix} \Gamma\widetilde{\rho_{22}} & -\frac{\Gamma}{2}\widetilde{\rho_{12}} \\ -\frac{\Gamma}{2}\widetilde{\rho_{21}} & -\Gamma\widetilde{\rho_{22}} \end{bmatrix} \tag{3.75}$$

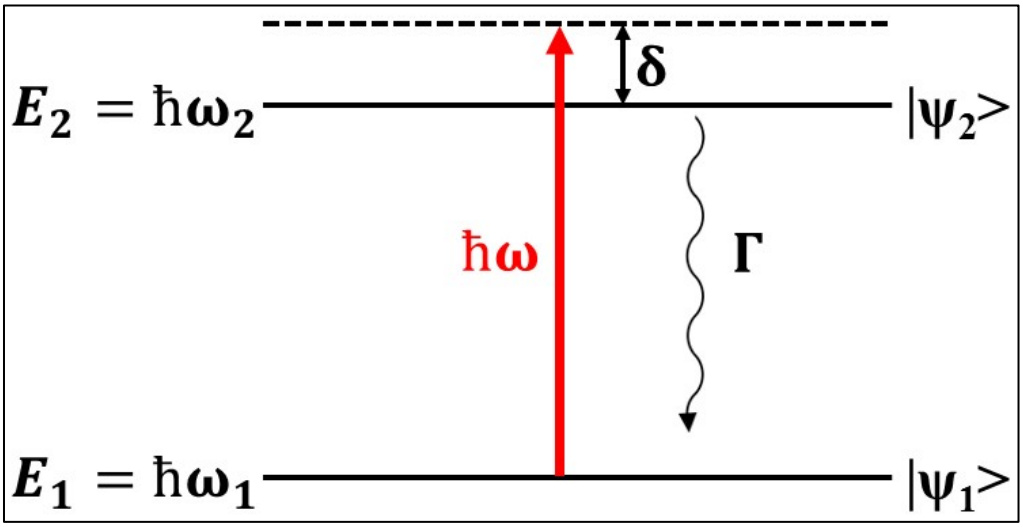

Fig. 3.7: Energy levels, optical field, and phenomenological decay rate in the two-level system

By setting $\dot{\tilde{\rho}} = 0$, in addition to the constraint that $\widetilde{\rho_{11}} + \widetilde{\rho_{22}} = 1$, we find the steady-state solution to the Liouville equation.

$$\widetilde{\rho_{11}} = \frac{{\Omega_o}^2 + \Gamma^2 + 4\delta^2}{2{\Omega_o}^2 + \Gamma^2 + 4\delta^2} \tag{3.76}$$

$$\widetilde{\rho_{12}} = \frac{2\Omega_o\delta + i\Omega_o\Gamma}{2{\Omega_o}^2 + \Gamma^2 + 4\delta^2} \tag{3.77}$$

$$\widetilde{\rho_{21}} = \frac{2\Omega_o\delta - i\Omega_o\Gamma}{2{\Omega_o}^2 + \Gamma^2 + 4\delta^2} = \widetilde{\rho_{12}}^* \tag{3.78}$$

$$\widetilde{\rho_{22}} = \frac{{\Omega_o}^2}{2{\Omega_o}^2 + \Gamma^2 + 4\delta^2} = 1 - \widetilde{\rho_{11}} \tag{3.79}$$

Equations 3.76-3.79 show that in the limit of large decay, $(\Gamma \to \infty)$, $\widetilde{\rho_{11}} \to 1$, while $\widetilde{\rho_{12}}$, $\widetilde{\rho_{21}}$, and $\widetilde{\rho_{22}} \to 0$. In the limit of large detuning $(\delta \to \infty)$, $\widetilde{\rho_{11}} \to 1$, while $\widetilde{\rho_{12}}$, $\widetilde{\rho_{21}}$, and $\widetilde{\rho_{22}} \to 0$. In the limit of strong electric dipole interaction $(\Omega_0 \to \infty)$, $\widetilde{\rho_{11}} \to {}^1\!/_2$, $\widetilde{\rho_{22}} \to {}^1\!/_2$, $\widetilde{\rho_{12}}$ and $\widetilde{\rho_{21}} \to 0$. We note that in a two-level system, $\widetilde{\rho_{22}}$ can never exceed $\widetilde{\rho_{11}}$ in the steady state. This has significant implications in the design of lasers, as will be discussed in Chapter 4.

With the decay terms taken into account, the system now resembles a *damped* driven harmonic oscillator. As a result, this system reaches a steady state which is independent of initial conditions. This steady state solution oscillates at the optical frequency, but is stationary in the rotating wave frame of reference.

The density matrix formulation is also powerful in its simplicity regarding the calculation of physical parameters (or more exactly, the expectation values of physical parameters). Consider an observable parameter, represented by the operator $\hat{A}$. The expectation value of this operator is:

$$\langle \hat{A} \rangle = \frac{1}{N}\sum_{m=1}^{N}\langle \psi_m|\hat{A}|\psi_m\rangle = \frac{1}{N}\sum_{m=1}^{N} tr\big(|\psi_m\rangle\langle\psi_m|\hat{A}\big) = tr\left(\frac{1}{N}\sum_{m=1}^{N}|\psi_m\rangle\langle\psi_m|\hat{A}\right) \\ = tr\big(\hat{\rho}\hat{A}\big) \tag{3.80}$$

This result is powerful because it applies to all physical observables such as position, energy, momentum, angular momentum, etc. More importantly, the index of refraction and coefficient of absorption of a medium, which are *macroscopic* physical parameters depending on *collective* atomic response to an applied electromagnetic wave, can be calculated using this formula. To begin the calculation of refractive index and absorption coefficient, we first calculate the (expectation value of the) position of an electron.

One may reasonably expect that the (expectation value of the) position of an electron relative to the nucleus should be sinusoidally-varying at the same frequency as the electromagnetic wave propagating through it, though not necessarily with the same phase. With this in mind, we can express the expectation value of the electron position as:

$$\langle \hat{x} \rangle = tr(\hat{\rho}\hat{x}) = tr\left(\begin{bmatrix}\rho_{11} & \rho_{12}\\ \rho_{21} & \rho_{22}\end{bmatrix}\begin{bmatrix}0 & x_0\\ x_0 & 0\end{bmatrix}\right) = x_0(\rho_{12}+\rho_{21}) \tag{3.81}$$

where $x_o = \sqrt{\hbar/2m(\omega_2-\omega_1)}$ [18]. Therefore, the expectation value of the dipole moment of a single atom would be:

$$\langle p \rangle = q\langle x \rangle = x_0(\rho_{12}+\rho_{21}) = x_0\big(\widetilde{\rho_{12}}e^{i\omega t}+\widetilde{\rho_{21}}e^{-i\omega t}\big) = x_0\big(\widetilde{\rho_{21}}e^{-i\omega t}+c.c.\big) \tag{3.82}$$

To express Equation 3.82 in phasor notation, the complex conjugate is dropped, so that:

$$\langle p \rangle = x_0\left(\frac{2\Omega_o\delta - i\Omega_o\Gamma}{2{\Omega_o}^2+\Gamma^2+4\delta^2}\right)e^{-i\omega t} \tag{3.83}$$

If there are N atoms per unit volume, then the bulk polarization of the medium is:

$$P \equiv \left|\vec{P}\right| = N\langle p\rangle = Nx_0\left(\frac{2\Omega_o\delta - i\Omega_o\Gamma}{2{\Omega_o}^2 + \Gamma^2 + 4\delta^2}\right)e^{-i\omega t} \tag{3.84}$$

The material susceptibility, $\tilde{\chi}$, is defined as $\vec{P} = (\varepsilon_o\tilde{\chi})\vec{E}$, so that:

$$P = Nx_0\left(\frac{2\Omega_o\delta - i\Omega_o\Gamma}{2{\Omega_o}^2 + \Gamma^2 + 4\delta^2}\right)e^{-i\omega t} = (\varepsilon_o\tilde{\chi})E_o e^{-i\omega t} \tag{3.85}$$

where we note that the tilde in the $\tilde{\chi}$ is because it is a complex function, which is in contrast with the other tildes we have used throughout this chapter to denote quantities in the rotating wave reference frame. We therefore see that:

$$\tilde{\chi} = \frac{Nx_0}{\varepsilon_o E_o}\left(\frac{2\Omega_o\delta - i\Omega_o\Gamma}{2{\Omega_o}^2 + \Gamma^2 + 4\delta^2}\right) \tag{3.86}$$

Once again, the real and imaginary parts of $\tilde{\chi}$ represent the dispersion profile and absorption/gain profile, respectively. Plotting these two quantities together shows the relationship between the two.

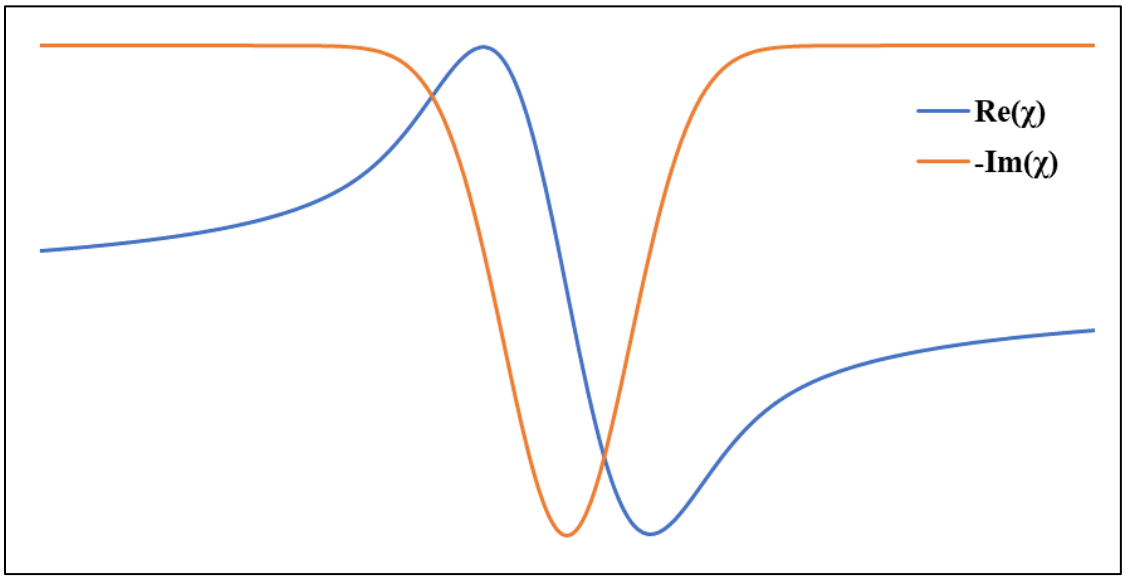

Fig. 3.8: The real and imaginary parts of $\tilde{\chi}$, plotted using Equation 3.86.

The density matrix calculation shows once again that negative dispersion occurs in a two-level absorptive resonance, which is consistent with the Kramers-Kronig relations as well as the

classical calculation of the atom-light interaction. We will eventually use the Liouville equation to solve the dynamics of a fast-light laser; however, as we will show in Chapter 4, all lasers must utilize at least three levels. At that point, the density matrix formulation will be extended from the two-level system to the N-level system, where $N \geq 3$.

CHAPTER 4

SUPERLUMINAL DPAL EXPERIMENT

4.1 Introduction to Laser Design

In Chapter 2, we explored many potential ways to use dispersion (both fast and slow light) for sensitivity enhancement in optical metrology. For the following reasons, we concluded by the end of Chapter 2 that the best way to implement dispersion for the purpose of optical metrological enhancement would be to build a "superluminal" or "fast-light" laser in which the *intra-cavity lasing beam* experiences negative dispersion:

1. The splitting between frequencies is enhanced by a factor of $n_g{}^{-1}$ in the region of linear dispersion. In principle, n_g can be equal to zero, so that this enhancement is limited only by higher-order nonlinearities in the dispersion profile.
2. The quantum-limited laser linewidth (the so-called Schawlow-Townes linewidth [25]) in general can be much narrower than the linewidth of the highest-finesse resonators that are experimentally achievable.
3. The linewidth of a resonator broadens in the presence of negative dispersion; however, as discussed in section 2.3, we have reason to believe that the Schawlow-Townes linewidth of a *laser* does *not* broaden in the presence of negative dispersion.

If we want to build a *superluminal* laser, it is important to first understand how to build a *conventional* laser. There are many types of lasers, but they all have two things in common: A gain medium and a cavity. Figure 4.1 shows a schematic of a conventional laser. The purpose of the

gain medium is to amplify the light going into it; for example, if 100 photons enter the "gain cell" and 120 photons exit it, then the gain is equal to twenty percent. After exiting the gain cell, the light bounces around until it hits a partial reflector, called an "output coupler". If, for example, the output coupler has a reflectivity of 90%, then 10% of the photons (which in this example would be twelve) are transmitted, while the other 90% (108 in this example) are reflected and re-amplified in the gain cell in the next pass through. However, the number of photons in each subsequent pass does not increase indefinitely; as the optical field becomes more powerful, the gain coefficient decreases. So, if the gain medium turns 100 photons into 120 photons, that does not necessarily mean it will turn 1,000 photons into 1,200 photons – it might only turn 1,000 photons into 1,100 photons, yielding a gain coefficient of 10%. The laser eventually reaches a steady state once the number of photons being created in one pass through the gain medium is balanced out by the number of the photons being emitted in one pass through the output coupler (plus any other losses occurring inside the cavity).

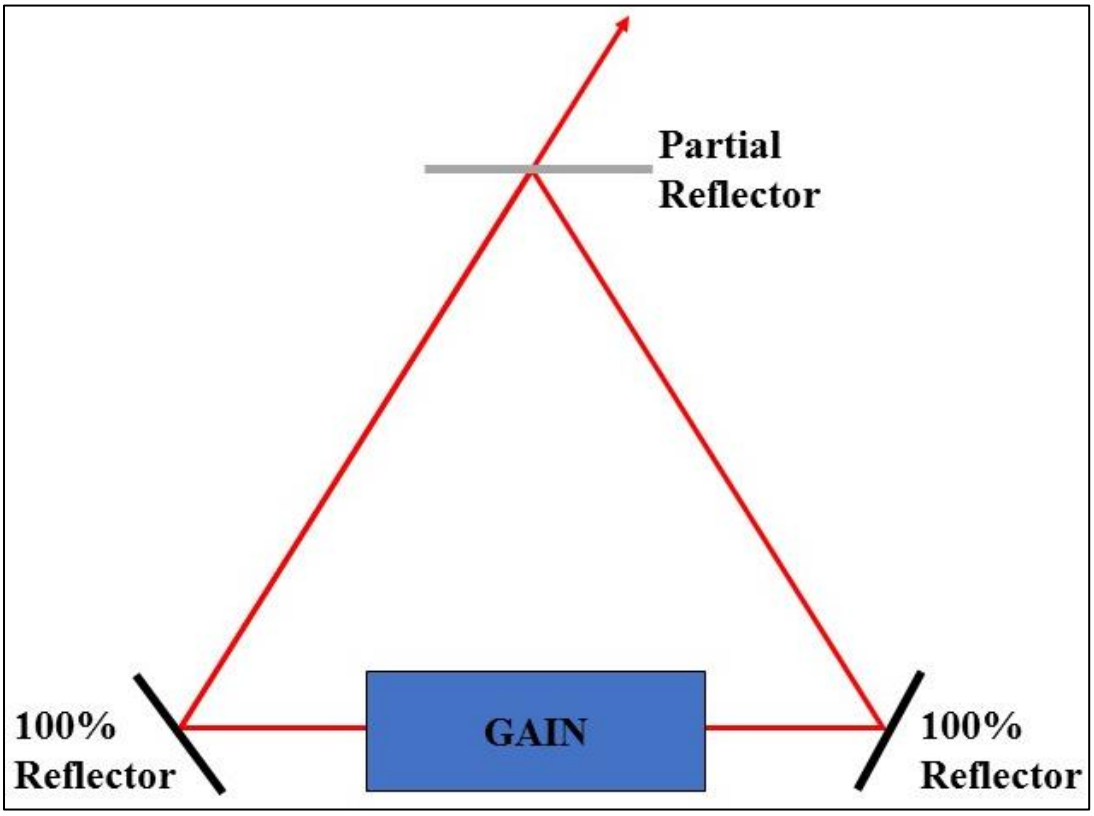

Fig. 4.1: Schematic of a conventional laser. In this example, the cavity contains three mirrors (one of them a partial reflector). However, in general, a laser cavity can contain any number of mirrors greater than or equal to two. The intra-cavity beam gets re-amplified each time it passes through the gain medium, and a fraction of it is then emitted from the partial reflector (which is called the "output coupler")

There are many types of lasers, each with their own mechanism for creating gain; however, all gain mechanisms rely on *population inversion*, a condition in which a higher-energy state has a greater population than a lower-energy state. When a resonant photon hits an atom in the upper energy state, it causes the atom to drop to the lower energy state, releasing a photon in the process. When a resonant photon hits an atom in the lower state, the photon is absorbed and the atom is excited into the higher energy state. Therefore, as long as there are more atoms in the upper state than in the lower state, the number of photons leaving the gain medium exceeds the number of photons entering it. This concept is illustrated in Figure 4.2.

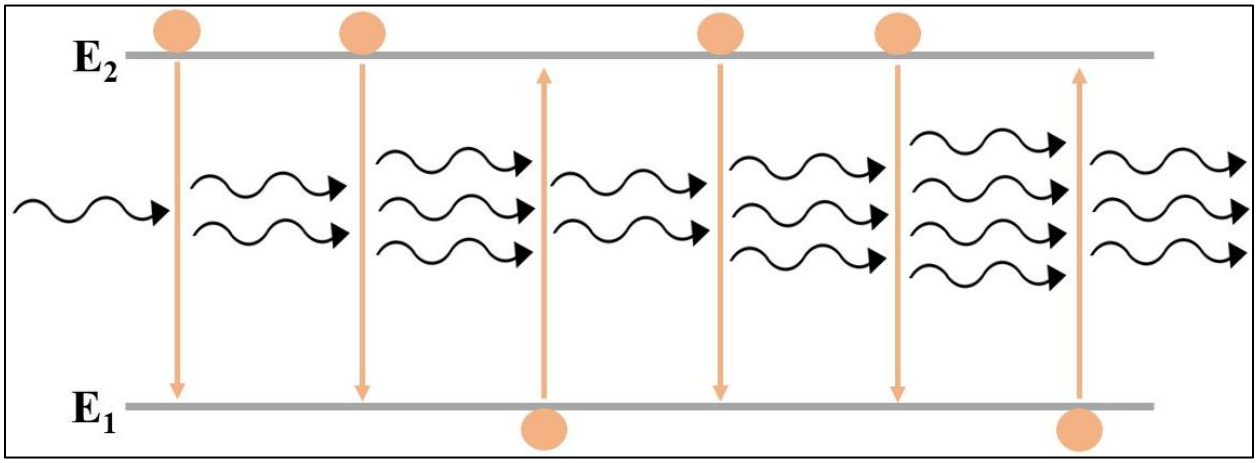

Fig. 4.2: Four atoms start out in the upper state and two atoms start out in the lower state. When a photon hits an atom in the upper state, the atom drops to the lower state, releasing a photon with it. When a photon hits an atom in the lower state, the atom absorbs the photon, thus exciting the atom to the higher state. Therefore, in this example, one photon enters the cell and three photons exit. This net gain of two photons results from the fact that the system started out with four atoms in the upper state and two atoms in the lower state.

We showed in Chapter 3 that in a two-level system, the steady-state value of $\widetilde{\rho_{22}}$, representing the fraction of atoms in the upper state, can never exceed $\frac{1}{2}$. Therefore, population inversion can never be achieved in a two-level system; as a result, all lasers must utilize *at least* three energy levels [26]. To understand how population inversion can be achieved in a three-level system, consider the three-level atom in Figure 4.3(a). This atom has decay rates from $|3\rangle \rightarrow |1\rangle$, $|2\rangle \rightarrow |1\rangle$, and $|3\rangle \rightarrow |2\rangle$, labeled Γ_{31}, Γ_{21}, and Γ_{32}, respectively. If $(E_2 - E_1) \gg k_B T$, then in thermal equilibrium, all atoms are in state $|1\rangle$ [27]. In Figure 4.3(b), we apply an optical pump resonant with the $|1\rangle \rightarrow |3\rangle$ transition, so that the atoms are transferred from $|1\rangle$ to $|3\rangle$ at a rate of R_{PUMP} [28].

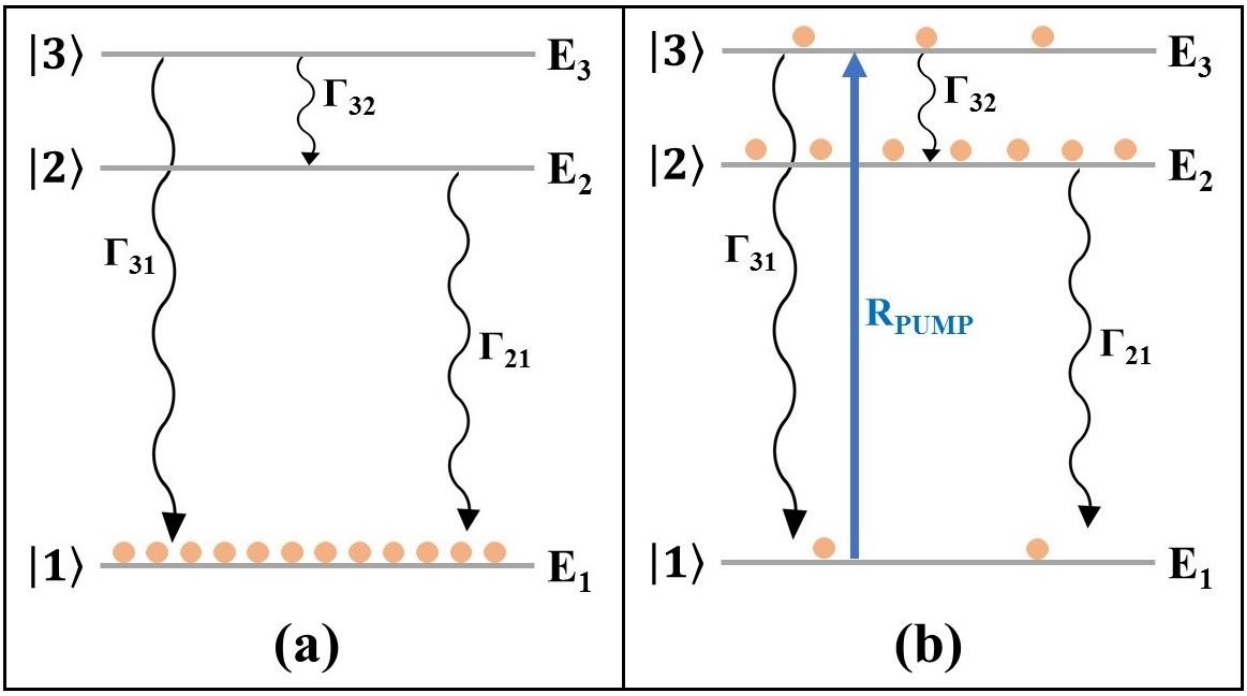

Fig. 4.3: (a) A three-level atom in thermal equilibrium, with associated energy levels and phenomenological decay rates; (b) The same atom, but with an "optical pump" which provides coupling between states $|1\rangle$ and $|3\rangle$.

If n_1, n_2, and n_3 are the fractions of atoms in states $|1\rangle$, $|2\rangle$, and $|3\rangle$, respectively, then the "atomic rate equations" can be written as follows:

$$\frac{dn_1}{dt} = -R_{PUMP}n_1 + \Gamma_{21}n_2 + \Gamma_{31}n_3 \tag{4.1}$$

$$\frac{dn_2}{dt} = -\Gamma_{21}n_2 + \Gamma_{32}n_3 \tag{4.2}$$

$$\frac{dn_3}{dt} = R_{PUMP}n_1 - (\Gamma_{32} + \Gamma_{31})n_3 \tag{4.3}$$

In addition, all atoms are assumed to be in one of these three states, so that $n_1 + n_2 + n_3 = 1$.

In the steady state, Equations 4.1-4.3 can be written in matrix form as:

$$\begin{bmatrix} -R_{PUMP} & \Gamma_{21} & \Gamma_{31} \\ 0 & -\Gamma_{21} & \Gamma_{32} \\ R_{PUMP} & 0 & -(\Gamma_{32} + \Gamma_{31}) \end{bmatrix} \begin{bmatrix} n_1 \\ n_2 \\ n_3 \end{bmatrix} = \begin{bmatrix} 0 \\ 0 \\ 0 \end{bmatrix} \tag{4.4}$$

Solving Equation 4.4, the ratio between the populations of states $|2\rangle$ and $|1\rangle$ in steady state is:

$$\left(\frac{n_2}{n_1}\right)_{STEADY\ STATE} = \frac{R_{PUMP}}{\Gamma_{21}\left(1+\frac{\Gamma_{31}}{\Gamma_{32}}\right)} \tag{4.5}$$

Population inversion between $|1\rangle$ and $|2\rangle$ can therefore be achieved for large enough values of R_{PUMP}, provided that $\Gamma_{32} \neq 0$. Once population inversion is achieved between $|1\rangle$ and $|2\rangle$, a photon with frequency $\frac{E_2-E_1}{\hbar}$ propagating through this medium would be amplified. Naturally, a photon with a frequency *very close* to this value may also be amplified because the gain always has some *bandwidth*. This "gain bandwidth" depends on many factors, including the pump rate, the decay rates, and the particular gain material being used. Lasers can have gain bandwidths less than 1 MHz, all the way up to tens of THz. In order for a laser to operate, the gain must exceed all losses inside the cavity, including photon transmission from the output coupler, as well as reflection, absorption, and scattering of photons from other optical elements inside the cavity. An empty cavity with round trip length L has longitudinal eigenmodes at frequencies of $f_m = \frac{mc}{L}$, where m is an integer called the "mode number". The free spectral range (FSR) is defined as the frequency spacing between neighboring modes, so that $FSR = \frac{c}{L}$. If the bandwidth over which the laser can operate is greater than the FSR, then there are multiple modes inside the "net gain bandwidth", as shown in Figure 4.4.

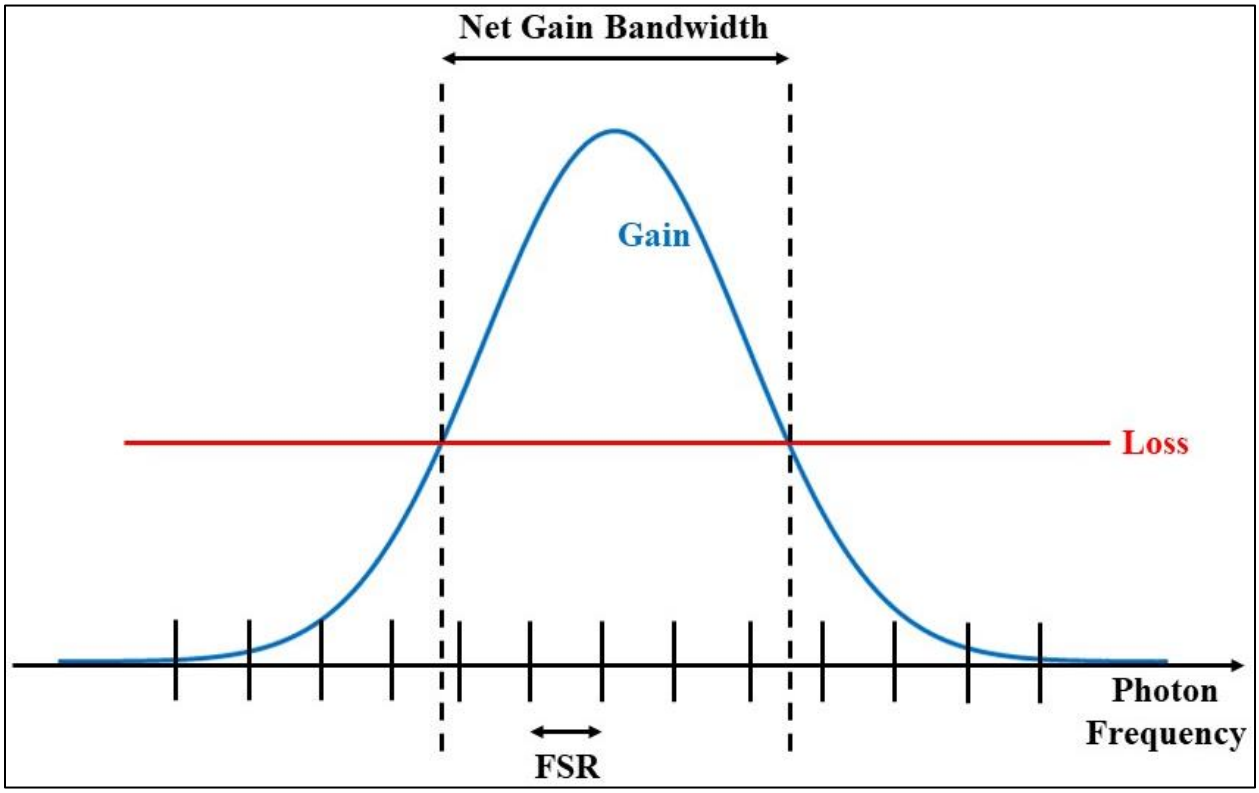

Fig. 4.4: The net gain bandwidth is the range of frequencies over which gain exceeds loss. In principle, the laser can operate anywhere within this range. In this diagram, there are five modes inside the net gain bandwidth.

There are two detrimental effects that can (and often do) arise from having multiple modes inside the net gain bandwidth:

1. Multi-mode operation: The laser operates simultaneously on two or more modes, so that there are two or more optical frequencies present. This is unacceptable for a laser interferometer which requires single-frequency operation.
2. Mode competition: The laser operates on one mode. However, if two or more modes have similar round trip gain, the laser can spontaneously jump from one mode to another (this is called mode hopping). Even if the laser does not mode hop, the existence of a competing

mode can destabilize the lasing mode. This is also unacceptable for a laser interferometer, where the optical frequency must have a known and stable value.

It is important to take these issues into consideration when selecting a suitable gain medium for a laser interferometer. Although gain can be narrowed with the insertion of an etalon into the cavity, the etalon also reduces the gain amplitude, thus making lasing more difficult to achieve. Additionally, intra-cavity components can de-phase and therefore broaden the optical field, which ultimately reduces sensitivity when using the device for optical metrology.

4.2 Designing a Superluminal Laser

In Chapter 3 we discussed the connection between the real and imaginary parts of the material susceptibility $\tilde{\chi}(\omega)$. Specifically, the real part, $\chi_R(\omega)$, which represents the dispersion spectrum, and the imaginary part, $\chi_I(\omega)$, which represents the gain/loss spectrum, are linked through the Kramers-Kronig relations. These relations tell us that positive dispersion (corresponding to subluminal group velocity) generally occurs inside a gain peak, while negative dispersion (corresponding to superluminal group velocity) generally occurs inside a loss (or absorption) peak. Therefore, it would be reasonable to suggest that a superluminal laser might be realized by creating a gain medium with a narrow spectral "dip" in the middle, as shown in Figure 4.5. If the laser operates on this dip, then it may experience negative dispersion, thus making it superluminal. In this section, we will calculate whether this hypothesis is plausible.

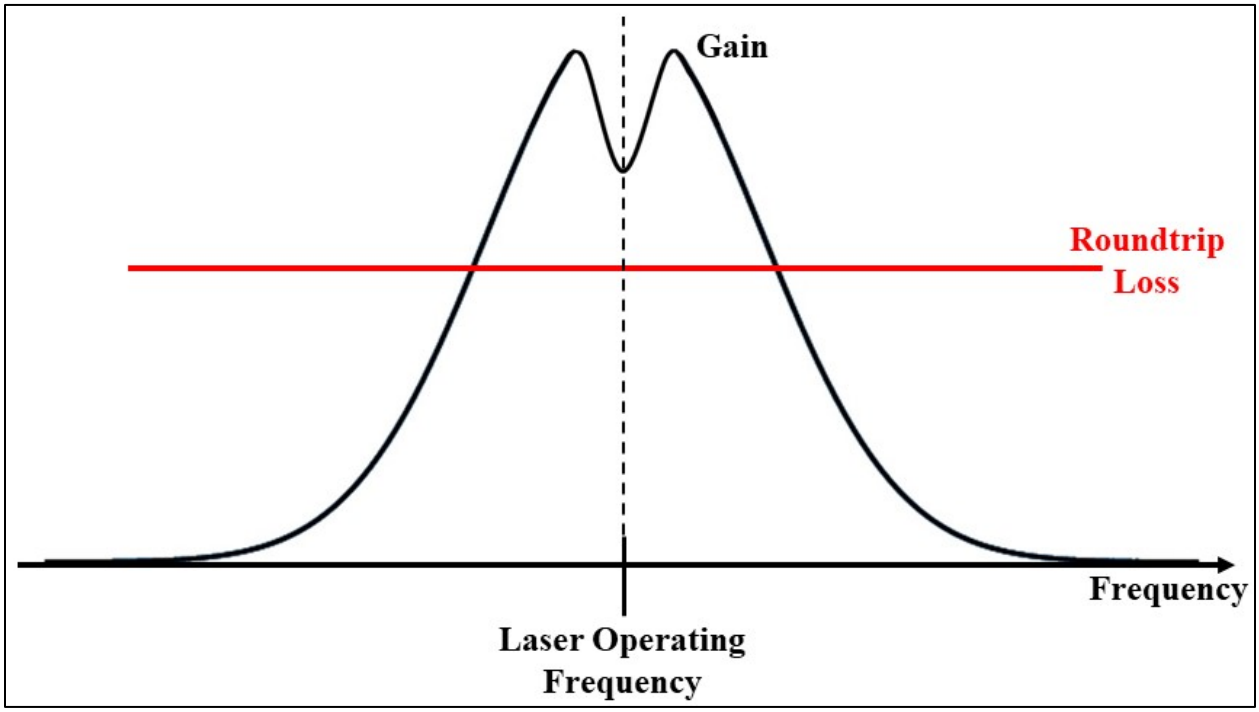

Fig. 4.5: A gain profile with a narrow dip in the center. We hypothesize (and will confirm) that a laser operating at this dip frequency should be superluminal.

In such a laser, the composite gain profile, $-\chi_I(\omega)$, can be expressed as the superposition of a broadband gain and a narrow dip. Using the two-level density matrix model developed in Chapter 3, the analytic expression for $\chi_I(\omega)$ could be written as:

$$\chi_I(\omega) = -\frac{G_g {\Gamma_g}^2}{2{\Omega_g}^2 + {\Gamma_g}^2 + 4(\omega - \omega_o)^2} + \frac{G_d {\Gamma_d}^2}{2{\Omega_d}^2 + {\Gamma_d}^2 + 4(\omega - \omega_o)^2} \tag{4.6}$$

where the subscripts "g" and "d" refer to "gain" and "dip, respectively, while G_g and G_d are the amplitudes of the (unsaturated) gain and dip profiles, respectively, which depend on the density of atoms, atomic dipole moments, and transition linewidths. Applying the Modified Kramers-Kronig (MKK) relations, which apply to saturable media [29,30,31] onto Equation 4.6, yields $\chi_R(\omega)$:

$$\chi_R(\omega) = \frac{2G_g(\omega - \omega_o)\Gamma_g}{2{\Omega_g}^2 + {\Gamma_g}^2 + 4(\omega - \omega_o)^2} - \frac{2G_d(\omega - \omega_o)\Gamma_d}{2{\Omega_d}^2 + {\Gamma_d}^2 + 4(\omega - \omega_o)^2} \tag{4.7}$$

In order to calculate whether a superluminal laser could be made by inserting this medium into a cavity, we solve the self-consistent single-mode laser equations [32] which govern the phase and amplitude of the electric field of a single-mode laser inside a cavity:

$$\frac{d\varphi}{dt} = (\Omega_C - \omega) - \frac{\chi_R}{2}\omega \tag{4.8}$$

$$\frac{dE}{dt} = -\frac{\omega E}{2Q} - \frac{\chi_I E}{2}\omega \tag{4.9}$$

where Q is the empty cavity quality factor and Ω_C is the empty cavity resonance frequency. If the round trip cavity length is L, then the sensitivity of the *empty cavity resonance frequency* to small length perturbations would be ${d\Omega_C}/{dL}$, while the sensitivity of the *laser frequency* to small length perturbations is ${d\omega}/{dL}$. The ratio between these two derivatives, $R \equiv \frac{{d\omega}/{dL}}{{d\Omega_C}/{dL}}$, would therefore be

the factor by which laser frequency sensitivity is enhanced ($R > 1$) or reduced ($R < 1$) relative to the empty cavity. Solving Equations 4.8 and 4.9 in the steady state results in:

$$R = \frac{1}{1 + \frac{\chi_R}{2} + \frac{\omega}{2}\frac{d\chi_R}{d\omega}} = \frac{1}{n_g} \tag{4.10}$$

In Chapter 2, we made the unsubstantiated claim that the enhancement factor of a fast-light laser is equal to ${n_g}^{-1}$ -- the same as that of a fast-light resonator. We have now verified that this is indeed the case.

Analytic expressions for n_g and R are then calculated using the analytic expression for χ_R in Equation 4.7. Figure 4.6(a) shows a plot of χ_R with a corresponding plot of R in Figure 4.6(b). The parameters used in this plot are as follows [33]: $\Gamma_g = 2\pi \times 10^9 s^{-1}$, $\Gamma_d = 2\pi \times 10^7 s^{-1}$, $\omega_o = 2\pi \times 3.8 \times 10^{14} s^{-1}$, $N_g = 9 \times 10^6 cm^{-3}$, $N_d = 1.2645 \times 10^{11} cm^{-3}$, $G_g = {}^{12}/_{Q}$, $G_d = {}^{10.11591}/_{Q}$. Here, N_g and N_d are the densities of gain and dip atoms, respectively.

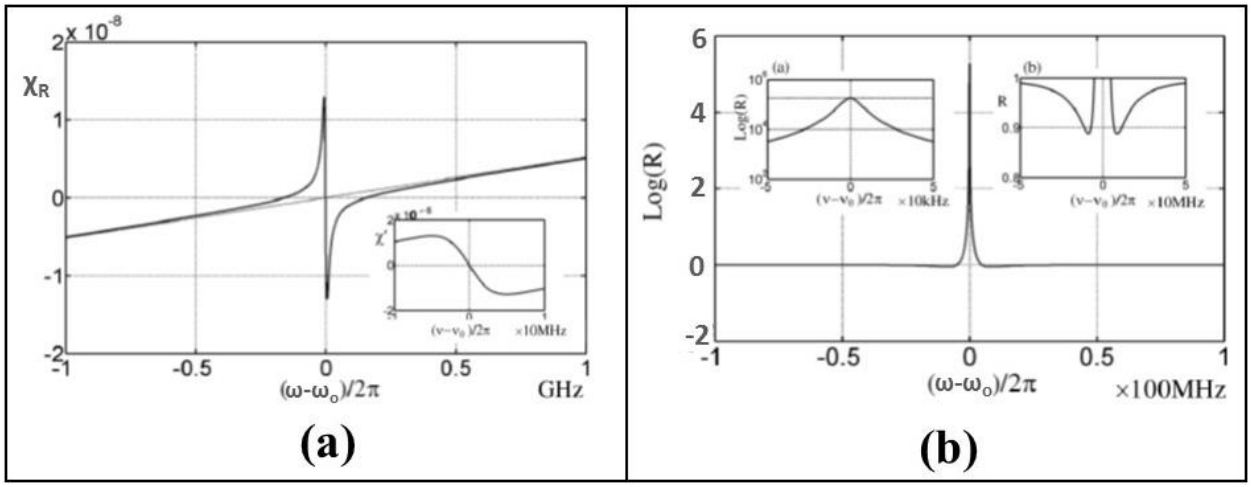

Fig. 4.6: (a) Numerical plot of χ_R versus detuning; (b) corresponding numerical plot of enhancement factor R versus detuning

Using these (experimentally realistic) parameters, R reaches a peak value of $\sim 1.8 \times 10^5$. Outside of the "dip region", the values of χ_R and R asymptotically approach those of the empty cavity.

With the expression for R as a function of frequency shift, we can now solve the frequency shift as a function of cavity length change. If the round trip cavity length is one meter and ω_o is $2\pi \times 3.8 \times 10^{14} s^{-1}$ (corresponding to the D2 transition in rubidium), then the mode number is $m = 1282051$. To be exact, this mode number yields a cavity length of 0.99999978 meter. Since $L = \frac{2\pi mc}{\Omega_c}$ and $\omega = \frac{\Omega_c}{1+\chi_R/2}$, this means that:

$$L = \frac{2\pi mc}{\omega\left(1 + \frac{\chi_R}{2}\right)} \tag{4.11}$$

With the frequency dependence of χ_R from Figure 4.6(a), cavity length L can be plotted as a function of frequency ω, as shown in Figure 4.7.

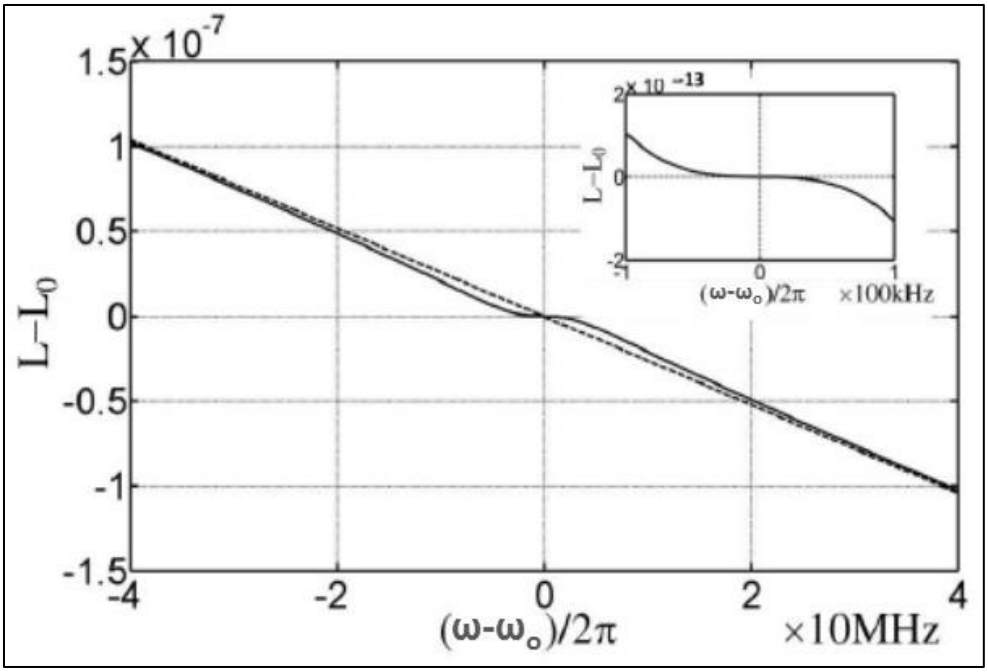

Fig. 4.7: Numerical plot of L versus ω, corresponding to Fig. 4.6

In the vicinity of $L = L_o$, ω is almost flat, indicating that the laser is operating under the so-called white-light cavity (WLC) condition. When the deviation from L_o increases, the slope eventually increases, implying that the enhancement factor decreases as the cavity moves further from L_o.

4.3 Choosing a Dip Mechanism

We showed in Section 4.2 that a superluminal laser can be built by putting a narrow dip in the middle of the gain profile. In principle, there are many different choices of gain mechanisms, as well as many choices of dip mechanisms. In order to produce values of n_g several orders of magnitude greater than unity, the slope of dispersion must be very steep. Because this slope is related to the absorption profile via the Kramers-Kronig relations, the linewidth of the dip should be very narrow; ideally a few MHz or less. Optical filters (such as notch filters) have linewidths of several GHz, making them unsuitable for this application. Doppler-broadened absorption in alkali vapor is narrower, but is still has a linewidth of several hundred MHz at room temperature. *Two-photon* resonant processes in atomic vapor, on the other hand, are much narrower because they are insensitive to Doppler broadening. As a result, we chose to use *Raman depletion in rubidium vapor* as the dip mechanism.

In 2009, our group had reported the demonstration of simultaneous fast and slow light effects in ^{85}Rb vapor via Raman gain and Raman depletion, respectively [34]. The setup from this experiment is shown in Figure 4.8(a), where states $|1\rangle$, $|2\rangle$, $|3\rangle$, and $|4\rangle$ are defined as the $5S_{1/2}$(F=2) hyperfine level, the $5S_{1/2}$(F=3) hyperfine level, the $5P_{1/2}$ manifold, and the $5P_{3/2}$ manifold, respectively. At room temperature, the energy difference between states $|1\rangle$ and $|2\rangle$, denoted as Δ_{12}, is far less than the thermal energy $k_B T$, so that these two states are roughly equally populated in thermal equilibrium. Population inversion between $|1\rangle$ and $|2\rangle$ is produced by optically pumping atoms from state $|1\rangle$ to state $|4\rangle$. The effective result is a decay from state $|1\rangle$ to state $|2\rangle$; this experimental configuration can therefore be simplified as an effective three-level system, shown in Figure 4.8(b). A *Raman pump* and *Raman probe* are applied to the $|2\rangle \rightarrow |3\rangle$ and

$|1\rangle \rightarrow |3\rangle$ transitions, respectively. Doppler-broadened absorption of the Raman pump and Raman probe requires that they be detuned from resonance, with an optimal detuning value of approximately 1 GHz; the Raman pump and Raman probe detunings are denoted as Δ_{RP} and Δ_L, respectively. When $\Delta_{RP} = \Delta_L$, the two-photon resonance condition is satisfied, so that the difference between the Raman pump and Raman probe frequencies is equal to Δ_{12}, the ground-state hyperfine splitting, which is approximately 3.0357 GHz in ^{85}Rb.

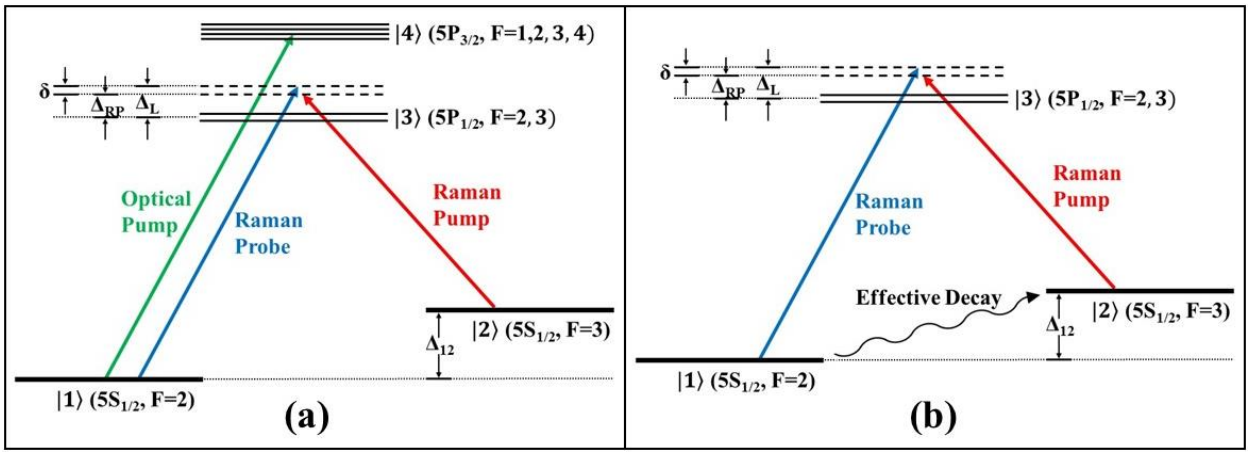

Fig. 4.8: (a) Relevant energy levels, optical fields, and detunings in the pump-probe experiment; (b) effective three-level system in which the optical pump is modeled as a decay rate

The population in state $|2\rangle$ exceeds that of state $|1\rangle$ as a result of the optical pumping. Therefore, when the pump and probe are two-photon resonant, the probe experiences Raman gain at the expense of the pump, which experiences "Raman depletion". The results of this experiment are presented in Figure 4.9(a), which shows that the full-width half maximum (FWHM) width of this Raman process is on the order of 1 MHz, thus making it several orders of magnitude narrower than Doppler-broadened absorptions and optical notch filters. A heterodyne detection technique then measured the corresponding indices of refraction, and found that the probe gain was

associated with positive dispersion, while the pump depletion was associated with negative dispersion, as shown in Figure 4.9(b).

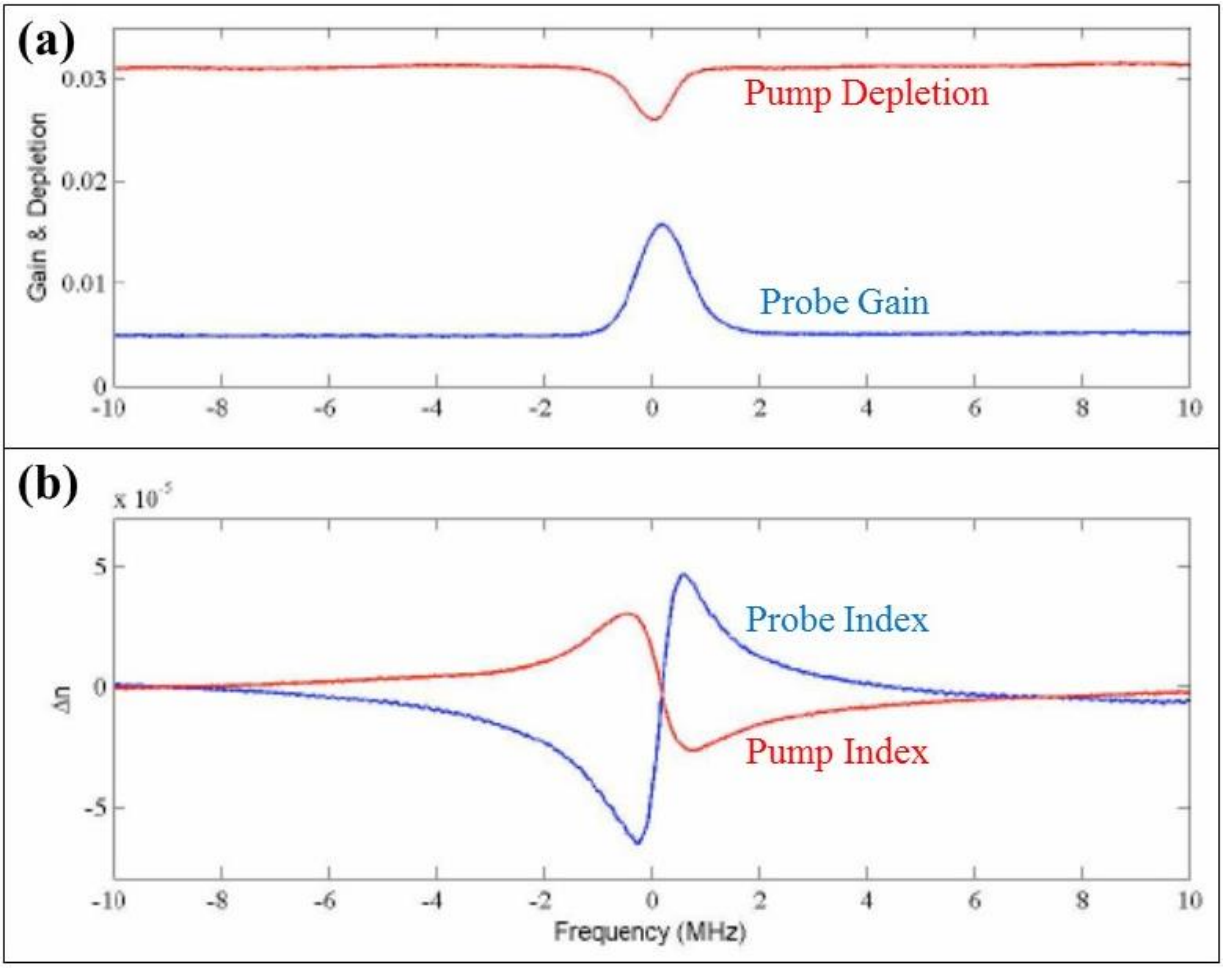

Fig. 4.9: (a) Experimental results showing gain in the Raman probe and depletion in the Raman pump; (b) corresponding experimentally-measured indices of refraction. These results are consistent with the Kramers-Kronig relations as well as the semiclassical two-level density matrix calculation.

This experiment provides a proof-of-concept for a narrowband (and therefore steep) anomalous dispersion which can be applied to an intra-cavity lasing beam in order to create a superluminal laser. In other words, steep anomalous dispersion in a laser can be created by setting

up precisely this type of system, where an *intra-cavity lasing beam* plays the role of the Raman pump.

4.4 Choosing a Gain Mechanism

After choosing the dip mechanism, the gain mechanism must be chosen. In principle, we can choose any gain with energy levels corresponding to the Raman depletion; however, as mentioned in Section 4.1, it is important to ensure that multi-mode operation and mode competition are eliminated. Additionally, the magnitude of gain must be high enough for the superluminal laser to lase with Raman depletion inside the cavity, which suppresses the round-trip gain to some extent. With these considerations in mind, the gain medium we first chose was optically-pumped rubidium vapor mixed with helium buffer gas. The first demonstration of an alkali laser was reported in 2003, in which the D2 line of rubidium vapor was optically pumped with a Ti-Sapphire laser [35]. The buffer gas, which in Ref. 35 was a mixture of ethane and helium, provided collisional relaxation from the $P_{3/2}$ manifold to the $P_{1/2}$ manifold, thus creating population inversion (and therefore lasing) on the D1 line, as shown in Figure 4.10. The collisional relaxation induced by the buffer gas also causes the atomic energy levels to broaden significantly. As a result, the $5S_{1/2}$ manifold (containing the F=2 and F=3 hyperfine levels which are split by 3.0357 GHz) can be treated as one energy level, denoted as $|a\rangle$.

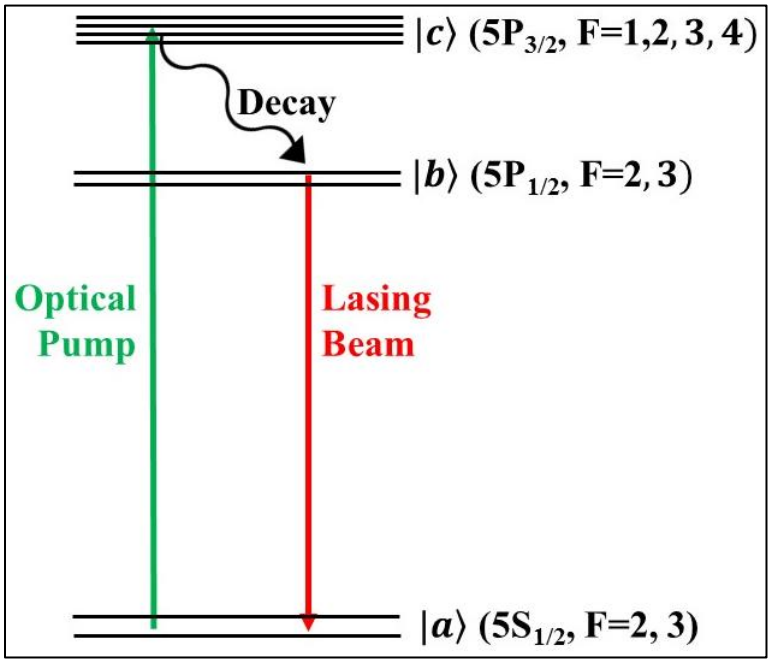

Fig. 4.10: Relevant energy levels, optical fields, and buffer-induced decay rate associated with the alkali laser.

The Diode-Pumped Alkali Laser (DPAL) is a good gain candidate for several reasons:

1. High Round Trip Gain: As mentioned previously, the gain must be high enough to compensate for the Raman depletion that the intra-cavity lasing beam experiences. To determine the magnitude of unsaturated gain, we conducted an experiment in which we measured the gain of a weak (1.3 μW) probe beam. In this experiment, a strong optical pump on the D2 line and a weak probe on the D1 line [Figure 4.11(a)] are cross-polarized and combined in a polarizing beam splitter (PBS). These beams, which spatially overlap, are sent through a cell containing rubidium vapor mixed with helium buffer gas [Figure 4.11(b)]. After the cell, another PBS separates the two beams, and the probe beam is sent into a photodetector (PD). The results in Figure 4.11(c) show that the single-pass gain was as high as ~3.3 with an optical pump power of 835 mW, and as high as ~4.0 with an optical pump power of 1.22 W. In Ref. [36], DPAL output power was measured versus pump

power, for five different output coupler reflectivities. Figure 4.12 shows that the 20%-reflectivity output coupler yielded the highest output power, which is further evidence of high round-trip gain.

2. Relatively Narrow Gain: In the experiment shown in Figure 4.11, the probe detuning [denoted as Δ in Figure 4.11(a)] was scanned in order to determine the unsaturated gain bandwidth. Depending on the pump strength, the FWHM is 5-10 GHz, as shown in Figure 4.11(c). Only modes experiencing gain within a few percent of the peak gain are candidates for mode competition and multi-mode lasing, so that a 30-centimeter cavity (which has a free spectral range of 1 GHz) would have relatively low susceptibility to these undesirable effects. The insertion of a low-finesse etalon into a laser cavity is enough to ensure mode-competition-free and single-mode lasing.

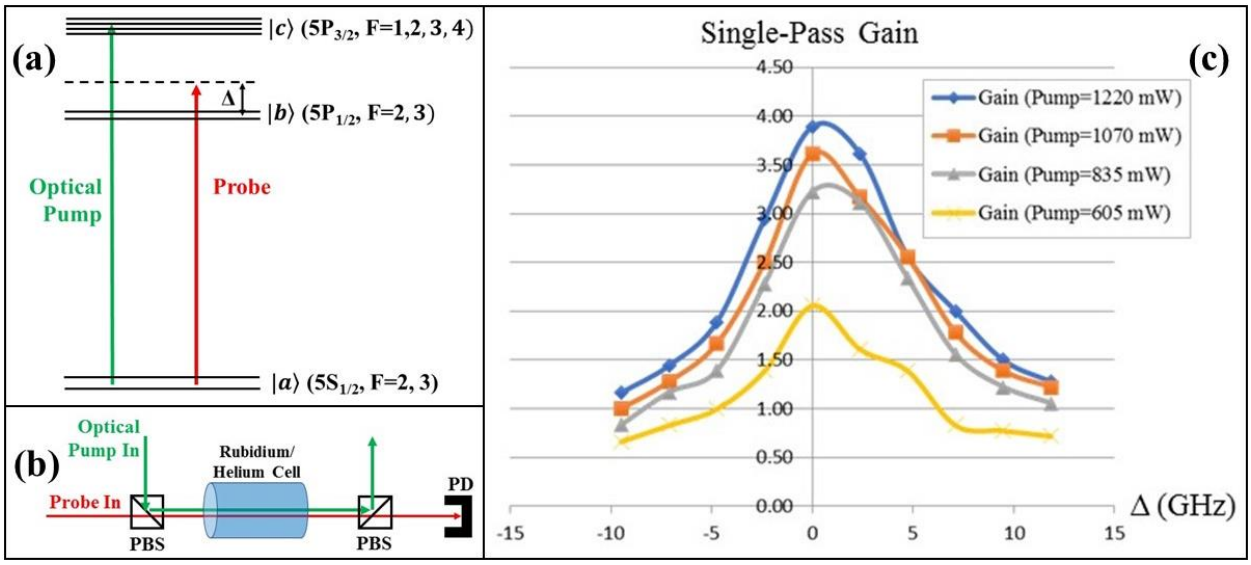

Fig. 4.11: (a) Energy levels and optical fields; (b) experimental setup; (c) results of the DPAL probe gain experiment

3. High Conversion Efficiency: The DPAL efficiently converts optical pump energy into lasing energy due to the low quantum defect (~1.9%) and broadband absorption on the D2

line. In fact, one of the main applications for which the DPAL was initially developed was the efficient conversion of low-quality (broadband, high M^2) light into high-quality (narrowband, low M^2) light [36,37,38,39,40,41]. The efficient conversion of energy makes it easier to reduce the size of the superluminal laser for applications in which miniaturization is important, such as inertial navigation in spacecrafts and satellites. In addition, the minimum-measurable linewidth (Equation 2.46) is inversely proportional to the square root of power, so that higher power laser means higher resolution. Figure 4.12, which was taken from Reference 36, shows that the DPAL has high slope efficiency, particularly with a 20%-reflectivity output coupler.

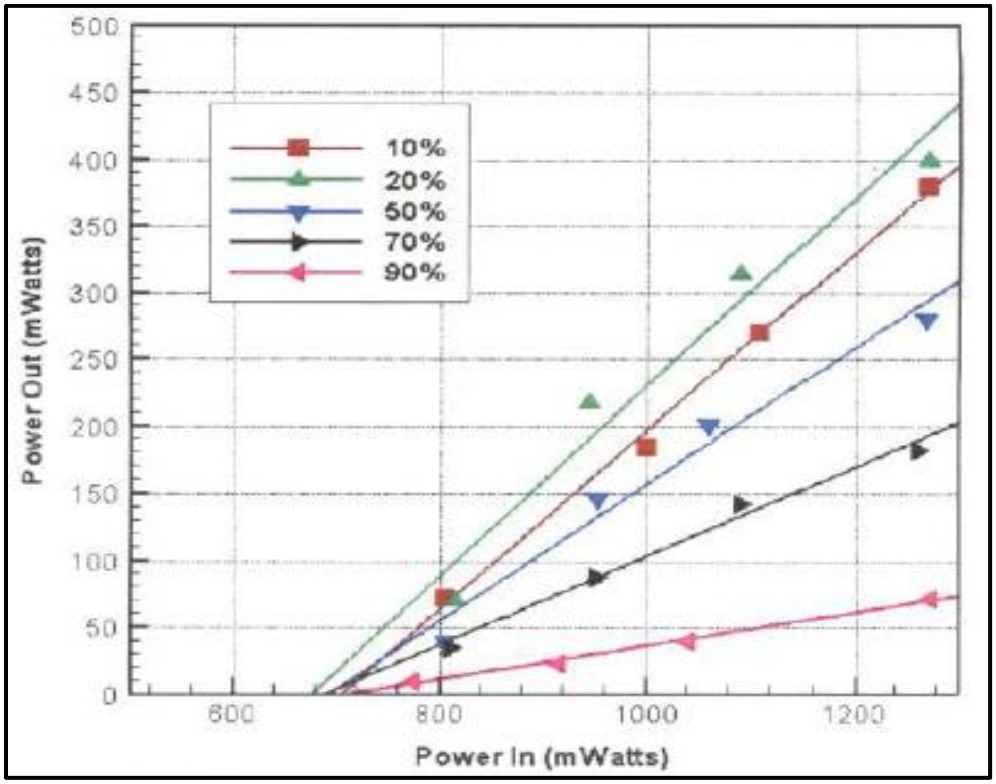

Fig. 4.12: Conversion efficiency of the DPAL with different output couplers

As mentioned previously, the buffer gas is usually chosen to be helium or ethane (or some combination of them). For the first few months of the DPAL project, we used helium buffer gas because of the fear that a hydrocarbon buffer gas would chemically react with the rubidium and leave deposits on the cell windows [42]. These chemical deposits would be detrimental to round-trip gain, and would cause the laser to stop working. From our experience, a few atmospheres of helium were necessary to achieve decent lasing, as shown in Figure 4.13, which was an issue because there was always a chance that the windows could explode outwards due to high pressure.

After a few months of using helium buffer gas, a colleague suggested that we try ethane. As it turns out, the chemical reaction we feared never occurred, and the ethane worked far better than helium, while requiring far lower (sub-atmospheric) pressure, as shown in Figure 4.13.

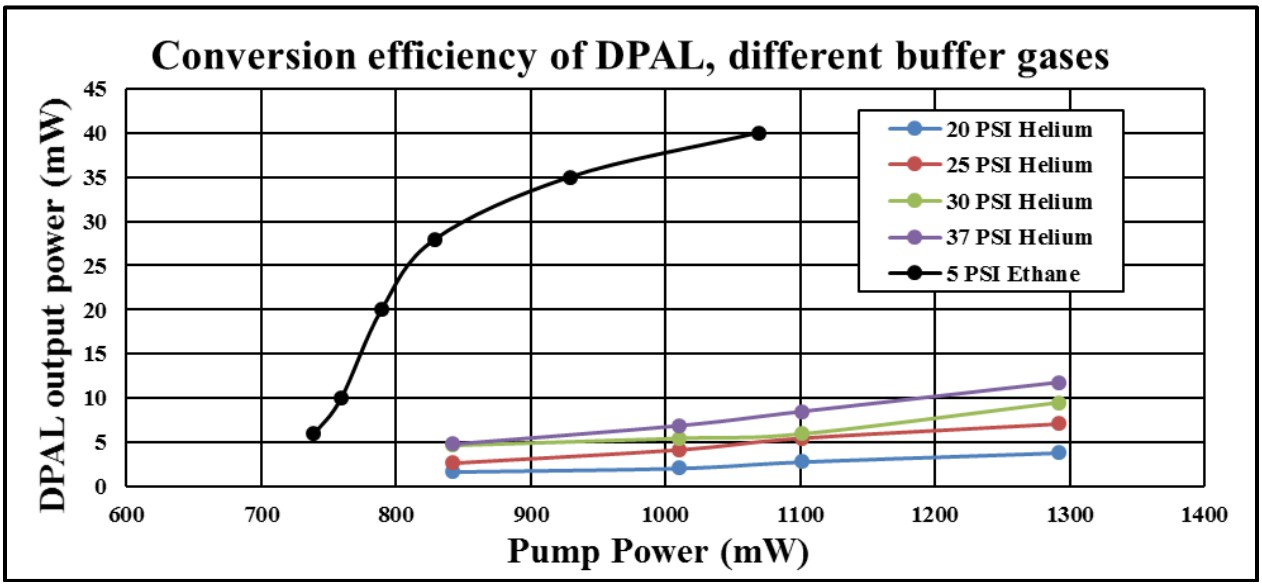

Fig. 4.13: DPAL output power with helium pressures ranging from 20 PSI to 37 PSI, and with ethane pressure of 5 PSI. Although the output power increases with increasing helium pressure, ethane is clearly superior to helium in conversion efficiency. All data in this figure were taken with an output coupler reflectivity of 50% and gain cell temperature of approximately 120°C.

4.5 Combining the Gain and Dip Mechanisms

The superluminal laser can now be built by inserting the gain and dip mechanisms into a cavity. A schematic of the single-direction superluminal laser is illustrated in Figure 4.14(a), while the energy levels associated with the gain and dip are shown in Figures 4.14(b) and 4.14(c), respectively. The gain cell contains naturally-occurring rubidium (72% ^{85}Rb, 28% ^{87}Rb) vapor mixed with ethane buffer gas, while the dip cell contains isotopically-pure ^{85}Rb vapor. The buffer gas broadens the transitions in the gain cell atoms by ~5-10 GHz; meanwhile, the hyperfine splitting between the ground-state levels is ~3.0 GHz in ^{85}Rb and ~6.8 GHz in ^{87}Rb, so that the optical pump excites atoms from both ground states in both isotopes to their respective $P_{3/2}$ manifolds. Polarizing beam splitters (PBSs) inject the optical pump and Raman probe, which are both s-polarized, into and out of the cavity. The lasing beam transmits through the PBS, and is therefore p-polarized.

For now, we want to demonstrate a single-direction superluminal DPAL without the complications associated with bi-directional lasing; the optical isolator ensures that lasing occurs in only one direction. A beam splitter (BS) diverts a small portion of the laser output to an acousto-optic modulator (AOM) which up-shifts the frequency of the input beam by a frequency of Δ_{12}, which is the hyperfine splitting between the $5S_{1/2}$(F=2) and $5S_{1/2}$(F=3) states of ^{85}Rb, as denoted in Figures 4.14(b) and 4.14(c). This up-shifted beam is the Raman probe, which is two-photon resonant with the intra-cavity lasing beam inside the dip cell. The optical pump in the dip cell transfers atoms from $|1\rangle$ to $|2\rangle$, thus creating a *Raman population inversion* between these two states. The Raman probe is therefore amplified inside the dip cell at the expense of the lasing beam, which is depleted.

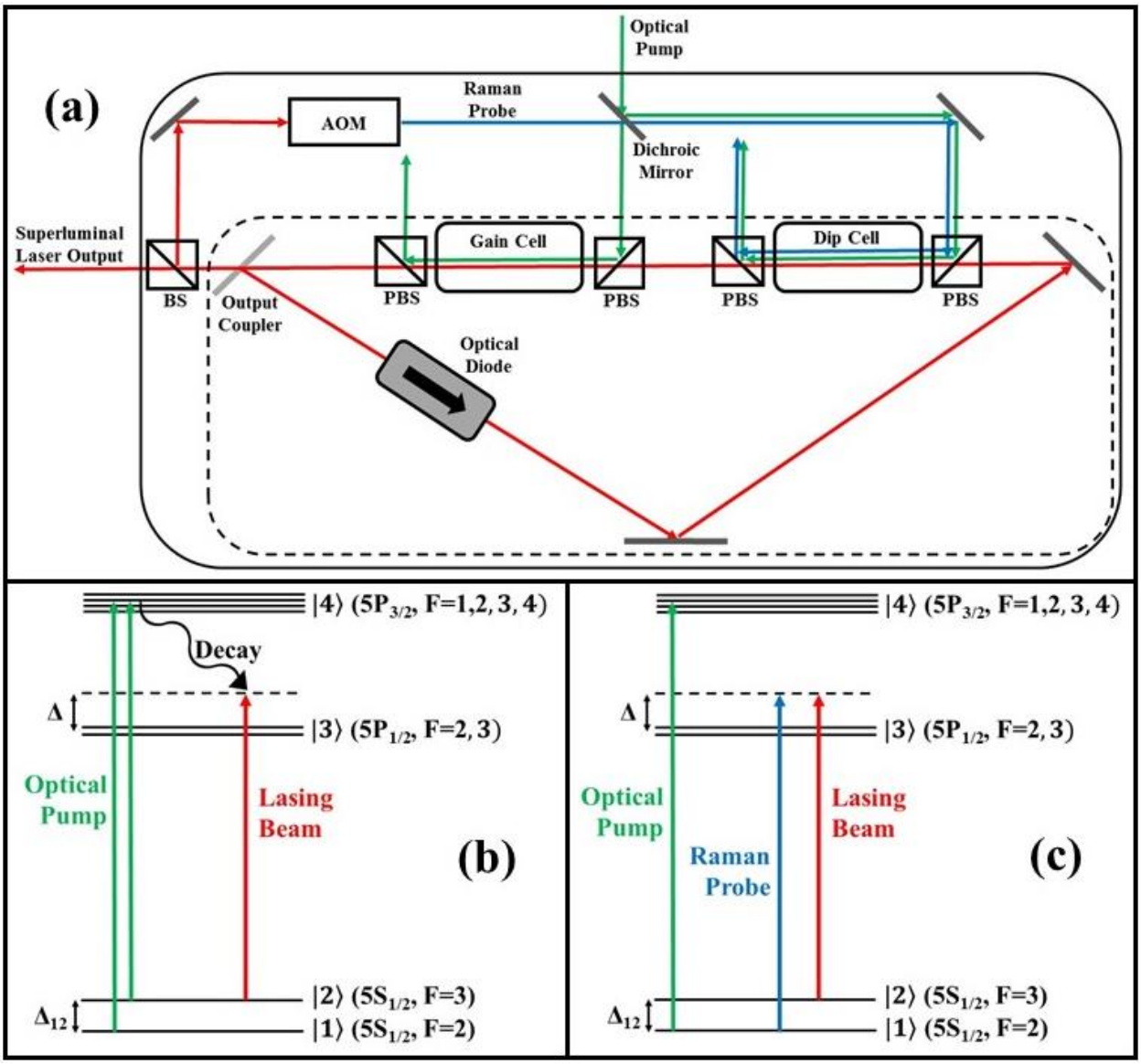

Figure 4.14: (a) Schematic of a single-direction superluminal DPAL; (b) gain cell containing both isotopes of rubidium. Because of buffer gas induced collisional broadening, both isotopes contribute approximately equal amounts (per atom) to the gain; (c) dip cell containing just the ^{85}Rb isotope. Two photon resonance in the dip cell creates Raman depletion of the lasing beam.

Figure 4.14 is a simplified schematic showing only the essential elements; Figure 4.15 shows a more detailed schematic of the system built in our laboratory [43]. The laser cavity is an equilateral triangle with each leg 24 cm in length. The output coupler is flat and has a reflectivity of 60% while the other two mirrors are high reflectors with 20 cm radii of curvature. These cavity

dimensions and radii of curvature are chosen so that the laser output is astigmatism-free without the use of an intra-cavity lens [44]. The cavity mode has two waists which are located at the output coupler and the center of the gain cell. The gain cell is made with ConFlat® components which support high vacuum, and the windows are anti-reflection coated on both sides to minimize roundtrip loss. The gain cell is connected to an oven containing an ampoule of naturally-occurring rubidium. A cylinder containing research-grade ethane gas is also connected to the gain cell, and the ethane pressure is controlled with a regulator. The oven and gain cell are each wrapped with heating wire, the temperatures of which are controlled with Variacs (variable AC voltage sources). The windows of the gain cell are wrapped with a separate heating wire which is kept at a higher temperature than the rest of the cell, in order to prevent vapor condensation on the windows.

The optical pump is produced by amplifying the output of a Toptica tunable diode laser with a Sacher Lasertechnik tapered amplifier (TA). This optical pump beam is s-polarized so that it is reflected into the gain cell by a polarizing beam splitter (PBS). A PBS at the other end of the gain cell expels the portion of optical pump not absorbed by the gain atoms, so that the optical pump does not make it through to the output coupler. Because of the presence of the PBS's, only p-polarized light experiences roundtrip gain, thus forcing the laser output to be p-polarized. The optical isolator prevents directional mode competition by ensuring lasing in only one direction. It also rotates the input light by 45º, necessitating the insertion of a half-wave plate directly after it to rotate the light back to p-polarization. A fraction of the output goes to a photodetector, while the remainder is diverted to an AOM. The frequency of the modulating acoustic signal is approximately 1.518 GHz (half the ground-state hyperfine splitting in ^{85}Rb) and is produced by a voltage-controlled oscillator (VCO). The sidebands from the AOM are separated spatially, and the first-order upshifted sideband is reflected back into the AOM to produce a double-shifted beam,

which is then diverted with a beam splitter. This upshifted Raman probe beam has a maximum power of a few hundred microwatts, which is not strong enough to provide the range of Raman depletion necessary for comprehensive characterization of the superluminal laser. Thus, the Raman probe is amplified through another TA. In addition to the amplified beam, the TA produces some stimulated emission with a spectrum a few THz wide. The holographic grating separates all unwanted frequency components from the TA output so that the Raman probe beam is spectrally pure. This Raman probe is then injected into the Raman cell with a PBS. The Raman chamber is a sealed quartz cell containing pure ^{85}Rb vapor. In order to prevent Zeeman and AC Stark splitting, heating wire is wrapped around the cell bifilarly, and the cell is housed inside a mu-metal box. The buffer gas broadens the transitions in the gain cell atoms by ~5-10 GHz while the hyperfine splitting between the ground-state levels is ~3.0 GHz in ^{85}Rb and ~6.8 GHz in ^{87}Rb. Therefore, the optical pump excites atoms from both ground states in both isotopes to their respective $P_{3/2}$ manifolds. Buffer gas induced broadening in the gain cell enables us to use same optical pump in the gain and dip cells. Therefore, a fraction of the DPAL optical pump is used as the optical pump for the Raman cell.

Because of Doppler broadening, two-photon interactions in the dip cell between the Raman probe and lasing beam only occur for the near-zero-velocity atoms if the Raman probe and lasing beam are counter-propagating; however, if the two are co-propagating, all velocity groups experience two-photon interaction. Therefore, to maximize Raman efficiency, the Raman probe is made to co-propagate with the lasing beam. However, the propagation direction of the *optical pump* does not matter in principle, because it is incoherent with the lasing beam. We therefore choose to inject the optical pump in the counter-propagating direction to circumvent the need to

combine the Raman probe and the optical pump with a beam splitter, which would waste half of the power and require more optical components.

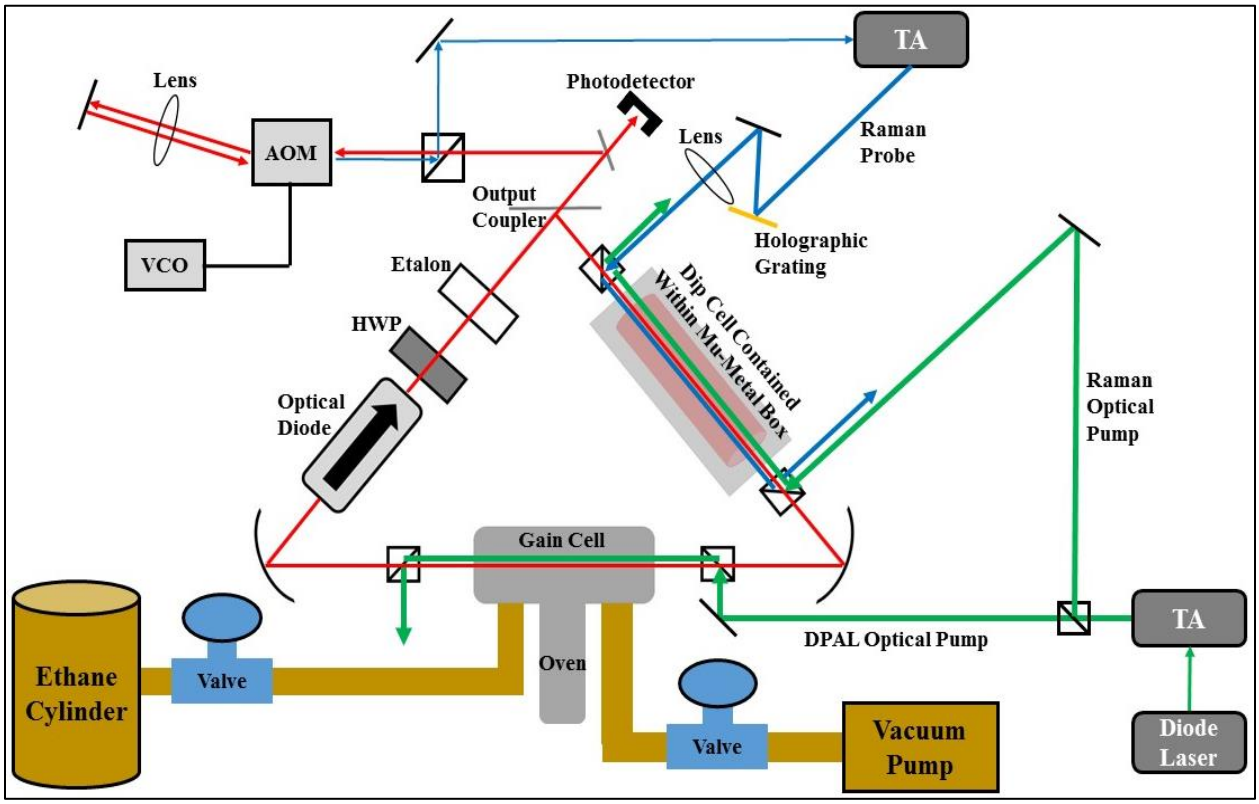

Figure 4.15: Detailed schematic of superluminal DPAL

The intra-cavity etalon prevents mode competition and controls the DPAL lasing frequency. The peak of the DPAL gain profile is generally several GHz above the maximum-frequency D1 transition in ^{85}Rb [$5S_{1/2}(F=2) \rightarrow 5P_{1/2}(F=3)$]; therefore, without the etalon, this is the frequency at which the DPAL lases; however, the optimal detuning for the Raman process is about 1 GHz above (or below) resonance. The etalon (which is a flat piece of glass with partially reflective surfaces) has its own set of resonances. Because the thickness of the etalon is far smaller than the cavity length, the free spectral range (FSR) of the etalon is far larger than the FSR of the cavity. The "composite" gain profile depends on the laser gain as well as the etalon transmission,

so that the DPAL operates on the mode within the broadband gain profile corresponding to an etalon peak, as shown in Figure 4.16. The effective length of the etalon (and therefore locations of etalon transmission peaks) can be changed by slightly rotating the etalon, which enables fine tuning of the output frequency.

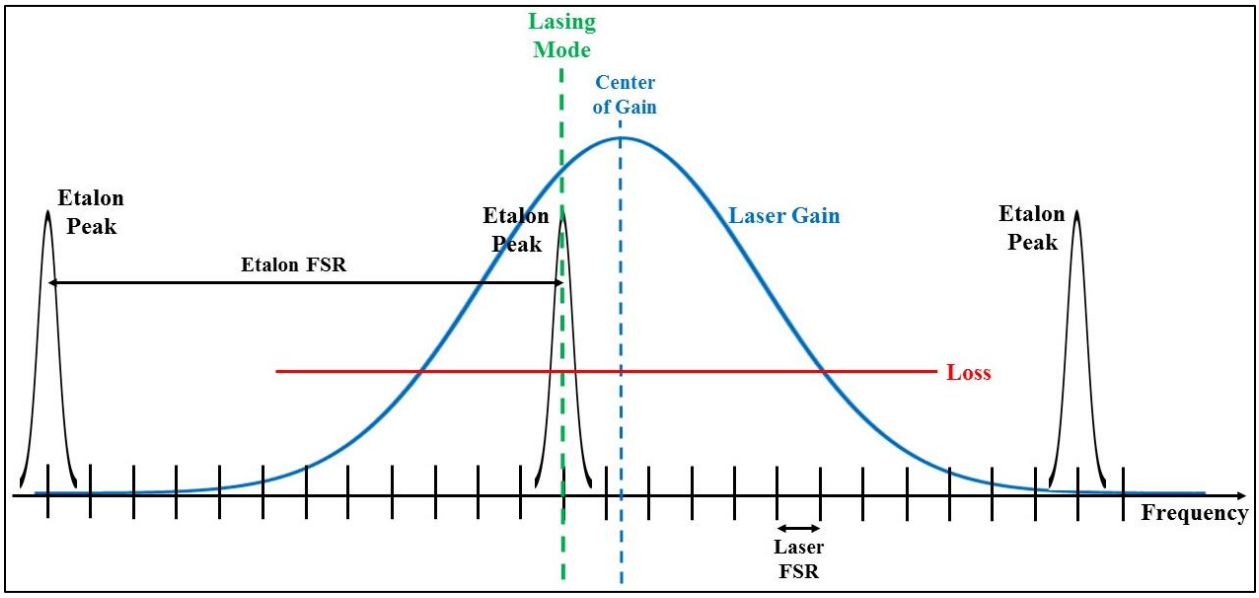

Figure 4.16: The lasing mode is the one with the highest "composite gain" which depends on the spectrum of the gain medium as well as the etalon transmission spectrum

4.6 Experiment Measuring DPAL Raman Depletion

After building the superluminal laser system, we conducted an experiment with the goal of demonstrating experimentally the existence of Raman depletion in our Raman-DPAL system and characterizing the results [43]. All relevant energy levels and detunings in this experiment are shown in Figure 4.17. As mentioned previously, the Raman probe is created by frequency-shifting the laser output through an acousto-optic modulator (AOM) by a frequency of *approximately* 3.0357 GHz, which is the hyperfine splitting between the $5S_{1/2}$(F=2) and $5S_{1/2}$(F=3) states of ^{85}Rb, denoted as Δ_{12}. The *exact* AOM frequency shift, Δ_{AOM}, is:

$$\Delta_{AOM} = f_{RP} - f_L = \Delta_{12} + (\Delta_{RP} - \Delta_L) \equiv \Delta_{12} + \delta \tag{4.12}$$

where f_{RP} and f_L are the Raman probe and lasing frequencies, respectively, and δ, the so-called *two-photon* detuning, is equal to $(\Delta_{RP} - \Delta_L)$, as denoted in Figure 4.17.

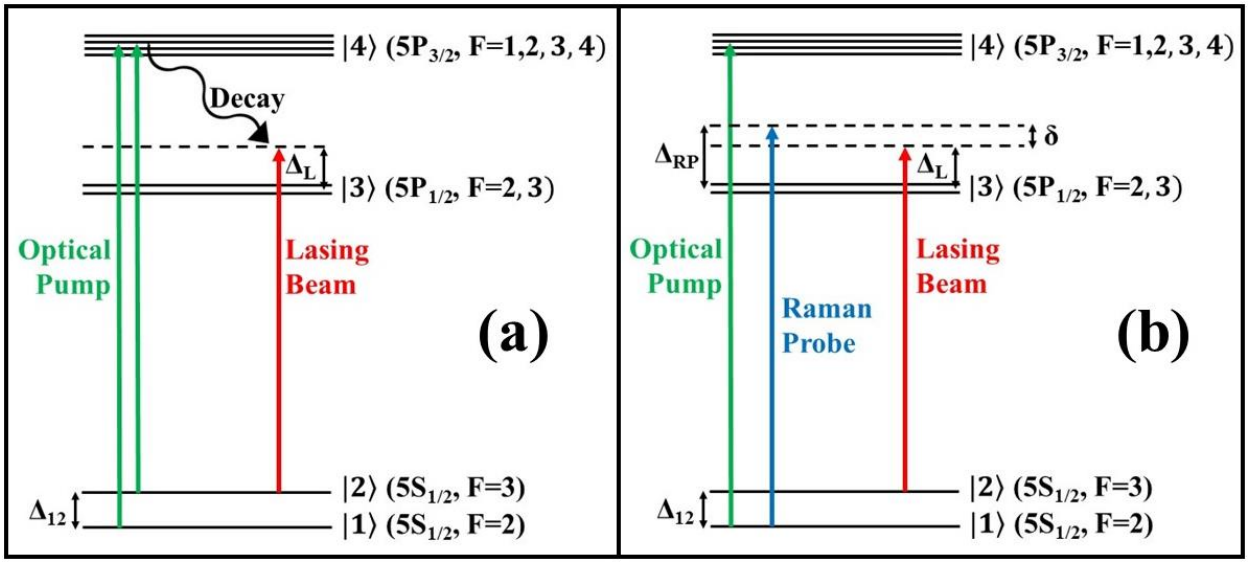

Fig. 4.17: (a) Relevant energy levels and optical fields in the gain cell;
(b) relevant energy levels and optical fields in the dip cell

The VCO controls the value of Δ_{AOM} and therefore the value of δ. Two-photon resonance between the Raman probe and intra-cavity lasing beam is maximized when $\delta = 0$, or when

$\Delta_{AOM} = \Delta_{12}$, under which the lasing beam should experience maximum Raman depletion. We should expect for the strength of the two-photon interaction to decrease as $|\delta|$ increases. The *Raman linewidth*, Γ_{RAMAN} (Figure 4.18), characterizes the bandwidth of δ over which the Raman process occurs.

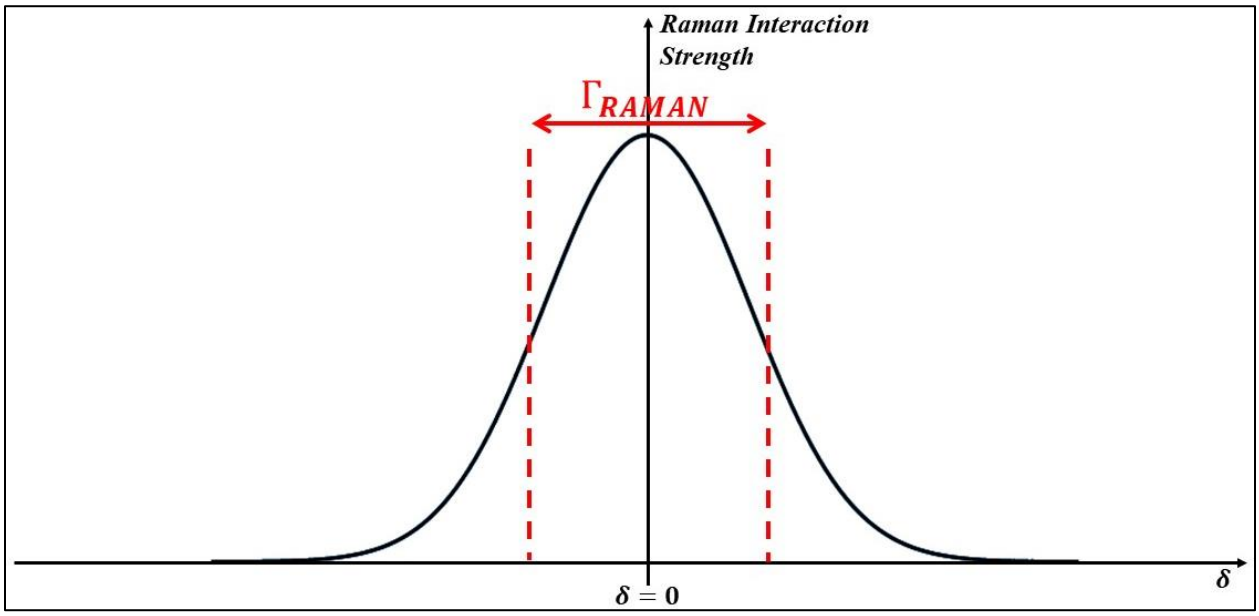

Fig. 4.18: The Raman interaction is strongest at $\delta = 0$. The width of this interaction, Γ_{RAMAN}, is the Raman linewidth.

In this experiment, the DPAL output power was measured as a function of δ, which was scanned about a central value of zero. The output power was measured for six different values of Raman probe power, as shown in Figure 4.19.

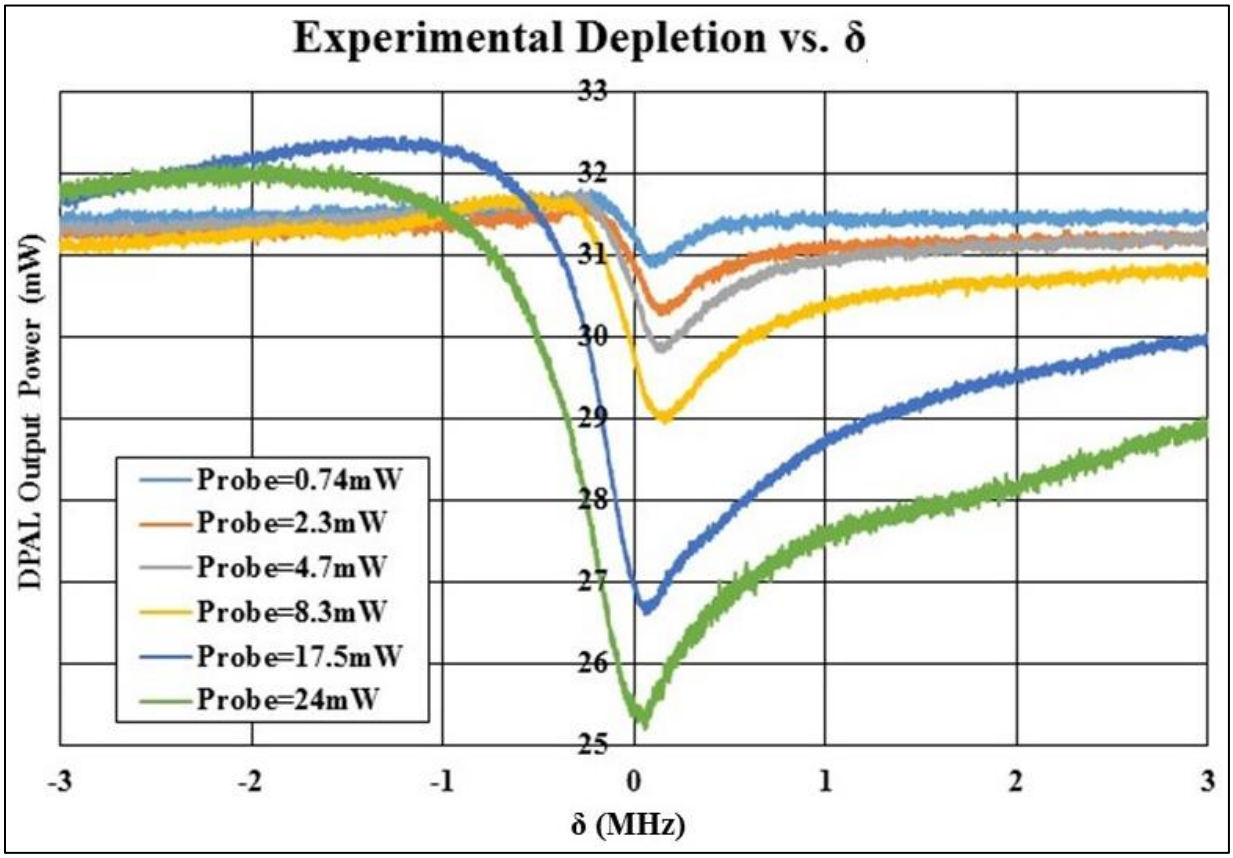

Fig. 4.19: DPAL output power versus δ, measured with six Raman probe powers. The gain cell and the dip cell are each 10 centimeters in length. The gain cell is heated to a temperature of 120ºC and contains ethane with pressure of 0.06 atm, while the dip cell is at a temperature of 100ºC. The DPAL optical pump is 200 μm in radius and 1.2 W in power, while the Raman optical pump is 1000 μm in radius and 10 mW in power.

The depth of the depletion increases monotonically with increasing Raman probe power, as should be expected. Furthermore, the Raman linewidth is generally on the order of ~1MHz, but also increases with increasing Raman probe power. In general, the Raman interaction linewidth depends on the intensities and detunings of the optical and Raman pumps and intra-cavity lasing beam, as well as the vapor temperature, but the ~1 MHz order of magnitude is consistent with the data in Figure 4.9 from Section 4.3.

Direct measurement of superluminal enhancement requires a high degree of classical noise suppression as well as fast servo-mechanisms to maintain a high degree of stability of the laser sources. At the time this experiment was performed, these systems were not yet precise enough to perform direct measurements of enhancement. However, we were able to infer the degree of superluminal enhancement by comparing the experimental results with a numerical model, and then using the parameters from this model to calculate the expected group index and therefore superluminal enhancement factor.

4.7 Numerical Model of Superluminal DPAL

In Section 4.2, we provided an analytic solution for the steady-state behavior of the superluminal laser, including the sensitivity enhancement factor. In this calculation, $\chi_I(\omega)$ was modeled as a superposition of a broadband Lorentzian gain profile and a narrowband Lorentzian dip centered at the lasing frequency ω_o (Equation 4.6). While this Lorentzian model is a good first-order approximation, the exact characteristics of the gain and dip profiles depend on many interconnected variables such as Doppler broadening, potential transverse and longitudinal mode competition, spectral hole burning, AC Stark shifts, and attenuation of optical fields due to absorption. Therefore, numerical methods are necessary for calculating and analyzing accurately the dynamics in the DPAL-Raman system.

In Chapter 3, we introduced the concept of the density matrix, presented the density matrix version of the Schrödinger equation (the so-called Optical Bloch equation), and solved this equation for a two-level atomic system in which the two states are coupled with a near-resonant optical field. In this chapter, we extend the density matrix analysis of the two-level system to that of an N-level system, where N≥3. Our approach for numerically solving the behavior of the Raman-DPAL system relies on solving the single-mode laser equations (Equations 4.8 and 4.9) and the Optical Bloch equation (Equation 3.75) simultaneously and iteratively until a self-consistent, steady-state solution is found. From this we can calculate the *intra-cavity lasing beam susceptibility*, $\chi(\omega)$, which can be then used to calculate superluminal enhancement factor, as well as many other potential quantities of interest. The MATLAB code for this calculation is included in Appendix A.

4.7.1 Density Matrix of Dip Medium

The dip cell contains pure ^{85}Rb vapor with no buffer gas, and has three different beams going through it (optical pump, Raman pump, intra-cavity lasing beam), as shown in Figure 4.20. The F=2 and F=3 hyperfine states in the $5S_{1/2}$ manifold are denoted as $|1\rangle$ and $|2\rangle$, respectively; the entire $5P_{1/2}$ manifold is denoted as $|3\rangle$; the entire $5P_{3/2}$ manifold is denoted as $|4\rangle$.

Several decay rates are taken into consideration, where, in Figure 4.20, the decay rate from state $|i\rangle$ to state $|j\rangle$ in general is denoted as Γ_{ij}. Γ_{3R} and Γ_{4R} are the inverse radiative lifetimes of the $5P_{1/2}$ and $5P_{3/2}$ manifolds, and are equal to 36.1×10^6 sec^{-1} and 38.1×10^6 sec^{-1}, respectively. The decay rates Γ_{31} and Γ_{32} are assumed to be equal, so that $\Gamma_{31} = \Gamma_{32} = \Gamma_{3R}/2$; the same is true for Γ_{41} and Γ_{42}. At experimental temperatures (approximately 120ºC), the values of Δ_{12} and Δ_{34} are several orders of magnitude smaller than the thermal energy k_BT, so that the ratios Γ_{12}/Γ_{21} and Γ_{34}/Γ_{43} are determined only by the ratios of the Zeeman degeneracies, which are equal to 7/5 and 2, respectively.

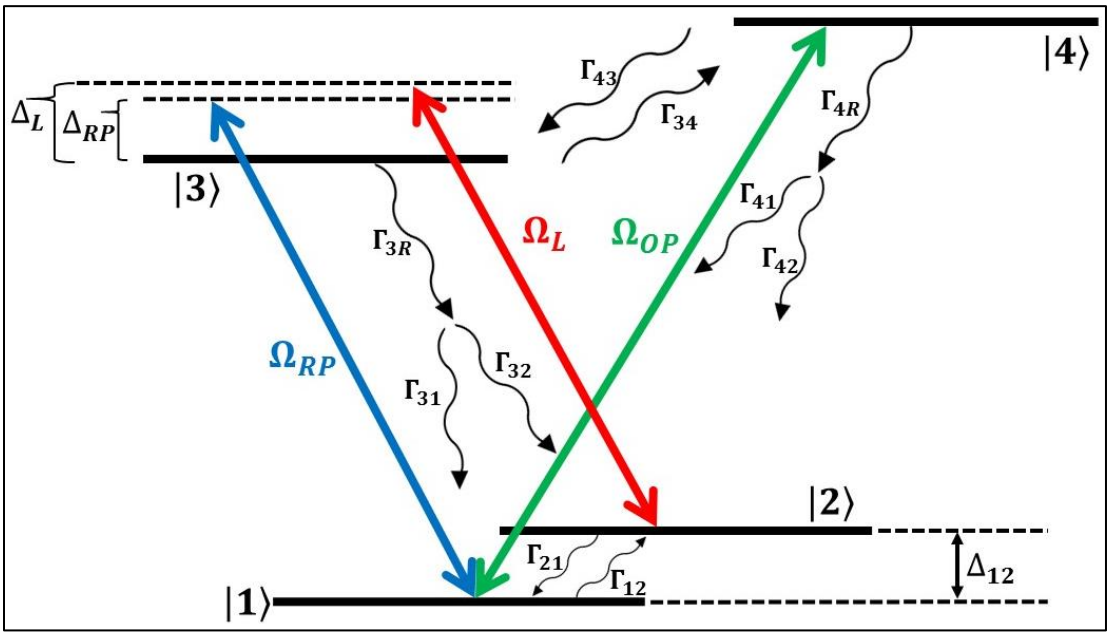

Fig. 4.20: The relevant energy levels, optical fields, and decay rates in the dip cell

Since the optical pump transfers atoms from $|1\rangle$ to $|2\rangle$, it can be modeled as an effective decay rate, denoted as Γ_{OP}. This enables the dip medium to be modeled as an effective three-level system in which the decay rate from $|1\rangle$ to $|2\rangle$ is now $\Gamma'_{12} \equiv \Gamma_{12} + \Gamma_{OP}$, as illustrated in Figure 4.21.

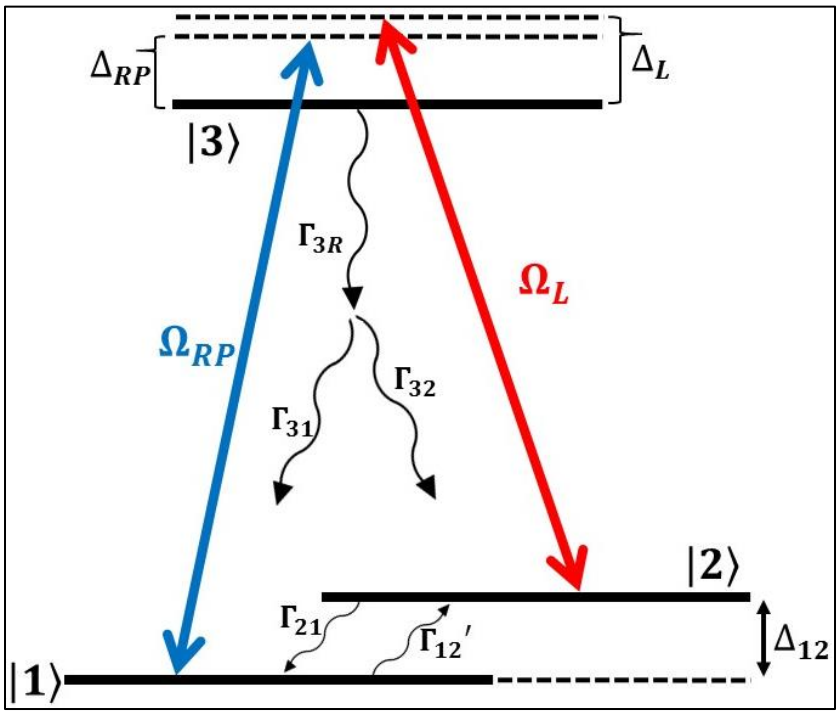

Fig. 4.21: The energy levels, optical fields, and decay rates used in the effective three-level model of the dip cell

The Optical Bloch equation governing the evolution of the density matrix of the dip medium, $\hat{\hat{\rho}}_D$, is:

$$\dot{\hat{\hat{\rho}}}_D = -\frac{i}{\hbar}\left[\hat{\hat{H}}_D, \hat{\hat{\rho}}_D\right] + \dot{\hat{\hat{\rho}}}_{D(DECAY)} + \dot{\hat{\hat{\rho}}}_{D(SOURCE)} \tag{4.13}$$

where the "D" subscript denotes "Dip". The $\dot{\hat{\hat{\rho}}}_{D(SOURCE)}$ term, which does not appear in the two-level system in Chapter 3, is relevant for systems with more than two levels, and accounts for equality between net population inflows and outflows [45,46,47,48,49]. In the "$|1\rangle$, $|2\rangle$, $|3\rangle$" basis, the modified rotating wave Hamiltonian for the three-level system in Figure 4.21 is:

$$\hat{\tilde{H}}_D = \frac{\hbar}{2}\begin{bmatrix} 0 & 0 & \Omega_L \\ 0 & 2(\Delta_L - \Delta_{RP}) & \Omega_{RP} \\ \Omega_L{}^* & \Omega_{RP}{}^* & -2\Delta_{RP} \end{bmatrix} \tag{4.14}$$

while the decay and source matrices are:

$$\dot{\hat{\tilde{\rho}}}_{D(DECAY)} = -\frac{i\hbar}{2}\begin{bmatrix} \Gamma'_{12} & 0 & 0 \\ 0 & \Gamma_{21} & 0 \\ 0 & 0 & \Gamma_{3R} \end{bmatrix} \tag{4.15}$$

$$\dot{\hat{\tilde{\rho}}}_{D(SOURCE)} = \begin{bmatrix} \left(\Gamma_{21}\tilde{\rho}_{D(22)} + \frac{\Gamma_{3R}\tilde{\rho}_{D(33)}}{2}\right) & 0 & 0 \\ 0 & \left(\Gamma'_{12}\tilde{\rho}_{D(11)} + \frac{\Gamma_{3R}\tilde{\rho}_{D(33)}}{2}\right) & 0 \\ 0 & 0 & 0 \end{bmatrix} \tag{4.16}$$

4.7.2 Density Matrix of Gain Medium

The gain cell contains naturally-occurring Rb vapor, which contains the ^{85}Rb and ^{87}Rb isotopes. Both isotopes are modeled as four-level systems, as shown in Figure 4.22. For ^{85}Rb, $|1\rangle$ and $|2\rangle$ are the F=2 and F=3 hyperfine states, respectively, in the $5S_{1/2}$ manifold; $|3\rangle$ is the entire $5P_{1/2}$ manifold; $|4\rangle$ is the entire $5P_{3/2}$ manifold. For ^{87}Rb, $|1\rangle$ and $|2\rangle$ are the F=1 and F=2 hyperfine states, respectively, in the $5S_{1/2}$ manifold; $|3\rangle$ is the $5P_{1/2}$ manifold; $|4\rangle$ is the $5P_{3/2}$ manifold. The buffer gas causes rapid dephasing in both isotopes, thus producing homogeneous broadening of ~5-10 GHz. The simulation therefore does not consider the hyperfine sublevels within the $5P_{1/2}$ and $5P_{3/2}$ manifolds, which are separated by a few hundred MHz or less. The width of the buffer gas-induced broadening is of the same order of magnitude as Δ_{12}, so that the optical pump excites atoms from both states $|1\rangle$ and $|2\rangle$ into state $|4\rangle$. The strengths of the $|1\rangle \rightarrow |4\rangle$ and $|2\rangle \rightarrow |4\rangle$ transitions (i.e. their Rabi frequencies) are assumed to be equal for simplicity, and denoted as Ω_{OP}.

The $|1\rangle \rightarrow |3\rangle$ and $|2\rangle \rightarrow |3\rangle$ transitions, which are coupled by the intra-cavity lasing beam itself, are also assumed to be equal in strength, labeled as Ω_L.

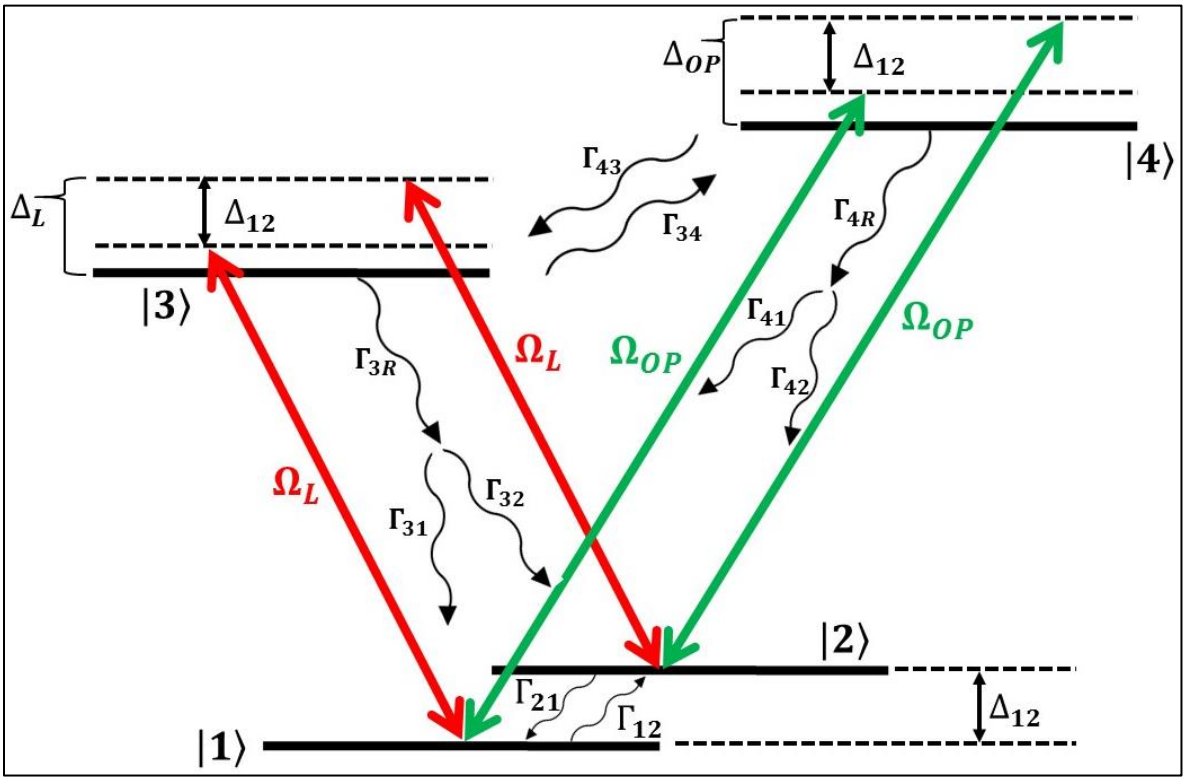

Fig. 4.22: All relevant energy levels, optical fields, and decay rates used in the density matrix numerical model of the gain medium

The Optical Bloch equation for the density matrix of the gain medium, $\hat{\tilde{\rho}}_G$, is:

$$\dot{\hat{\tilde{\rho}}}_G = -\frac{i}{\hbar}\left[\hat{\tilde{H}}_G, \hat{\tilde{\rho}}_G\right] + \dot{\hat{\tilde{\rho}}}_{G(DECAY)} + \dot{\hat{\tilde{\rho}}}_{G(SOURCE)} + \dot{\hat{\tilde{\rho}}}_{G(BUFFER)} \tag{4.17}$$

where the "G" subscript denotes "Gain". The "buffer" term, which does not appear in the dip medium, accounts for the buffer gas induced dephasing between different states. The buffer gas is assumed to broaden all dephasing rates by the same amount, denoted as Γ_d, so that in the "$|1\rangle$, $|2\rangle$, $|3\rangle$, $|4\rangle$" basis:

$$\dot{\tilde{\tilde{\rho}}}_{G(BUFFER)} = -\Gamma_d \begin{bmatrix} 0 & \tilde{\rho}_{G(12)} & \tilde{\rho}_{G(13)} & \tilde{\rho}_{G(14)} \\ \tilde{\rho}_{G(21)} & 0 & \tilde{\rho}_{G(23)} & \tilde{\rho}_{G(24)} \\ \tilde{\rho}_{G(31)} & \tilde{\rho}_{G(32)} & 0 & \tilde{\rho}_{G(34)} \\ \tilde{\rho}_{G(41)} & \tilde{\rho}_{G(42)} & \tilde{\rho}_{G(43)} & 0 \end{bmatrix} \tag{4.18}$$

The modified rotating wave Hamiltonian for the four-level system shown in Figure 4.22 is:

$$\hat{\tilde{H}}_G = \frac{\hbar}{2} \begin{bmatrix} 0 & 0 & \Omega_L & \Omega_{OP} \\ 0 & 2\Delta_{12} & \Omega_L & \Omega_{OP} \\ \Omega_L{}^* & \Omega_L{}^* & -2\Delta_L & 0 \\ \Omega_{OP}{}^* & \Omega_{OP}{}^* & 0 & -2\Delta_{OP} \end{bmatrix} \tag{4.19}$$

while the decay and source matrices are:

$$\dot{\tilde{\tilde{\rho}}}_{G(DECAY)} = -\frac{i\hbar}{2} \begin{bmatrix} \Gamma_{12} & 0 & 0 & 0 \\ 0 & \Gamma_{21} & 0 & 0 \\ 0 & 0 & (\Gamma_{31} + \Gamma_{32} + \Gamma_{34}) & 0 \\ 0 & 0 & 0 & (\Gamma_{41} + \Gamma_{42} + \Gamma_{43}) \end{bmatrix} \tag{4.20}$$

$$\dot{\tilde{\tilde{\rho}}}_{G(SOURCE)} = \begin{bmatrix} \Gamma_{21}\tilde{\rho}_{G(22)} + \frac{\left(\Gamma_{3R}\tilde{\rho}_{G(33)} + \Gamma_{4R}\tilde{\rho}_{G(44)}\right)}{2} & 0 & 0 & 0 \\ 0 & \Gamma_{12}\tilde{\rho}_{G(11)} + \frac{\left(\Gamma_{3R}\tilde{\rho}_{G(33)} + \Gamma_{4R}\tilde{\rho}_{G(44)}\right)}{2} & 0 & 0 \\ 0 & 0 & \Gamma_{43}\tilde{\rho}_{G(44)} & 0 \\ 0 & 0 & 0 & \Gamma_{34}\tilde{\rho}_{G(33)} \end{bmatrix} \tag{4.21}$$

4.7.3 Effective Susceptibility of the Gain and Dip Cells

The dip cell contains only the ^{85}Rb isotope, in which the lasing beam couples to the $|1\rangle \rightarrow |3\rangle$ transition. Therefore, the susceptibility of the lasing beam in the dip cell is:

$$\chi_D = \left(\tilde{\rho}_{31(D)}\right) \frac{\hbar c n_D}{I_{SAT13(D)} \Omega_{L(D)}} \left(\frac{\Gamma_{31(D)}}{2}\right)^2 \tag{4.22}$$

where n_D is the number density of atoms in the dip cell, and $I_{SAT13(D)}$ is the effective saturation intensity of the $|1\rangle \rightarrow |3\rangle$ transition in ^{85}Rb. This quantity is calculated by averaging the saturation

intensities of all constituent Zeeman transitions for σ^+ or σ^- excitation [50] (the laser polarization is linear, which consists of equal parts of σ^+ and σ^-). I_{SAT13} is found to be 8.347 mW/cm^2 [43].

Due to buffer gas induced broadening in the gain cell, the lasing beam interacts with the $|1\rangle \rightarrow |3\rangle$ and $|2\rangle \rightarrow |3\rangle$ transitions, in both the ^{85}Rb and ^{87}Rb isotopes. The susceptibility of the lasing beam to the ^{85}Rb atoms in the gain cell, $\chi_{G(85)}$, is therefore related to the density matrix through the following relation:

$$\chi_{G(85)} = \left(\tilde{\rho}_{31(85)}\right)\frac{\hbar c n_{85}}{I_{SAT13(85)}\Omega_{L(85)}}\left(\frac{\Gamma_{31(85)}}{2}\right)^2 + \left(\tilde{\rho}_{32(85)}\right)\frac{\hbar c n_{85}}{I_{SAT23(85)}\Omega_{L(85)}}\left(\frac{\Gamma_{32(85)}}{2}\right)^2 \quad (4.23)$$

where the "85" subscript refers to the ^{85}Rb isotope. n_{85} is the number density of ^{85}Rb atoms; $I_{SAT13(85)}$ and $I_{SAT23(85)}$ are the effective saturation intensities of the $|1\rangle \rightarrow |3\rangle$ and $|2\rangle \rightarrow |3\rangle$ transitions, respectively, in ^{85}Rb, and are equal to 8.347 mW/cm^2 and 6.283 mW/cm^2, respectively. A similar expression applies to $\chi_{G(87)}$ [51], the susceptibility of the lasing beam to the ^{87}Rb atoms, with $I_{SAT13(87)}$ and $I_{SAT23(87)}$ equaling 7.011 mW/cm^2 and 4.531 mW/cm^2, respectively. The total susceptibility in the gain cell, χ_G, is therefore:

$$\chi_G = 0.72\chi_{G(85)} + 0.28\chi_{G(87)} \quad (4.24)$$

where 72% and 28% are the natural abundance of these isotopes. The effective susceptibility experienced by the intra-cavity lasing beam, χ_L, is the sum of the gain and dip susceptibilities, weighted by their respective cell lengths.

$$\chi_L(\omega) = \frac{L_G}{L_o}\chi_G(\omega) + \frac{L_D}{L_o}\chi_D(\omega) \quad (4.25)$$

where the "L" subscript is for "Lasing". Here, L_o is round-trip cavity length, and L_G and L_D are the distances over which the intra-cavity lasing beam propagates through the gain cell and dip cells, respectively, in one round trip.

4.7.4 Flow Chart of Algorithm

Figure 4.23 is a flow chart of the algorithmic procedure used in the numerical calculation of the DPAL-Raman system [52,53]. The algorithm begins at time $t = 0$ by "guessing" the lasing detuning and coupling strength, Δ_L and Ω_L, and plugs these initial values into the gain and dip Hamiltonians, $\hat{\tilde{H}}_G$ and $\hat{\tilde{H}}_D$. The combined Hamiltonian is then used to solve the Optical Bloch equations in the steady state, which yield the density matrix components of the gain and dip cells. From this, we calculate χ_L, which is plugged into the single-mode laser equations:

$$\frac{d\varphi_L}{dt} = (\Omega_C - \omega_L) - \frac{\chi_{L(R)}}{2}\omega_L \tag{4.26}$$

$$\frac{dE_L}{dt} = -\frac{\omega_L E_L}{2Q} - \frac{\chi_{L(I)} E_L}{2}\omega_L \tag{4.27}$$

where φ_L, ω_L, and E_L are the phase, frequency, and amplitude, respectively, of the laser output. Q and Ω_C are the empty cavity quality factor and resonance frequency, respectively, and $\chi_L \equiv \chi_{L(R)} + i\chi_{L(I)}$. The algorithm calculates $\Delta\varphi_L$ and ΔE_L, the change in phase and amplitude, respectively, over a time step of Δt, so that $\Delta\varphi_L = \Delta t\left(\frac{d\varphi_L}{dt}\right)$, and $\Delta E_L = \Delta t\left(\frac{dE_L}{dt}\right)$. The new values of φ_L and E_L result in new values of Δ_L and Ω_L. The algorithm then reaches the "stepping decision" to determine if the algorithm has reached a steady-state solution. If the values of Δ_L and Ω_L are determined to have converged sufficiently, then the algorithm is complete. Otherwise, the procedure repeats for the next time interval Δt. After enough iterations, the density matrices, cavity parameters, and intra-cavity beam parameters eventually reach a steady-state and *self-consistent* solution.

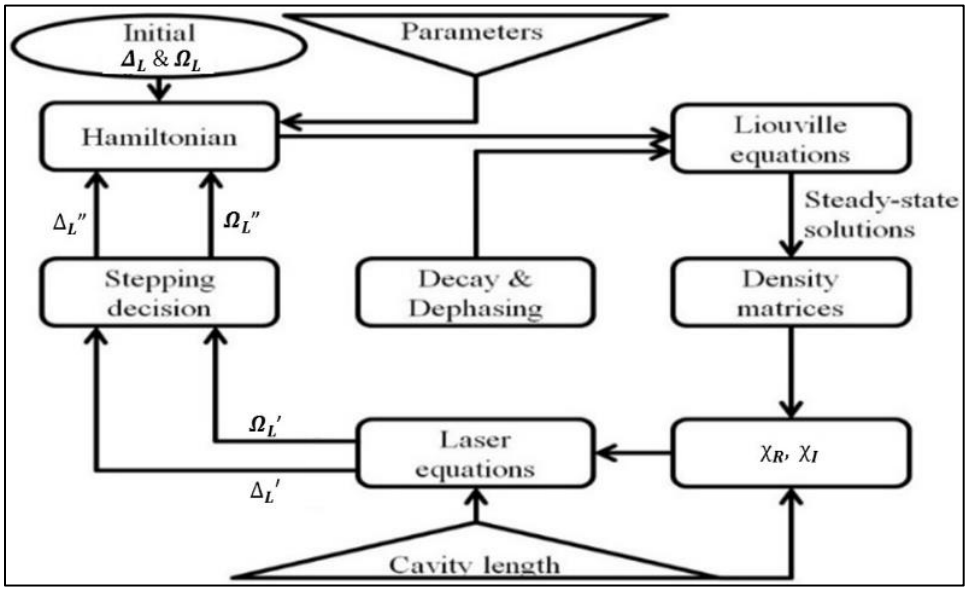

Fig. 4.23: Flow chart illustrating the algorithmic procedure for numerically solving the DPAL-Raman superluminal laser. After enough iterations, the algorithm reaches a self-consistent steady-state solution.

4.7.5 Comparison of Experimental and Numerical Results

The algorithmic procedure from Section 4.7.4 is used to determine the steady-state density matrices (and therefore steady-state values of $\chi_{L(R)}$ and $\chi_{L(I)}$) for one set of experimental parameters. In order to compare the experimental results from Section 4.6 to the numerical model, we calculate numerically (using the code included in Appendix A) the DPAL output power for 101 different values of δ, centered at $\delta = 0$. The simulation parameters correspond to the experimental parameters documented in the caption of Figure 4.19. The experimental and theoretical plots of DPAL output power versus δ are shown in Figures 4.24(a) and 4.24(b), respectively.

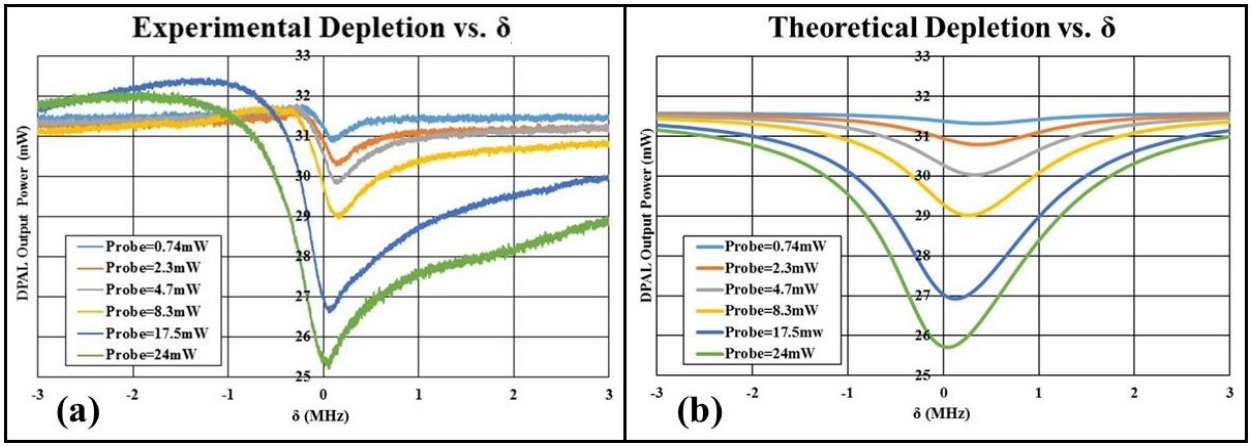

Fig. 4.24: (a) Experimentally-measured DPAL output power versus two-photon detuning δ; (b) Numerically-calculated DPAL output power versus δ

There appears to be reasonable qualitative and quantitative agreement between the numerical model and the experimental data. The depth and width of the Raman depletion both increase monotonically with increasing Raman probe power, with values matching reasonably well between theory and experiment. However, there are two main discrepancies to note: First, the experimental data appear to have a higher degree of asymmetry than the numerical model, especially for higher Raman probe power. Second, the calculation shows the dip shifting towards the left with increasing Raman probe power, whereas the dip location is roughly constant in the experimental data.

There are a few potential sources of these discrepancies. First, the numerical model for the atomic transitions is somewhat simplified, for both the DPAL gain and Raman depletion. Specifically, states $|1\rangle$, $|2\rangle$, $|3\rangle$, and $|4\rangle$ each contain several Zeeman sub-levels, but are treated as a single state. Since the DPAL gain is quite broad, ignoring these details is not likely to affect the numerically-calculated DPAL gain spectrum significantly. Furthermore, during this experiment, the parameters affecting DPAL gain were held at constant values. Thus, simplification in the

modeling of the DPAL gain is unlikely the source of the discrepancy. In contrast, the Raman depletion process has a much narrower bandwidth, and the details of the relevant energy levels may affect the spectral shapes of the dip. The number of Zeeman sublevels in a hyperfine state is [18]:

$$N_{ZEEMAN} = 2F + 1 \tag{4.28}$$

where $F = \left|\vec{F}\right| = \left|\vec{I} + \vec{J}\right|$, where $\vec{I}$ is the nuclear spin and $\vec{J} = \vec{L} + \vec{S}$ is the total electron spin, where $\vec{L}$ is electron orbital angular momentum and $\vec{S}$ is electron spin angular momentum. Therefore, in the ^{85}Rb isotope (in which $\left|\vec{I}\right| = {}^{5}/_{2}$), states $|1\rangle$ ($S_{1/2}$,F=2) and $|2\rangle$ ($S_{1/2}$,F=3) in the dip cell have Zeeman degeneracies of 5 and 7, respectively, while state $|3\rangle$ (the entire $P_{1/2}$ manifold, which contains F=2 and F=3 hyperfine-split levels) has a total of 12 Zeeman sublevels. State $|4\rangle$, which is the entire $P_{3/2}$ manifold, contains all four (F=1,2,3,4) hyperfine levels, and therefore has a total of 24 Zeeman sublevels. There are thus 48 individual Zeeman sublevels in this "three-level" system. In the algorithm, the matrix which solves this system has a size of $N^2 \times N^2$, where N is the number of energy levels. Thus, accounting for every Zeeman sublevel would increase the size of this matrix by a factor of $(48/3)^4$=65536. Given that our algorithm is iterative, such an increase would enormously inflate the computation time, thus making it very difficult to explore the entire parameter space.

It is also important to note that the numerical model assumes that the Raman pump couples only to the $|2\rangle \rightarrow |3\rangle$ transition, and not to the $|1\rangle \rightarrow |3\rangle$ transition, while the Raman probe couples only to the $|1\rangle \rightarrow |3\rangle$ transition, and not the $|2\rangle \rightarrow |3\rangle$ transition. In reality, *both* the Raman pump *and* Raman probe couple to *both* of these transitions, and the difference between the degree of coupling to the $|1\rangle \rightarrow |3\rangle$ transition and the $|2\rangle \rightarrow |3\rangle$ transition depends on their respective

detunings relative to state $|3\rangle$. However, developing codes that go beyond this approximation is difficult, because it is no longer possible to make the rotating wave approximation, and one must take into account higher order harmonics of the beat note between the Raman pump and the Raman probe [54]. This approximation may account for the absence of asymmetry in the theoretical results. In the near future, we will develop a more comprehensive code that will not make these approximations and use it to determine whether the discrepancies between experiment and theory can be eliminated.

4.7.6 Using the Numerical Model to Calculate Superluminal Enhancement

In order to calculate the sensitivity of the DPAL output frequency to cavity length change, the algorithm solves the superluminal laser frequency, f_L, for 101 different values of L, centered at L_o. Figure 4.25(a) shows $\Delta f_L (\equiv f_L - f_o)$ versus $\Delta L (\equiv L - L_o)$, for the same values of Raman pump power as used in the experiment. The enhancement factor [Figure 4.25(b)] is simply the factor by which the slope of $\Delta f_L / \Delta L$ is greater than the slope of the dotted line in Figure 4.25(a), which represents the empty-cavity sensitivity. As expected, the superluminal enhancement becomes more pronounced with increasing values of Raman probe power. For example, a Raman probe power of 24 mW yields an enhancement factor as high as 190($=10^{2.28}$). In principle, the enhancement factor can be several orders of magnitude greater than unity with the proper choice of experimental parameters.

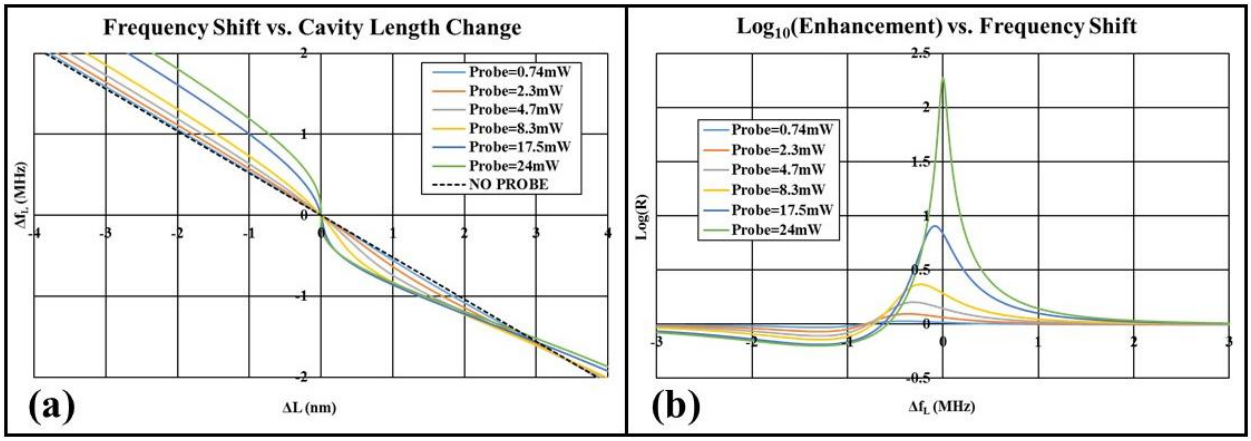

Fig. 4.25: (a) Frequency shift versus cavity length change for various values of Raman probe power. The dotted line represents change in DPAL output frequency versus cavity length change for a conventional laser without Raman depletion; (b): Sensitivity enhancement factors (log scale), calculated as the ratio of the slope of $\Delta f_L/\Delta L$ with Raman depletion to the slope of $\Delta f_L/\Delta L$ without Raman depletion (dotted line in Fig. 4.25(a)).

4.8 Making a Bi-Directional DPAL

In this chapter, we have demonstrated a *single-direction* Diode-Pumped Alkali Laser (DPAL) in which the intra-cavity lasing beam experienced Raman depletion. However, for practical reasons, a laser interferometer should operate with *bi-directionally*, with counter-propagating and *spatially-overlapping* modes. This is because mirror vibrations and thermal fluctuations, as well as other environmental noise sources, cause the round-trip optical path length to fluctuate randomly, which in creates "classical noise" in the laser frequency. In a bi-directional laser, the clockwise and counter-clockwise frequencies propagate through the same path and therefore "see" the same noise, so that the *difference* between their frequencies is insensitive to these random fluctuations. Having a narrow beat note is crucial for device sensitivity, as explained in Chapter 2. Therefore, now that we have demonstrated a single-direction superluminal DPAL, the next step is to demonstrate a bi-directional superluminal DPAL in which the counter-propagating modes *overlap spatially*, and in which one (or both) of the lasing modes experiences Raman depletion.

In the single-mode DPAL, the intra-cavity optical isolator forced single-direction lasing. To build the bi-directional DPAL, we therefore removed the isolator from the cavity, as shown in Figure 4.26(a). Because the optical pump is incoherent with the intra-cavity lasing beam, the clockwise and counter-clockwise gain are equal, regardless of the direction in which the optical pump propagates through the gain cell. It turns out that the equal gain created severe mode competition between the clockwise and counter-clockwise directions. This led to a high degree of instability, which is made evident by Figure 4.26(b), which shows the clockwise and counter-clockwise output power monitored simultaneously over a ten-second time period. Whenever the clockwise mode is "on", the counter-clockwise mode is "off", and vice versa. Therefore, the

counter-propagating modes cannot and do not co-exist. It turns out also that there was also *transverse mode competition* for certain experimental parameters; in other words, the lasing modes were sometimes in the TEM_{00} spatial mode, but were also sometimes in the TEM_{10}, TEM_{01}, TEM_{20}, etc. modes.

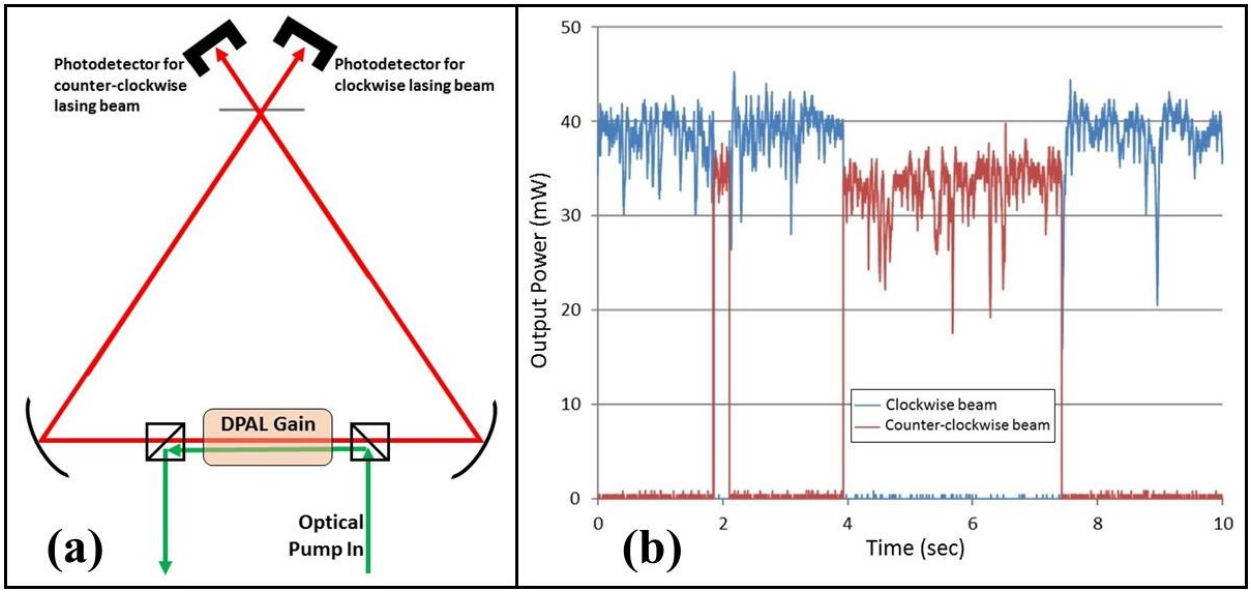

Fig. 4.26: (a) Schematic of bi-directional DPAL; (b) Mode competition between the counter-propagating modes, showing that only one mode can lase at a time. In addition, the mode that *is* lasing is highly unstable due to this mode competition.

Unfortunately, there was no literature at the time regarding mode competition in DPALs. This likely due to the combination of the fact that DPALs were still a relatively new technology (the first experimental demonstration of a DPAL was published in 2003 [35]), and, more importantly, the fact that DPALs were being developed mainly as a method for efficiently converting high-M^2 (and therefore highly-divergent) light into $M^2 \cong 1$ (diffraction-limited divergence) light [36,37,38,39,40,41]. For this reason, all of the prior DPAL studies used two-mirror cavities, which do not have "clockwise" and "counter-clockwise" modes, and therefore, in which directional mode competition is not even possible. Due to the inability for the DPAL to lase

bi-directionally in a *stable* manner, we concluded that if we want to demonstrate a stable bi-directional laser interferometer, we need to switch gain media altogether. Although the DPAL-Raman system turned out to not be ideal for our application, the experiments thereof were still instructive in understanding how to create a superluminal laser, and in demonstrating experimentally an ultra-narrowband dip in a laser with corresponding sensitivity enhancement.

CHAPTER 5

RAMAN LASER EXPERIMENTS

5.1 Introduction to the Raman Laser

Fundamentally, directional mode competition in the DPAL occurred because there was only one gain cell in the cavity, so that the clockwise and counter-clockwise modes used the same atoms to achieve gain [26]. In other words, the counter-propagating modes "competed" for the same gain atoms, which created instability and rendered the DPAL incapable of lasing bi-directionally. Therefore, to avoid the problem of mode competition, we would like to use a gain medium in which the clockwise and counter-clockwise modes use different atoms for gain. Furthermore, we do not want the clockwise lasing beam to interact with the counter-clockwise gain cell, and vice versa.

Recall from Chapter 4 that Raman resonance between *counter-propagating* beams occurs only in the *near-zero-velocity* atoms in Doppler-broadened atomic vapor; more specifically, only an atom with a small enough Doppler shift to still be within the "Raman interaction linewidth", Γ_{RAMAN}, can be two-photon resonant with a counter-propagating beam. Therefore, if $\Gamma_{DOPPLER}$ (the FWHM Doppler linewidth) is approximately 560 MHz while Γ_{RAMAN} is approximately 1 MHz (which are typical values), then only $1/560^{th}$ of atoms would be able to mediate two-photon resonance between counter-propagating beams. On the other hand, *all* velocity groups of atoms can mediate two-photon resonance between *co-propagating* beams. Therefore, the output of a laser using Raman gain in atomic vapor would co-propagate with the Raman pump, since gain in the co-propagating direction would far exceed that in the counter-propagating direction. Figure 5.1(a)

shows the energy levels and optical fields that would be involved in a single-direction version of this laser. The optical pump provides an effective decay rate from state $|2\rangle$ to state $|1\rangle$, thus enabling us to model this *Raman laser* as a three-level system, as shown in Figure 5.1(b). In other words, the optical pump creates "Raman population inversion" between states $|1\rangle$ and $|2\rangle$, which would otherwise have roughly equal populations in thermal equilibrium. A near-resonant Raman pump on the $|1\rangle \rightarrow |3\rangle$ transition (with detuning of Δ) creates two-photon gain on the $|2\rangle \rightarrow |3\rangle$ transition in the co-propagating direction. A laser is made by inserting this medium into a resonant cavity.

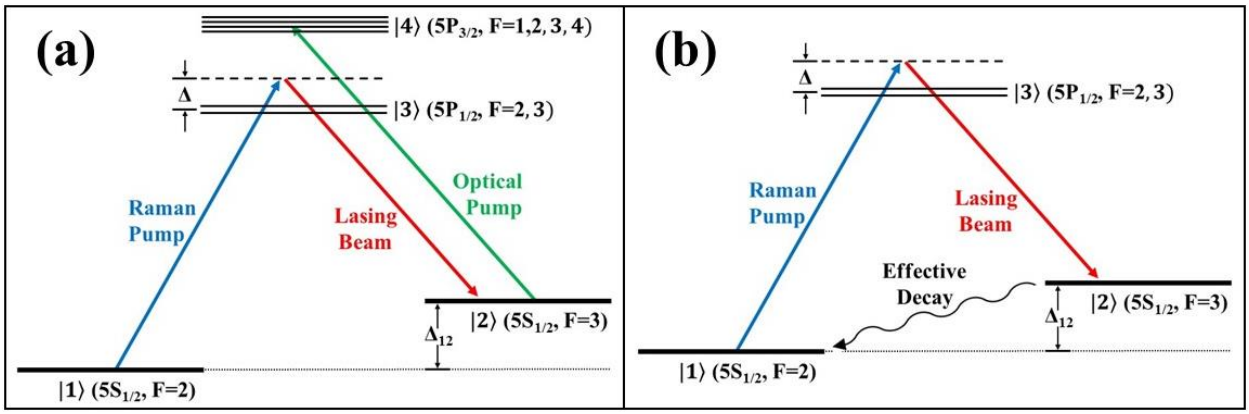

Fig. 5.1: (a) Energy levels and optical fields involved in a single-direction Raman laser; (b) equivalent three-level system in which the optical pump is treated as a decay rate

We can make a *bi-directional* Raman laser by using one gain cell for the clockwise direction and another gain cell for the counter-clockwise direction. In principle, there are many energy configurations which could accomplish this goal; in Figure 5.2, the clockwise lasing beam has positive detuning (Δ_{CW}) relative to the $|1\rangle \rightarrow |3\rangle$ transition, while the counter-clockwise gain cell has negative detuning (Δ_{CCW}) relative to the $|2\rangle \rightarrow |3\rangle$ transition. With this choice of Δ_{CW} and Δ_{CW}, the counter-propagating lasing beams are significantly detuned from one another (~5 GHz apart), which provides an additional benefit: In the Helium-Neon laser gyroscope, which is

currently the standard optical gyroscope used for the highest-precision rotation measurements, the counter-propagating lasing modes are degenerate in frequency. It is well-known [55,56,57] that in degenerate laser gyroscopes, backscattering from optical surfaces causes the counter-propagating frequencies to lock to one another other, which is a significant experimental issue. The non-degeneracy of the mode frequencies in the Raman laser circumvents this issue, alleviating the need to use dithering (or other techniques) to prevent mode locking.

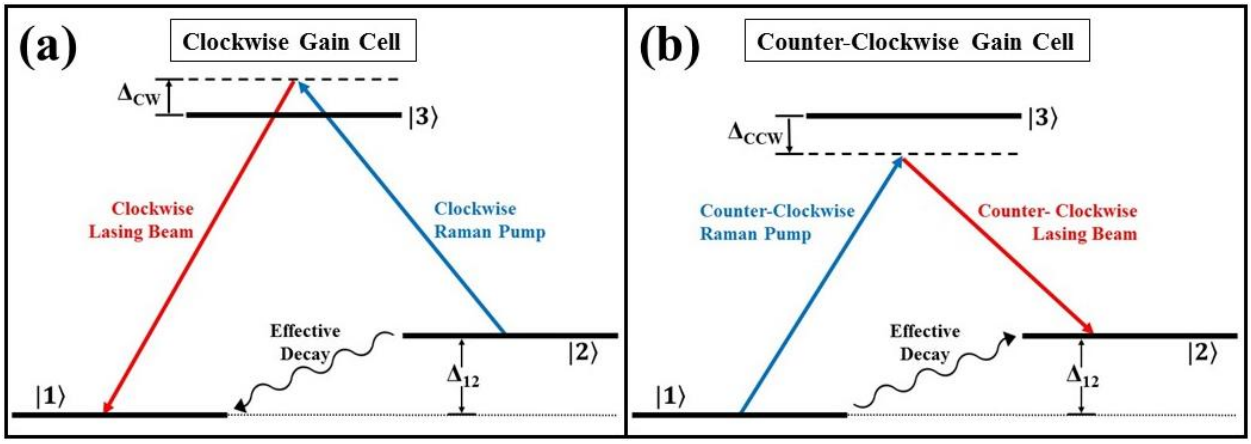

Fig. 5.2: (a) One example of the energy levels, optical fields, and effective decay rates that could be used in the clockwise and; (b) counter-clockwise gain cells of a bi-directional Raman laser

To make a superluminal Raman laser gyroscope, we propose a laser in which Raman gain is created in the ^{85}Rb isotope, while Raman depletion of the lasing beam is produced in the ^{87}Rb isotope. Since naturally-occurring rubidium is composed of 72% ^{85}Rb and 28% ^{87}Rb, this allows us to use one hybrid gain/dip cell for each direction, which significantly reduces the number of optical components (beam splitters, etc.) needed, which thus reduces intra-cavity loss and more easily enables miniaturization. It is also cheaper, since isotopically-pure rubidium is more expensive than naturally-occurring rubidium. The relevant ^{87}Rb and ^{85}Rb energy levels are shown in Figure 5.3. Note that the hyperfine splitting of the $S_{1/2}$ state is 3.036 GHz in ^{85}Rb and 6.835 GHz

in ^{87}Rb. These data were obtained from References 50 and 51, which contain much more comprehensive data on these isotopes.

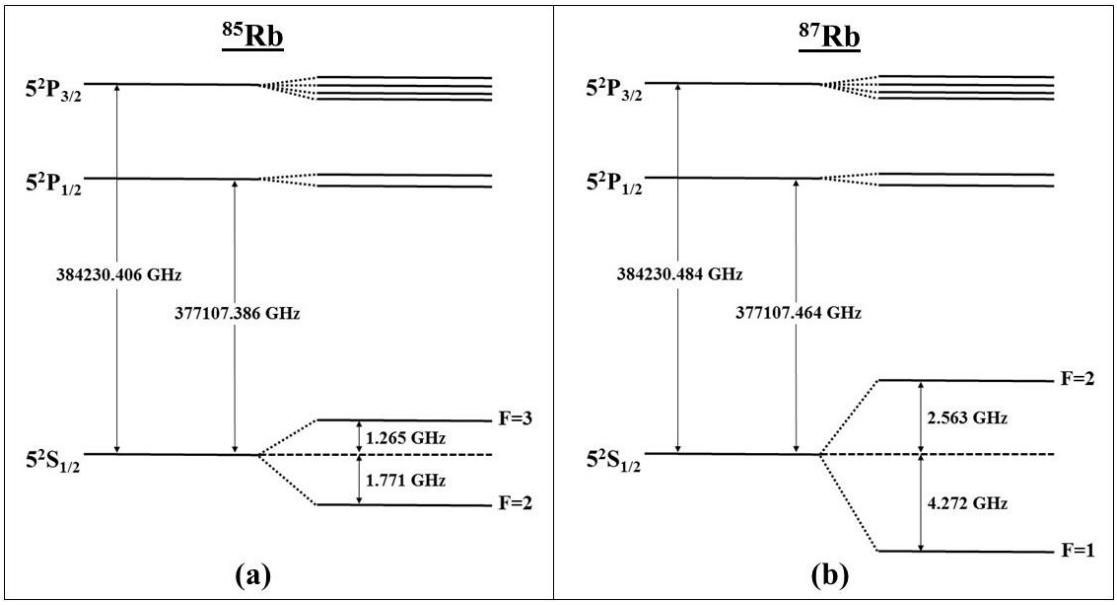

Fig. 5.3: (a) Relevant energy levels in ^{85}Rb and; (b) ^{87}Rb.

Figure 5.4 is one example configuration of the optical fields which could be used for creating a *single-direction* superluminal Raman laser. In this particular configuration, the detuning of the lasing beam relative to the gain transition ($|2_{85}\rangle \rightarrow |3_{85}\rangle$) is positive, while its detuning relative to the dip transition ($|1_{87}\rangle \rightarrow |3_{87}\rangle$) is negative.

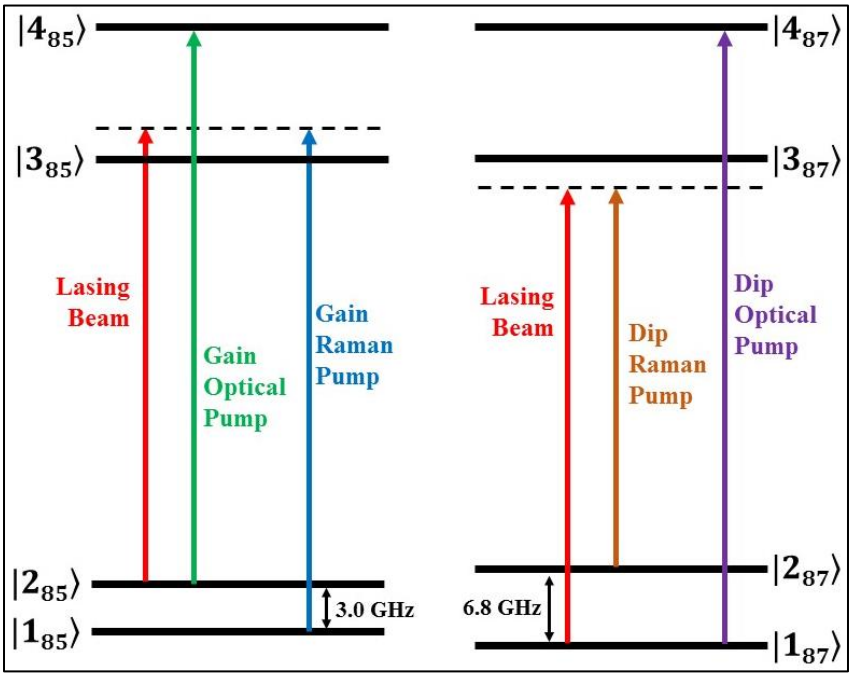

Fig. 5.4: Schematic of optical fields used in a superluminal Raman laser

Before attempting to build a *bi-directional*, *superluminal* Raman laser, we first need to understand the behavior of a *single-direction*, *non-superluminal* Raman laser. We therefore built and characterized such a system; Figure 5.5(a) shows a schematic of this laser, with the associated energy levels and optical fields shown in Figure 5.5(b), and the effective three-level simplified system shown in Figure 5.5(c). Although the standard Raman laser makes use of only the ^{85}Rb isotope, we still used a vapor cell with natural rubidium, since we would eventually need to utilize ^{87}Rb for Raman depletion. The laser cavity was a square with a perimeter of one meter. Because all four mirrors were flat, an intra-cavity lens with a focal length of at least 250 mm (one quarter the roundtrip length) was required to stabilize the cavity [26]; the lens we used had a focal length of 750 mm. The minimum waist size of the lasing mode occurs exactly opposite the location of the lens; we placed a circular aperture (iris) at that location to spatially filter out all transverse

modes besides the TEM_{00} mode. It turns out that this iris helped tremendously in stabilizing the laser output and ensuring single-transverse-mode operation.

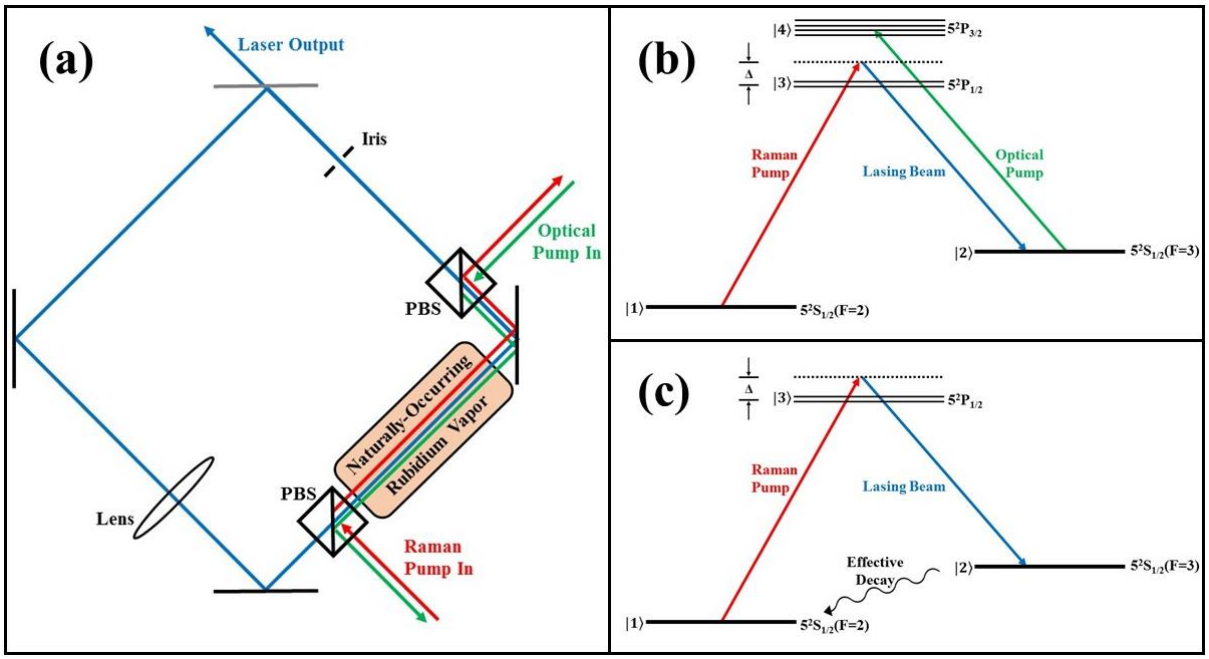

Fig. 5.5: (a) Schematic of single-direction Raman laser using rubidium vapor as gain; (b) associated energy levels and optical fields; (c) effective three-level system treating the optical pump as a decay rate

5.2 Mode Spacing in the Raman Laser

We first measured the laser output power while scanning the Raman pump detuning (denoted as Δ in Figure 5.5), keeping all other parameters constant. The purpose of this experiment was to determine the range of Δ over which the Raman laser could operate. A small piece of the Raman pump was diverted to an outside rubidium vapor cell, in which the saturated absorption profile was measured, which provided a frequency reference. Figure 5.6 shows a typical oscilloscope image obtained from this experiment; the orange scan is the saturated absorption profile (labeled with the corresponding transitions), and the blue scan is the laser output power. Figure 5.6(b), which is a zoomed-in version of Figure 5.6(a), labels the individual lasing modes. This data is important because it shows the values of Δ over which the Raman laser operates, which we must understand in order to design the superluminal version of this laser.

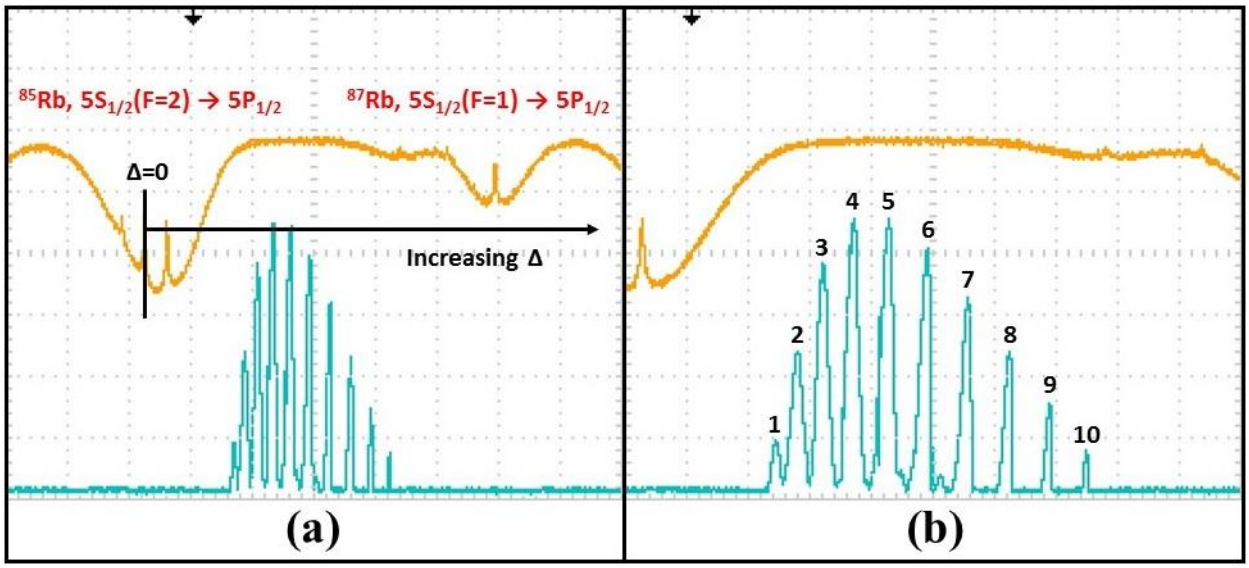

Fig. 5.6: (a) Oscilloscope scan showing Raman lasing modes (blue) with corresponding saturated absorption profile (orange) used as a frequency reference; (b) zoomed-in version of (a), with the individual modes labeled.

Before looking at the data, we naïvely expected that because the refractive index is very close to unity, the spacing between neighboring lasing modes (the so-called *laser FSR*) should be equal to $^{c}/_{L}$, where L is the round-trip cavity length. Thus, with a cavity perimeter of one meter, the laser FSR should be 300 MHz. Using the saturated absorption profile as a frequency reference, we found the laser FSR to be *significantly less* than 300 MHz, and furthermore, we found it was *not constant*. In other words, the spacing between modes 1 and 2 is different from the spacing between modes 2 and 3, which is different from the spacing between modes 3 and 4, etc. In order to characterize this effect, we took many oscilloscope images (the same type of data as shown in Figure 5.6) at four different cell temperatures, five different optical pump powers, and two different Raman pump powers, yielding a total of 4×5×2=40 different combinations of experimental parameters. Lasing occurred for 29 of these 40 combinations of parameters, for which we documented each individual mode with its corresponding Raman pump detuning (Δ). The data are shown in Table 5.1.

Data Set	Temp (°C)	O.P. Power (mW)	R.P. Power (mW)	Mode #	Δ (MHz)
1	80.2	3.82	8.90	1	690
1	80.2	3.82	8.90	2	945
2	80.2	5.95	8.90	1	692
2	80.2	5.95	8.90	2	948
3	80.2	11.20	8.90	1	777
3	80.2	11.20	8.90	2	1043
4	80.2	23.30	8.90	1	470
4	80.2	23.30	8.90	2	715
4	80.2	23.30	8.90	3	975
5	80.2	48.50	8.90	1	497
5	80.2	48.50	8.90	2	746
5	80.2	48.50	8.90	3	1014
5	80.2	48.50	8.90	4	1292
6	80.2	11.20	3.75	1	460

6	80.2	11.20	3.75	2	701
7	80.2	23.30	3.75	1	462
7	80.2	23.30	3.75	2	703
7	80.2	23.30	3.75	3	963
8	80.2	48.50	3.75	1	371
8	80.2	48.50	3.75	2	612
8	80.2	48.50	3.75	3	864
9	91.2	3.82	8.90	1	768
9	91.2	3.82	8.90	2	991
10	91.2	5.95	8.90	1	826
10	91.2	5.95	8.90	2	1060
10	91.2	5.95	8.90	3	1309
11	91.2	11.20	8.90	1	639
11	91.2	11.20	8.90	2	850
11	91.2	11.20	8.90	3	1083
11	91.2	11.20	8.90	4	1336
11	91.2	11.20	8.90	5	1591
12	91.2	23.30	8.90	1	466
12	91.2	23.30	8.90	2	632
12	91.2	23.30	8.90	3	846
12	91.2	23.30	8.90	4	1087
12	91.2	23.30	8.90	5	1340
12	91.2	23.30	8.90	6	1585
13	91.2	48.50	8.90	1	566
13	91.2	48.50	8.90	2	755
13	91.2	48.50	8.90	3	985
13	91.2	48.50	8.90	4	1234
13	91.2	48.50	8.90	5	1489
13	91.2	48.50	8.90	6	1733
14	91.2	5.95	3.75	1	650
14	91.2	5.95	3.75	2	861
15	91.2	11.20	3.75	1	637
15	91.2	11.20	3.75	2	853
15	91.2	11.20	3.75	3	1093
16	91.2	23.30	3.75	1	413
16	91.2	23.30	3.75	2	590
16	91.2	23.30	3.75	3	799
16	91.2	23.30	3.75	4	1030
17	91.2	48.50	3.75	1	288
17	91.2	48.50	3.75	2	422

17	91.2	48.50	3.75	3	610
17	91.2	48.50	3.75	4	852
17	91.2	48.50	3.75	5	1085
18	104.1	5.95	8.90	1	917
18	104.1	5.95	8.90	2	1104
18	104.1	5.95	8.90	3	1307
19	104.1	11.20	8.90	1	841
19	104.1	11.20	8.90	2	1023
19	104.1	11.20	8.90	3	1223
19	104.1	11.20	8.90	4	1431
20	104.1	23.30	8.90	1	706
20	104.1	23.30	8.90	2	859
20	104.1	23.30	8.90	3	1050
20	104.1	23.30	8.90	4	1261
20	104.1	23.30	8.90	5	1478
20	104.1	23.30	8.90	6	1691
21	104.1	48.50	8.90	1	621
21	104.1	48.50	8.90	2	739
21	104.1	48.50	8.90	3	917
21	104.1	48.50	8.90	4	1123
21	104.1	48.50	8.90	5	1336
21	104.1	48.50	8.90	6	1551
21	104.1	48.50	8.90	7	1753
21	104.1	48.50	8.90	8	1931
22	104.1	11.20	3.75	1	755
22	104.1	11.20	3.75	2	932
22	104.1	11.20	3.75	3	1128
23	104.1	23.30	3.75	1	493
23	104.1	23.30	3.75	2	615
23	104.1	23.30	3.75	3	759
23	104.1	23.30	3.75	4	943
23	104.1	23.30	3.75	5	1132
23	104.1	23.30	3.75	6	1338
24	104.1	48.50	3.75	1	544
24	104.1	48.50	3.75	2	677
24	104.1	48.50	3.75	3	848
24	104.1	48.50	3.75	4	1047
24	104.1	48.50	3.75	5	1252
24	104.1	48.50	3.75	6	1449
25	117.9	11.20	8.90	1	976

25	117.9	11.20	8.90	2	1115
25	117.9	11.20	8.90	3	1270
25	117.9	11.20	8.90	4	1428
25	117.9	11.20	8.90	5	1589
26	117.9	23.30	8.90	1	905
26	117.9	23.30	8.90	2	1037
26	117.9	23.30	8.90	3	1184
26	117.9	23.30	8.90	4	1345
26	117.9	23.30	8.90	5	1506
26	117.9	23.30	8.90	6	1667
26	117.9	23.30	8.90	7	1815
27	117.9	48.50	8.90	1	755
27	117.9	48.50	8.90	2	859
27	117.9	48.50	8.90	3	981
27	117.9	48.50	8.90	4	1121
27	117.9	48.50	8.90	5	1278
27	117.9	48.50	8.90	6	1436
27	117.9	48.50	8.90	7	1600
27	117.9	48.50	8.90	8	1755
27	117.9	48.50	8.90	9	1889
28	117.9	23.30	3.75	1	921
28	117.9	23.30	3.75	2	1055
28	117.9	23.30	3.75	3	1202
28	117.9	23.30	3.75	4	1356
29	117.9	48.50	3.75	1	883
29	117.9	48.50	3.75	2	1011
29	117.9	48.50	3.75	3	1155
29	117.9	48.50	3.75	4	1305

Table 5.1: Documented here is the detuning of each individual lasing mode, for 29 different combinations of cell temperature, optical pump power, and Raman pump power.

After tabulating this data, we wanted to see if there was a relationship between lasing FSR (FSR_L) and Raman pump detuning (Δ). To do this, we plotted the *average* detuning of two neighboring modes versus their difference. For example, if two consecutive modes have detunings of 500 MHz and 600 MHz, we would say "at Δ=550 MHz, FSR_L=100 MHz". Figure 5.7 is a plot of FSR_L versus Δ, corresponding to the data from Table 5.1.

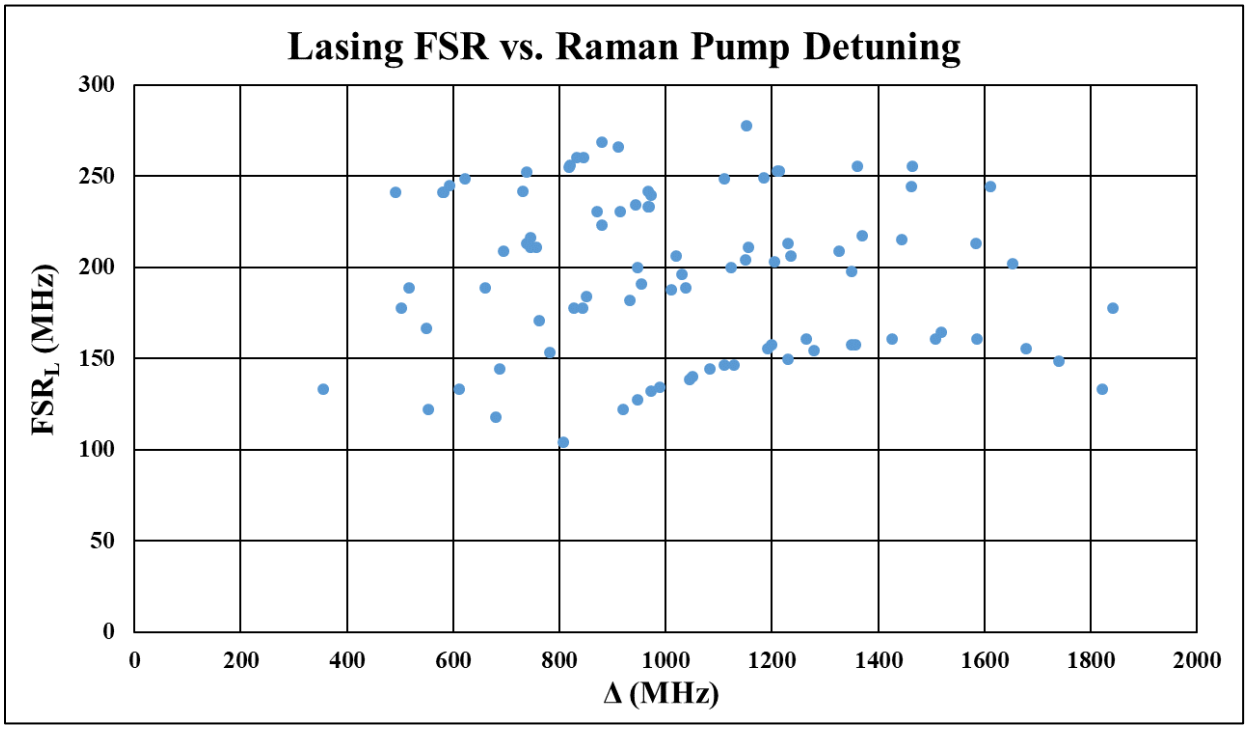

Fig. 5.7: Mode spacing in the Raman laser as a function of Raman pump detuning. Every data point from all 29 data sets is plotted here.

Figure 5.7 by itself does not give much information, except that it appears to contain four separate curves. It turns out that these curves correspond to the four different cell temperatures used in this experiment, as shown in Figure 5.8.

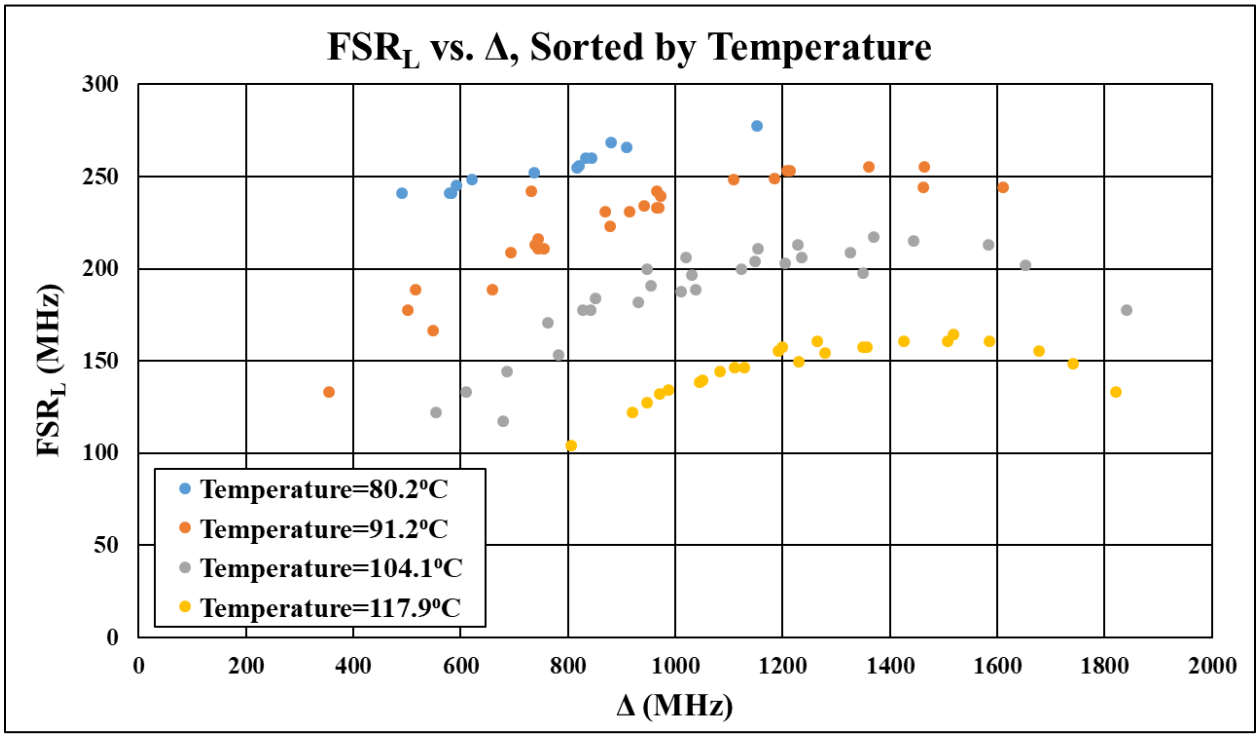

Fig. 5.8: Mode spacing in the Raman laser as a function of Raman pump detuning, sorted by temperature. Evidently the mode spacing depends on detuning and temperature.

Therefore, the laser FSR appears to depend on the cell temperature and the Raman pump detuning. The most trivial explanation for the reduction of laser FSR would be that if a cavity is filled with a medium of index n, the optical path length is increased by a factor of n relative to the empty cavity, thus reducing FSR_L by the same factor relative to FSR_{EC}; but that would mean that if the laser FSR is 150 MHz, then $n = 2$. This is completely unrealistic, since 90% of cavity is free space while the other 10% is dilute atomic vapor. The more plausible explanation is that *dispersion* is the source of this FSR narrowing, which we show by considering a medium where the index n has the following linear dispersion relation in the vicinity of frequency f_0:

$$n(f) = n(f_o) + \frac{dn}{df} \cdot (f - f_o) \equiv n_o + \alpha \cdot (f - f_o) \tag{5.1}$$

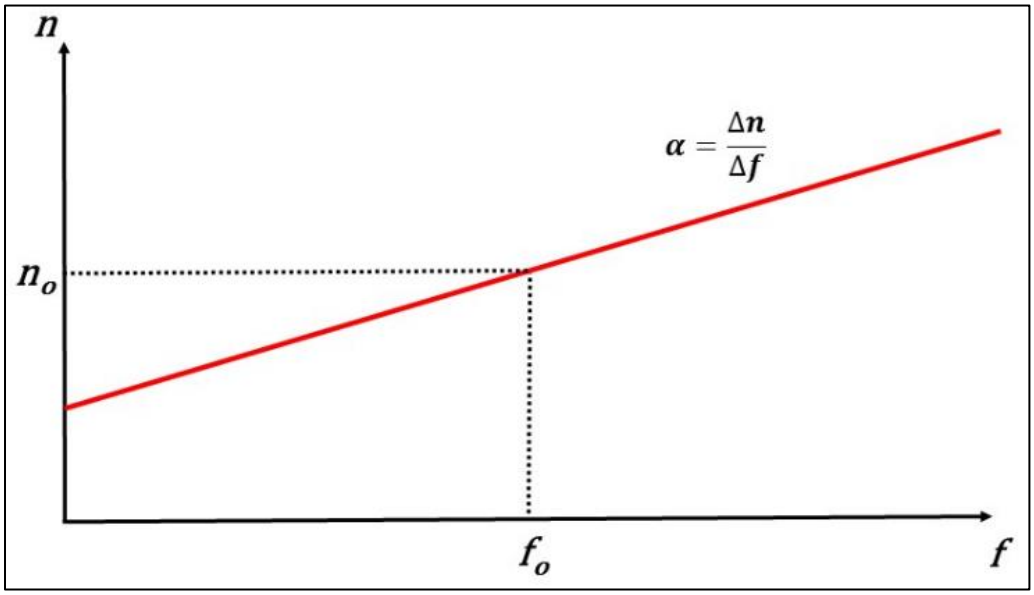

Fig. 5.9: Dispersion relation in which index is linearly proportional to frequency

This dispersion relation can be expressed as a relationship between λ and f:

$$\lambda = \frac{c/n}{f} = \frac{c}{f} \cdot \frac{1}{n_o + \alpha \cdot (f - f_o)} = \frac{c}{n_o f + \alpha f^2 - \alpha f_o f} = c \cdot [\alpha f^2 + (n_o - \alpha f_o) f]^{-1} \quad (5.2)$$

so that:

$$\frac{d\lambda}{df} = -c \cdot \frac{2\alpha f - \alpha f_o + n_o}{[\alpha f^2 + (n_o - \alpha f_o) f]^2} \quad (5.3)$$

Therefore, for values of $\Delta f \ll f_o$ (and $\Delta\lambda \ll \lambda$):

$$\Delta\lambda = -c \cdot \frac{2\alpha f - \alpha f_o + n_o}{[\alpha f^2 + (n_o - \alpha f_o) f]^2} \cdot \Delta f \quad (5.4)$$

$\Delta f \ll f_o$ also means that $f = f_o + \Delta f \cong f_o$ so that:

$$\Delta\lambda = -c \cdot \frac{\alpha f_o + n_o}{(n_o f_o)^2} \cdot \Delta f \quad (5.5)$$

The mode number, m, is the number of wavelengths that fit into one cavity round trip. Thus, $m = \frac{L}{\lambda}$, or $\lambda = \frac{L}{m}$. Therefore:

$$\frac{d\lambda}{dm} = \frac{-L}{m^2} \tag{5.6}$$

so that for values of $\Delta m \ll m$:

$$\Delta\lambda = \frac{-L}{m^2} \cdot \Delta m \tag{5.7}$$

Equating the right-hand side of Equation 5.5 and the right-hand side of Equation 5.7 then yields:

$$\Delta f = \frac{L}{m^2 c} \cdot \frac{(n_o f_o)^2}{\alpha f_o + n_o} \cdot \Delta m \tag{5.8}$$

$\Delta m = 1$ for consecutive modes, so that the dispersive-cavity free spectral range (FSR_{DC}) is:

$$FSR_{DC} = \frac{L}{m^2 c} \cdot \frac{(n_o f_o)^2}{\alpha f_o + n_o} = \frac{c}{L} \cdot \frac{1}{\alpha f_o + n_o} = \frac{FSR_{EC}}{\alpha f_o + n_o} = \frac{FSR_{EC}}{\left(\frac{dn}{df} f_o\right) + n_o} \tag{5.9}$$

where FSR_{EC} is the empty cavity free spectral range. In the non-dispersive limit ($\frac{dn}{df} = 0$), the FSR is reduced by a factor of n_o relative to that of the empty cavity, as we would expect. Furthermore, we use Equation 2.5 to identify the denominator in Equation 5.9 as the definition of "group index". In the case of the Raman laser mode spacing, this would be the group index experienced by a *weak probe which is always two-photon detuned from the Raman pump*. This hypothetical "probe" is amplified into a lasing beam only when it meets cavity resonance conditions. We can therefore write the laser FSR (FSR_L) as a function of the group index seen by this probe:

$$FSR_L = \frac{FSR_{EC}}{\left(\frac{dn}{df} f_o\right) + n_o} \equiv \frac{FSR_{EC}}{n_{g(PROBE)}} \tag{5.10}$$

In summary, we have concluded that the disparity between the empty cavity FSR and lasing FSR is far more likely to result from *dispersion* rather than much-larger-than-unity values of refractive index. More specifically, $FSR_L < FSR_{EC}$ for every data point we took, which implies that

$n_{g(PROBE)} > 1$, indicating a *slow light* effect. Figure 5.10 shows $n_{g(PROBE)}$ versus Δ at the four temperatures, which appears to show a *roughly* parabolic relationship for a given temperature.

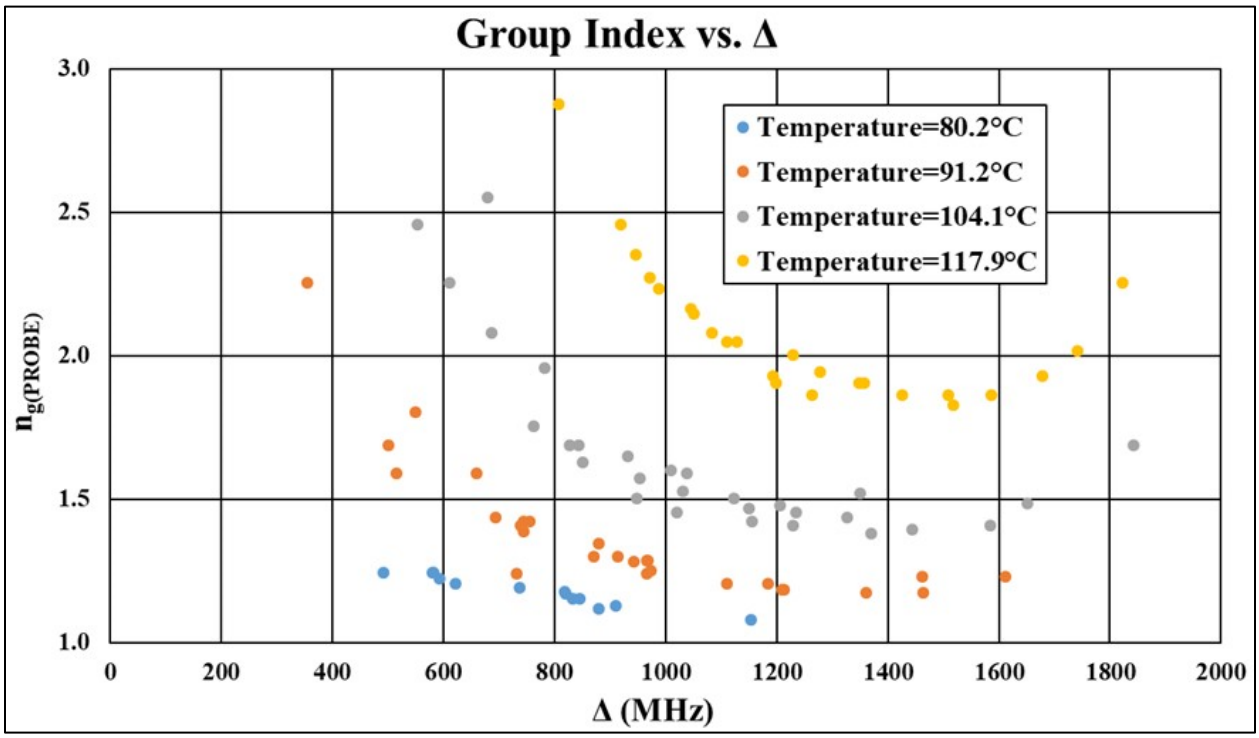

Fig. 5.10: Plot of $n_{g(PROBE)}$ as a function of Δ, where we use Equation 5.10 to calculate the group index corresponding to the data from Fig. 5.8

Figure 5.11 shows the saturated absorption profile of naturally-occurring rubidium; the frequencies over which the Raman pump was scanned are in blue, while the lasing beam, which was downshifted from the Raman pump by approximately 3.0357 GHz and therefore was always between the $S_{1/2}(F = 3) \rightarrow P_{1/2}$ and $S_{1/2}(F = 2) \rightarrow P_{1/2}$ transitions, is shown in red.

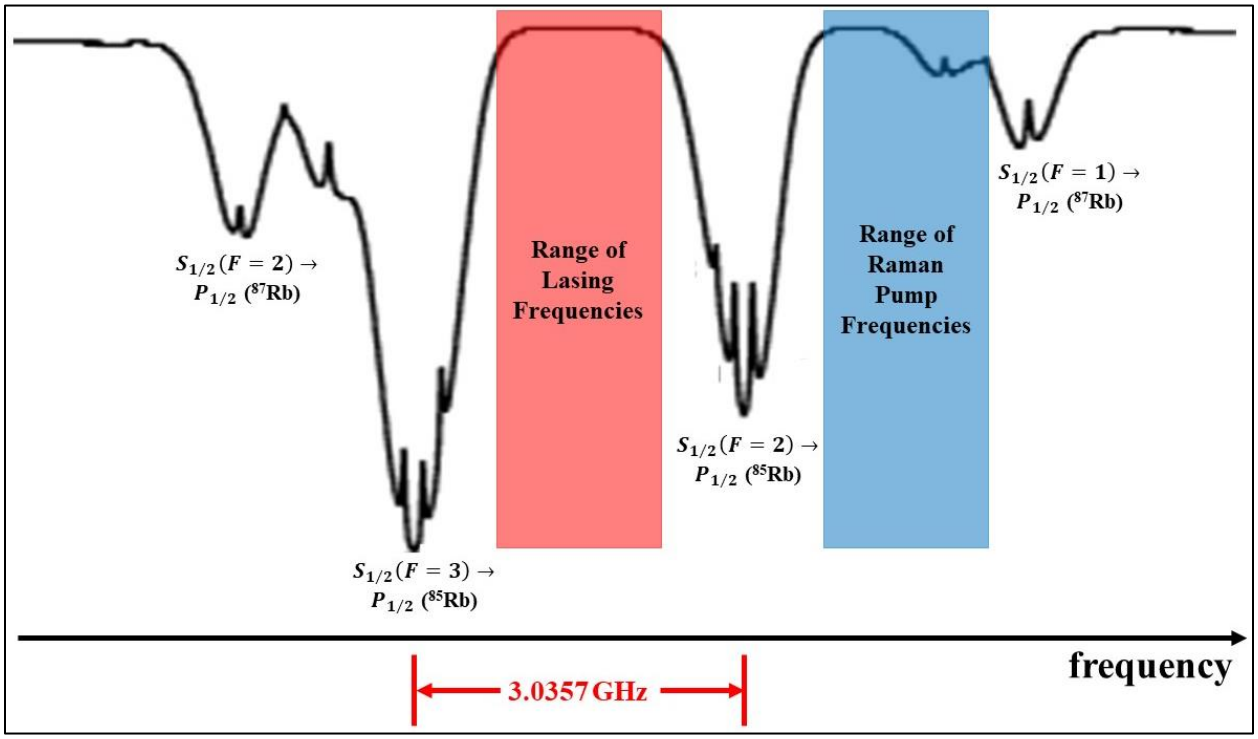

Fig. 5.11: Saturated absorption profile of naturally-occurring rubidium, with the Raman pump (blue) and lasing (red) frequencies highlighted for reference.

We now make the claim that the roughly parabolic shape of $n_{g(PROBE)}$ versus Δ is a result of the fact that the "probe" frequency (which is equal to the lasing frequency) is between two absorptive resonances. To substantiate this claim, we first recall that, for values of $\chi_{R(PROBE)} \ll 1$, the group index, $n_{g(PROBE)}$, takes the following form:

$$n_{g(PROBE)} \cong 1 + \frac{\chi_{R(PROBE)}}{2} + \frac{\omega}{2}\frac{d\chi_{R(PROBE)}}{d\omega} \cong 1 + \frac{\omega}{2}\frac{d\chi_{R(PROBE)}}{d\omega} = 1 + \frac{f}{2}\frac{d\chi_{R(PROBE)}}{df} \tag{5.11}$$

so that:

$$\frac{d\chi_{R(PROBE)}}{df} = \frac{2(n_g - 1)}{f} \tag{5.12}$$

We now plot $\frac{d\chi_{R(PROBE)}}{df}$ versus Δ in Figure 5.12. Since $\chi_{R(PROBE)}$ is unitless and f has the units of Hz, the standard unit for $\frac{d\chi_{R(PROBE)}}{df}$ is seconds.

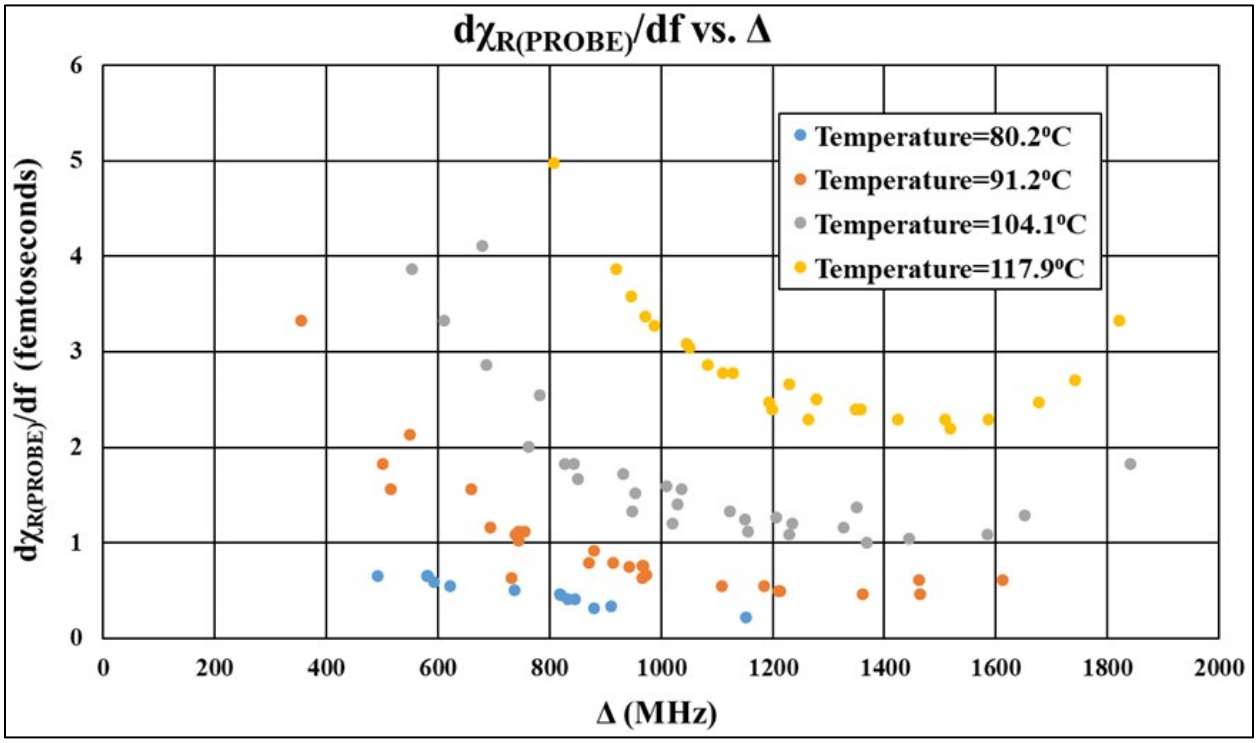

Fig. 5.12: Probe dispersion (expressed in femtoseconds) as a function of Raman pump detuning

For the linear absorption profile, $-\chi_{I(PROBE)}(f)$, shown in black in Figure 5.13, the Kramers-Kronig relations give the corresponding index, $\chi_{R(PROBE)}(f)$ (shown in blue) as well as $\frac{d\chi_{R(PROBE)}}{df}$ (shown in yellow). In range of lasing frequencies, the profile of $\frac{d\chi_{R(PROBE)}}{df}$ is indeed roughly parabolic. On this basis we can therefore conclude that the Kramers-Kronig relations governing a weak probe at the lasing frequency are likely to be responsible for the parabolic group index.

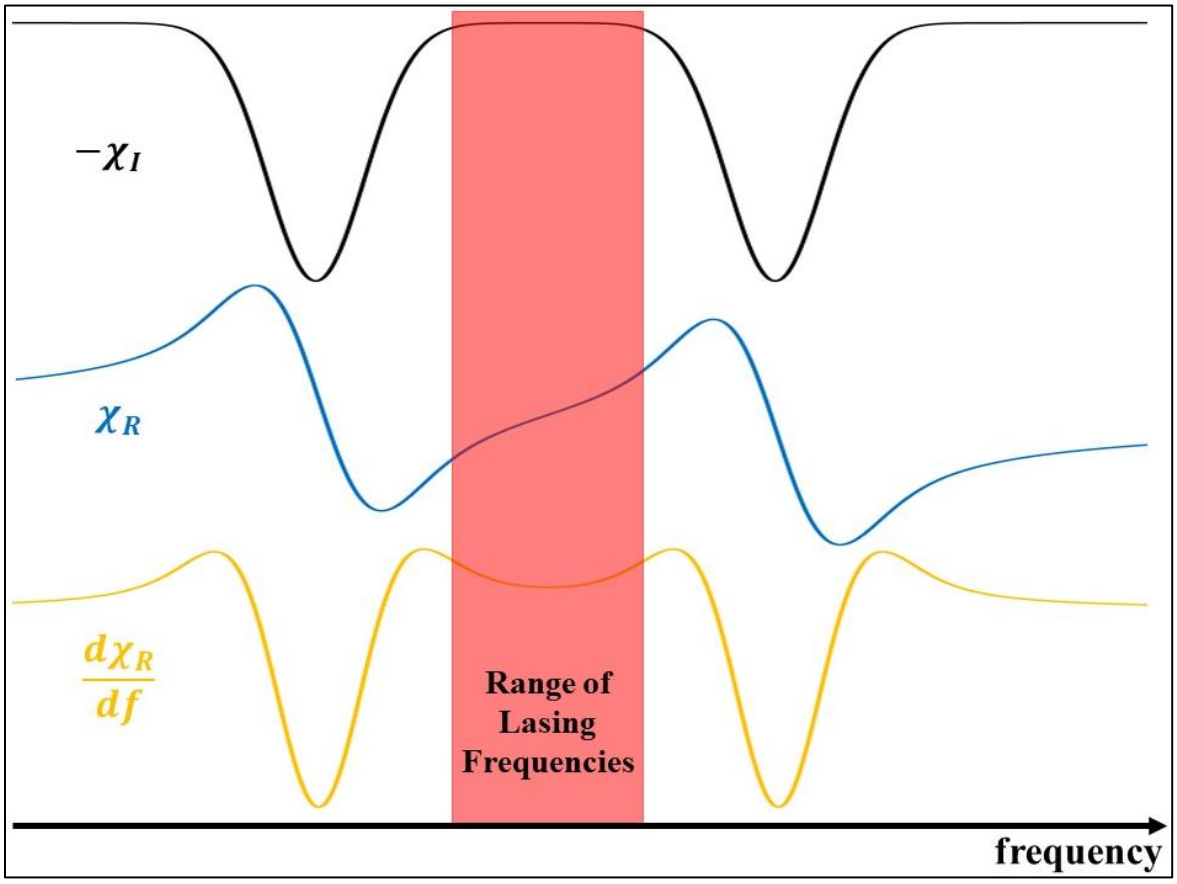

Fig. 5.13: If a probe is between two absorption peaks (shown in black), then, based on the Kramers-Kronig relations, it has an index of refraction shown in blue. The dispersion is the derivative of the index with respect to frequency, shown in yellow. This dispersion is parabolic within this frequency range.

Since $\frac{d\chi_{R(PROBE)}}{df}$ (or equivalently $\frac{d\chi_{R(PROBE)}}{d\Delta}$) is parabolic, higher-order nonlinear terms in the dispersion profile up to the $\frac{d^3\chi_{R(PROBE)}}{d\Delta^3}$ term are present. Over this frequency range, $\chi_{R(PROBE)}(\Delta)$ is therefore approximated as:

$$\chi_{R(PROBE)}(\Delta) \cong \chi_{R(PROBE)}(\Delta_o) + (\Delta - \Delta_o)\frac{d\chi_{R(PROBE)}}{d\Delta} + \frac{(\Delta - \Delta_o)^2}{2!}\frac{d^2\chi_{R(PROBE)}}{d\Delta^2} + \frac{(\Delta - \Delta_o)^3}{3!}\frac{d^3\chi_{R(PROBE)}}{d\Delta^3} \tag{5.13}$$

The other evident trend is that at a given value of Δ, the value of $n_{g(PROBE)}$ (and therefore $\frac{d\chi_{R(PROBE)}}{df}$) increases with increasing temperature. This should make sense on an intuitive level since refractive index should increase with increasing atomic density, and therefore, so should all derivatives of refractive index with respect to frequency. More specifically, in dilute vapor where $\chi_{R(PROBE)} \ll 1$, the value of $\chi_{R(PROBE)}$ (and therefore all its derivatives with respect to frequency) should be proportional to atomic density. To see if this is the case, we plot $\chi_{R(PROBE)}$ as a function of temperature using best-fit parabolas fitted to the data in Figure 5.12. Figure 5.14 shows $\frac{d\chi_{R(PROBE)}}{df}$ versus temperature for Δ=800 MHz, 900 MHz, and 1 GHz.

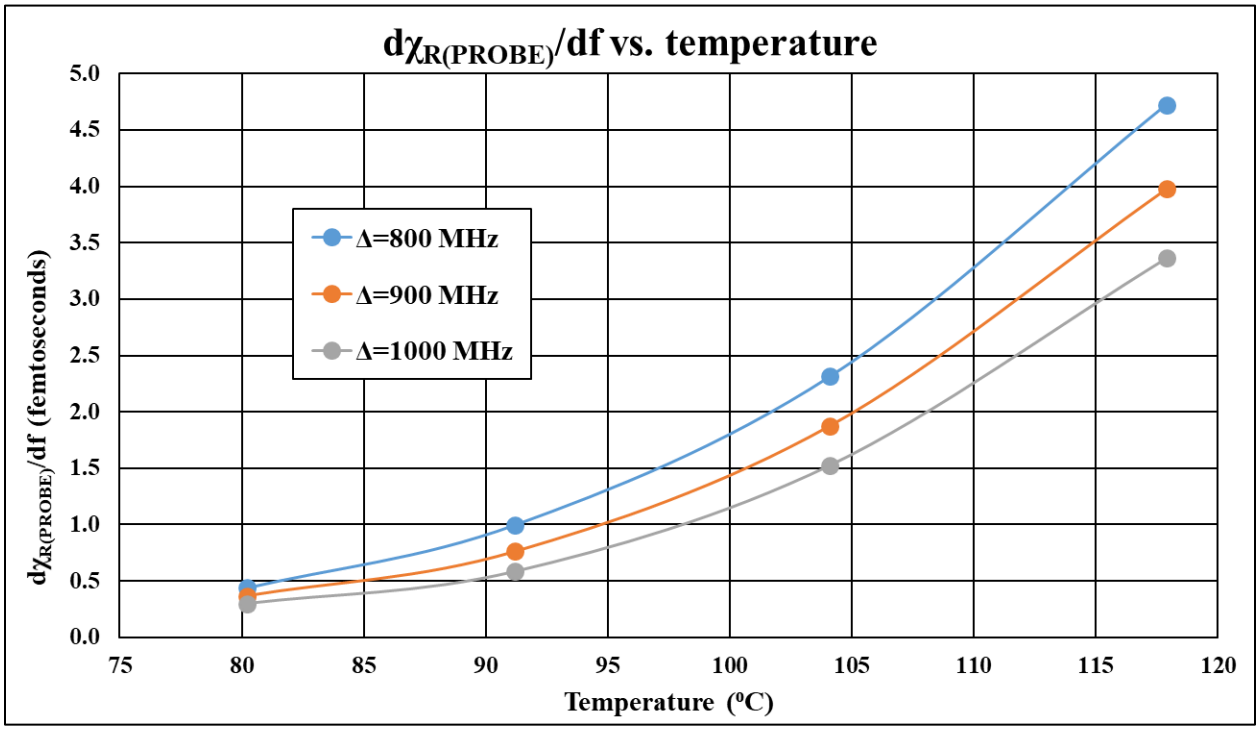

Fig. 5.14: The temperature dependence of probe dispersion, at three different values of Δ.

Evidently, the value of $\frac{d\chi_{R(PROBE)}}{df}$ doubles approximately every 10-12 degrees Celsius. Since $\chi_{R(PROBE)} \ll 1$, the value of $\chi_{R(PROBE)}$ should double at the same rate as its derivatives. The

empirical vapor pressure of rubidium as a function of temperature is given in References 58 and 59:

$$log_{10}(P) = A - \frac{B}{T} + CT + Dlog_{10}(T) \tag{5.14}$$

where P is measured in atmospheres, T is measured in Kelvin, $A = 15.88$, $B = 4530$, $C = 0.0005866$, and $D = -2.991$. In dilute vapor, the ideal gas law ($PV = nk_BT$) can be used to calculate the number density, $^{n}/_{V}$:

$$\frac{n}{V} = \frac{P}{k_BT} = \frac{10^{\left[A-\frac{B}{T}+CT+Dlog_{10}(T)\right]}}{k_BT} \tag{5.15}$$

After converting the pressure from atmospheres to Pascals (the SI unit of pressure, equal to newtons per meter squared), we plot the number density versus temperature in Figure 5.15.

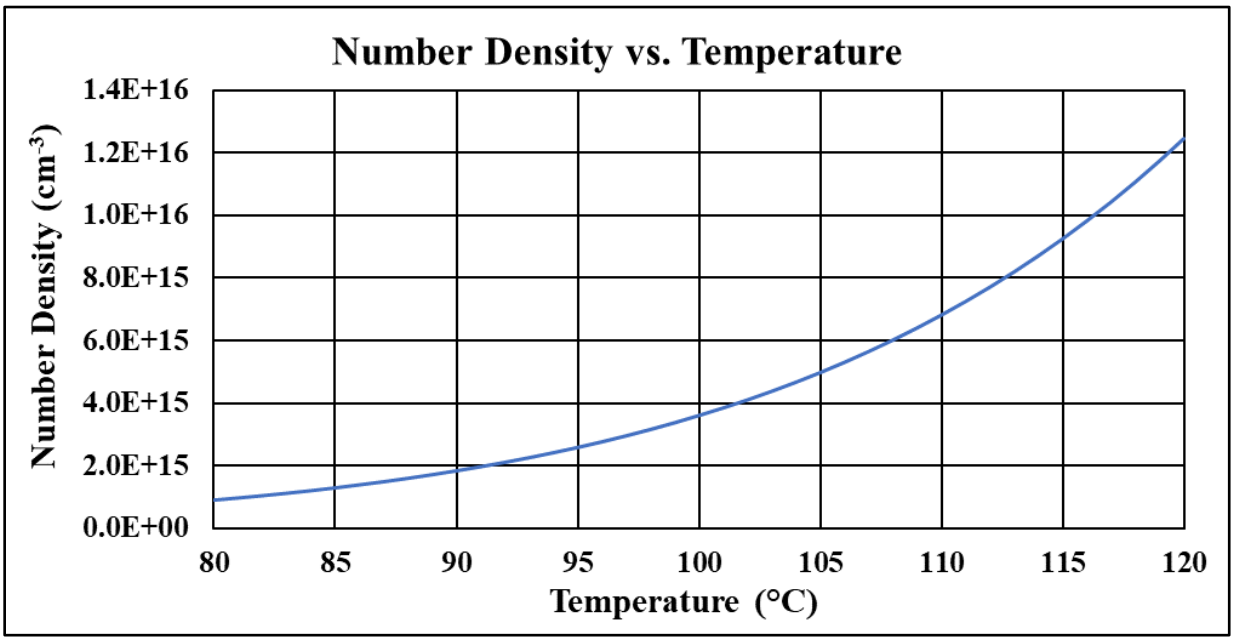

Fig. 5.15: Number density of rubidium atoms versus temperature, plotted using Equation 5.15

Evidently the number density *also* doubles every 10-12 degrees Celsius, which implies that $\frac{d\chi_{R(PROBE)}}{df}$ (and therefore $\chi_{R(PROBE)}$) is proportional to number density. Therefore, we conclude

that temperature dependence of the laser FSR arises from linear proportionality between number density and susceptibility.

The experiment characterizing the Raman lasing modes was valuable for two reasons: First, we were able to see over what range of frequencies the laser would operate. This is important when determining the range of detunings over which the Raman pumps which would realistically work. Second, understanding that the modes do not have equal spacing is an important practical consideration when designing the superluminal laser. During this experiment, we encountered some interesting and sometimes unexpected effects; it was important to understand these effects before moving on to the next step.

5.3 Demonstration of a Highly Subluminal Raman Laser

In Section 5.2, we saw reduction in the mode spacing of the Raman laser relative to the empty cavity free spectral range, which we determined to be the result of slow light effects arising from near-resonant Doppler-broadened dispersion. This dispersion, as mentioned previously, is the dispersion that would be seen by a *weak probe* whose frequency is equal to that of the lasing beam. This therefore does not prove that we demonstrated a *slow-light laser*; in order to do this, we would need to show that the *lasing beam itself* experiences slow light effects. Although we had not yet experimentally demonstrated this, we had reason to believe that the Raman laser would in fact be a slow-light laser because the Raman interaction linewidth, Γ_{RAMAN}, is very narrow (~1 MHz), which corresponds to steep positive dispersion via the Kramers-Kronig relations.

Until now, this thesis has been mainly focused on *fast-light* lasers, but *slow-light* lasers also have important applications. As opposed to fast-light lasers which are *more* sensitive to cavity-length fluctuations by a factor of ${n_g}^{-1}$, slow-light lasers are *less* sensitive to these fluctuations by the same factor. This makes them an ideal candidate for passive frequency stabilization applications. Another interesting and potentially very important aspect of the subluminal laser is that its quantum noise limited linewidth (the Schawlow-Townes linewidth) is expected to be smaller than that of a conventional laser by a factor of ${n_g}^{2}$. This conclusion is based on the argument that the energy flow rate is proportional to the group velocity, v_g [60]. However, as shown in Reference 61, this relationship is not valid when the dispersion is anomalous, so that this expected dependence of the Schawlow-Townes linewidth on n_g only applies when $n_g \geq 1$. Therefore, a highly subluminal laser has the potential to find important applications in laser stabilization as well as high-precision metrology.

One of the constraints in using Raman gain to make a slow-light laser is that the linewidth of the gain, which should be narrow in order to produce substantial n_g, tends to increase with increasing value of peak gain. This dependence can be understood by noting that the effective population inversion between the $S_{1/2}$ hyperfine states, is produced via optically pumping atoms from one of these states to the other. This rate of optical pumping serves as an effective decay rate, which, along with collisional dephasing rate of the coherence between the $S_{1/2}$ hyperfine states, determines the width of the Raman gain. In order to circumvent this constraint, we, in Reference 53, proposed a design for a slow-light laser where Raman gain produced in an alkali vapor cell is combined with the DPAL gain, which, as shown in Chapter 4, is very strong and broad. In such a system, a high output power laser can be produced while still achieving a significant SSF. Aside from the obvious utility of high output power, it should also be noted that the Schawlow-Townes linewidth decreases with increasing power. Thus, such a hybrid system should still be the preferred method for making a slow-light laser. The experiment, which will be described in the next section, is meant to establish the value of sensitivity reduction (and therefore the factor of n_g) that can be achieved using the Raman gain by itself.

5.3.1 Experimental Setup

The Raman laser makes use of ^{85}Rb vapor inside the same four-mirror resonator from Sections 5.1 and 5.2. The relevant energy levels, as shown in Figure 5.16(a), are denoted as follows: $|1\rangle \equiv S_{1/2}(F=2)$; $|2\rangle \equiv S_{1/2}(F=3)$; $|3\rangle \equiv P_{1/2}$ manifold; $|4\rangle \equiv P_{3/2}$ manifold. The optical pump couples $|2\rangle$ to $|4\rangle$ in order to transfer atoms from $|2\rangle$ to $|1\rangle$, which results in an effective decay rate from $|2\rangle$ to $|1\rangle$, as indicated in Figure 5.16(b), and therefore creates Raman population

inversion between these two states. The Raman pump is applied on the $|1\rangle \rightarrow |3\rangle$ transition with a detuning of Δ_{RP}, thus producing Raman gain on the $|2\rangle \rightarrow |3\rangle$ transition. If a probe is applied on this transition with a detuning of Δ_L, then the gain is maximized under the condition of two-photon resonance: $\delta \equiv \Delta_L - \Delta_{RP} = 0$. The Raman gain linewidth, which is the range of values of δ over which the Raman laser operates, is on the order of 1 MHz, as demonstrated throughout Chapter 4. At experimental temperatures (~100°C), the optical transitions are Doppler-broadened with a FWHM of ~560 MHz. Since the Raman gain linewidth is much narrower than this, the probe gain is far higher when it is co-propagating with the Raman pump than when it is counter-propagating, as discussed in Section 5.1, causing the laser to operate in the same direction as the Raman pump.

It is important to note that in Figure 5.16, the Raman pump and the optical pump are on the $S_{1/2}(F=2) \rightarrow P_{1/2}$ and $S_{1/2}(F=3) \rightarrow P_{3/2}$ transitions, respectively, resulting in lasing on the $S_{1/2}(F=3) \rightarrow P_{1/2}$ transition. In what follows, this will be referred to as "configuration A". However, a subluminal laser can just as easily be realized by placing the Raman pump and the optical pump on the $S_{1/2}(F=3) \rightarrow P_{1/2}$ and $S_{1/2}(F=2) \rightarrow P_{3/2}$ transitions, respectively, resulting in lasing on the $S_{1/2}(F=2) \rightarrow P_{1/2}$ transition; this will be referred to as "configuration B". It is also important to note that there are two hyperfine levels in the $P_{1/2}$ manifold (F=2 and F=3, which are split by approximately 362 MHz). Throughout the rest of this chapter, Δ_{RP} will be defined as the Raman pump detuning relative to the *midpoint* between these two hyperfine levels.

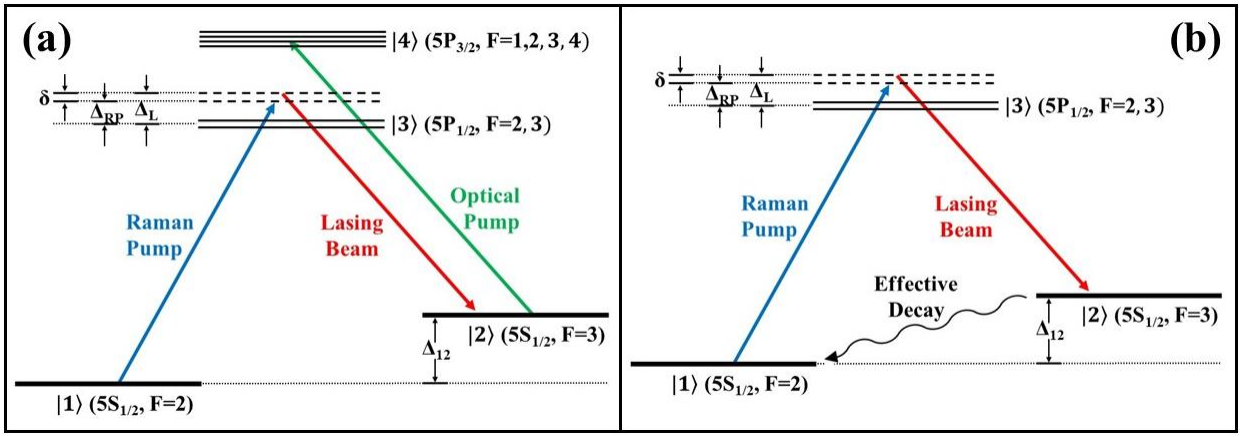

Fig. 5.16: (a) Energy levels and optical fields involved in the Raman gain; (b) Energy levels and optical fields, with the optical pump modeled as an effective decay rate

The experimental setup is illustrated schematically in Figure 5.17. The Raman pump, generated from a Toptica DL-Pro 100 external cavity diode laser, is s-polarized and inserted into the lasing cavity using a polarizing beam splitter (PBS). It is then expelled from the cavity using another PBS, after passing through a vapor cell containing isotopically pure ^{85}Rb atoms. The optical pumping beam, generated from a Photodigm DBR diode laser, is also s-polarized, and is inserted into and expelled from the cavity using the same pair of PBS's, but in the opposite direction. The cavity is a square with a perimeter of one meter. A lens with focal length of 750 cm is used to stabilize the cavity. The minimum waist size of the lasing mode occurs exactly opposite the location of the lens; an iris is placed at that location to spatially filter out all transverse modes besides the TEM_{00} mode. A beam splitter (BS) diverts a small fraction of the Raman pump, which is combined with the Raman laser output and sent into a photodetector (PD); the resulting beat note has a frequency of:

$$f_B = f_{RP} - f_L = \Delta_{12} - \delta \tag{5.16}$$

where Δ_{12} is the hyperfine splitting between the F=2 and F=3 ground states in ^{85}Rb, which is approximately 3.0357 GHz. In order to scan the cavity length, one of the cavity mirrors is attached

to a piezo-electric transducer (PZT). The Raman pump frequency remains fixed while the mirror position is scanned, which causes the beat frequency to change accordingly. The PD converts this beat note into an electrical signal, which is heterodyned with a stable reference signal with a frequency 3.2 MHz less than Δ_{12}. The output of the heterodyning process therefore has a frequency centered around 3.2 MHz, which is then demodulated to produce a DC voltage proportional to the frequency. Having a 3.2 MHz central frequency enables us to distinguish between positive and negative values of δ, provided that δ remains above -3.2 MHz ($|\delta|$ is less than the Raman gain width, which is ~1 MHz, so this should always be the case).

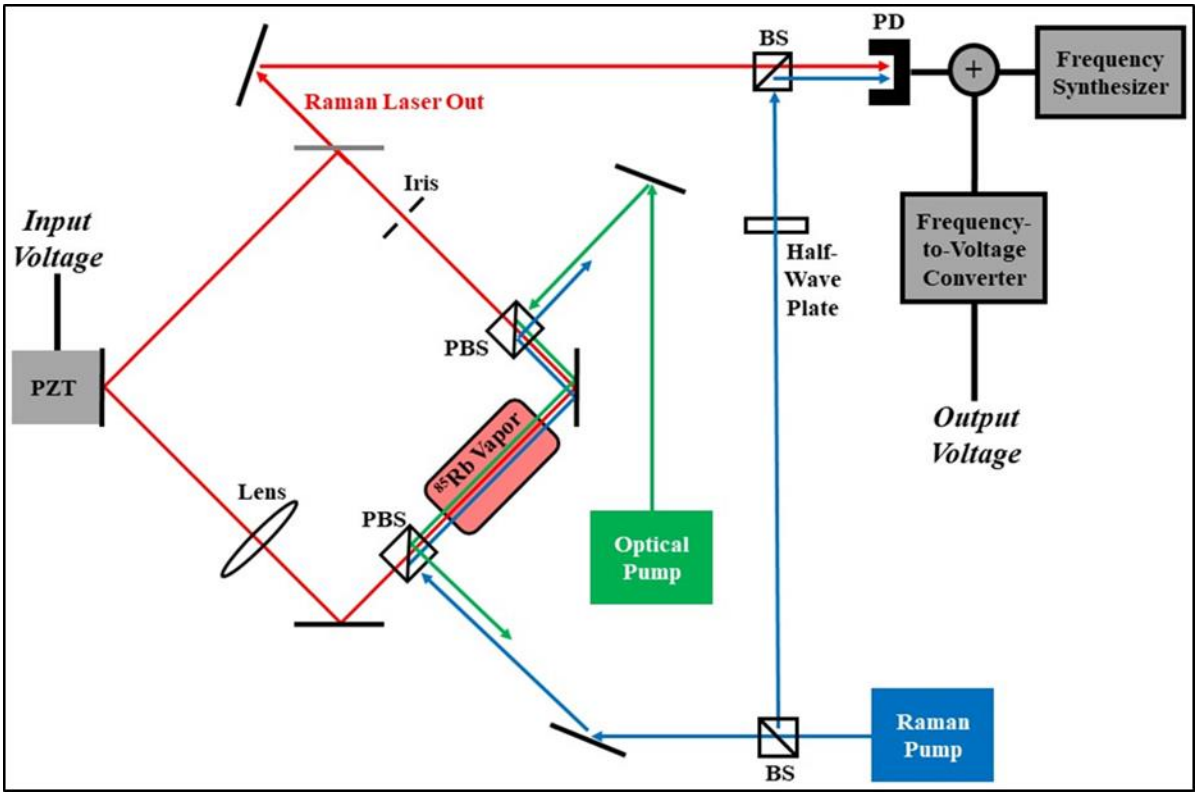

Fig. 5.17: Schematic of the system used to measure the Raman laser frequency shift versus cavity length change

5.3.2 Experimental Results

Two examples of plots showing input voltage (proportional to length change) versus output voltage (proportional to frequency shift) are shown in Figures 5.18(a) and 5.18(b). Such plots are used to determine the laser frequency sensitivity to length change, which is compared with the sensitivity of an empty cavity to determine the factor of sensitivity suppression. This factor is inferred to be equal to the laser group index, n_g.

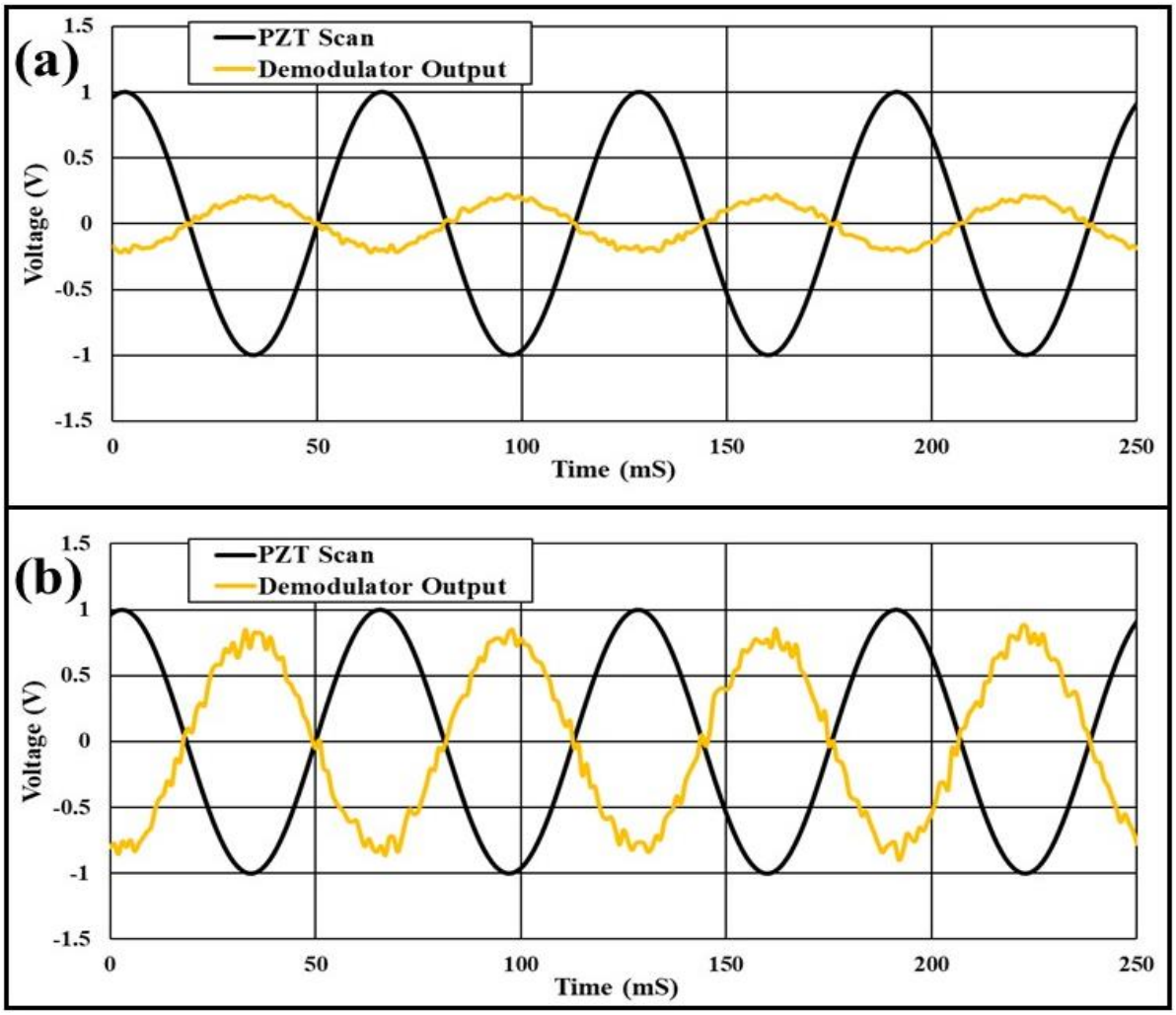

Fig. 5.18: (a) One example of an oscilloscope measurement produced by this experiment. The black curve is the PZT input voltage, while the curve is the demodulator output voltage; (b) Another example of a scope measurement. Though the peak-to-peak input voltage is the Same as in (a), the peak-to-peak output voltage is larger in (b), indicating *higher* sensitivity to cavity length changes, or lower *suppression* of sensitivity.

There are several experimental parameters which have the potential to affect the *Sensitivity Suppression Factor* (SSF) of the laser. Accordingly, the laser sensitivity was measured for many combinations of output coupler reflectivity, configuration, temperature, Raman pump power, optical pump power, and Raman pump detuning. Table 5.2 is a summary of the results from this experiment.

OC Refl. (%)	Configuration	Temp (°C)	RP Power (mW)	OP Power (mW)	Δ_{RP} (MHz)	SSF
50	A	85	2.1	200	-1264	70.7
50	A	85	2.1	200	-903	109.0
50	A	85	2.1	200	1433	545.0
50	A	85	2.1	200	1088	663.0
50	A	90	2.1	200	-1553	68.0
50	A	90	2.1	200	-1164	97.1
50	A	90	2.1	200	-855	134.1
50	A	90	2.1	200	2134	191.8
50	A	90	2.1	200	1880	242.1
50	A	90	2.1	200	-624	242.3
50	A	90	2.1	200	1911	243.4
50	A	90	2.1	200	1586	277.8
50	A	90	2.1	200	1627	319.0
50	A	90	2.1	200	1256	333.4
50	A	90	2.1	200	998	425.9
50	A	90	2.1	200	1310	463.0
50	A	100	2.1	200	-2091	65.5
50	A	100	2.1	200	-1681	80.3
50	A	100	2.1	200	-1304	114.2
50	A	100	2.1	200	-974	165.1
50	A	100	2.1	200	-717	240.9
50	A	100	2.1	200	1715	341.5
50	A	100	2.1	200	1447	396.9
50	A	100	2.1	200	1186	479.6
50	A	105	2.1	200	-1660	79.8
50	A	105	2.1	200	-1327	100.8
50	A	105	2.1	200	-1059	138.9

50	A	105	2.1	200	-847	203.8
50	A	105	2.1	200	-701	318.3
50	A	115	2.1	200	-1585	72.3
50	A	115	2.1	200	-1318	103.9
50	A	115	2.1	200	-1099	146.2
50	A	115	2.1	200	-932	193.4
50	A	115	2.1	200	-806	254.9
50	A	125	2.1	200	-1388	93.7
50	A	125	2.1	200	-1225	117.8
50	A	125	2.1	200	-1082	145.0
50	A	125	2.1	200	-966	154.6
50	A	125	2.1	200	-877	221.7
80	A	90	12.2	27	-2006	8.3
80	A	90	12.2	27	-1581	13.5
80	A	90	12.2	27	-1199	23.2
80	A	90	12.2	27	-897	27.5
80	A	90	12.2	27	-681	31.9
80	A	100	2.1	200	2013	155.7
80	A	100	2.1	200	1589	164.0
80	A	100	2.1	200	1817	175.5
80	A	100	2.1	200	1340	223.9
80	A	100	2.1	200	1092	244.8
80	A	100	2.1	200	875	421.3
80	A	100	12.2	58	-2335	11.6
80	A	100	12.2	58	-1950	13.2
80	A	100	12.2	58	-1591	17.4
80	A	100	12.2	58	-1295	23.2
80	A	100	12.2	58	-1044	24.6
80	A	100	12.2	58	-865	27.5
80	A	115	2.1	27	1243	64.1
80	A	115	2.1	27	1389	66.3
80	A	115	2.1	27	1102	66.8
80	A	115	2.1	27	975	75.9
80	A	115	2.1	27	872	81.1
80	A	115	2.1	58	-1698	84.9
80	A	115	2.1	58	-1455	91.3
80	A	115	2.1	58	-1263	98.7
80	A	115	2.1	58	-1114	123.0
80	A	115	2.1	58	-992	131.2
80	A	115	2.1	58	-894	174.7

80	A	115	12.2	58	-2326	9.7
80	A	115	12.2	58	-1990	17.5
80	A	115	12.2	58	-1673	18.8
80	A	115	12.2	58	-1418	20.0
80	A	115	12.2	58	-1042	22.6
80	A	115	12.2	58	-1207	26.2
80	A	115	12.2	58	-911	28.4
80	A	115	12.2	58	-796	81.1
80	A	130	12.2	200	-1911	20.3
80	A	130	12.2	200	-1704	25.3
80	A	130	12.2	200	-1519	35.3
80	A	130	12.2	200	-1364	48.5
80	A	130	12.2	200	-1237	53.8
80	A	130	12.2	200	-1122	70.7
80	A	130	12.2	200	-1027	80.7
80	A	130	12.2	200	-944	95.2
80	B	90	2.5	58	2216	37.8
80	B	90	2.5	58	1791	67.3
80	B	90	2.5	58	1390	111.3
80	B	90	2.5	58	1030	187.9
80	B	100	2.5	58	2546	35.9
80	B	100	2.5	58	2146	47.1
80	B	100	2.5	58	1753	71.3
80	B	100	2.5	58	1395	122.0
80	B	100	2.5	58	-1284	171.0
80	B	100	2.5	58	-1046	187.4
80	B	100	2.5	58	-836	244.2
80	B	100	2.5	58	1100	247.6
80	B	115	2.5	58	2375	56.9
80	B	115	2.5	58	2043	82.9
80	B	115	2.5	58	1728	126.0
80	B	115	2.5	58	1456	184.0
80	B	115	2.5	58	1227	276.6
80	B	115	2.5	58	1045	376.2
80	B	115	2.5	200	-1366	260.9
80	B	115	2.5	200	-1198	269.1
80	B	115	2.5	200	-766	272.5
80	B	115	2.5	200	-887	277.8
80	B	115	2.5	200	-668	279.0
80	B	115	2.5	200	-1037	281.4

80	B	115	2.5	200	-1533	285.1
80	B	130	2.5	58	2020	44.5
80	B	130	2.5	58	2242	44.9
80	B	130	2.5	58	1812	51.1
80	B	130	2.5	58	1626	58.7
80	B	130	2.5	58	1468	69.5
80	B	130	2.5	550	2014	35.9
80	B	130	2.5	550	1758	40.9
80	B	130	2.5	550	1533	45.3
80	B	130	2.5	550	1347	53.4

Table 5.2: Sensitivity Suppression Factor (SSF) measured for many combinations of output coupler reflectivity, configuration, temperature, Raman pump power, optical pump power, and Raman pump detuning

Table 5.2 shows that the Raman laser exhibited values of SSF as low as 8.3 and high as 663. Therefore, our intuition that the narrow Raman gain could result in significant sensitivity suppression seems plausible. In addition, the experimental parameters clearly have a significant effect on the value of the SSF.

To get a better sense of how the SSF is affected by various parameters, we need to plot some of the data from Table 5.2. Figure 5.19 illustrates how the temperature and the Raman pump detuning affect the SSF. All the data in Figure 5.19 were taken with the optical fields in configuration B, 2.5 mW Raman pump power, 58 mW optical pump power, and 80% output coupler reflectivity. At a given cell temperature, the SSF evidently increases as resonance is approached; however, when too close to resonance, lasing cannot occur due to increased absorption resulting from the proximity to the optical transition. The inset figure shows the SSF versus temperature at Δ_{RP}=1800 MHz and Δ_{RP}=2100 MHz. The SSF increases as temperature increases from 100°C to 115°C, but then decreases from 115°C to 130°C and then to 145°C. The SSF is therefore maximized at some temperature, T_{MAX}, which in this case is somewhere between

100°C and 130°C. In general, T_{MAX} can depend on many factors such as Raman pump intensity, optical pump intensity, output coupler reflectivity, and configuration.

In order to interpret this behavior qualitatively, we note that the number density doubles approximately every 10-12°C in the experimental temperature range, which was shown in Figure 5.15. In Section 5.2, we saw that the susceptibility of a *weak probe* is proportional to number density. However, this does not hold in the lasing regime where nonlinearities occur due to high intensities, and where the Raman pump, optical pump, and lasing beam become mostly or completely absorbed when the number density becomes too high. Absorption of these beams causes a decrease in the total overlap between the lasing mode and the Raman and optical pumps, thus reducing the effective susceptibility experienced by the laser.

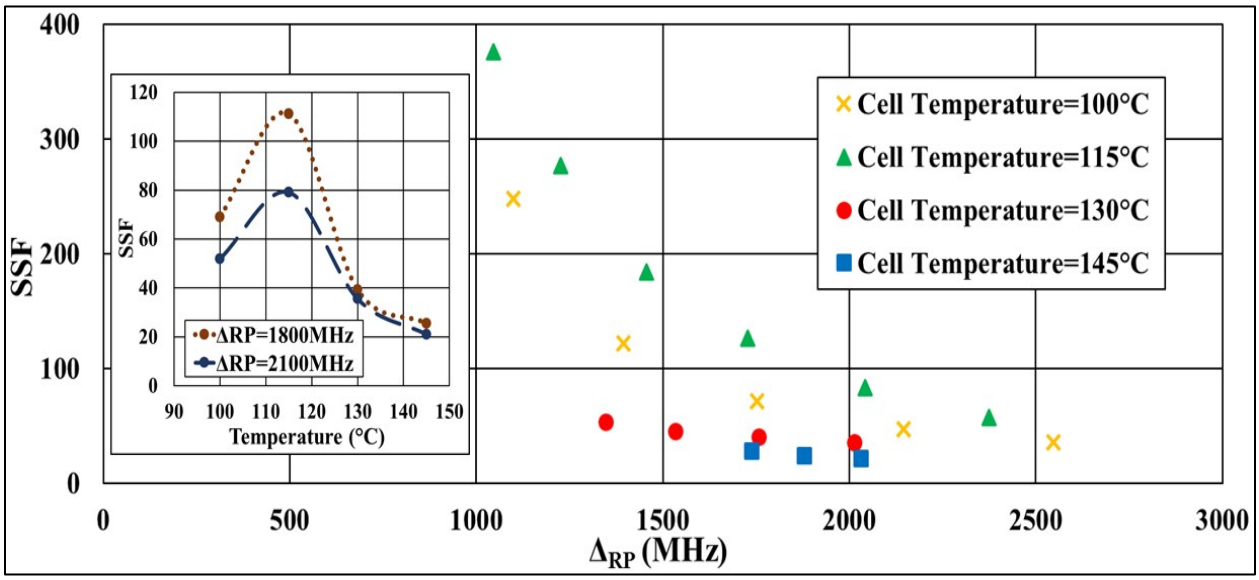

Fig. 5.19: Measured values of SSF versus Δ_{RP} at four different temperatures. These data were then used to create the inset plots of SSF versus temperature at Δ_{RP}=1800 and Δ_{RP}=2100 MHz.

Figure 5.20 shows one example of how the SSF and the output power are affected by the power of the Raman pump. The data in Figure 5.20 were taken with the energy levels in configuration A, 115°C cell temperature, 58 mW optical pump power, and 80% output coupler

reflectivity. For this set of data, the Raman pump detuning is negative. Consider first the behavior of the output power. With stronger Raman pump power, the output power is significantly higher, and lasing occurs over a wider range of Δ_{RP}, as expected. It is also evident that in this case there is an optimal Raman pump detuning that produces maximum output power. This is due to the fact that Raman gain increases as the Raman pump approaches resonance, but so does Doppler-broadened absorption of the Raman pump and the lasing beam. These two competing effects determine the detuning at which maximum lasing power is achieved. Consider next the behavior of the SSF. For a given value of Δ_{RP}, the value of the SSF is approximately 4 to 6 times higher for the weaker Raman pump. This behavior can be understood qualitatively by noting that the width of the Raman gain is power broadened for a strong Raman pump, thus decreasing the slope of the dispersion.

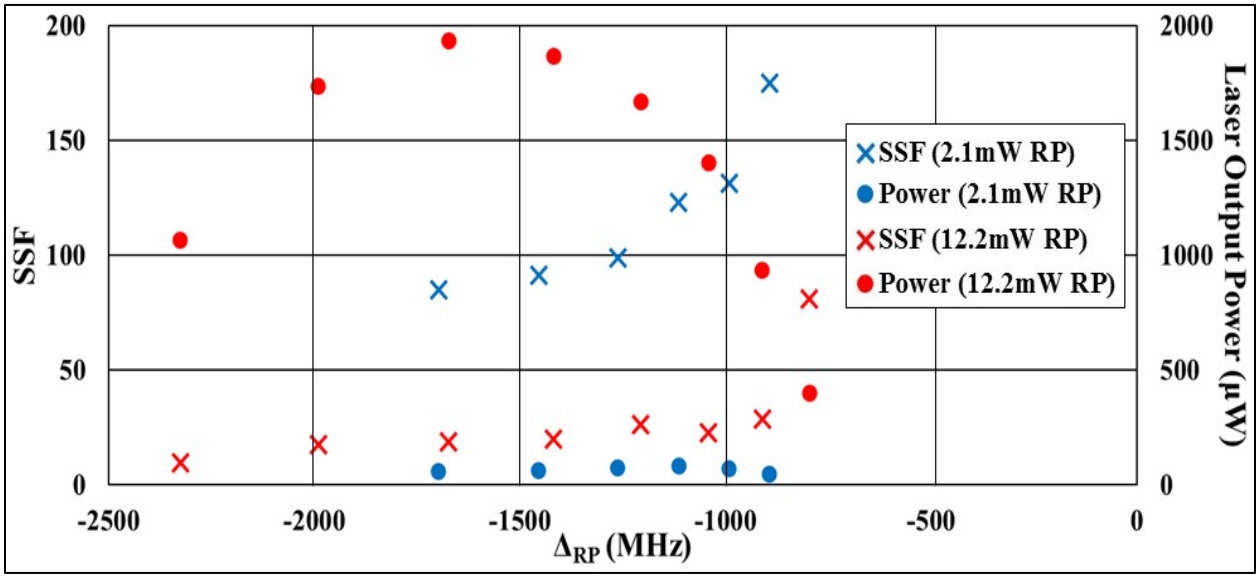

Fig. 5.20: SSF (left axis) and output power (right axis) vs. detuning, using two different values of Raman pump power

Figure 5.21 compares data obtained with a 50% reflectivity output coupler (OC) to that obtained with an 80% reflectivity OC. The data in Figure 5.21 were taken with the energy levels

in configuration A, 115°C cell temperature, 200 mW optical pump power, and 2.1 mW Raman pump power. For all values of Raman pump detuning, the OC reflectivity does not appear to make a significant difference in the SSF. However, the OC with the lower reflectivity enables operation of the laser at a value of $|\Delta_{RP}|$ that is closer to resonance. Since SSF increases as the Raman pump approaches resonance, the highest achievable SSF with the 50% OC was greater than that with the 80% OC.

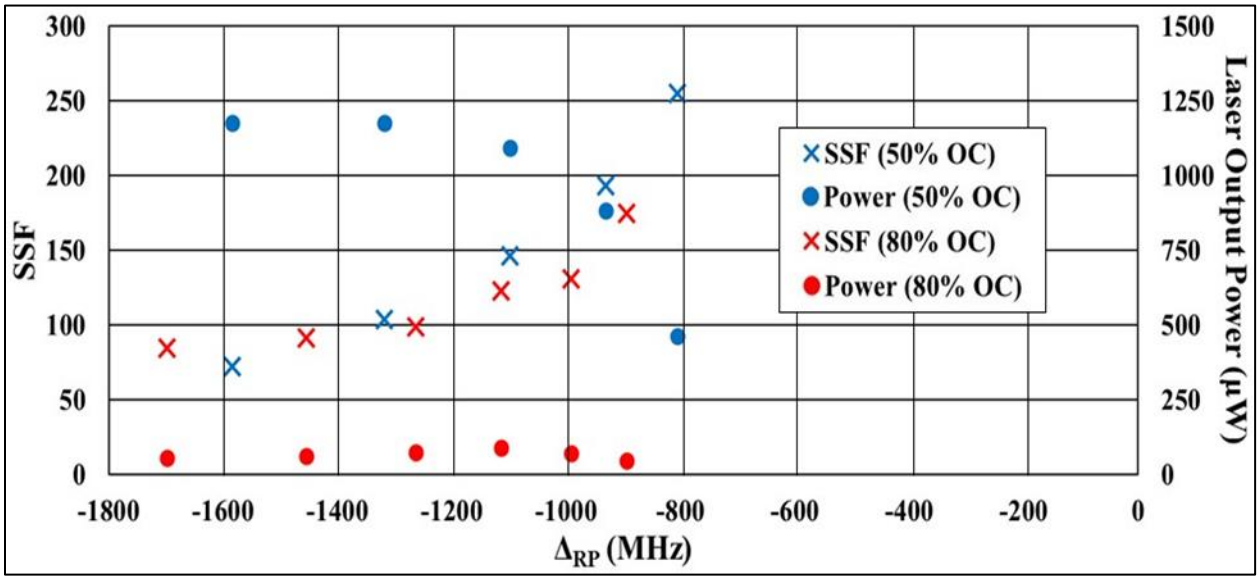

Fig. 5.21: SSF (left axis) and output power (right axis) vs. detuning, using two different output coupler reflectivities

The highest SSF achieved during the experiment (with a value of 663) is presented in Figure 5.22, which also shows that the SSF is not symmetric with respect to the sign of Δ_{RP}. All the data in Figure 5.22 were taken with the energy levels in configuration A, 200 mW optical pump power, 2.1 mW Raman pump power, and a 50% OC. We generally see larger values of SSF for positive Δ_{RP} than for negative Δ_{RP}, despite the fact that the laser is able to operate closer to resonance for negative Δ_{RP}. Additionally, T_{MAX} appears to depend on the sign of Δ_{RP}; 85°C yielded the lowest values of SSF for negative Δ_{RP}, but yielded the highest values for positive Δ_{RP}.

These asymmetries are possibly due to the fact that states $|1\rangle$, $|2\rangle$, and $|3\rangle$ contain five, seven, and twelve Zeeman sub-levels, respectively. Each sub-level has its own unique matrix element and therefore contributes differently to the two-photon gain and lasing processes for different signs of Δ_{RP}.

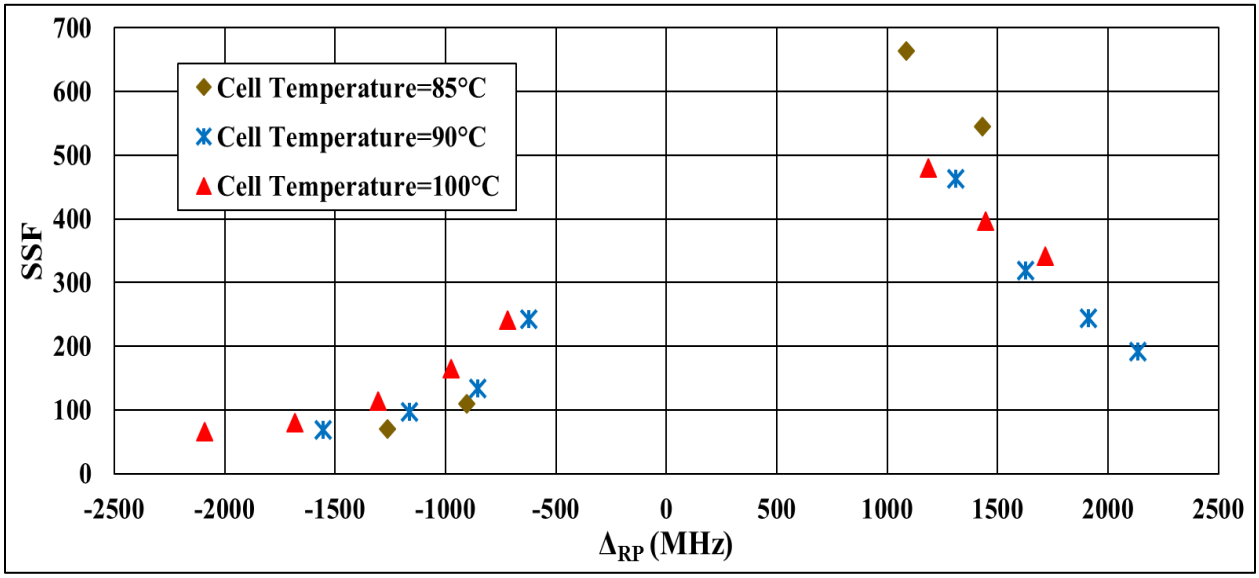

Fig. 5.22: SSF vs. detuning, for positive and negative values of Δ_{RP}, at three different temperatures

One ubiquitous effect is that for all combinations of experimental parameters, the SSF increases as the Raman pump approaches resonance. There are two factors which possibly cause this universal trend: the positive dispersion profile outside of a Doppler-broadened resonance, and narrowing of two-photon laser gain as Δ_{RP} and Δ_L approach zero. It is not clear as to how much each effect contributes to the effective dispersion of the lasing beam; however, the simulations, described in the next section, agree with this trend.

There were two more parameters considered during this experiment: optical pump power and configuration. While the optical pump power affects the output power of the laser, it does not

appear to affect the SSF drastically. Meanwhile, configuration does not appear to make a significant difference in the output power nor the SSF.

As previously mentioned, the Schawlow-Townes Linewidth of a subluminal laser is predicted [60,61] to be reduced by a factor of $n_g{}^2$ relative to a conventional laser. The standard formula for the full-width half maximum (FWHM) Schawlow-Townes linewidth, without considering the effect of dispersion, is:

$$\Gamma_{ST} = \frac{\hbar\omega_o}{2P_{OUT}{\tau_C}^2} \tag{5.17}$$

where ω_o is the laser (angular) frequency, P_{OUT} is laser output power, and τ_C is the empty cavity decay time, which is given by:

$$\tau_C = \frac{R^{1/4}L}{c\left(1-\sqrt{R}\right)} \tag{5.18}$$

where R is the intensity reflectivity of the output coupler. For a laser with R=0.5 and P_{OUT}=400 μW, the value of Γ_{ST} is ~3.52 Hz. For n_g=663, assuming a suppression factor of $n_g{}^2$, the value of Γ_{ST} would be ~7.5 μHz. To reach this linewidth, the cavity must be highly stabilized in order to suppress all sources of classical noise. We are currently working on implementing advanced techniques that may enable us to reach a degree of stability high enough to measure such a small linewidth, directly or indirectly.

5.3.3 Comparison with Simulation

Because of the numerous variables and interconnected processes occurring in the subluminal laser (AC Stark shifts, Doppler broadening, spectral hole burning, etc.), numerical methods are necessary to provide a quantitative model of the laser behavior. Our simulation solves

the single-mode laser equations and the density matrix equations in an iterative fashion until a steady-state solution is reached, just as it was done in the case of the superluminal DPAL. The MATLAB code for this simulation is included in Appendix B.

In the single-mode laser equations, χ is the effective susceptibility experienced by the lasing beam during one round trip. The gain cell in the experiment was 8 cm long while the cavity perimeter was 60 cm, so that only ~13% of the cavity was filled with gain. Because χ depends on the total number of atoms interacting with the lasing beam in one round trip, the calculation assumes that the gain medium fills the entire cavity with a number density equal to ~13% of the gain cell number density. This also means that the group index experienced by the lasing beam *inside the vapor cell* is ~7.5 times the SSF. For example, when the SSF of the subluminal laser was measured to be 663, the group index of the gain cell was almost 5,000.

The Optical Bloch equation, describing the evolution of the gain medium, is:

$$\frac{\partial \tilde{\rho}}{\partial t} = -\frac{i}{\hbar}\left[\widetilde{H}, \tilde{\rho}\right] + \frac{\partial \tilde{\rho}_{SOURCE}}{\partial t} \tag{5.19}$$

where $\tilde{\rho}$ and $\widetilde{H}$ are the density matrix of the atoms, and the modified Hamiltonian that includes the effect of population decays, respectively, in the rotating wave basis. The source term accounts for the influx of atoms into the relevant atomic states. Figure 5.23(a) shows how the three-level system is modeled in configuration B. The optical pump is treated as a decay rate from $|1\rangle$ to $|2\rangle$, denoted as Γ_{OP}. The lasing beam couples states $|1\rangle$ and $|3\rangle$ while the Raman pump couples states $|2\rangle$ and $|3\rangle$ with coupling strengths (i.e. Rabi frequencies) of Ω_L and Ω_{RP}, respectively. The natural decay rate from state $|i\rangle$ to $|j\rangle$ is denoted as Γ_{ij} (for $i,j = 1, 2, 3$). The susceptibility of the lasing beam, χ_L, is governed by the following relationship:

$$\chi_L = \tilde{\rho}_{31}\left(\frac{\hbar cn}{I_{SAT(13)}\Omega_L}\right)\left(\frac{\Gamma_{31}}{2}\right)^2 \tag{5.20}$$

where n is atomic number density and $I_{SAT(13)}$ is the effective saturation intensity of the $|1\rangle \rightarrow |3\rangle$ transition, which is approximately 8.35 mW/cm^2. The algorithm then solves the single-mode laser equations and Optical Bloch equation in an iterative fashion until a steady-state solution is reached. To compute the SSF, this calculation must be performed for two different cavity roundtrip lengths: $L_o - \frac{dL}{2}$ and $L_o + \frac{dL}{2}$, where L_o is the initial cavity length and dL is a small perturbation in length. The sensitivity of this laser, df/dL, is compared to that of the empty cavity to determine the SSF. Figure 5.23(b) shows two examples of the simulation output.

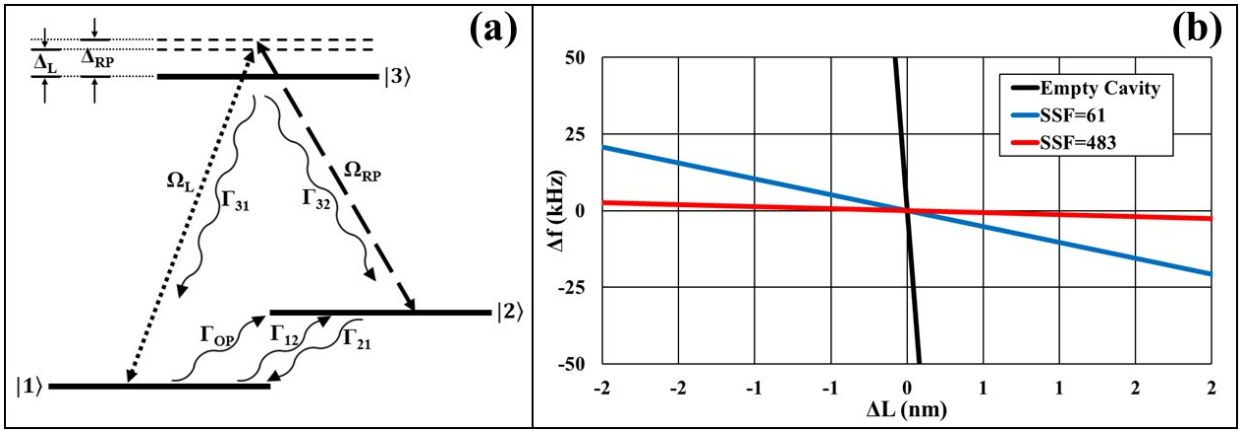

Fig. 5.23: (a) Energy levels, coupling fields, and decay rates used in the simulation, corresponding to configuration B; (b) The SSF is the ratio between the "empty cavity" slope (df_{EC}/dL) and the laser output slope (df/dL).

Figure 5.24 compares simulation results with experimental results for the following set of parameters: 2.5 mW Raman pump power, 58 mW optical pump power, 80% output coupler reflectivity, 115°C cell temperature, configuration B. There appears to be good qualitative match, showing increasing SSF as resonance is approached. There are several potential reasons why simulation results do not match up more accurately with experimental results. First, we use a three-

level model, where the optical pump is treated as a decay rate. In reality, states $|1\rangle$ and $|2\rangle$ contain five and seven Zeeman sublevels, respectively; state $|3\rangle$ contains two hyperfine levels, which contain 12 Zeeman sublevels in total; state $|4\rangle$ contains four hyperfine levels, which contain 24 Zeeman sublevels in total. Therefore, the experimental process corresponds to a 48-level system. The matrix used in the algorithm has dimensions of $N^2 \times N^2$ (where N is the number of energy levels), so that a 48-level system is $(48/3)^4$=65536 times as data-intensive as a three-level system, which takes typically 30 seconds to solve. Another limitation is the assumption that each optical field couples only two energy levels. For example, the Raman pump [Fig. 5.23(a)] is assumed to couple states $|2\rangle$ and $|3\rangle$, but not states $|1\rangle$ and $|3\rangle$. This is not entirely true, but the Rotating-Wave Approximation relies on this assumption. In principle, this constraint can be circumvented by using the Floquet technique where the solution is made up of a truncated set of harmonics [54]; however, for the iterative algorithm employed here, this process would be prohibitively time-consuming.

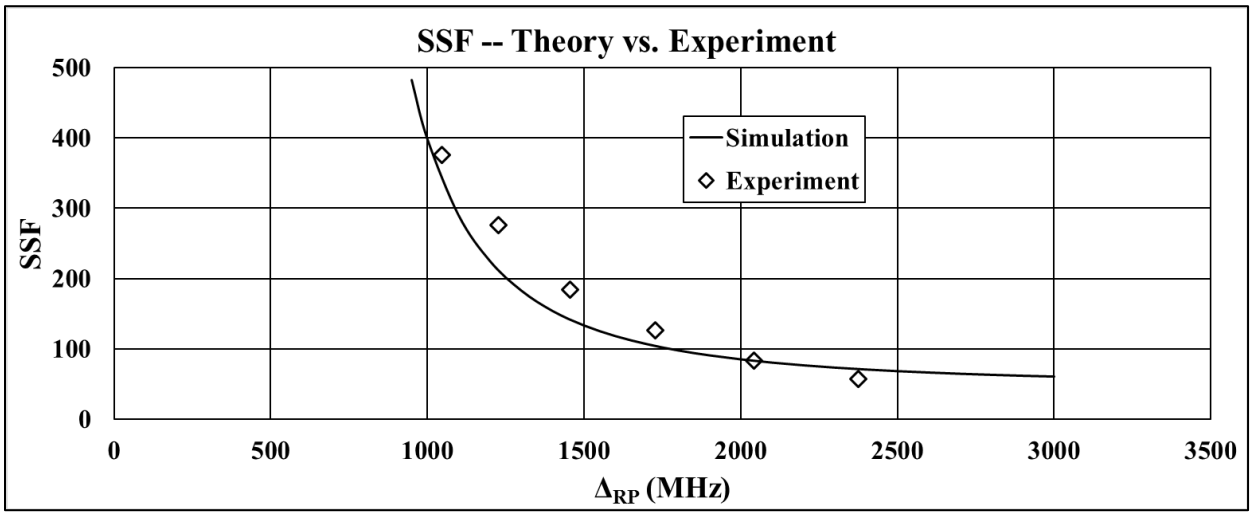

Fig. 5.24: SSF versus Δ_{RP} -- comparison between simulation and experiment

CHAPTER 6

CONCLUSION

In this thesis, we demonstrated a highly superluminal Diode-Pumped Alkali Laser (DPAL) in which the intra-cavity lasing beam experienced Raman depletion, and in which the sensitivity to perturbations was enhanced by a factor as high as 190 relative to a conventional laser interferometer. We also demonstrated a Raman laser in which the mode spacing, and more importantly the intra-cavity lasing beam itself, exhibited significant subluminal effects. This Raman laser was shown to be highly insensitive to perturbations, with reduction in sensitivity reaching factors as high as 663 relative to a conventional laser interferometer.

The *superluminal* effect observed in the DPAL results in enhanced sensitivity which can be used for high-sensitivity optical metrology. On the other hand, the *subluminal* effect in the Raman laser serves as a stabilization mechanism while simultaneously reducing the quantum-limited noise linewidth in a laser, so that a subluminal laser can be used as an ultra-precise frequency reference for applications such as atomic clocks.

REFERENCES

[1] A.A. Michelson and E.W. Morley, “On the Relative Motion of the Earth and the Luminiferous Ether,” American Journal of Science, 34: 333–345 (1887).

[2] F.T. Trouton and H.R. Noble, “The mechanical forces acting on a charged electric condenser moving through space,” Philosophical Transactions of the Royal Society A 202, 165–181 (1903).

[3] F.T. Trouton and H.R. Noble, “The Forces Acting on a Charged Condenser moving through Space,” Proceedings of the Royal Society 74 (479): 132-133 (1903).

[4] Lord Rayleigh, “Does Motion through the Aether cause Double Refraction?”, Philosophical Magazine, 4: 678–683 (1902).

[5] D.B. Brace, “On Double Refraction in Matter moving through the Aether,” Philosophical Magazine, 7 (40): 317–329 (1904).

[6] H.A. Lorentz, “Electromagnetic phenomena in a system moving with any velocity smaller than that of light,” Proceedings of the Royal Netherlands Academy of Arts and Sciences, 6: 809–831 (1904).

[7] J. Larmor, “On the ascertained Absence of Effects of Motion through the Aether, in relation to the Constitution of Matter, and on the FitzGerald-Lorentz Hypothesis,” Philosophical Magazine, 7 (42): 621–625 (1904).

[8] B.P. Abbott et. al., “Observation of Gravitational Waves from a Binary Black Hole Merger,” Physical Review Letters 116, 061102 (2016).

[9] C.W. Misner, K.S. Thorne, J.A. Wheeler, *Gravitation*. W.H. Freeman, 1970. Print.

[10] R.B. Hurst, J-P.R. Wells, and G.E. Stedman, “An elementary proof of the geometrical dependence of the Sagnac effect,” Journal of Optics, 9 :838–841 (2007).

[11] M.S. Shahriar, G.S. Pati, R. Tripathi, V. Gopal, M. Messall, and K. Salit, “Ultrahigh enhancement in absolute and relative rotation sensing using fast and slow light,” Physical Review A 75, 053807 (2007).

[12] G. A. Sanders and S. Ezekiel, “Measurement of Fresnel drag in moving media using a ring-resonator technique,” Journal of the Optical Society of America 5(3): 674-678 (1988).

[13] G.E. Stedman, “Ring-laser tests of fundamental physics and geophysics,” Reports on Progress in Physics, 60(6): 615 (1997).

[14] D.J. Griffiths, *Introduction to Electrodynamics (3rd Edition)*. Prentice Hall, 1998. Print.

[15] R.L. Kronig, "On the theory of the dispersion of X-rays," Journal of the Optical Society of America, 12: 547–557 (1926).

[16] H.A. Kramers, "La diffusion de la lumière par les atomes," Transactions of Volta Centenary Congress, 2: 545–557 (1927).

[17] J.S. Toll, "Causality and the Dispersion Relation: Logical Foundations," Physical Review, 104: 1760–1770 (1956).

[18] R. Shankar, *Principles of Quantum Mechanics (2nd Edition)*. Springer US, 1994. Print.

[19] D.J. Griffiths, *Introduction to Quantum Mechanics (2nd Edition)*. Prentice Hall, 2005. Print.

[20] M.O. Scully and M.S. Zubairy, *Quantum Optics*, Cambridge University Press, 1997. Print.

[21] V. Weisskopf, E. Wigner, "Berechnung der natürlichen Linienbreite auf Grund der Diracschen Lichttheorie," Zeitschrift für Physik, 63(54) (1930).

[22] U. Fano, "Description of States in Quantum Mechanics by Density Matrix and Operator Techniques," Reviews of Modern Physics, 29: 74–93 (1957).

[23] B.C. Hall, *Quantum Theory for Mathematicians*. Springer, 2013. Print.

[24] F. T. Arecchi and R. Bonifacio, "Theory of Optical Maser Amplifiers," IEEE Journal of Quantum Electronics, 1: 169-178 (1965).

[25] A.L. Schawlow and C.H. Townes, "Infrared and optical masers," Physical Review, 112(6): 1940-1949 (1958).

[26] A.E. Siegman, *Lasers*. University Science Books, 1986. Print.

[27] N.R. Davidson, *Statistical Mechanics*. MacGraw-Hill, 1962. Print.

[28] W. Happer, Y. Jau, T. Walker, *Optically Pumped Atoms*. Wiley, 2010. Print.

[29] H.C. Bolton and G.J. Troup, "The modification of the Kronig-Kramers relations under saturation conditions," Philosophical Magazine 19(159), 477–485 (1969).

[30] G.J. Troup and A. Bambini, "The use of the modified Kramers-Kronig relation in the rate equation approach of laser theory," Physics Letters 45(5), 393–394 (1973).

[31] H.N. Yum and M.S. Shahriar, "Pump-probe model for the Kramers-Kronig relations in a laser," Journal of Optics 12(10), 104018 (2010).

[32] M. Sargent III, M.O. Scully, W.E. Lamb Jr., *Laser Physics*. Addison-Wesley, 1974. Print.

[33] H.N. Yum, M. Salit, J. Yablon, K. Salit, Y. Wang, and M.S. Shahriar, "Superluminal ring laser for hypersensitive sensing," Optics Express, 18(17), 17658-17665 (2010).

[34] G.S. Pati, M. Salit, K. Salit, and M.S. Shahriar, "Simultaneous slow and fast light effects using probe gain and pump depletion via Raman gain in atomic vapor," Optics Express 17(11), 8775–8780 (2009).

[35] W.F. Krupke, R.J. Beach, V.K. Kanz, and S.A. Payne, "Resonance transition 795-nm rubidium laser," Optics Letters 28(23), 2336–2338 (2003).

[36] T.A. Perschbacher, D.A. Hostutler, T.M. Shay, "High-efficiency diode-pumped rubidium laser: experimental results," Proceedings of the SPIE, 6346 (2007).

[37] J. Zweiback and W.F. Krupke, "28W average power hydrocarbon-free rubidium diode pumped alkali laser," Optics Express 18(2), 1444-1449 (2010).

[38] W.F. Krupke, R.J. Beach, V.K. Kanz, S.A. Payne, and J.T. Early, "New class of CW high-power diode-pumped alkali lasers (DPALs)," Proceedings of the SPIE, 5448 (2004).

[39] R.J. Beach, W.F. Krupke, V.K. Kanz, S.A. Payne, M.A. Dubinskii and L.D. Merkle, "End-pumped continuous-wave alkali vapor lasers: experiment, model, and power scaling," Journal of the Optical Society of America B 21(12), 2151-2163 (2004).

[40] B. Zhdanov and R.J. Knize, "Advanced diode-pumped alkali lasers," Proceedings of the SPIE, 7022 (2008).

[41] B.V. Zhdanov and R.J. Knize, "Progress in Alkali lasers development," Proceedings of the SPIE, 6874 (2008).

[42] S.S.Q. Wu, T.F. Soules, R.H. Page, S.C. Mitchell, V.K. Kanz, and R.J. Beach, "Hydrocarbon-free resonance transition 795-nm rubidium laser," Optics Letters 32(16), 2423-2425 (2007).

[43] J. Yablon, Z. Zhou, M. Zhou, Y. Wang, S. Tseng, and M.S. Shahriar, "Theoretical modeling and experimental demonstration of Raman probe induced spectral dip for realizing a superluminal laser," Optics Express 24(24), 27444-27456 (2016).

[44] T. Skettrup, T. Meelby, K. Færch, S.L. Frederiksen, and C. Pedersen, "Triangular laser resonators with asigmatic compensation," Applied Optics 39(24), 4306-4312 (2000).

[45] M.S. Shahriar, P. Hemmer, D.P. Katz, A. Lee, and M. Prentiss, "Dark-state-based three-element vector model for the stimulated Raman interaction," Physical Review A 55, 2272 (1997).

[46] P.E. Coleman and P.L. Knight, “Population trapping in photoionisation to dressed continuum states,” Journal of Physics B, 15, 561 (1982).

[47] E. Arimondo, “V Coherent Population Trapping in Laser Spectroscopy,” Progress in Optics 35, 257-354 (1996).

[48] R.M. Whitley and C.R. Stroud, Jr., “Double optical resonance,” Physical Review A 14, 1498 (1976).

[49] H.R. Gray, R.M. Whitley, and C.R. Stroud, “Coherent trapping of atomic populations,” Optics Letters 3(6), 218-220 (1978).

[50] D.A. Steck, “Rubidium 85 D Line Data,” available online at http://steck.us/alkalidata (revision 2.1.6, 20 September 2013).

[51] D.A. Steck, “Rubidium 87 D Line Data,” available online at http://steck.us/alkalidata (revision 2.0.1, 2 May 2008).

[52] M.S. Shahriar, Y. Wang, S. Krishnamurthy, Y. Tu, G.S. Pati, and S. Tseng, “Evolution of an N-level system via automated vectorization of the Liouville equations and application to optically controlled polarization rotation,” Journal of Modern Optics 61(4) 351-367 (2014).

[53] Z. Zhou, J. Yablon, M. Zhou, Y. Wang, A. Heifetz, and M.S. Shahriar, “Modeling and analysis of an ultra-stable subluminal laser,” Optics Communications 358, 6-19 (2016).

[54] Y. Wang, Z. Zhou, J. Yablon, and M.S. Shahriar, “Effect of multi-order harmonics in a double-Raman pumped gain medium for a superluminal laser,” Optical Engineering 54(5) 057106 (2015).

[55] N. Rabeendran, *A Study of Ring Laser Gyroscopes*. MS thesis, University of Canterbury, 2008.

[56] J.R. Wilkinson, “Ring Lasers,” Progress in Quantum Electronics 11, 1-103 (1987).

[57] S. Ezekiel, “Optical Gyroscope Options: Principles and Challenges,” OSA Technical Digest, MC1 (2006).

[58] “Vapor pressure of the metallic elements,” in CRC Handbook of Chemistry and Physics, Internet Version 2005, David R. Lide, ed., <http://www.hbcpnetbase.com>, CRC Press, Boca Raton, FL, 2005.

[59] D. Phillips, “Notes on the Rb Maser and the CPT Clock,” https://www.cfa.harvard.edu/~dphil/work/rbmaser/masernotes.pdf.

[60] C. Henry, “Theory of the Linewidth of Semiconductor Lasers,” IEEE Journal of Quantum Electronics 18(2), 259-264 (1982).

[61] M.A. Biot, “General Theorems on the Equivalence of Group Velocity and Energy Transport,” The Physical Review 105(4), 1129-1137 (1957).

APPENDIX A

MATLAB Code for Calculating Susceptibility and Frequency Sensitivity of a DPAL with a Raman Induced Dip

```
clear all;

% Physical Parameters
kB = 1.38e-23;   % Boltzmann constant
h = 6.626e-34;   % Planck's constant
c = 3e8;         % Speed of light
p2den = 0.02504e27;   % Factor between pressure and number density
amu2kg = 1.66e-27;    % Factor between amu and kg
mC = 12.0107;         % Atomic mass of carbon in amu
mH = 1.00794;         % Atomic mass of hydrogen in amu
FSMCS = 7.7e-19;    % Fine-structure mixing cross section for Rb85

wm85 = 2 * pi * 3.036e9;   % Rb-85: Frequency difference between level 1 and level 2 in
radian/s
wm87 = 2 * pi * 6.835e9;   % Rb-87: Frequency difference between level 1 and level 2 in
radian/s
Offset87 = - 2 * pi * 2.501e9;   % Difference between the lowest level of Rb-85 and Rb-87

Temp = 120 + 273.15;   % DPAL gain cell temperature in Kelvin
TempRaman = 100 + 273.15;   % Raman cell temperature in Kelvin
Pressure = 760*0.06;   % Pressure of ethane in torr

Isat = 66.51;
Isat85 = 72.10;
Isat87 = 55.64;
IsatProbe = 62.82;
IsatPump = 83.45;

nethane = Pressure / 760 * p2den;  % Number density of ethane in meters^-3
methane = (2 * mC + 6 * mH) * amu2kg;  % Molecular mass of ethane in kg
vr = (3 * kB * Temp / methane)^0.5;  % Relative velocity between Rb and ethane molecules
Gamma43 = nethane * FSMCS * vr;   % In rad/s
Gamma34 = Gamma43 * 2 * exp(-dE / (kB * Temp));  % In rad/s
```

```
dE = h * c * (1/780.2 - 1/795) * 1e9;  % Energy difference between level 3 and level 4
NumberDensityDPAL = 10^(9.318-4040/Temp)/(kB*Temp);
NumberDensityRaman = 10^(9.318-4040/TempRaman)/(kB*TempRaman);
n0 = NumberDensityDPAL; % Number density of gain atoms
nRaman = 1.9796e17; % Number density of dip atoms

% Cavity Related Parameters
L = 0.72 + 3.36388e-7;   % Cavity length (meters)
LGain = 0.1;   % Gain medium length (meters)
LRaman = 0.1;   % Dip medium length (meters)
Roc = 0.60;   % Reflectivity of the output coupler
ICL = 0.10;   % Intra-cavity loss
v0 = c * 2 * pi / (795e-9); % Laser frequency
kwav = 2 * pi / (795e-9); % Laser wavevector
FSR = c / L; % Free spectral range
Finnesse = pi / ((1 - Roc)+ICL);
GammaC = FSR / Finnesse; % Empty cavity linewidth
Qcav = v0 / (2 * GammaC);   % Cavity quality factor
FF = 4 * Roc /((1-Roc)^2);

% Beam size
AreaRP = pi * (1000e-6)^2; % Beam area of the Raman probe inside the Raman cell
AreaDPAL = pi * (130e-6)^2; % Beam area of the laser inside DPAL gain cell
AreaRS = pi * (350e-6)^2; % Beam area of the laser (Raman pump) inside the Raman cell

OmegaS_R = (AreaDPAL/AreaRS)^0.5; % Rabi frequency ratio between Raman cell and DPAL
gain cell

% Decay rate between level 1 and 2
Gamma12 = 2 * pi * 7/5*1e6;   % Decay rate from level 1 to level 2 in rad/s
Gamma21 = 2 * pi * 1e6;       % Decay rate from level 2 to level 1 in rad/s

a = 1;   % Signal fraction between 3-2 and 3-1
b = 1;   % Pump fraction between 4-2 and 4-1

tD1 = 27.7e-9;   % Lifetime of D1 (sec)
tD2 = 26.24e-9;   % Lifetime of D2 (sec)
GammaS = 1 / tD1;   % Decay rate of D1 in rad/s
GammaP = 1 / tD2;   % Decay rate of D2 in rad/s

GammaVAS = 2*pi*0e9; % Doppler broadening in S orbital
GammaVAP = 2*pi*0.6e9; % Doppler broadening in P orbital
```

```
Asus = h/(2*pi) * c * n0 * GammaS/2 / Isat;   % Prefactor of susceptibility
Asus85 = h/(2*pi) * c * n0 * GammaS/2 / Isat85;  % Prefactor of 85Rb susceptibility
Asus87 = h/(2*pi) * c * n0 * GammaS/2 / Isat87; % Prefactor of 87Rb susceptibility
AsusOP = h/(2*pi) * c * n0 * GammaP/2 / Isat;
AsusRaman = h/(2*pi) * c * nRaman * GammaS/2 / Isat;
AsusProbe = h/(2*pi) * c * nRaman * GammaS/2 / IsatProbe;
AsusPump = h/(2*pi) * c * nRaman * GammaS/2 / IsatPump;

% Dephasing rates
GammaDph = 2 * pi * 20e6 * Pressure;
GammaDph21 = GammaDph * 1;
GammaDph43 = GammaDph * 1;

R = 5e2+1;   % Number of sample points
StepLimit = 1e2;  % Maximum trial times
T = 1;
N = 4;   % Number of levels in the DPAL gain medium
NRaman = 4;  % Number of levels in the Raman cell medium

PowerRP = 8.3e-3;
IRP0 = PowerRP/AreaRP;
OmegaRP = GammaS/2 * (PowerRP / AreaRP / IsatProbe)^0.5;

CenterFreq = 2 * pi * 3.7e9;
DeltaR = CenterFreq;
Initial = 3e1;
MOD = 0.22;

PowerROP = 10e-3;
AreaROP = pi*(900e-6)^2;
OmegaROP = GammaP/2 * (PowerROP / AreaROP / Isat)^0.5;
Nmode = round((v0+CenterFreq) * L / (2 * pi * c));

PowerOP = 1.2; % DPAL optical pump power in Watts
AreaOP = pi*(200e-6)^2; % Area of the optial pump for DPAL (m^2)
OmegaP = ((PowerOP/AreaOP)/Isat)^0.5 * GammaP;

% Initialize matrices
H85 = zeros(N, N);  % Hamiltonnian of Rb-85
H87 = zeros(N, N);  % Hamiltonnian of Rb-87
HRaman = zeros(N,N);
```

```
Psource = zeros(N, N);  % Source term matrix
Pdephasing = zeros(N, N);  % Dephasing term matrix
Density = zeros(N, N);  % Density matrix
M = zeros(N^2, N^2);   % M matrix
Q = zeros(N, N);  % Q matrix
MRaman = zeros(NRaman^2,NRaman^2);
QRaman = zeros(NRaman, NRaman);
DeltaP = 0;   % Pump detuning
Delta10 = zeros(1,R); % DeltaRP = DeltaR.*ones(T,R); x`
DeltaOff = zeros(1,R);

Offset = 2*pi*4e8 * 0;

DetuningMin =  - 2 * pi * 3e6;
DetuningMax =  + 2 * pi * 1e6;
DetuningSpacing = (DetuningMax - DetuningMin)/(R-1);
Delta2 = 2.*pi.*1.2e6.*ones(1,R);
Delta2x = (Delta2)./(2.*pi);
DeltaRP = DetuningMin : DetuningSpacing : DetuningMax;
DeltaRP = DeltaRP + DeltaR;

A85 = zeros(N^2, R); % A vector (85Rb)
A87 = zeros(N^2, R); % A vector (87Rb)
ARaman = zeros(N^2, R);
B = zeros((N^2-1), 1);  % B vector
S = zeros((N^2-1), 1);  % S vector
W = zeros((N^2-1), (N^2-1));  % W matrix
BRaman = zeros((NRaman^2-1), 1);
SRaman = zeros((NRaman^2-1), 1);
WRaman = zeros((NRaman^2-1), (NRaman^2-1));
Susceptibility = zeros(1, R);
Susceptibility85 = zeros(1, R);
Susceptibility87 = zeros(1, R);
SusceptibilityRaman = zeros(1, R);
ChiOP = zeros(1, R);
SusProbe = zeros(1, R);
TotSus = zeros(1,R);
Gain = zeros(1,R);
GainRaman = zeros(1,R);
```

```
% Lasing condition judgement parameters
DeltaSFinal = zeros(1,R);
OmegaSFinal = zeros(1,R);
Fail = ones(1,R);
Difference = zeros(T,R);
Error = zeros(1,T);
Position = zeros(1,T);
FreqLength = zeros(1,T);
OmegaSLength = zeros(1,T);
LMin = -8e-9;
LMax = +12e-9;
LSpacing = (LMax - LMin) / (T-1);
DeltaL = LMin : LSpacing : LMax;

OmegaSSolve = 0;
OmegaSLaser = 0;

LasingConOmega = 0;
CountOmega = 1;  % Count how many times tried

tic;

% Solving Liouville eqaution and laser equations
for n = 1 : T

   for m = 1 : R
      DeltaSolve = 0;
      CountDelta = 1;
      OmegaS = Initial * GammaS;
      LasingConOmega = 0;
      CountOmega = 1;
      OmegaSSolve = 0;
      StepSize = GammaS * 5e1;
      Cross = 0;

      while CountOmega <= StepLimit && OmegaSSolve == 0
         H85 = [-0.5i*Gamma12, 0, 1/(1+a)*OmegaS/2, 1/(1+b)*OmegaP/2; ...
                0, wm85-0.5i*Gamma21, a/(1+a)*OmegaS/2, b/(1+b)*OmegaP/2; ...
                 1/(1+a)*OmegaS/2, a/(1+a)*OmegaS/2, -DeltaRP(n,m)-
                 0.5i*(GammaS+Gamma34),0                        ; ...
                1/(1+b)*OmegaP/2, b/(1+b)*OmegaP/2, 0, -DeltaP-0.5i*(GammaP+Gamma43)];
```

```
for p = 1 : N^2
   for q = 1 : N^2

      % Find indices
      remainder = rem(p, N);
      if remainder == 0
         beta = N;
      else beta = remainder;
      end

      alpha = ( 1 + (p-beta) / N);
      remainder = rem(q, N);

      if remainder == 0
         sigma = N;
      else sigma = remainder;
      end

      eps = (1 + (q-sigma) / N);

      % Set a certain term to 1
      Density = zeros(N,N);
      Density(eps,sigma) = 1;

      Q = (H85 * Density - Density * conj(H85)) * (-1i);

% Source matrix
Psource =
[Gamma21*Density(2,2)+(1/(1+a))*GammaS*Density(3,3)+(1/(1+b))*GammaP*Density(4,4),
0, 0, 0; ...
0, Gamma12*Density(1,1)+(a/(1+a))*GammaS*Density(3,3)+(b/(1+b))*GammaP*Density(4,4),
0, 0; ...
0, 0, Gamma43*Density(4,4), 0; ...
0, 0, 0, Gamma34*Density(3,3)];

Pdephasing = [0, -GammaDph21*Density(1,2),   -GammaDph*Density(1,3),  -
GammaDph*Density(1,4); ...
-GammaDph21*Density(2,1), 0,  -GammaDph*Density(2,3),  -GammaDph*Density(2,4) ; ...
-GammaDph*Density(3,1),  -GammaDph*Density(3,2),  0,  -GammaDph43*Density(3,4); ...
-GammaDph*Density(4,1),  -GammaDph*Density(4,2), -GammaDph43*Density(4,3), 0];
```

```
% Add source terms and dephasing terms
Q = Q + Psource + Pdephasing;
M(p,q) = Q(alpha,beta);
            end
        end

        S = M(1 : (N^2-1), N^2 : N^2);
        W = M(1 : (N^2-1), 1 : (N^2-1));

        for x = 1 : (N - 1)
            W(:, ((x-1) * N + x)) = W(:, ((x-1) * N + x)) - S;
        end

        B = - W \ S;
        A85(N^2, m) = 1;
        A85(1:(N^2-1), m) = B;

        for y = 1 : (N-1)
            A85(N^2, m) = A85(N^2, m) - B(((y-1) * N + y), 1);
        end

        Susceptibility85(1,m) = - Asus85 * (GammaS/2 / OmegaS) * ...,

% Calculate susceptibility
(A85(9,m) + A85(10,m));

H87 = [Offset87-0.5i*Gamma12, 0, 1/(1+a)*OmegaS/2, 1/(1+b)*OmegaP/2; ...
0, Offset87+wm87-0.5i*Gamma21, a/(1+a)*OmegaS/2, b/(1+b)*OmegaP/2; ...
1/(1+a)*OmegaS/2, a/(1+a)*OmegaS/2, -DeltaRP(n,m)-0.5i*(GammaS+Gamma34), 0; ...
1/(1+b)*OmegaP/2, b/(1+b)*OmegaP/2, 0, -DeltaP-0.5i*(GammaP+Gamma43)];

        for p = 1 : N^2
            for q = 1 : N^2

                % Find indices
                remainder = rem(p, N);

                if remainder == 0
                    beta = N;
                else beta = remainder;
                end
```

```
                alpha = ( 1 + (p-beta) / N);
                remainder = rem(q, N);

                if remainder == 0
                   sigma = N;
                else sigma = remainder;
                end

                eps = (1 + (q-sigma) / N);

                % Set a certain term to 1

                Density = zeros(N,N);
                Density(eps,sigma) = 1;

                Q = (H87 * Density - Density * conj(H87)) * (-1i);

% Source matrix
Psource =
[Gamma21*Density(2,2)+(1/(1+a))*GammaS*Density(3,3)+(1/(1+b))*GammaP*Density(4,4),
0,  0,  0; ...
0, Gamma12*Density(1,1)+(a/(1+a))*GammaS*Density(3,3)+(b/(1+b))*GammaP*Density(4,4),
0, 0; ...
0,  0,  Gamma43*Density(4,4), 0; ...
0,  0,  0,  Gamma34*Density(3,3)];

Pdephasing = [0, -GammaDph21*Density(1,2), -GammaDph*Density(1,3),
GammaDph*Density(1,4); ...
-GammaDph21*Density(2,1), 0, -GammaDph*Density(2,3), -GammaDph*Density(2,4); ...
-GammaDph*Density(3,1), -GammaDph*Density(3,2), 0, -GammaDph43*Density(3,4); ...
-GammaDph*Density(4,1), -GammaDph*Density(4,2), -GammaDph43*Density(4,3), 0];

% Add source terms and dephasing terms
Q = Q + Psource + Pdephasing;
M(p,q) = Q(alpha,beta);

            end
        end

        S = M(1 : (N^2-1), N^2 : N^2);
        W = M(1 : (N^2-1), 1 : (N^2-1));
```

```
            for x = 1 : (N - 1)
               W(:, ((x-1) * N + x)) = W(:, ((x-1) * N + x)) - S;
            end

            B = - W \ S;
            A87(N^2, m) = 1;
            A87(1:(N^2-1), m) = B;

            for y = 1 : (N-1)
               A87(N^2, m) = A87(N^2, m) - B(((y-1) * N + y), 1);
            end

            Susceptibility87(1,m) = - Asus87 * (GammaS/2 / OmegaS) * ...,

 % Calculate susceptibility
            (A87(9,m) + A87(10,m));
            Susceptibility(1,m) = (Susceptibility85(1,m) .* 0.72 + ...,
            Susceptibility87(1,m) .* 0.28);

% Raman Cell Hamiltonian
HRaman = [-0.5i*(MOD*Gamma12), 0, OmegaRP/2, OmegaROP/2  ; ...
0, -(DeltaR+Delta2(1,m))+DeltaRP(n,m)-0.5i*(MOD*Gamma21), OmegaS*OmegaS_R/2, 0; ...
OmegaRP/2, OmegaS*OmegaS_R/2, -(DeltaR+Delta2(1,m))-0.5i*(GammaS+GammaVAS), 0;...
OmegaROP/2, 0,  0, -0.5i*(GammaP+GammaVAP)];

            for p = 1 : NRaman^2
               for q = 1 : NRaman^2

                  % Find indices
                  remainder = rem(p, NRaman);

                  if remainder == 0
                     beta = NRaman;
                  else beta = remainder;
                  end

                  alpha = ( 1 + (p-beta) / NRaman);
                  remainder = rem(q, NRaman);
```

```
            if remainder == 0
               sigma = NRaman;
            else sigma = remainder;
            end

            eps = (1 + (q-sigma) / NRaman);

            % Set a certain term to 1
            densityRaman = zeros(NRaman,NRaman);
            densityRaman(eps,sigma) = 1;

            QRaman = (HRaman * densityRaman - densityRaman * conj(HRaman)) * (-1i);

% Source matrix
PsourceRaman =
[(MOD*Gamma21)*densityRaman(2,2)+(1/(1+a))*(GammaS+GammaVAS)*densityRaman(3,3
)+(1/(1+b))*(GammaP+GammaVAP)*densityRaman(4,4), 0, 0, 0; ...
0,
(MOD*Gamma12)*densityRaman(1,1)+(a/(1+a))*(GammaS+GammaVAS)*densityRaman(3,3)
+(b/(1+b))*(GammaP+GammaVAP)*densityRaman(4,4), 0, 0; ...
0, 0, 0, 0; ...
0, 0, 0, 0];

% Add source terms and dephasing terms
QRaman = QRaman + PsourceRaman;
MRaman(p,q) = QRaman(alpha,beta);
               end
            end

            SRaman = MRaman(1 : (NRaman^2-1), NRaman^2 : NRaman^2);
            WRaman = MRaman(1 : (NRaman^2-1), 1 : (NRaman^2-1));

            for x = 1 : (NRaman - 1)
               WRaman(:, ((x-1) * NRaman + x)) = WRaman(:, ((x-1) * NRaman + x)) - SRaman;
            end

            BRaman = - WRaman \ SRaman;
            ARaman(NRaman^2, m) = 1;
            ARaman(1:(NRaman^2-1), m) = BRaman;
```

```
        for y = 1 : (NRaman-1)
            ARaman(NRaman^2, m) = ARaman(NRaman^2, m) - BRaman(((y-1) * NRaman +
y), 1);
        end

            SusceptibilityRaman(1,m) = - AsusProbe * ((1/(1+a))*GammaS / OmegaS) *
ARaman(10,m);
            SusProbe(1,m) = - AsusPump * ((1/(1+a))*GammaS / OmegaRP) * ARaman(9,m);

TotSus(1,m) = Susceptibility(1,m) * LGain / L + SusceptibilityRaman(1,m) * LRaman / L;
        Gain(1,m) = -imag(TotSus(1,m)) * kwav * L;
        GainRaman(1,m) = -imag(SusceptibilityRaman(1,m)) * kwav * L;

        if abs(imag(TotSus(1,m)) + (1/Qcav)) < 1e-9 * abs(1/Qcav)
            OmegaSFinal(1,m) = OmegaS;
            OmegaSSolve = 1;
            LasingConOmega = 1;
            Fail(1,m) = 0;

        else if (-imag(TotSus(1,m)) < (1/Qcav)) && (LasingConOmega == 0)
            OmegaSFinal(1,m) = 0;
            OmegaSSolve = 1;
            Fail(1,m) = 0;

        else if (-imag(TotSus(1,m)) > (1/Qcav)) && (Cross == 1)
            StepSize = - StepSize/2;
            LasingConOmega = 1;
            Cross = 0;

        else if (-imag(TotSus(1,m)) < (1/Qcav)) && (Cross == 0)
            StepSize = - StepSize/2;
            LasingConOmega = 1;
            Cross = 1;

        else if (-imag(TotSus(1,m)) > (1/Qcav)) && (Cross == 0)
            LasingConOmega = 1;
            end
            end
            end
            end
        end
```

```
            OmegaS = OmegaS + StepSize;
            CountOmega = CountOmega + 1;

        end

        Wcav = 2 * pi * Nmode * c / (L);
        Delta10(1,m) = Wcav/(1 + real(TotSus(1,m)) / 2);
        Difference(n,m) = v0 + DeltaRP(n,m) - Delta10(1,m);

    end
    Lx = 2 * pi * Nmode * c ./ (DeltaRP + v0) ./ (1 + real(TotSus)./2);
    L0 = Lx(1,(R + 1)/ 2);
    dL = Lx - L0;
end

Time = toc;

if Time < 60
    TimeStr = [num2str(round(Time)) ' sec'];
    display(TimeStr);

else if Time < 3600
    TimeMin = floor(Time/60);
    TimeSec = round(Time - TimeMin*60);
    TimeStr = [num2str(TimeMin) ' min ' num2str(TimeSec) ' sec'];
    display(TimeStr);

else
    TimeHour = floor(Time/3600);
    TimeMin = floor((Time-TimeHour*3600)/60);
    TimeSec = round(Time -TimeHour*3600 - TimeMin*60);
    TimeStr = [num2str(TimeHour) ' hour ' num2str(TimeMin) ' min ' num2str(TimeSec) ' sec'];
    display(TimeStr);
    end
end

Failure = sum(Fail);
display(Failure);

Delta1 = (DeltaRP-DeltaR);
Delta1x = Delta1./(2.*pi);
```

```
Intensity = (1-Roc) .* Isat .* (OmegaSFinal ./ (GammaS/2)).^2;  % Laser output intensity in
W/(m^2)
Power = Intensity .* AreaDPAL .* 1e3;  % Laser power in mW
IRP = IRP0 .* exp(-imag(SusProbe).*kwav.*LRaman);
PowerProbe = IRP.* AreaRP .* 1e3;

df = zeros(T,R);
Enhancement = zeros(T,R);
Empty = -2*pi*Nmode*c/(L^2);
df(1,2:R) = DetuningSpacing./diff(dL);
df(1,1) = df(1,2);
Enhancement(1,:) = df(1,:)./Empty;

% Plot susceptibility and output power
figure(1);
plot(Delta2, DeltaSx);
xlabel('Delta2');
ylabel('{\delta}_{AOM}');
grid on;

figure(2);
plot(dL,Delta1x,'Color', 'k','Linewidth',3);
xlabel('{\Delta}L');
ylabel('{\delta}_1');
grid on;

figure(3);
plot(Delta1x,Enhancement);
xlabel('{\delta}_{1}');
ylabel('Enhancement');
grid on;
```

APPENDIX B

MATLAB Code for Calculating Susceptibility and Frequency Sensitivity of a Raman Laser

```
clear all;

% Parameters
kB = 1.38e-23;  % Boltzmann constant
h = 6.626e-34;  % Planck's constant
c = 3e8;          % Speed of light
mRb = 85.4678;
p2den = 0.02504e27;% Factor between pressure and number density
amu2kg = 1.66e-27;  % Factor between amu and kg

wm85 = 2 * pi * 3.036e9; % Rb-85: Frequency difference between level 1 and level 2 in radian/s
wm87 = 2 * pi * 6.835e9;  % Rb-87: Frequency difference between level 1 and level 2 in
radian/s
HF85 = 361.58e6;
HF87 = 814.5e6;
Ratio = 0.72;   % Percentage of 85Rb atoms

IsatD1 = 66.76;    % Saturation intensity (D1 line) in W/(m^2)
IsatD2 = 43.283;  % Saturation intensity (D2 line) in W/(m^2)

% Cavity related
L = 1+7.06e-8;  % Cavity length (meters)
LGain = 0.10;  % Length of gain cell (meters)
Roc = 0.90;     % Reflectivity of the output coupler

v0 = c * 2 * pi / (795e-9);
Lambda = 795e-9;
kwav = 2 * pi / (795e-9);

kD1 = 2 * pi / (795e-9);
kD2 = 2 * pi / (780e-9);

Num = round(v0 * L / (2 * pi * c));
FSR = c / L;
Finnesse = pi / (1 - Roc);
```

```
GammaC = FSR / Finnesse;
Qcav = v0 / (2 * GammaC);   % Cavity quality factor

% Decay rate between level 1 and 2
Gamma12_85 = 2 * pi * 1e6;   % Decay rate from level 1 to level 2 in rad/s
Gamma21_85 = 2 * pi * 1e6;   % Decay rate from level 2 to level 1 in rad/s

tD1 = 27.7e-9;    % Lifetime of D1 (sec)
tD2 = 26.24e-9;  % Lifetime of D2 (sec)
GammaD1 = 1 / tD1;   % Decay rate of D1 in rad/s
GammaD2 = 1 / tD2;   % Decay rate of D2 in rad/s

R = 11;   % Number of sample points
T = 1;
G = 101;
N = 4;    % Number of levels
StepLimit = 1e0;   % Maximum trial times

n0 = 8e17;
Temp = 273.15 + 100;
AsusD1 = h/(2*pi) * c * n0 * 0.5 * GammaD1 / IsatD1;  % Used for calculating susceptibility
(D1)
AsusD2 = h/(2*pi) * c * n0 * 0.5 * GammaD2 / IsatD2;  % Used for calculating susceptibility
(D2)

% Initialize matrices
H85 = zeros(N, N);    % Hamiltonnian of 85Rb
H87 = zeros(N, N);    % Hamiltonnian of 87Rb
Psource = zeros(N, N);   % Source term matrix
density = zeros(N, N);    % Density matrix
M = zeros(N^2, N^2);    % M matrix
Q = zeros(N, N);       % Q matrix

A85 = zeros(N^2, R);    % A vector (85Rb)
A87 = zeros(N^2, R);    % A vector (87Rb)
B = zeros((N^2-1), 1);   % B vector
S = zeros((N^2-1), 1);   % S vector
W = zeros((N^2-1), (N^2-1));   % W matrix

Susceptibility85 = zeros(1, R);
TotSus = zeros(1,R);
NumLasing = zeros(1,R);
```

```
% Doppler broadening
if G == 1

    Velocity = 0;
    VWeight = 1;

else

    VSigma = (2*kB*Temp/(mRb*amu2kg))^0.5;

    VMin = - 2*VSigma;
    VMax = + 2*VSigma;
    VSpacing = (VMax - VMin)/(G-1);
    Velocity = VMin : VSpacing : VMax;

    VDis = exp(-Velocity.^2./VSigma.^2);
    VNor = sum(VDis);
    VWeight = 1./VNor.*VDis;

end

DeltaVD2 = kD2.*Velocity;
DeltaVD1 = 1.*kD1.*Velocity;

DiaRS = 950e-6;
DiaRP = 950e-6;
DiaOP = 950e-6;

PowerRP = 12e-3;
OmegaRP = GammaD1 * (PowerRP / (pi*(DiaRP/2)^2 * IsatD1)).^0.5;

PowerOP = 20e-6;
OmegaOP = GammaD2 * (PowerOP / (pi*(DiaOP/2)^2 * IsatD2)).^0.5;

Initial = 1e-1;
OmegaRS = 1e-1 * GammaD1;   % Rabi frequency of Raman signal

% Define detuning
RamanDetuning = + 1e9 + 7.72e7;
CenterFreq = RamanDetuning;

LSPg = OmegaRP^2/(4*2*pi*RamanDetuning);
```

```
DetuningMin = + 2*pi*RamanDetuning - 2*pi*0.9e6;
DetuningMax = + 2*pi*RamanDetuning - 2*pi*0.6e6;
DetuningSpacing = (DetuningMax - DetuningMin)/(R-1);
DeltaRP = + 2*pi*RamanDetuning - 0*LSPg;
DeltaRS = DetuningMin : DetuningSpacing : DetuningMax;
DeltaRSx = DeltaRS ./(2*pi) - RamanDetuning;

% Lasing condition judgement parameters
DeltaSFinal = zeros(1,R);
OmegaSFinal = zeros(1,R);
Fail = zeros(1,R);
Difference = zeros(1,R);

NumVec = zeros(1,T);
Error = zeros(1,T);
Position = zeros(1,T);
FreqSol = zeros(1,T);
OmegaSSol = zeros(1,T);

OmegaSSolve = 0;
OmegaSLaser = 0;

LasingConOmega = 0;
CountOmega = 1;

tic;

for n = 1 : T
   for m = 1 : R
      OmegaRS = Initial * GammaD1;   % D1 rabi frequency
      OmegaSSolve = 0;
      CountOmega = 1;
      Cross = 0;
      LasingConOmega = 0;
      StepSize = GammaD1 * 1e0;

      while CountOmega <= StepLimit && OmegaSSolve == 0
         TotSus(1,m) = 0;
```

```
for g = 1 : G
   H85 = [-0.5i*Gamma12_85, 0, OmegaRS/2, OmegaOP/2; ...
   0, -DeltaRS(1,m)+DeltaRP-0.5i*Gamma21_85, OmegaRP/2, 0; ...
   OmegaRS/2, OmegaRP/2, -DeltaRS(1,m)-DeltaVD1(1,g)-0.5i*GammaD1, 0; ...
   OmegaOP/2, 0, 0, -DeltaVD2(1,g)-0.5i*GammaD2];

   % Deploy N-level algorithm
   for p = 1 : N^2
      for q = 1 : N^2

         % Find indices
         remainder = rem(p, N);
         if remainder == 0
            beta = N;

         else beta = remainder;
         end

         alpha = ( 1 + (p-beta) / N);
         remainder = rem(q, N);

         if remainder == 0
            sigma = N;

         else sigma = remainder;
         end

         eps = (1 + (q-sigma) / N);

         % Set a certain term to 1
         density = zeros(N,N);
         density(eps,sigma) = 1;

         Q = (H85 * density - density * conj(H85)) * (-1i);

         % Source matrix
         Psource =
[Gamma21_85*density(2,2)+0.5*GammaD1*density(3,3)+0.5*GammaD2*density(4,4),  0,  0,
0; ...
0, Gamma12_85*density(1,1)+0.5*GammaD1*density(3,3)+0.5*GammaD2*density(4,4), 0, 0;
...
```

```
0, 0, 0, 0; ...
0, 0, 0, 0 ];

% Add source terms
                Q = Q + Psource;
                M(p,q) = Q(alpha,beta);
              end
            end

            S = M(1 : (N^2-1), N^2 : N^2);
            W = M(1 : (N^2-1), 1 : (N^2-1));

            for x = 1 : (N - 1)
              W(:, ((x-1) * N + x)) = W(:, ((x-1) * N + x)) - S;
            end

            B = - W \ S;
            A85(N^2, m) = 1;
            A85(1:(N^2-1), m) = B;

            for y = 1 : (N-1)
              A85(N^2, m) = A85(N^2, m) - B(((y-1) * N + y), 1);
            end

            Susceptibility85(1,m) = - AsusD1 * (0.5*GammaD1 / OmegaRS)* A85(9,m);
            TotSus(1,m) = TotSus(1,m) + VWeight(1,g) * Susceptibility85(1,m) * LGain / L;
          end

          if abs(imag(TotSus(1,m)) + (1/Qcav)) < 1e-10 * abs(1/Qcav)
            OmegaSFinal(1,m) = OmegaRS;
            OmegaSSolve = 1;
            LasingConOmega = 1;
            NumLasing(1,m) = round((v0+DeltaRS(1,m)) * L * (1+real(TotSus(1,m))/2) / (2 * pi *
c));

            elseif (-imag(TotSus(1,m)) < (1/Qcav)) && (LasingConOmega == 0)
            OmegaSFinal(1,m) = 0;
            OmegaSSolve = 1;

            elseif (-imag(TotSus(1,m)) > (1/Qcav)) && (Cross == 1)
            StepSize = - StepSize/5;
            Cross = 0;
```

```
            elseif (-imag(TotSus(1,m)) < (1/Qcav)) && (Cross == 0)
            StepSize = - StepSize/5;
            LasingConOmega = 1;
            Cross = 1;

            elseif (-imag(TotSus(1,m)) > (1/Qcav)) && (Cross == 0)
            LasingConOmega = 1;
          end

          CountOmega = CountOmega + 1;
          OmegaRS = OmegaRS + StepSize;
        end

        if OmegaSSolve == 0
          Fail(1,m) = 1;
        end

        NumVec(1,n) = round((1 + real(TotSus(1,m)) ./ 2) .*(v0+DeltaRS(1,m)) .* L ./ (2 .* pi .*
c));
        Wcav = 2 * pi * NumVec(1,n) * c / L;
        Difference(1,m) = Wcav - (1 + real(TotSus(1,m)) / 2) * ...,
        (v0 + DeltaRS(1,m));

    end

    [Error(1,n), Position(1,n)] = min(abs(Difference));

    FreqSol(1,n) = DeltaRS(1, Position(1,n));
    OmegaSSol(1,n) = OmegaSFinal(1, Position(1,n));

end

Power = IsatD1.* (1-Roc) .* (OmegaSSol./GammaD1).^2.*pi*(DiaRS/2)^2.*1e6;

Lx = 2 * pi * Num * c ./ (DeltaRS + v0) ./ (1 + real(TotSus)./2);
Lcen = Lx(1,(R + 1)/ 2);
dL = Lx - Lcen;

LxEmpty = 2 * pi * Num * c ./ (DeltaRS + v0);
L0Empty = LxEmpty(1,(R + 1)/ 2);
dLEmpty = LxEmpty - L0Empty;
```

```
Empty = -2*pi*Num*c/(L^2);
Enhancement = (dL(end) - dL(1))/(dLEmpty(end) - dLEmpty(1));
TimeN = toc;

if TimeN < 60
   Time = [num2str(round(TimeN)) ' sec'];
   display(Time);

else if TimeN < 3600
   TimeMin = floor(TimeN/60);
   TimeSec = round(TimeN - TimeMin*60);
   Time = [num2str(TimeMin) ' min ' num2str(TimeSec) ' sec'];
   display(Time);

else
   TimeHour = floor(TimeN/3600);
   TimeMin = floor((TimeN-TimeHour*3600)/60);
   TimeSec = round(TimeN -TimeHour*3600 - TimeMin*60);
   Time = [num2str(TimeHour) ' hour ' num2str(TimeMin) ' min ' num2str(TimeSec) ' sec'];
   display(Time);
   end
end

display(['The power is ' num2str(Power) ' uW.']);
display(['The slow light enhancement is ' num2str(Enhancement) '.']);

% Plot real and imaginary parts of susceptibility
figure(1);
subplot(2,1,1);
plot(DeltaRSx, -imag(TotSus),DeltaRSx, ones(1,R)./Qcav,DeltaRSx(1,Position).*ones(1,R),-
imag(TotSus));
set(gca,'FontName','Times New Roman','FontSize',16);
xlabel('Lasing Frequency','FontName','Times New Roman','FontSize',20);
ylabel('-{\chi}''''','FontName','Times New Roman','FontSize',20);
grid on;

subplot(2,1,2);
plot(DeltaRSx, real(TotSus));
set(gca,'FontName','Times New Roman','FontSize',16);
xlabel('Lasing Frequency','FontName','Times New Roman','FontSize',20);
ylabel('-{\chi}''','FontName','Times New Roman','FontSize',20);
grid on;
```